

Electro-formation of Cu-graphene composites and its property evaluation

Akhya Kumar Behera



Department of Metallurgical and Materials Engineering
National Institute of Technology, Rourkela

Electro-formation of Cu-graphene composites and its property evaluation

*Dissertation submitted in partial fulfillment
of the requirements of the degree of*

Doctor of Philosophy

in

Metallurgical and Materials Engineering

by

Akhya Kumar Behera

(Roll Number: 514MM1012)

*based on research carried out
under the supervision of
Prof. Archana Mallik*



October 2020

Department of Metallurgical and Materials Engineering
National Institute of Technology Rourkela



Department of Metallurgical and Materials Engineering
National Institute of Technology Rourkela

October 2020

Certificate of Examination

Roll Number: *514MM1012*

Name: *Akhya Kumar Behera*

Title of Dissertation: *Electro-formation of Cu-graphene composites and its property evaluation*

We the below signed, after checking the dissertation mentioned above and the official record book (s) of the student, hereby state our approval of the dissertation submitted in partial fulfillment of the requirements of the degree of *Doctor of Philosophy in Metallurgical and Materials Engineering* at *National Institute of Technology Rourkela*. We are satisfied with the volume, quality, correctness, and originality of the work.

Archana Mallik
Supervisor

Bankim Chandra Ray
Member, DSC

S.Sen
Member, DSC

S.C.Mishra
Chair person

Shantanu K.Behera
Member, DSC

G. S. Mohobia, IIT BHU
External Examiner

A. Basu
Head of the Department



Department of Metallurgical and Materials Engineering
National Institute of Technology Rourkela

Prof. Archana Mallik
Associate Professor

5th October 2020

Supervisors' Certificate

This is to certify that the work presented in the dissertation entitled *Electro-formation of Cu-graphene composites and its property evaluation* submitted by *Akhya Kumar Behera*, Roll Number 514MM1012, is a record of original research carried out by him under our supervision and guidance in partial fulfillment of the requirements of the degree of *Doctor of Philosophy in Metallurgical and Materials Engineering*. Neither this dissertation nor any part of it has been submitted earlier for any degree or diploma to any institute or university in India or abroad.

Archana Mallik
Supervisor

Dedication

This thesis is dedicated

To

My beloved

Family

Dear father and mother,

"It could not be possible without your support, love, care, faith and encouragement. Despite many odds, you let me pursue my dreams. I will always remain thankful to God, that he gave me to have you."

With love, your happiest son

Declaration of Originality

I, Mr. Akhya Kumar Behera, Roll Number *514MM1012* hereby declare that this dissertation entitled *Electro-formation of Cu-graphene composites and its property evaluation* presents is my original work carried out as a doctoral student of NIT Rourkela and, to the best of my knowledge, contains no material previously published or written by another person, nor any material presented by me for the award of any degree or diploma of NIT Rourkela or any other institution. Any contribution made to this research by others, with whom I have worked at NIT Rourkela or elsewhere, is explicitly acknowledged in the dissertation. Works of other authors cited in this dissertation have been duly acknowledged under the sections “Reference” or “Bibliography”. I have also submitted my original research records to the scrutiny committee for the evaluation of my dissertation.

I am fully aware that in case of any non-compliance detected in the future, the senate of NIT Rourkela may withdraw the degree awarded to me on the basis of the present dissertation.

October 2020
NIT Rourkela

Akhya Kumar Behera

Acknowledgment

Herewith ending the novel piece of the research work, which involves unconditional help and support by each mentioned personnel and institutions, will be memorized forever.

I bow down to the temple of learning, the National Institute of Technology, Rourkela for every support to carry out the research work.

My sincere gratitude to the supervisor *Prof. Archana Mallik*, for her excellent guidance, constant encouragement, continuous support, generous help, and inspiration during the entire period of the research work. It is a blessing for me to be associating with her, who helped me for the realization and utilization of my knowledge to face the challenges to the current scenario of world's materials science research community. Her persistency, dedication, and involvement towards the work are a gift, which I learned and enjoyed most during this curriculum of this research work. Above all, her loving heart and caring nature are the most memorable entity, which I was fascinated during this research journey of my life.

My sincere thanks are to *Prof. A. Basu*, Head, Department of Metallurgical and Materials Engineering, for providing all necessary facilities for this work.

The 'pearl' of the Institute, the Director with his motivational guidance, unconditional support and continuous forecasting the vision paved and energized me to drive patiently and efficiently in my research career on staying period at NIT Rourkela. I am glad for being a scholar under his administratorship to this learning temple.

I sincerely thank my doctoral scrutiny committee members, *Prof. S. C. Mishra, Prof. B. C. Ray, Prof. S. Sen and Prof. S. K. Behera* for spending their valuable time and useful suggestion for shaping the thesis work.

I am very much thankful to the technical team of Metallurgical and Materials Engineering Department, especially *Mr. U. K. Sahu, Mr. S. Pradhan and Mr. R. Pattnaik* for gesturing their technical expert during the research work.

It is a great pleasure for me to acknowledge all my lab mates *Sumant bhai, Ramkumar, Amlan, Deepak, Pundrikaksha, Sudeshna, Priti, Prekshya, Duleshwar, Gaurav, Azmera, Ravi, Preeti, Rakesh, Rajat and Alok* for being helping hand and supportiveness.

I would like to express my deepest gratitude to my family members who have always been supporting throughout my studies. The lovely peoples are my Parents, *Mr. Bhikari Behera and Ms. Padma Behera*; my uncle Trinath ; my brothers, *Satya, Narayan and Late*

Sanysi; my brother-in-law *Pabitra*; my sister *Rasmita* and to my cute niece *Kunu*, *Ganesh, babu, Laxmipriya, Krishna and saina*. Being with them, the god-like people, I enjoy my pride within.

I am also grateful to my close friends, *Er. Ananta Ram Sabat, Krushna, Rajiba, Srikar, Santosh, Jitendra, Somonath, Bharat, Satya and Nilamani* for making me what I am today!

All errors and limitations remaining in this thesis are mine alone.

Date: October 2020
NIT Rourkela

Akhya Kumar Behera
Roll Number: 514MM1012

Abstract

In the current study, few-layer graphene particles (FLGPs) have been synthesized by electrochemical exfoliation method. Two different electrolytes of 1M H₂SO₄ and HNO₃ were used. The electrolyte produces anions of SO₄²⁻ and NO₃⁻ which interact with pyrolytic graphite sheets to intercalate and produce FLGPs. Further, the prepared FLGPs are reduced by ascorbic acid and hydrazine hydrate and are leveled as RFLGPs(Vc) and RFLGPs(Hy) respectively. The prepared graphene particles were then analyzed by various scientific analyses such as TGA, XRD, FTIR, XPS, UV and Raman spectroscopy. Thermal stability and yield of graphene particles are done by TGA analysis. XRD and Raman spectroscopy were used for structural properties, lattice spacing and crystal structure of graphene particles. The (001) and (002) lattice plane of graphene oxide and graphene has been observed at 13° and 26.2° from XRD analysis. The as-synthesized graphene were expected to be functionalized which was confirmed by FTIR analysis and the functional groups are hydroxy, carboxy, epoxides and alcohol. The prepared FLGPs were then analyzed by XPS to quantify carbon oxygen ratio. The electronic transitions of π - π^* and n - π^* have been analyzed by UV-visible spectra. The topographical and morphological analysis of graphene has been carried out by FESEM and TEM analysis. The FESEM microscopy shows the agglomeration and layer structure. The TEM analysis gives the number of layers of graphene particles. The in-house synthesized graphene was found to consist of few layers and was partially functionalized too. The prepared FLGPs and RFLGPs have been used as reinforcement with the copper matrix to synthesize Cu-FLGPs nanocomposite.

Copper-graphene nano-composites were synthesized by the electrodeposition method. FLGPs and RFLGPs of different concentrations (0.1, 0.3 and 0.5 g/L) were added into the copper matrix. The Cu films are plated first onto the steel substrate at different temperatures (25, 20 and 15 °C) to decide the deposition temperature (based upon the film characteristics obtained). Synthesis of the composite films were then carried out and compared in both silent and ultrasonic stirring conditions in the aqueous electrolyte. Cu deposited at 15 °C was best and was chosen to carry out the composite film deposition. The synthesized specimens (Cu and composite films) were characterized by surface Profilometry, XRD, SEM, EDS and AFM analyses. Furthermore, the distribution of

graphene was found to be better in the presence of ultrasound as witnessed from the structural and micro-graphical analysis. Then after the micro and nano-mechanical as well as electrical resistivity properties of the composites were measured to evaluate the performance of the films. The composite films have 31% improved hardness as compared to the pure copper films. The electrical resistivity has been increased from $1.6 \times 10^{-6} \Omega\text{-cm}$ to $3.6 \times 10^{-6} \Omega\text{-cm}$. The electrodeposited Cu-FLGPs composite shows improved mechanical and comparable electrical properties as well as compared to the pure copper thin film. The Cu-RFLGPs composite shows 38% higher hardness as compared to pure copper thin film. The Cu-RFLGPs composites did show an adhesive type of wear leading to delamination of Cu layers. Apart from mechanical properties, the electrical resistivity of the sono-electroplated films was found to be improved as well. The corrosion behaviors of Cu-FLGPs as well as Cu-RFLGPs composite films have been analyzed by three-electrode cell setup. Tests were carried out in two solutions i.e. standard borate buffer and 3.5% NaCl to simulate the general and pitting corrosion behavior respectively. All the composite films show well developed passivation regions in borate buffer and the pitting was also evident from the potentiodynamic polarization plots. The general corrosion tendency and rate was found to be less in composite films. Further pitting was also less in composite films. The mechanism of such observation was proposed by EIS study. Out of the two types, Cu-RFLGPs composites have superior mechanical, electrical and anti-corrosive properties.

Keywords: Graphene, Copper, Nano-composite, Electroplating, Powder Metallurgy, Hardness, Electrical conductivity, Corrosion

Contents

Akhya Kumar Behera.....	i
Certificate of Examination.....	iii
Supervisors' Certificate	iv
Dedication.....	v
Declaration of Originality.....	vi
Acknowledgment.....	viii
Abstract	x
List of Figures	xvi
List of Tables	xxiv
Abbreviations.....	xxvi
1: Introduction	1
1.1 Background.....	2
1.2 Motivation of the research work	3
1.3 Objectives.....	4
1.4 Structure of the dissertation.....	4
2: Literature survey.....	6
2.2 Application of graphene-based composites.....	11
2.3 Categorization of Fabrication Techniques	15
2.3.1 Wet phase Techniques.....	17
2.3.1.1 Direct current electrodeposition.....	17
2.3.1.2 Pulse reverse electro-deposition (PRED).....	20
2.3.1.3 Electroless co-deposition route	22
2.3.1.4 One-pot reduction method	23
2.3.2.1 Powder metallurgy Method	24
2.3.2.1.1 Powder metallurgy with pre-synthesized graphene powders	25
2.3.2.1.1.1 Cold pressing and sintering:	25
2.3.2.1.1.2 Hot pressing and sintering	27
2.3.2.1.2 Powder metallurgy with ball milled graphene powders	29
2.3.2.1.2.1 Ball milling and high-ratio differential speed rolling.....	32
2.3.2.1.2.2 Ball milling and vacuum uniaxial hot pressing	33
2.3.2.2 Accumulative roll bonding (ARB)	33
2.3.3 Mixed phase fabrication techniques	38
2.3.3.1 Molecular-level mixing process with SPS.....	38

2.3.3.2 Freeze-drying and spark plasma sintering.....	41
2.3.3.3 Electroless plating with SPS.....	42
2.3.3.4 In situ chemical reduction and spark plasma sintering.....	43
2.3.3.5 Semi powder mixing and SPS route	44
2.4 Mechanism of property adaptations of Cu-Gr nano-composites:.....	45
2.5 Concluding remarks	49
3: Materials, methods and characterization techniques of FLGPs, RFLGPs, Cu-FLGPs and Cu-RFLGPs	51
3.1 Introduction.....	52
3.2 Materials.....	52
3.3 Synthesis of Few layer graphene particles (FLGPs)	52
3.4 Synthesis of Reduced Few layer graphene particles (RFLGPs).....	53
3.5 Substrate preparation.....	53
3.6 Electrolytic bath preparation, deposition setup and process parameters of Cu and Cu-FLGPs composite	54
3.7 Nomenclature of the as-synthesized FLGPs and composites.....	55
3.8 Instrumentation	55
3.8.1 Two electrode DC system	55
3.8.2 Particle size analyzer	56
3.8.3 Thermo-gravimetric analysis (TGA).....	56
3.8.4 X-ray diffraction (XRD).....	56
3.8.5 Raman spectroscopy	57
3.8.6 X-ray photoelectron spectroscopy (XPS).....	58
3.8.7 Fourier transmission infrared (FTIR) spectroscopy	58
3.8.8 UV-Visible spectroscopy.....	59
3.8.9 SEM, Field emission scanning electron microscope (FESEM) with EDS	59
3.8.10 Transmission electron microscope (TEM).....	60
3.8.11 Atomic force microscope (AFM)	60
3.8.12 Surface profilometer	61
3.8.13 Microhardness measurement.....	61
3.8.14 Wear testing.....	61
3.8.15 Electrical conductivity	62
3.8.16 Corrosion study	62
4: Physicochemical properties of electrochemically synthesized FLGPs and RFLGPs	63
4.1 Introduction.....	64

4.2 Mechanism	65
4.3 Thermal stability and yield in FLGPs and RFLGPs synthesis	66
4.4 Structural analysis of FLGPs.....	68
4.4.1 XRD studies.....	68
4.4.2 Raman studies	69
4.5 Functional analysis.....	70
4.5.1 FTIR studies	70
4.5.2 XPS studies	71
4.5.3 UV-Visible studies.....	75
4.6 Morphological analyses.....	76
4.6.1 FESEM studies	76
4.6.2 TEM studies	79
4.7 Concluding remarks	82
5: Micro and nano-mechanical Properties of Cu-FLGPs and Cu-RFLGPs composites	83
5.1 Ultrasound-assisted electroplating of nano-composite thin film of Cu matrix with electrochemically in-house synthesized few-layer graphene nano-particles as reinforcement ...	84
5.1.1 Introduction.....	84
5.1.2 Electrodeposition of copper and Cu-FLGPs films	84
5.1.3 Analysis of Copper thin films.....	85
5.1.4 Structural analysis of Cu-FLGPs	88
5.1.5 Compositional analysis by EDS elemental mapping study.....	92
5.1.6 Surface micro and nano-mechanical properties	95
5.1.7 Electrical resistivity.....	98
5.1.8 Concluding remarks.....	99
5.2 An exploration of the use of in-house synthesized reduced few-layer graphene particles as reinforcement during sono-electroplating of Cu matrix composite films	100
5.2.1 Introduction.....	100
5.2.2 Analysis of Cu-RFLGPs composite films.....	101
5.2.4 Concluding remarks.....	109
5.3 Wear performance and nano-mechanical behaviour of sono-electroplated Cu-graphene nano-composite thin films	110
5.3.1 Introduction.....	110
5.3.3 Deposition of Cu-graphene onto copper	110
5.3.4 Analysis of Cu-FLGPs and Cu-RFLGPs composite films.....	110
5.3.5 Wear behaviour of Cu-FLGPs and Cu-RFLGPs films.....	116

5.3.6 Concluding remarks.....	124
6: Electrochemical corrosion behaviour of sono-electroplated Cu-graphene nanocomposites in simulated standard and aggressive environment	125
6.1 Introduction.....	126
6.2 Experimental details.....	128
6.2.1 Electrodeposition of Copper-FLGPs nanocomposite films.....	128
6.2.2 Corrosion and other characterization techniques:	128
6.3 Results and discussion.....	129
6.3.1 Electrochemical corrosion studies	129
6.3.2 Corrosion study of Cu-RFLGPs.....	136
6.3.2 EIS Analysis.....	139
6.3.3 Phase and microstructure of samples after corrosion test.....	151
6.3.4 Mechanism:.....	160
6.4 Concluding remarks	163
7: Conclusions.....	164
7.1 Concluding remarks	165
References	167
Dissemination	1777

List of Figures

Figure No.	Caption	Page No.
2.1	(a) No. of publications on Cu-Gr composite from 2011-December 2019, (b) Application of Cu-Gr composite in various sectors	9
2.2	Images of graphene and its properties. Reprinted from Behera et al. [42] Copyright (2018) with permission from Elsevier	11
2.3	Schematic image of application of graphene-based composites	12
2.4	Categorization and schematic image of various synthesis routes and techniques of Cu-Gr composite	16
2.5	Schematic image of Cu-Gr composite prepared by DC electrodeposition route. Reprinted from Behera et al. Copyright (2018) with permission from Elsevier [42]	19
2.6	FESEM images of (a) graphene, Cu-GNSs composite of various graphene concentration (b) 0.1 g/L, (c) 0.5 g/L reprinted from Behera et al. and composites with Gr concentrations of (d) 0.2 g/L, (e) 0.5 g/L and (f) 0.8 g/L reprinted from Song et al. [42,117]	19
2.7	Schematic image of PRED process to synthesize Cu-Gr composite	22
2.8	TEM images of (a) Graphene layer, (b) Cu-Gr nanocomposite and HRTEM image of the Cu-Gr by One-pot reduction method. Reprinted from Li et al. [131]	24
2.9	Schematic of the fabrication process of Cu-Gr composite by cold pressing and sintering (a) Graphite, (b) Cu powders, (c) GO with the negative charge, (d) CTAB modified Cu powders (CTAB\Cu) with the positive charge, (e) GO-Cu powders,(f) Cu-Gr composite. and TEM images of 0.3 wt.% Cu-Gr composite, (g) 0.5 wt.% Cu-Gr composite, (h) TEM image of graphene at the boundary of Cu grains and (i) TEM image of graphene in the triple region of Cu grains Reprinted from Gao et al. [132]. Copyright (2016) with permission from Elsevier	27

	(a) Schematic diagram of the preparation process of Cu-Gr composites by hot pressing and sintering, SEM images of (b) graphene nano-sheets, Cu-Gr powder mixture (c) 2.5% Gr and (d) 10% Gr, Cu-Gr composites Reprinted from Li et al. [83]. Copy right (2015) with permission from Elsevier	28
2.10		
	(a) Schematic of preparation of Cu-Gr composite by Powder metallurgy route with ball milled powder, (b) SEM images of Graphene Nano-sheets and Cu-Gr composite for concentration (c) 0.5 wt% GNSs and (d) 2.0 wt% GNSs. Reprinted from Yue et al. [141]. Copyright (2017) with permission from Elsevier.	31
2.11		
	(a) Schematic image of Cu-Gr composite by MLM and SPS method and SEM image of (b) Graphene flake, fracture surface of Cu-Gr composites (c) 2.5 vol.% and (d) 7.5 vol.%. Reprinted from Yang et al. [154]. Copyright (2018) with permission from Elsevier	39
2.12		
	(a) Schematic illustration of the fabrication process of Cu-Gr composites by freeze-drying and spark plasma sintering route and SEM image of (b) dried CF/Gr/Cu composite powder, (c) CF/Gr/Cu-matrix composite where the dark and white arrows respectively show the agglomerated and dispersed rGO and (d) TEM image of Gr/Cu interface. Reprinted from Zhang et al. [157]. Copyright (2016) with permission from Elsevier	42
2.13		
	SEM image of (a) as-prepared GO, (b) as-prepared Cu-Gr powders and (c) Cu-Gr composites (inset for high magnification) fabricated by Electroless plating with SPS Reprinted from Zhao et al. [155]	43
2.14		
	(a) TEM images of GO nanosheets, SEM images of the fracture surfaces of (b) Cu and (c) 1.0 vol.% GNS–Ni/Cu composites fabricated by In-situ chemical reduction and SPS technique Reprinted from Tang et al. [156]	44
2.15		
	SEM images of the fracture surface of (a) pure Cu, (b) 0.5 vol.% Cu-Gr and (c) 0.5 vol.% Cu-Gr fabricated by Semi powder mixing and SPS technique. Reprinted from Zhang et al.	45
2.16		

2.17	Variation of mechanical properties of Cu-Gr composites prepared by (a) and (d) wet method [117], (b) and (e) dry method [141], (c) and (f) mixed method [151]	45
2.18	Variation of the coefficient of friction of Cu-Gr composite prepared by (a) wet method [123], (b) dry method [146] and (c) mixed method [158]	47
2.19	Variation of electrical properties (a) wet method [42], (b) dry method [134] and (c) mixed method [154]	47
2.20	Variation of corrosion properties of Cu-Gr composites [42,164]	49
4.1	Schematic diagram showing the steps for the synthesis of graphene particles (FLGPs and RFLGPs)	64
4.2	Mechanism of reduced FLGPs (a) Ascorbic acid and (b) Hydrazine hydrate	65
4.3	TGA analysis of (a) PGr, H, HHY1, HHY2, HVC1 and HVC2 RFLGPs and (b) PGr, N, NHY1, NHY2, NVC1 and NVC2 RFLGPs	66
4.4	XRD analysis of (a) PGr, (b) H group (H, HHY1, HHY2, HVC1 and HVC2 RFLGPs) and (c) N Group (N, NHY1, NHY2, NVC1 and NVC2 RFLGPs)	68
4.5	Raman spectra of (a) PGr, (b) H group FLGPs (H, HHY1, HHY2, HVC1 and HVC2 RFLGPs) and (c) N group FLGPs (N, NHY1, NHY2, NVC1 and NVC2 RFLGPs)	69
4.6	FTIR analysis of (a) H Group (H, HHY1, HHY2, HVC1 and HVC2 RFLGPs) and (b) N Group (N, NHY1, NHY2, NVC1 and NVC2 RFLGPs)	70
4.7	XPS spectrum of (a) survey scan of graphene sheets and high resolution C 1s spectrum of (b) H, (c) HHY1, (d) HHY2, (e) HVC1 and (f) HVC2 RFLGPs	72
4.8	XPS spectrum of (a) survey scan of graphene sheets and high resolution C 1s spectrum of (b) N, (c) NHY1, (d) NHY2, (e) NVC1 and (f) NVC2 RFLGPs	73
4.9	UV analysis of (a) H Group (H, HHY1, HHY2, HVC1 and HVC2 RFLGPs) and (b) N Group (N, NHY1, NHY2, NVC1 and	75

	NVC2 RFLGPs)	
4.10	FESEM image of PGr sheets (a) and (c) magnified structure , (b) and (d) high magnified surface view	76
4.11	FESEM image of graphene particles (a) H, (b) HHY1, (c) HHY2, (d) HVC1 and (e) HVC2	77
4.12	FESEM image of graphene particles (a) N, (b) NHY1, (c) NHY2, (d) NVC1 and (e) NVC2	78
4.13	TEM image of graphene particles (a) H, (b) HHY1, (c) HHY2, (d) HVC1 and (e) HVC2	80
4.14	TEM image of graphene particles (a) N, (b) NHY1, (c) NHY2, (d) NVC1 and (e) NVC2	81
5.1.1	(a) Experimental setup of pure copper deposition with sonication at a temperature of 15 °C and (b) Experimental setup of copper-FLGPs electrodeposition with sonication	84
5.1.2	(a) Thickness measurement of Cu thin film by surface profiler, (b) Photography images of as-deposited Cu thin films, XRD pattern for Cu deposited in (c) silent and (d) sonication condition	86
5.1.3	SEM images of Copper samples at different temperature	87
5.1.4	AFM images of Copper samples at different temperature	87
5.1.5	(a) Thickness measurement of Cu-FLGPs thin film by surface profiler, (b) Photography images of as-deposited Cu-FLGPs thin films, XRD pattern for Cu-FLGPs deposited in (c) silent and (d) sonication condition	89
5.1.6	(a) Texture coefficient of Cu-FLGPs composite, (b) grain size and dislocation density of films on silent and ultrasound conditions	89
5.1.7	SEM and 3D AFM images of electroplated Cu-FLGPs composites prepared with varying graphene concentrations: (a,b) 0.1 g/L silent , (c, d) 0.5 g/L silent, (e, f) 0.1 g/L ultrasound and (g, h) 0.5 g/L ultrasound conditions	91
5.1.8	3D AFM images of electroplated Cu-FLGPs composites prepared with varying graphene concentrations	92
5.1.9	EDS image of Cu-FLGPs samples at various graphene concentration	93

5.1.10	Elemental mapping for carbon in electroplated Cu-FLGPs composites prepared with varying graphene concentrations	94
5.1.11	Elemental mapping for copper in electroplated Cu-FLGPs composites prepared with varying graphene concentrations	94
5.1.12	Hardness variation of Cu-FLGPs thin films deposited in (a) silent and (b) sonication conditions	95
5.1.13	FD analysis image of Cu-FLGPs composite at various graphene concentration	97
5.1.14	Electrical resistivity of Cu-FLGPs thin films deposited in (a) silent and (b) sonication conditions.	98
5.2.1	Schematic image of the synthesis route of RFLGPs and Cu-RFLGPs nanocomposite (a) Graphite plates, (b) Electrochemical exfoliation setup, (c), (d) reduced few layered graphene nanoparticles, (e) electrolyte of Cu-RFLGPs composite synthesis, (f) Electrodeposition setup and (g) Cu-RFLGPs thin films	100
5.2.2	XRD analysis of (a) Cu-RFLGPs(Hy) composites, (b) Cu-RFLGPs(Vc) composites and (c) Texture coefficient of Cu-RFLGPs composites	101
5.2.3	SEM image of (a) Cu thin film, (b) Cu-RFLGPs(Hy) and (c) Cu-RFLGPs(Vc) composite of RFLGPs concentration 0.5 g/L	103
5.2.4	AFM image of Cu-RFLGPs composite with various RFLGPs concentration	105
5.2.5	EDS mapping of Cu-FLGPs composite thin films of different concentrations of RFLGPs	105
5.2.6	EDS mapping of Cu-FLGPs composite thin films of different concentrations of RFLGPs	106
5.2.7	EDS image of (a) Cu-0.5RFLGPs(Hy) and (b) Cu-0.5RFLGPs(Vc)	106
5.2.8	FD image of (a) 0.1Cu-RFLGPs(Hy), (b) 0.1Cu-RFLGPs(Vc), (c) 0.3Cu-RFLGPs(Hy), (d) 0.3Cu-RFLGPs(Vc), (e) 0.5Cu-RFLGPs(Hy), (f) 0.5Cu-RFLGPs(Vc)	108
5.2.9	(a) Micro-hardness analysis of Cu-RFLGPs(Hy) and Cu-	109

	RFLGPs(Vc) composite, (b) electrical resistivity of Cu-RFLGPs(Hy) and Cu-RFLGPs(Vc)	
5.3.1	XRD analysis of Copper and Copper-FLGPs thin film: (a) Cu- and Cu- FLGPs films, (b) Cu-RFLGPs films, (c) Texture coefficient of films and (d) comparison of dislocation density, grain size and thickness with various graphene concentrations	112
5.3.2	SEM images of Cu-FLGPs and Cu-RFLGPs at various graphene concentrations	113
5.3.3	AFM images of Cu-FLGPs and Cu-RFLGPs at various graphene concentration	114
5.3.4	XPS spectra of 0.5FLGPs and 0.5RFLGPs composite films	115
5.3.5	X-ray elemental mapping of Cu-FLGPs composite	116
5.3.6	X-ray elemental mapping of Cu-RFLGPs composite	116
5.3.7	SEM image of wear track of Cu(a)and (b), wear depth of Cu (c) and (d) coefficient of friction of Cu	117
5.3.8	SEM image of wear track with wear depth and width of wear track of composites with various FLGPs concentration of (a) 0.1 g/L, (c) 0.3 g/L, (e) 0.5 g/L and RFLGPs concentration of (b) 0.1 g/L, (d) 0.3 g/L and (f) 0.5 g/L	120
5.3.9	SEM image of worn wear track surface of composites with various FLGPs concentration of (a) 0.1 g/L, (c) 0.3 g/L, (e) 0.5 g/L and RFLGPS concentration of (b) 0.1 g/L, (d) 0.3 g/L and (f) 0.5 g/L	122
5.3.10	X-ray elemental mapping on worn surface of composites (Cu-FLGPs)	123
5.3.11	X-ray elemental mapping on worn surface of composites (Cu-RFLGPs)	123
5.3.12	Coefficient of friction (a) and hardness (b) of Cu and composite films with various graphene concentrations, FD image of (c) 0.1g/L FLGPs and (d) 0.1g/L RFLGPs concentration and (e)	124
6.1	Electrical resistivity of Cu, Cu-FLGPs, Cu-RFLGPs thin films Schematic image of synthesis of graphene particles, electrodeposition of Cu-FLGPs composite and Corrosion setup	128

	of Cu-FLGPs composite	
6.2	OCP of Cu-FLGPs composites deposited in silent and ultrasonic conditions in (a) borate buffer, (b) borate with 3.5% NaCl and (c) 3.5% NaCl solution	130
6.3	Potential-dynamic polarization curves of Cu-FLGPs composites deposited in silent and ultrasonic conditions in (a) borate buffer, (b) borate buffer with 3.5% NaCl and (c) 3.5% NaCl solution at a scan rate 0.1667 mV/s	131
6.4	Potential-dynamic polarization curves of Cu-FLGPs composites deposited in silent and ultrasonic conditions in (a) borate buffer, (b) 3.5% NaCl solution at a scan rate 5 mV/s	133
6.5	Corrosion resistance of Cu-FLGPs nanocomposite (a) 3.5% NaCl and (b) borate buffer solution	134
6.6A	OCP of Cu-RFLGPs composite	137
6.6B	Potential-dynamic polarization curves (a) Cu-RFLGPs(Hy), (b) Cu-RFLGPs(Vc) nano-composites and (c) corrosion rate and variation of corrosion potential vs RFLGPs concentration	137
6.7	KK plot of Nyquist (a) silent, (b) sonic and Bode plots in (c, d) silent and (e, f) sonic condition of Cu and Cu-FLGPs sample with borate buffer solution	143
6.8	KK plot of Nyquist (a) silent, (b) sonic and Bode plots in (c, d) silent and (e, f) sonic condition of Cu and Cu-FLGPs sample borate buffer with 3.5% NaCl solution	144
6.9	KK plot of Nyquist (a) silent, (b) sonic and Bode plots in (c, d) silent and (e, f) sonic condition of Cu and Cu-FLGPs sample with 3.5% NaCl solution	145
6.10	Nyquist and Bode plots of Cu and Cu-FLGPs sample in borate buffer solution and deposited in (a), (b) silent condition and (c), (d) ultrasonic condition	146
6.11	Nyquist and Bode plots of Cu and Cu-FLGPs sample in borate buffer with 3.5% NaCl solution and deposited in (a), (b) silent condition and (c), (d) ultrasonic condition	147
6.12	Nyquist and Bode plots of Cu and Cu-FLGPs sample in 3.5% NaCl solution and deposited in (a), (b) silent condition and (c), (d) ultrasonic	147

	condition	
6.13	Circuit diagram of EIS analysis on (a) borate buffer and borate buffer with 3.5% NaCl and (b) 3.5% NaCl	148
6.14	XRD pattern for Cu-FLGPs of before and after corrosion in borate buffer (a) silent, (b) ultrasonic condition films, borate buffer with 3.5% NaCl solution (c) silent, (d) ultrasonic condition films and 3.5% NaCl (e) silent and (f) ultrasonic condition films in borate buffer solution	154
6.15	Texture co-efficient of composite samples after corrosion tests in (a) borate buffer, (b) borate buffer with 3.5% NaCl and (c) 3.5% NaCl	155
6.16	SEM image of Cu and Cu-FLGPs composite(silent condition) before and after corrosion of films in and borate buffer, borate buffer with 3.5% NaCl and 3.5% NaCl solution at scan rate 0.1667 mV/s	156
6.17	SEM image of Cu and Cu-FLGPs composite(Ultra sonic condition) before and after corrosion of films in and borate buffer, borate buffer with 3.5% NaCl and 3.5% NaCl solution at scan rate 0.1667 mV/s	157
6.18	EDS analysis of corrosion samples in borate buffer solution (a) Cu (S), (b) 0.5Cu-FLGPs (S), (c) Cu(US) and (d) 0.5Cu-FLGPs (US)	158
6.19	EDS analysis of thin films in 3.5% NaCl solution (a) Cu (S), (b) 0.5Cu-FLGPs (S), (c) Cu (US) and (d) 0.5Cu-FLGPs (US)	158
6.20	SEM image of Cu and Cu-FLGPs composite before and after corrosion of films in 3.5% NaCl solution and borate buffer solution at a scan rate of 5 mV/s	159
6.21	SEM image of (a) Cu, (c) 0.5Cu-RFLGPs(Hy) and (e) 0.5Cu-RFLGPs(Vc) before corrosion (b) Cu, (d) 0.5Cu-RFLGPs(Hy) and (f) 0.5Cu-RFLGPs(Vc) after corrosion, EDS spectra of (g) Copper and (h) Cu-RFLGPs	160
6.22	Schematic image of mechanism for corrosion resistance of Cu and Cu-FLGPs thin films	163

List of Tables

Table No.	Caption	Page No.
2.1	List of various properties of Cu, single-layer graphene and Cu-Gr composite	10
2.2	Applications of Graphene-based composite materials	13
2.3	The development of copper-graphene composite synthesis and their main results	34
2.4	The development of copper-graphene composite synthesis and their main results	48
4.1	Yield of graphene particles after TGA analysis	67
4.2	XPS analysis of FLGPs	74
5.1.1	Variation of average roughness of electroplated Cu and Cu-FLGPs thin films	90
5.2.1	Thickness, crystallite size(D), dislocation density(δ) and the number of crystallites per unit area(N) of pure Cu, Cu-RFLGPs composite	101
5.3.1	Average wears depth, wears width and wear rate of composite	120
6.1	Electrochemical corrosion parameter in borate buffer solution by Potentio-dynamic polarization curve at a scan rate 5 mV/s	133
6.2	Electrochemical corrosion parameter in 3.5% NaCl solutions by Potentio-dynamic polarization curve at a scan rate 5 mV/s	134
6.3	Electrochemical corrosion parameter in borate buffer solution by Potentio-dynamic polarization curve at a scan rate 0.1667 mV/s	134
6.4	Electrochemical corrosion parameter in Nacl with borate buffer solution by Potentio-dynamic polarization curve at a scan rate 0.1667 mV/s	135
6.5	Electrochemical corrosion parameter in 3.5% NaCl solutions by Potentio-dynamic polarization curve at a scan	135

	rate 0.1667 mV/s	
6.6	Corrosion parameters of Potentio-dynamic polarization curves in 3.5% NaCl solution of Cu-RFLGPs	137
6.7	Electrochemical parameters of Cu and Cu-FLGPs composites with borate buffer solution	142
6.8	Electrochemical parameters of Cu and Cu-FLGPs composites in NaCl solution	143
6.9	Electrochemical parameters of Cu and Cu-FLGPs composites in borate with 3.5% NaCl solution	145
6.10	Elemental analysis of corroded copper and Cu-RFLGPs composite films	151
6.11	Comparison of MPY with Equivalent Metric-Rate Expressions	153
6.12	List of reactions during corrosion, passivation and dissolution of composite films	155
6.13	List of reactions during corrosion, passivation and dissolution of composite films	155

Abbreviations

AFM	Atomic force microscopy
CV	Cyclic voltammetry
CVD	Chemical vapor deposition
CNT	carbon nanotube
DD	Double distilled
FD	Force displacement
FLG	Few layer graphene
FLGPs	Few layer graphene particles
RFLGPs	Reduced Few layer graphene particles
FTIR	Fourier transform infrared spectroscopy
FESEM	Field emission scanning electron microscopy
FWHM	Full width at half maximum
GO	Graphene oxide
GNSs	Graphene nanosheets
HF	High frequency
HRTEM	High resolution transmission electron microscopy
HOPG	Highly oriented pyrolytic graphite
LM	Low frequency
MF	Medium frequency
ML	Multilayer
PGr	Pyrolytic graphite
RGO	Reduce graphene oxide
SDS	sodium dodecyl sulphate
SEM	Scanning electron microscopy
SiC	Silicon carbide

SLG	Single layer graphene		
STM	scanning tunneling microscopy		
TEM	Transmission electron microscopy		
TGA	Thermogravimetric analysis		
WE	working electrode		
XRD	X-ray diffraction		
XPS	X-ray	photoelectron	spectroscop

Chapter 1

1: Introduction

1.1 Background

Metal matrix composites (MMC) are extensively used in various applications due to its outstanding mechanical properties such as hardness, elastic modulus, Young's modulus, tribological properties and corrosion properties as compared to pure metal [1,2]. These composites consist of at least two constituents, the matrix is metal and the reinforcement can be either ceramics or organic compounds. If there are more than two reinforcements that have been mixed in a composite then it is known as a hybrid composite. Matrix materials are generally softer than the reinforcement and metals like aluminum, copper, and magnesium have been significantly used as matrix [3–5]. The reinforcement material embedded with the matrix changes various properties such as hardness, wear resistance, electrical conductivity, and thermal conductivity. The metal matrix composites are being prepared by various techniques such as electrodeposition, chemical vapor deposition, laser-based techniques, powder metallurgy route and other chemical routes [6–8]. From the above available techniques, electrodeposition technique is one of the simple, easy and economically superior techniques to prepare metal matrix.

From 8000 BC, Cu has been used in several applications in our daily life. Copper is a metal that is easily available in nature. It is famous for its unique properties such as high electrical conductivity (of 5.96×10^7 S/m) and thermal conductivity (of $394 \text{ Wm}^{-1}\text{K}^{-1}$), good ductility, excellent corrosion resistance at ambient temperature and superior heat transfer capacity [9]. It also can be easily alloyed with other metals. Most well-known copper-based alloys are copper-brass and copper-bronze [10,11]. Copper and its alloys are used in various electrical and heat applications such as electrical conductors, wires, contact brushes, electric plugs, heat spreaders and electrodes. The main limitation of copper is its mechanical properties. Hence, Cu is alloyed with metal/non-metal to address this particular behavioral aspect without affecting other properties i.e. electrical conductivity. One of such approaches includes formation of composites by adding ceramic reinforcements. Though ceramic materials increase mechanical properties of copper, the original electrical conductivity of copper was found to be decreased. Hence, carbon materials (i.e. carbon nanotube, graphite and graphene) have been introduced as reinforcement with copper to synthesize composite materials [12].

Out of the several carbon derivatives, graphene has been emerging as one of the promising materials for the said purpose. Graphene is a 2D material discovered by Andre

Giem and Konstantin Novoselov in 2004 [13]. It is a monolayer, sp^2 hybridized and carbon atoms arranged in hexagonal lattice structure look like honeycomb structure [14]. Graphene sheets used as reinforcement with copper matrix to synthesis Cu-Gr composite have been found to have enhanced mechanical, electrical, thermal and corrosion properties as compared to pure copper material.

1.2 Motivation of the research work

As stated above, graphene is being explored as a reinforcement to synthesize Cu-Gr composites for versatile applications. Accordingly research has been focused onto finding a suitable route to synthesize Cu-Gr composites. Out of many techniques, electrodeposition is one of the significant routes to synthesize the Cu-Gr composites in form of films. The method uses either a simple two-electrode system (either DC current supply or reverse pulse deposition) or the most conventional three-electrode single pulse deposition. This route has been simple, fast and cost-effective than other techniques and deposits customary thin composite films. The said technique has the ability to disperse uniformly the graphene particles in the composite films [5,12]. Furthermore, the composites obtained by the electrodeposition route have shown significant variations and few of the observations can be listed from the reported literature. The composite films synthesized by electrochemical deposition have increased thermal conductivity and electrical resistivity up to 460 W/mK and $2 \times 10^{-6} \Omega \cdot \text{cm}$ from values of 380 W/mK and $1.66 \times 10^{-6} \Omega \cdot \text{cm}$ as compared to pure copper thin films [1,15]. The composite films synthesized by pulse reverse electrodeposition technique have shown 30% higher elastic modulus and 96% improvement in hardness [16,17]. The composite films also have shown 17.2% higher Young's modulus as compared to copper films via pulse power electrodeposition route [18]. Moreover, the composites synthesized by pulse electrodeposition route have shown better hardness and wear resistance properties [19]. Conceiving the above statistics, the versatile electrodeposition technique has been opted to synthesize composite films in the present investigation. However in all these reported researchers, the dispersion of the non-metallic graphene in a metallic matrix has been a challenge for better and synergistic property development. Hence the research needs an urgent insight in this direction. One such approach could be towards venturing into experimentation to add an external energy field to the depositing bath while electroplating the films. The said energy field would activate the bath which may have several effects on

the process as well as the film properties. Coupling of ultrasounds during electroplating can increase the deposition rate; henceforth can alter the physicochemical and other structural properties of the nano-composites to a great extent if one can manipulate the parameters optimally. Hwang et al. have reported an increase in electrical conductivity as well as the hardness of the Cu and reduced graphene composites prepared in an ultrasonic environment [5]. Majumdar et al. have fabricated CuO and reduced graphene composite by ultrasound-assisted electroplating, where the application of the as-synthesized composites in energy sector has been explored [20]. Apart from these few reports, there have been very few accounts available on the aforementioned studies to establish a critical conclusion on the definite effect of the above parameters; hence the field has immense scope to explore several new avenues.

1.3 Objectives

Pertaining to the above challenges of the chosen research field, the objectives of the current investigation are:

- Scalable production of few-layer graphene particles (FLGPs) in various aqueous electrolytes such as H_2SO_4 , and HNO_3 : Effect of anion sizes and concentration
- To reduce FLGPs by suitable reducing agents such as hydrazine hydrate and ascorbic acid.
- To optimize the deposition condition for electroplating of the copper-graphene nano-composites.
- To electrochemically synthesize and subsequently characterize the Cu-graphene nano-composite films with proper and uniform distribution of graphene. Accordingly, the properties of the deposited films including hardness, elasticity, wear and electrical conductivity have to be analyzed.
- To explore the films as an anti-corrosion coating for several infrastructural uses and applications.

1.4 Structure of the dissertation

The thesis contains 7 chapters and brief descriptions of each chapter are presented below:

Chapter- 1: It contains the introduction and motivation of the present investigation.

Chapter-2: It contains ‘Literature Review’ and is starting from the fundamental properties of graphene and Cu-graphene composite. This chapter further reports an extensive survey of work carried out by other scientist groups in the same field. Various synthesis routes of Cu-Gr composite have been reported. This chapter gives the information on microstructure and mechanical properties of copper-based composites.

Chapter- 3: The chapter gives information about the ‘Materials and Methods’, with sample preparation and bath solution preparation. Details of FLGPs and RFLGPs, Cu-FLGPs and Cu-RFLGPs synthesis and description of various scientific instruments used for characterization have also been elaborated.

Chapter- 4: The chapter explains the mechanism of synthesis of FLGPs, RFLGPs and discussion of the various physico-chemical properties of the as-synthesized graphene and its derivatives.

Chapter- 5: This chapter describes our significant contribution to the said research field which summarizes the detailed results and discussion of the underlying mechanisms and other obtained results.

Chapter- 6: This chapter describes the corrosion behaviors of the Cu-FLGPs composite with a comparative analysis to estimate whether the films can be explored as anti-corrosive coatings.

Chapter- 7: This is the concluding chapter and has summarized the results obtained and the discussion put forward in each chapter and has also mentioned the future scope of the thesis.

Chapter 2

2: Literature survey

2.1 Introduction

Copper and its alloys have been extensively used in electronic and electro friction applications, due to their outstanding electrical and thermal properties [17–19]. However, they have poor tribological and wear properties thus posing a disadvantage in electrical applications. To improve mechanical and wear properties, copper is reinforced with various materials including Sn, Ni, SiC, B₄C, and TiO₂ [20–22]. With the addition of these reinforcements, Cu based composites get improved mechanical properties but suffer from poor electrical conductivity [23]. Hence as an alternative, graphene (Gr) was explored as a versatile reinforcement, as it was observed to enhance mechanical, thermal and self-lubricating properties without decreasing the original electrical conductivity of Cu matrix [24–26]. The property enhancement by graphene addition is higher than that of its contemporary rivals: carbon nanotubes and graphite as can be seen from figure 2.1(a), which shows the amount of research citations about Cu-Gr composites from the year 2011 onwards.

Graphene as a material needs no introduction; however, it can be defined as a thin, two-dimensional nano-material where the carbon atoms are arranged in a hexagonal honeycomb-like crystal structure, with a carbon-carbon bond length of 0.142 nm. Novoselov et al. discovered graphene by an easy exfoliation method in around 2004 [27–29]. Since then it has been emerging for its outstanding properties i.e. a high specific surface area of 2630 m²g⁻¹, Young's Modulus of 1100 GPa, the electron mobility of 15000 cm²V⁻¹S⁻¹, thermal conductivities of 5000 WmK⁻¹, etc. With such superior properties, graphene has found its use in many novel applications such as energy storage, supercapacitors, lithium-ion batteries, solar cells, energy storage devices, hydrogen storage, fuel cell sensors chemical sensors, biomedical applications, reinforcement for polymer and metal matrix composites, and components in the automotive industries [30–35]. Figure 2.1(b) is the sector-wise use of this wonderful material. This huge demand for graphene can be addressed by implementing a suitable mass-producing synthesis route. A large number of methods have been developed to produce graphene such as Hummers method, modified Hummers method, chemical vapor deposition (CVD), mechanical and electrochemical exfoliation [36–40]. Among the above synthesis routes, electrochemical exfoliation route is a simple and cost-effective method for large-scale production of graphene. Presently, chemical/electro-chemical exfoliation is the most explored method for abundant synthesis of graphene in comparison to other methods. In chemical

exfoliation, irrespective of the electrolyte used, the principle is broadly the same. Graphene intercalated compounds are formed due to weakening of Van der Waal forces between the graphene sheets which is followed by exfoliation of few (or single) layered graphene sheets during rapid sonication or heating. The electrolyte used may be an acid or base but should have ions that can penetrate the interlayer spacing of graphite [41]. Figure 2.2 shows the morphological structure of few-layered graphene particles (FLGPs) synthesized by electrochemical exfoliation method [42].

Researchers have used various acid and base oriented aqueous solutions as an electrolyte to synthesize graphene sheets by electrochemical exfoliation technique [41,43–50]. Parvez et al. have reported graphene sheets synthesis by an aqueous solution of inorganic salt and an acidic electrolyte containing C/O ratio of 17.2 and 12.3 respectively [51]. Zhou et al. have also reported few-layer graphene sheets with acidic electrolyte which has a C/O ratio of 12.56 [52,53]. Sahoo et al. have reported C/O ratio of 3.3 by the same method of acidic electrolyte [35,54]. It can be followed from the data that the prepared graphene sheets from electro exfoliation routes contain a small amount of oxygen functional groups and structural defects during electrochemical exfoliation reactions. Hence, the oxygen functional groups, if needed, can be reduced by various routes such as photo reduction, thermal reduction, microwave reduction, hydrothermal reduction, UV induced reduction, solvothermal reduction and chemical reduction [55–60]. In chemical reduction methods, various reducing agents can be used including hydrazine monohydrate, hydrazine hydrate, amino acid, glucose, ascorbic acid, sodium borohydride and uric acid [61–63]. Among the various chemicals, hydrazine hydrate has been used significantly to produce reduced graphene oxide (RGO) of very thin graphene sheets [64]. However, hydrazine hydrate and hydrazine monohydrate are highly toxic and harmful to the environment. Therefore, it is avoided in graphene synthesis [65,66]. Further, in thermal reduction high temperature is required for reduction of FLGPs which is equally difficult. To avoid these problems, researchers have used non-toxic and eco-friendly environmental reducing agents such as ascorbic acid, amino acid and glucose as a replacement of hydrazine hydrate [67–69]. Ascorbic acid (AA) is a food product and is available naturally. Ascorbic acid is non-toxic and non-explosive [70,71]. It reduces graphene oxide to reduced graphene oxide at room temperature [72,73]. Zhang et al. reported ascorbic acid was an environmental friendly reducing agent at room temperature [72,74]. Ding et al. also reported RGO produced by

ascorbic acid was comparable to that of hydrazine hydrate reduced RGO [75]. Fernandez-Merino et al. reported that ascorbic acid can be an ideal substitute for hydrazine [55].

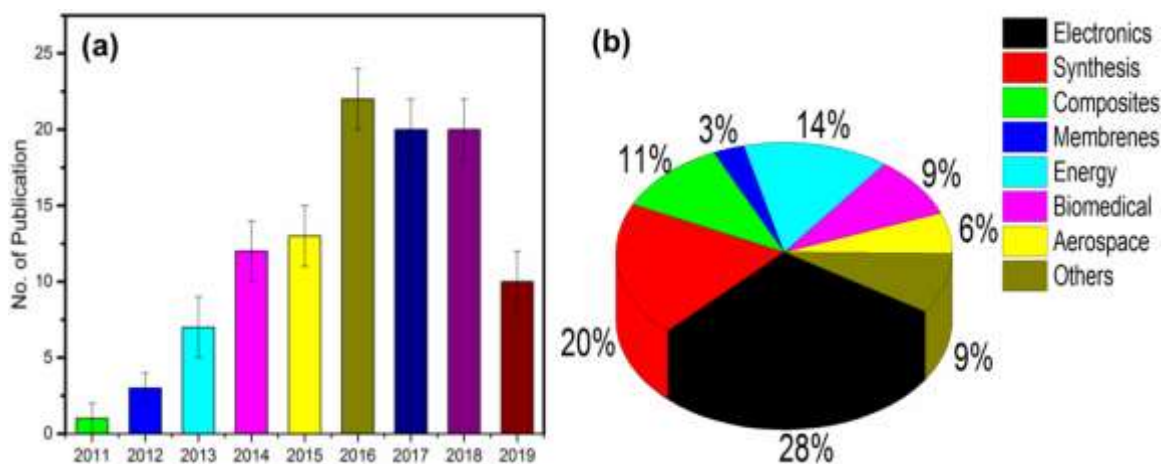


Figure 2.1: (a) No. of publications on Cu-Gr composite from 2011-December 2019, (b) Application of Cu-Gr composite in various sectors

The current research trends direct towards the use of graphene and its derivatives i.e. graphene oxide (GO) and reduced graphene oxide (RGO) as a reinforcement to produce novel nano-composites with modified structural interaction driven enhanced properties. The graphene-based nano-composites can range from Al-Gr, Ni-Gr, Cu-Gr, graphene-polypyrrole, graphene-silicon rubber, graphene-MnO₂ and graphene-ZnO [42,76–79]. Discussing the whole range of composites is beyond the scope of the current section of literature review; hence the focus is only on Cu-Gr nano-composites. As has been discussed before, graphene incorporation has been observed to enhance the mechanical, thermal and self-lubricating properties of the Cu-Gr nano-composites without decreasing the original electrical conductivity of the Cu matrix. Table 2.1 summarizes the individual properties of Cu and graphene and is compared to that of Cu-Gr composite prepared by various routes. The increase in mechanical properties is mainly due to the blocking of dislocations by graphene nano-sheets and short-peening with the copper matrix. The said effect is possible only if there is a uniform distribution of graphene sheet and proper bonding between the copper matrixes. However, the graphene particles have a general tendency to agglomerate due to strong Van der Waal's forces between carbon atoms in graphene, high surface area and density difference between the graphene reinforcement and copper matrix. As a result, the key issue of Cu-Gr or as a matter of fact, all graphene-based nanocomposites is the determination of optimal quantity of graphene addition during the synthesis process in order to achieve proper and uniform distribution of these

reinforcements. An excess amount of graphene could lead to agglomeration and hence instead of beneficial effect it may end up with detrimental effects by introducing pores and voids.

Table 2.1: List of various properties of Cu, single-layer graphene and Cu-Gr composite

Properties	Copper	Single layer of Graphene	Cu-Gr composite
Tensile strength	210 MPa	130 GPa	234-608 MPa [90,92]
Young's modulus	110-128 GPa	0.5-1 TPa	132 GPa [92]
Coefficient of thermal expansion	17×10^{-6} K	-6×10^{-6} K	Data not available
Electron mobility(at 298K)	1.26×10^{-3} m ² /V.s	15000 cm ² /V.s	Data not available
Electrical conductivity	5.96×10^7 S/m	7200	Data not available
Thermal conductivity	394 W/m/K	4840-5300 W/m/K	440 W /m/ K
Corrosion rate	62.76 mil/year	Data not available	6.62 mil/year
Coefficient of friction	0.84	Data not available	0.06

In recent years, researchers have developed several techniques to reduce the agglomeration of graphene particles in the copper matrix composites to improve the properties. Hence the current literature is focused on the various fabrication techniques where the morphological evolutions along with the physico-chemical properties of the composites have been elaborated. The different methods to synthesize Cu-Gr composites with an optimal concentration of graphene addition include electrochemical deposition, powder metallurgy route, molecular level mixing (MLM), spark plasma sintering (SPS) and pulse electrodeposition processes etc. [2,80–85]. This literature also pays attention to the latest progress made in the applications of graphene-based composites.

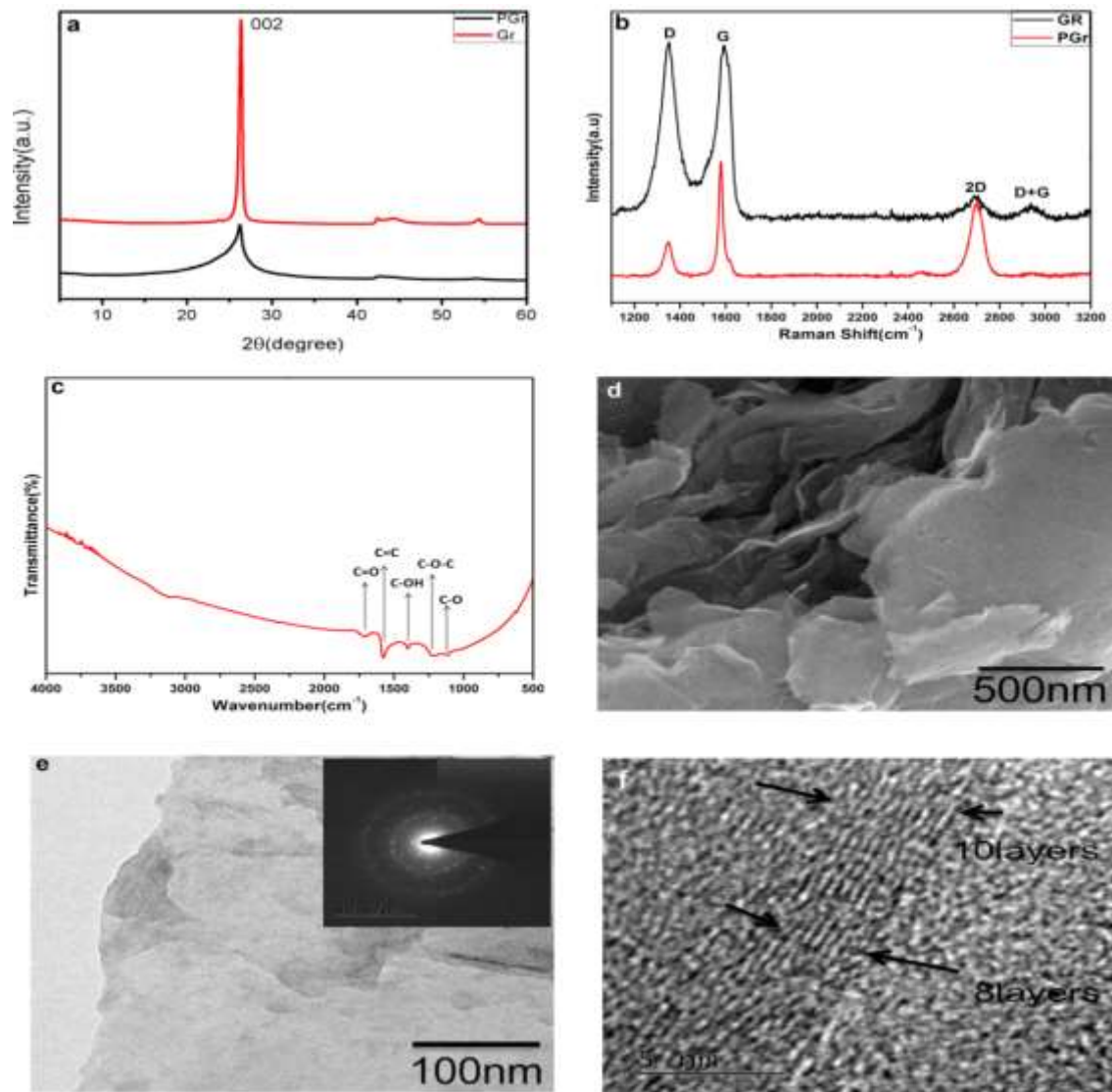


Figure 2.2: Images of graphene and its properties. Reprinted from Behera et al. [42] Copyright (2018) with permission from Elsevier

2.2 Application of graphene-based composites

Graphene based composites have immense amount of applications. Therefore, it is essential to highlight them in order to substantiate the current study. Figure 2.3 is a representative figure of major fields and Table 2.2 is an extensive collection of all possible applications of graphene-based composites in various fields.

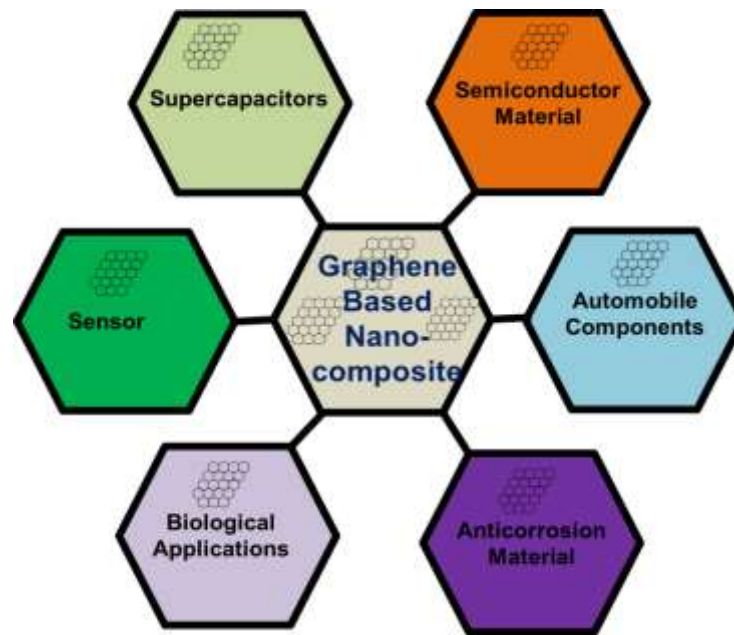


Figure 2.3: Schematic image of application of graphene-based composites

Due to its superior and challenging properties, graphene is being extensively explored as reinforcement in polymer, ceramic and metal matrices. Various types of polymer matrices such as epoxy polymer, polystyrene, PANI, Nafion and poly (3, 4-ethyldioxythiophene) have incorporated graphene to get enhanced thermal, electrical conductivity and mechanical properties. The polymer-graphene nanocomposites have been tested for stable use in Li-ion batteries, fuel cells, electronic packings, electronic devices, solar cells, supercapacitors, transparent conducting electrodes, gas barrier membranes, chips, aerospace, sporting, goods, corrosion resistance materials, drug delivery and biosensors [86]. Graphene nano-fillers introduced with CNT have been explored in multifunctional applications including electrical energy storage, sensing and actuation areas [87].

Researchers have developed various graphene-based ceramics matrix nano-composites such as ZnO-graphene, SnO₂-graphene, MnO₂-graphene, Cu₂O-graphene, and CuO-graphene which find applications in energy industry, aerospace industry, military ballistic equipment, nose caps in space shuttles and anti-corrosion applications.

Table 2.2 Applications of Graphene-based composite materials

	Graphene-based composites	Applications	Year	Refer ences
Polymer base graphene composites	Graphene/polypyrrole	Supercapacitor	2012	[88]
	Graphene/polypyrrole	Supercapacitors electrode	2013	[89]
	Graphene oxide/hydroxyapatite	Biological applications	2013	[90]
	Graphene/hydroxyapatite	Tissue engineering	2013	[91]
	Graphene-polymer	Structural and functional applications	2014	[86]
	Bioactive hydroxyapatite/graphene	Corrosion	2015	[92]
	Graphene/poly(vinylidene fluoride)	Nanocomposite membrane	2017	[93]
	Poly(vinyl alcohol) and graphene oxide	Supercapacitor	2017	[94]
	Graphene/polypyrrole nanotube	Multifunctional applications	2017	[95]
	Graphene	Supercapacitor	2018	[96]
	Oxide/Polyaniline/Polyvinyl Alcohol			
	Hydroxyapatite/graphene oxide/chitosan	Bone tissue engineering	2017	[97]
		Interdigitated		
	Polylactic acid/graphene	microelectrodes for Sensor	2018	[98]
	Graphene-based hydroxyapatite	Orthopedic	2018	[99]
	Graphene/PANI	Ammonia sensor	2018	[100]
	Polyaniline-Graphene nanoplatelet	Microwave shielding applications	2019	[101]
BaTiO ₃ /graphene	Thermoelectric	2016	[102]	
Bi ₂ O ₃ decorated graphene	Supercapacitor	2018	[103]	
	High-performance			
Graphene/SiBCN	electromagnetic interference shielding	2018	[104]	
Graphene/Co ₃ O ₄	Hybrid capacitive deionization system	2019	[105]	

Ceramic base graphene
composites

Metal base applications	Graphene–ZnO	Supercapacitor	2009	[106]
	Gold nanocluster decorated RGO	Drug delivery	2011	[107]
	Copper nanoparticles/graphene oxide	Surface-enhanced Raman scattering	2012	[108]
	Graphene-Encapsulated Cu	Nonenzymatic Glucose Sensing	2018	[109]
	Graphene-silicone rubber	Strain sensing	2018	[110]
	Gr-Al	High-pressure torsion	2019	[77]
	Metal oxide/graphene	Sodium-ion batteries	2019	[111]
	Cu-gr	Electrical contact material	2019	[112]
	Manganese dioxide/ reduced graphene oxide	Electrode material for high-performance solid state supercapacitor	2019	[113]
	ZnS/graphene	Photocatalytic performance	2019	[114]
	Graphene/MnO ₂	Supercapacitor	2019	[115]
	Copper oxide/reduced graphene oxide	Chemi-resistive sensors.	2019	[116]

In recent years, researchers have reinforced graphene with metals like Cu, Fe, Au, Ag, Pt, Ni, Ru and Pd to fabricate graphene-metal nanocomposites. These nanocomposites with enhanced mechanical, electrical, electronic and thermal properties are used in electrical wirings, wear applications, thermal applications, sensors, supercapacitors and biomedical applications. The recent development of Cu-Gr composites is replacing conventional structural materials such as copper, carbon fiber, CNT-reinforced metal composites and copper alloys in modern electronic packing, soft magnetic materials, and brushes in electric motors due to their excellent electrical and thermal properties along with good mechanical properties. The enhanced mechanical properties of Cu-Gr composites are suitable for electro friction applications as well. The composites are also used in load bearings, electrical contacts and supercapacitor electrodes due to high electrical conductivity. The thermal conductivity of Cu-Gr composite is higher than the copper material which is suitable for heat spreader and electronic circuit applications. It is also suitable for nuclear engineering applications due to its excellent radiation tolerance [98].

2.3 Categorization of Fabrication Techniques

The graphene particles have an agglomeration tendency due to attractive Van der Waals bonding which separates it from the copper phase (metallic bonding) during the fabrication process of composite. To avoid this problem of agglomeration, researchers have used several techniques which has been critically categorized by the authors based on their phase of synthesis. Broadly categorizing them as dry, wet and mixed/hybrid phase of synthesis. Figure 2.4 explicitly covers the methods of synthesis of Cu-Gr composite that have been investigated by different researchers in recent years. The flowchart represents only generalized and distinct methods while avoiding the very specific ones, though they have been elaborated further in the subsequent sections. Chemical and electrochemical exfoliation broadly covers the wet phase of exfoliation. For a cleaner and greener route of synthesis and low-temperature operation, wet phase methodology is generally preferred. However, these routes may need further additional post-synthesis steps to produce the final desired composites. The dry phase, however, helps to avoid subsequent forming processes. Additionally, the temperature of operation can be varied as per requirement. This helps in achieving a higher purity graphene with stoichiometric accuracy. However, the dry phase also holds the disadvantage of using impact or shear force on the graphene sheets which may induce mechanical damage to the graphene sheets. So, an optimization between the two phases was felt essential which led the researchers to the mixed/hybrid phase of synthesis.

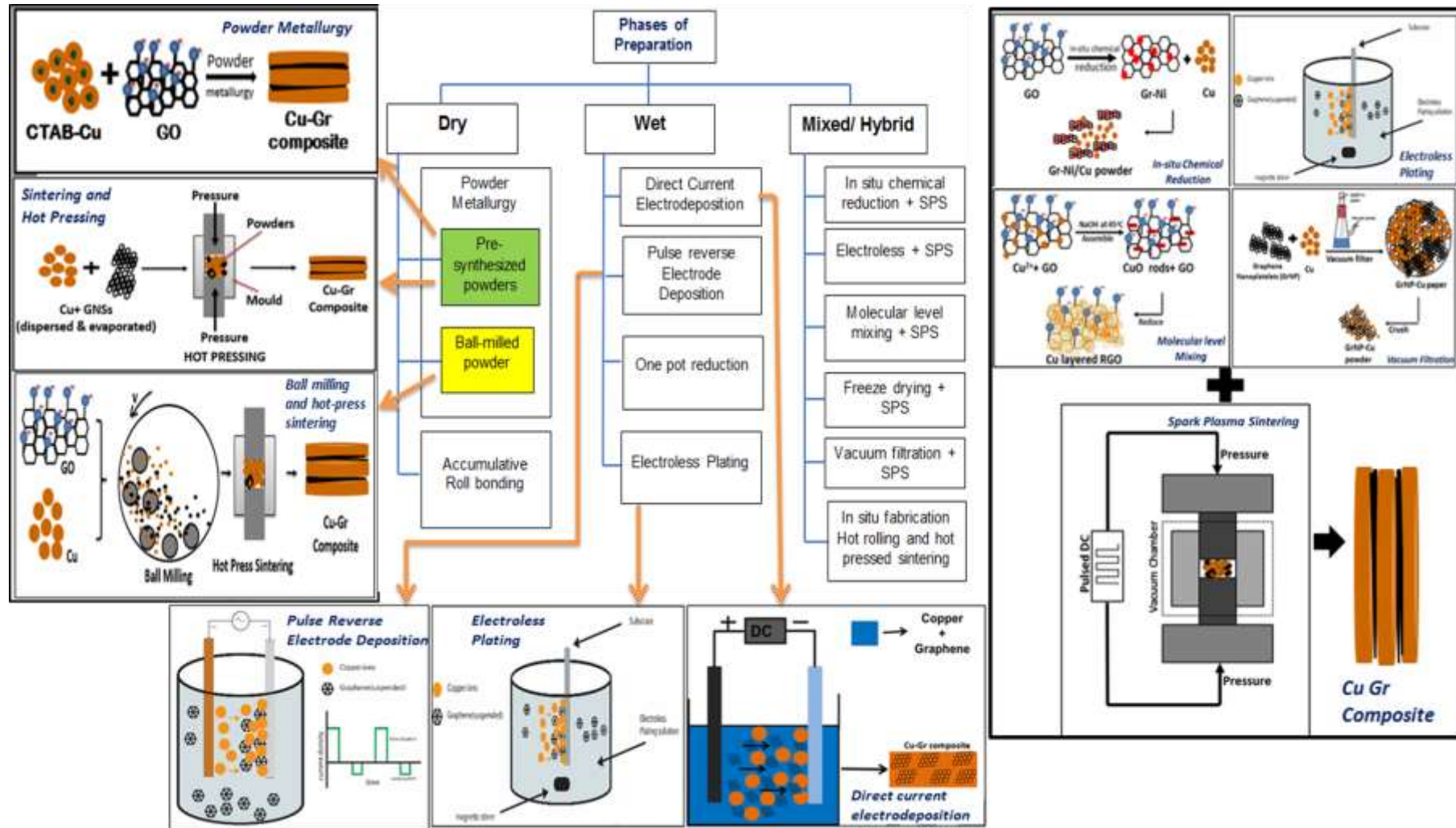


Figure 2.4: Categorization and schematic image of various synthesis routes and techniques of Cu-Gr composite

The mixed-phase of synthesis fuses the essence of both the dry and the wet phase in an attempt to improve the process parameters thereby eliminating the lacunae of either of them. Table 3 summarizes the chronological development of techniques to synthesize Cu-Gr nano-composites, percentage of graphene reinforcement used and any alterations in the properties including mechanical, electrical, thermal and corrosion behaviors. The next sections describe the processes under each category and the structure and properties of the obtained composites have also been discussed.

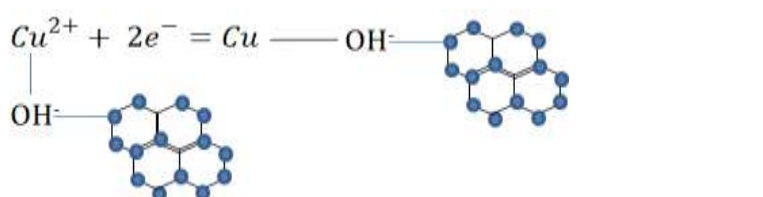
2.3.1 Wet phase Techniques

Wet phase technique uses various chemicals and electrochemical reactions to synthesize Cu-Gr nano-composites. Several wet phase processes such as direct current electrodeposition, pulse reverse electro-deposition, electroless co-deposition route and one-pot reduction methods are the most general and practiced ones. Further, these techniques has been elaborated as mentioned below.

2.3.1.1 Direct current electrodeposition

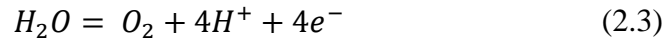
The electrodeposition process is an old conventional technique which has been used to synthesize materials of any form and dimension i.e. macro to nano-scale ranging from powders to bulk materials. The process can be either current controlled or voltage controlled, wherein the electric current reduces/discharges the dissolved metal cations in the electrolyte to form a metal coating on-to the electrode. CuSO_4 solution has a prevalent use in the electrodeposition of Cu-Gr composites; it is used with various concentrations of graphene or its derivatives, which is then electrodeposited on suitable substrates. The electrochemical reactions during the deposition of the composite films are mentioned in eqs. 2.1, 2.2 and 2.3:

Cathodic reaction





Anodic reaction



Several researchers have reported using this process with various graphene concentrations and suitable surfactants so as to reduce agglomeration during electrodeposition of Cu-Gr composite. Figure 2.5 shows the schematic image of Cu-Gr composite synthesis route prepared by Behera et al. [42]. Graphene particles were synthesized by electrochemical exfoliation process and were subsequently used in the preparation of Cu-Gr composite. Graphene particles of concentrations 0.1 g/L, 0.3 g/L, and 0.5 g/L were used as reinforcement in the depositing electrolyte. The electrolyte was maintained at pH 1 with a temperature of 15-17 °C. Sodium dodecyl sulfate (SDS), a surfactant was added simultaneously during sonication and stirring of the solution. Figure 2.6 shows the (a) FESEM image of Gr and SEM image of 0.1 g/L Cu-Gr and (c) 0.5 g/L Cu-Gr. The graphene used in the study have wrinkled or folded morphology and have few stacked layers at the edges after exfoliation. From figure 2.6(b-c), it can be seen that the grain size of Cu-Gr composite has increased with an increase in graphene composition. The hardness of 0.5 g/L graphene concentrated Cu-Gr composite was found to be 2.11 GPa which was 31% higher than pure copper's hardness of 1.61GPa prepared by the same route. The electrical resistivity of the composite increased in comparison to Cu film which may be due to the defects of graphene particles or due to presence of oxygen functional groups in graphene particles [42].

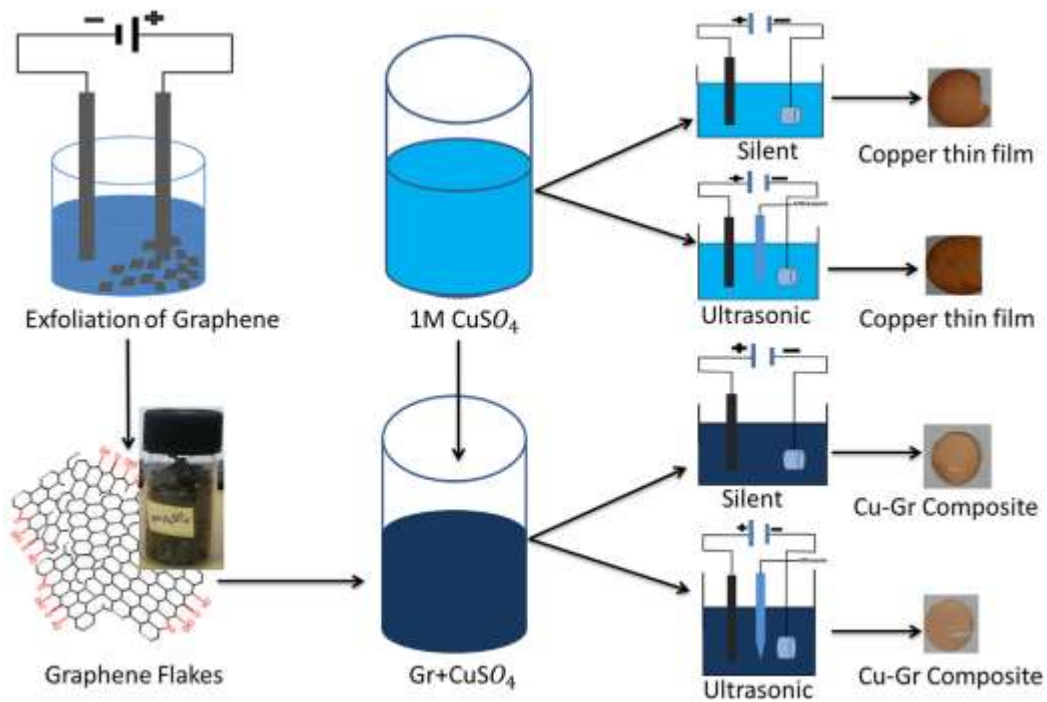


Figure 2.5: Schematic image of Cu-Gr composite prepared by DC electrodeposition route. Reprinted from Behera et al. Copyright (2018) with permission from Elsevier [42]

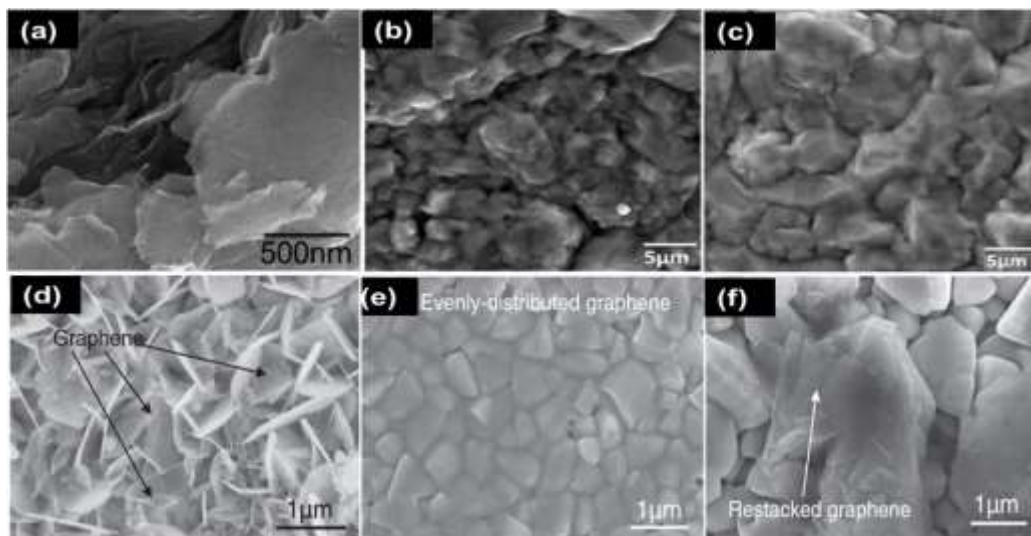


Figure 2.6: FESEM images of (a) graphene, Cu-GNSs composite of various graphene concentrations (b) 0.1 g/L, (c) 0.5 g/L reprinted from Behera et al. and composites with Gr concentrations of (d) 0.2 g/L, (e) 0.5 g/L and (f) 0.8 g/L reprinted from Song et al. [42,117]

Using the same route, Cu-Gr composite was synthesized by Jagannadham et al. with GO as reinforcement, where thickness of the films are in between 365-515 μm [118–121]. The pH of electrolyte was maintained at a value of 6 by adding H₂SO₄ and electrodeposition was carried out without any surfactant. The concentration of GO was very less in the electrolyte. The thermal conductivity of the composite improved from 3.8 to 5.0 W/cm.K.

and electrical resistivity reduced from 2.031 to 1.966 $\mu\Omega\text{cm}$. Song et al. also reported the synthesis of Cu-Gr composite by the same route but with different bath temperatures [117]. Polyacrylic acid (PAA 5000) was added into the electrolyte as a surfactant to avoid agglomeration of GO sheets during electrodeposition. The thickness of composite films was less than 20 μm . Figures 2.6(d-f) shows the morphological structure of the composites with different GO concentrations i.e. 0.2 g/L, 0.5 g/L and 0.8 g/L respectively [117]. The GO sheets are distributed uniformly in the Cu-Gr composite and the microstructure shows compact and fine grain size of the Cu-Gr composite. The GO concentration of 0.8 g/L shows restacked GO sheets in the composite foil due to agglomeration of GO particles in the electrolyte [117]. Hence the mechanical properties of the composite are observed to increase as GO concentration increases up to 0.5 g/L in the copper matrix. The GO concentration of 0.8 g/L did not give better results than 0.5 g/L concentration due to agglomeration. The Cu-Gr composite have been synthesized by Raghupathy et al. in the same process. The graphene concentration of 0.125, 0.25 and 1 g/L were added in copper matrix. During electrodeposition, a pH of 2.4 and temperature of 25 $^{\circ}\text{C}$ was maintained. In order to reduce agglomeration sodium lauryl sulphate (SLS) was used as a surfactant. Authors have also reported about corrosion performance of the composite. The Cu-Gr composite gives improved corrosion resistance as compared to copper thin films [122]. Similar fabrication process for Cu-Gr composite was reported by Mai et al. but without the addition of any surfactants into the electrolyte. The electrolyte consisted of copper disodium ethylene diamine tetra-acetate tetrahydrate with a pH of 1.5 by adding H_3PO_4 and electrodeposition was done by using a magnetic stirrer under ultrasonic conditions. And a graphene concentration of 0-0.4 g/L was used for electrodeposition of Cu-Gr composite without any surfactant. The microhardness of composite increased by up to 30% and wear resistance also increased. The coefficient of friction decreased up to 35-40% (4.17 to 0.24) and wear rate decreased to 10-18 times as compared to pure copper [123].

2.3.1.2 Pulse reverse electro-deposition (PRED)

PRED is a novel technique to prepare thin and composite films. In this technique current and potential are varied in a series of pulses with the same amplitude, different duration and electric field is separated by zero current. The pulse gives an on-time (T_{on}) when the current and potential is applied and off time (T_{off}) when the current and potential is zero. PRED produces a current wave which helps in controlling the composition and thickness

of the deposited film by varying pulse parameters. Many researchers have used PRED to synthesize Cu-Gr composite films. Chokkakula et al. synthesized Cu-Gr composite by both DC and pulsed DC supply, carried out under magnetic stirring conditions [85,124]. In DC electrodeposition process the applied current density was 0.025 A/cm^2 whereas in PRED the applied current density was in the range of $0.05\text{-}0.2 \text{ A/cm}^2$ and $0.005\text{-}0.015 \text{ A/cm}^2$ for forward and backward pulses respectively. The forward pulse range for T_{on} and T_{off} is $15\text{-}50 \text{ ms}$ and $50\text{-}100 \text{ ms}$ respectively whereas for a reverse pulse T_{on} and T_{off} time was in the range of $1\text{-}10 \text{ ms}$. Graphene concentration of $0\text{-}1 \text{ g/L}$ was added to copper electrolyte and pH was maintained at 1 in the temperature range of $15\text{-}20 \text{ }^\circ\text{C}$. PPA 5000 was added to the electrolyte as a surfactant to reduce the agglomeration problem of graphene sheets. Figure 2.7 shows the schematic image of pulse reverse electrodeposition of Cu-Gr composite. Through FESEM images, the distribution and alignment of graphene in the matrix has been examined by researchers. It was observed that uniform distribution of graphene in composites increased upto 0.5 g/L . The electrodeposited Cu-Gr composite had a thickness of $30 \text{ }\mu\text{m}$ from both PRED and DC routes. The composite showed enhanced hardness of $2.1\text{-}2.5 \text{ GPa}$ which is 96% higher than bulk copper value of $1.4\text{-}1.6 \text{ GPa}$ and elastic modulus increased up-to $127\text{-}137 \text{ GPa}$ which is 30% higher than bulk copper value of 116 GPa . Graphene concentration of 0.5 g/L composite gave best properties due to uniform distribution of Gr within the copper matrix; however 1 g/L Gr agglomerated within the matrix.

Cu-Gr composite has also been prepared by Hwang et al. via both DC and pulse electrodeposition route in magnetic and ultrasound stirring conditions to disperse graphene sheets [125]. A current density of 10 mA/cm^2 was applied for electrodeposition in a duty cycle of 0.2 ms and 0.4 ms for t_{on} and t_{off} respectively. The graphene concentration was maintained in the range of 0.5 mg/L to 300 mg/L in the depositing electrolyte. The authors did not mention any details about pH of the electrolyte and electrodeposition was carried out without any surfactant. The Young's modulus, yield strength and breaking strength of the composite films were 82.5 GPa , 24.2 MPa and 386.7 MPa respectively which showed an increase of 17.2%, 39% and 21.1% in comparison to pure copper synthesized by the same process. The thermal conductivity of the composite showed a value of 300.5 W/mK which is 5% higher than pure copper value of 286.5 W/mK synthesized by the same process. The mechanical property of composite increased without any decrease in thermal conductivity and electrical conductivity. Sonicated

samples have shown better properties than the samples produced by magnetic stirring conditions in the said study. Cu-Gr composite synthesized by Maharana et al. through PRED process had a graphene concentration of 0-1 g/L in the bath [126,127]. The electrolyte was maintained at pH~1 and deposition was carried out at room temperature using a surfactant of polyacrylic acid (PAA) under magnetic stirring condition.

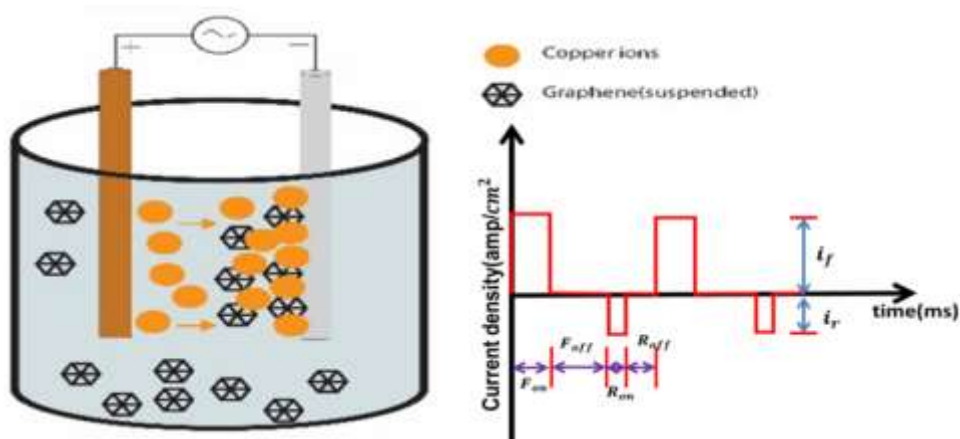


Figure 2.7: Schematic image of PRED process to synthesize Cu-Gr composite

The Cu-Gr composite gave 40% higher hardness as compared to that of pure copper. The wear resistance of composite had increased and the coefficient of friction decreased upto 0.04 and 0.17 respectively. It was also observed that at 0.5 g/L of graphene concentration Cu-Gr composite has enhanced mechanical properties whereas it decreased in the case of 1 g/L graphene concentration due to agglomeration even in presence of surfactant [126,127].

2.3.1.3 Electroless co-deposition route

Electroless co-deposition method is a simple, easy and environment friendly deposition process. In this process, there are no essentials like voltage, current and electrodes. The deposition takes place in open circuit condition, also known as the mixed potential where the rate of cathodic reaction (deposition of composites) is equal to the rate of anodic reaction (evolution of oxygen) as per the reactions mentioned in DC electrodeposition section. Zhang et al. had reported Cu-Gr composite synthesis by this route where the Cu-Gr composite films were deposited onto carbon-steel substrate and the electrolyte constituted of 8 g/L $\text{CuSO}_4 \cdot 5\text{H}_2\text{O}$, 0.5 g/L $\text{NiSO}_4 \cdot 6\text{H}_2\text{O}$, 20 g/L $\text{Na}_3\text{C}_6\text{H}_5\text{O}_7 \cdot 2\text{H}_2\text{O}$, 30 g/L H_3BO_3 and 40 g/L $\text{NaH}_2\text{PO}_2 \cdot \text{H}_2\text{O}$ respectively [128]. Graphene concentration of 0-7 mg/L had been added to the electrolyte in the study. The electrolyte was maintained at pH

9 by adding NaOH and there was no use of any surfactant. The Cu-Gr composite for 5 mg/L of graphene concentration showed higher hardness of 2.33 GPa as compared to the value of pure Cu which is 1.47 GPa. The hardness of the composite increased when the graphene concentration increased from 0-5mg/L, but the hardness significantly decreased with further increase of graphene concentration. Li et al. have also synthesized Cu-Gr composite by electroless plating [129]. The GO concentration of (20 mg/L, 60 mg/L and 100 mg/L) was added to the electroless copper bath composed of 10 g/L $\text{CuSO}_4 \cdot 5\text{H}_2\text{O}$, 15 g/L $\text{Na}_3\text{C}_6\text{H}_5\text{O}_7 \cdot 2\text{H}_2\text{O}$, 28 g/L $\text{NaH}_2\text{PO}_2 \cdot \text{H}_2\text{O}$, 30 g/L H_3BO_3 , 1 g/L $\text{NiSO}_4 \cdot 7\text{H}_2\text{O}$ respectively. The Cu-Gr composite film was deposited onto the iron substrate and pH of electrolyte was maintained at 9-9.5 at a temperature of 65 °C under magnetic stirring condition. The GO concentration of 60 mg/L in the electrolyte gave enhanced hardness and elastic modulus of 3.4 and 96.2 GPa which is 4.2 times and 26% higher than the values for pure copper i.e. 0.83 GPa and 76.2 GPa. The same concentration graphene gave enhanced corrosion resistance of 0.05 mil/a as compared to the corrosion resistance of copper and iron of 6.45 mil/a and 8.52 mil/a respectively. Peng et al. have reported Cu-RGO composite by ultrasound assisted electroless plating [130]. A 200 ml electroless copper solution was prepared from 25 g of $\text{CuSO}_4 \cdot 5\text{H}_2\text{O}$ and 0.8 g of complex agent (EDTA $\text{Na}_2\text{H}_2\text{O}$). The pH of the solution was maintained at 11 by adding sodium hydrate. GO was introduced to the electroless copper solution aided by an ultrasonic bath. The composites showed a highly dispersed 2D sandwich-like structured Cu-Gr nanocomposite. Also, the composites had a large aspect ratio and high surface area [130].

2.3.1.4 One-pot reduction method

One-pot reduction is a technique by which Cu-Gr composites are produced via several complex chemical reaction sequences in a singular vessel. The chemicals used in the process need to be chosen carefully in order to initiate sequential graphene synthesis with less surface defects and then finally terminate the reactions. Li et al. have reported Cu-Gr composite by one-pot reduction method [131]. In this method, 0.1 g of GO and 0.4 g of $\text{CuSO}_4 \cdot 5\text{H}_2\text{O}$ were dispersed in deionized water and an appropriate amount of citric acid was added to it. Then the solutions were stirred and during the stirring process span-80 and base oil were mixed ultrasonically to get uniform dispersion and stable suspension. Figure 2.8 shows the TEM image of (a) graphene sheet, (b) Cu-Gr composite and (c) HRTEM of Cu-Gr composite. The figure demonstrates that the two-dimensional graphene sheets are well decorated by many spherical Cu nanoparticles and there is no apparent

aggregation of Cu nanoparticles on the Gr sheets. It resulted in an improvement in the load-carrying capacity of upto 50% [131]. The researchers were able to produce FLGPSs with very low concentration of defects and a very low count of oxygen functional groups. The Cu ion deposited graphene nanoparticle were explored as antifriction additives and have been found to perform better as compared to pure Cu nanoparticles but the higher content of Gr in Cu-Gr composite couldn't achieve lower friction due to their agglomerating tendency.

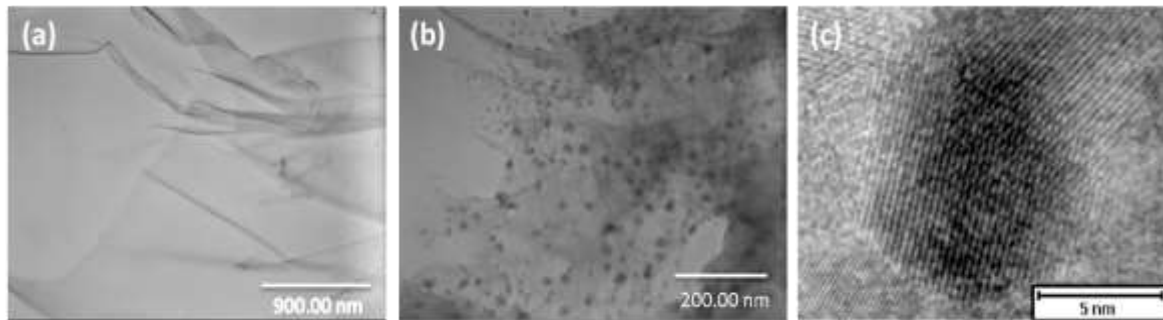


Figure 2.8: TEM images of (a) Graphene layer, (b) Cu-Gr nanocomposite and HRTEM image of the Cu-Gr by One-pot reduction method. Reprinted from Li et al. [131]

2.3.2 Dry phase Technique

Dry phase technique mainly consists of the processes in which there is no liquid media involved and the reaction takes place during the synthesis of the composite. Some of the significant dry phase processes are: powder metallurgy and accumulated roll bonding. Further, these processes have been sub-classified into different routes depending on the combination of other techniques and have been briefly described below.

2.3.2.1 Powder metallurgy Method

Powder metallurgy (PM) is a process in which metals or components are made from metal powders without any significant metal removal processes or manufacturing losses. Often it is used in the production of near net-shaped complex design materials with high accuracy which is impossible to get from melting or forming routes. It consists of three important steps (i) powder manufacture, (ii) blending of powders, (iii) compaction of powders and (iv) sintering. The powders which are used in synthesis are either produced by ball milling or pre-synthesized through other various routes and blended with some additives to increase the bonding strength between them. Compaction and sintering stages

are the deciding factors for a good composite. The compaction of powders is usually performed at room temperature or in some cases at higher temperatures. Sintering is the process of compacting and forming a solid mass of material by subjecting it to heat or pressure without melting it to the point of liquefaction. The atoms in the materials diffuse across the boundaries of the particles, fusing them together and creating one solid piece. The temperature used for sintering is below the melting point of the major constituent of the powder mixture. Depending on the material constituents and the processing conditions, there are many types of sintering processes such as general sintering, ceramic sintering, liquid phase sintering, SPS, pressure less (vacuum) sintering and microwave sintering. Among this, the most used ones for fabricating Cu-Gr composites are conventional sintering and spark plasma sintering (SPS). In general sintering, temperature is the main variable along with hot pressing. In SPS, an external pressure and electric field are applied simultaneously which enhances the densification of the metallic powder compacts. The electric field drives the densification process which is a similar type of sintering process with hot pressing but at relatively lower temperatures and shorter duration of time.

2.3.2.1.1 Powder metallurgy with pre-synthesized graphene powders

For fabricating Cu-Gr composites through this process, the copper matrix is mixed with different concentrations of graphene particles and are either cold or hot pressed and then sintered via any of the above mentioned available processes. Graphene used in the following processes have been prepared by different routes and were obtained from the manufacturers as per the standard laboratory grade. The following section will briefly review the methods by categorizing them as cold pressing - sintering and hot pressing - sintering.

2.3.2.1.1.1 Cold pressing and sintering:

This process route does not involve amalgamation of other techniques. Generally in this process, graphene materials are mixed with the copper matrix so as to synthesize Cu-Gr composite powders and subsequently milled to obtain bulk composites. Gao et al. have used this technique to synthesize Cu-Gr composite efficiently [132]. Graphene concentration of 0.1, 0.3 and 0.5 wt% were added to the copper matrix. Figure 2.9 shows the fabrication route of Cu-Gr composite following the route. The cold compacted powders were sintered in an argon atmosphere at 900 °C for 1 h under a pressure of 25

MPa so as to synthesize the Cu-Gr composite. Later on, during analysis the presence of graphene particles near copper grain boundaries was confirmed by TEM analysis as shown in figures 2.9[g-i]. The as-prepared Cu-Gr composite showed enhanced hardness of 43-53 HV and thermal conductivity of 360-396 W.m⁻¹k⁻¹ for 0.3 wt% Cu-Gr composite. However for 0.5 wt% graphene concentration, holes were observed around Cu grain boundaries on the fracture surface of the composite. Hence composites with high graphene concentration i.e. 0.5 g/L showed a decrease in the mechanical properties and thermal conductivity due to agglomeration of graphene [132]. Jiang et al. prepared pristine graphene (PG)/Cu and RGO/Cu composites by powder metallurgy route in combination with spark plasma sintering (SPS). The concentration of PG and RGO was maintained at 0.3 wt% in the copper matrix for the synthesis of (PG)/Cu and RGO/Cu composite. The yield strength ($\sigma_{0.2}$) and 5% compression strength of PG/Cu composite were found to increase upto 172 and 228 MPa respectively which is 90% and 81% higher than pure copper. But electrical conductivity of PG/Cu composite decreased by 15% as compared to pure Cu. PG was more suitable than RGO in increasing the strength of copper due to presence of less defects and a small number of functional groups [133]. Das et al. have also reported Cu-Gr composite through powder metallurgy route via conventional and microwave sintering processes after cold pressing of the powders [134]. Different graphene concentrations (0.9, 1.8, 2.7 and 3.6 vol.%) were mixed with copper matrix to make the composites. The prepared Cu-Gr composite gave enhanced hardness of 46-89 HV and a decrease in the coefficient of friction from 0.51 to 0.21. The electrical conductivity of samples of Cu-0.9 vol.% Gr composite prepared by conventional and microwave sintering showed 92% and 94% IACS respectively. The highest graphene concentration in Cu i.e. 3.6 vol.% sample showed the lowest electrical conductivity of 82% IACS. Hence it can be said that conductivity decreases with higher volume percentage of graphene concentration which was primarily due to presence of pores in the composite material breaking the continuity of the electrically conductive path [134]. Ponraj et al. also reported Cu-Gr composite prepared by powder metallurgy method [135]. Graphene of 1 wt.% and 2 wt.% were introduced as reinforcement within the copper matrix so as to synthesize the composite. A slurry based mixing process was used which gave good interfacial bonding between graphene reinforcement and the copper matrix. The compressive stress data of 2 wt% Cu-Gr composite gave maximum compression stress for 284 MPa which had increased up to 10% as compared to that of pure copper of 260 MPa [135].

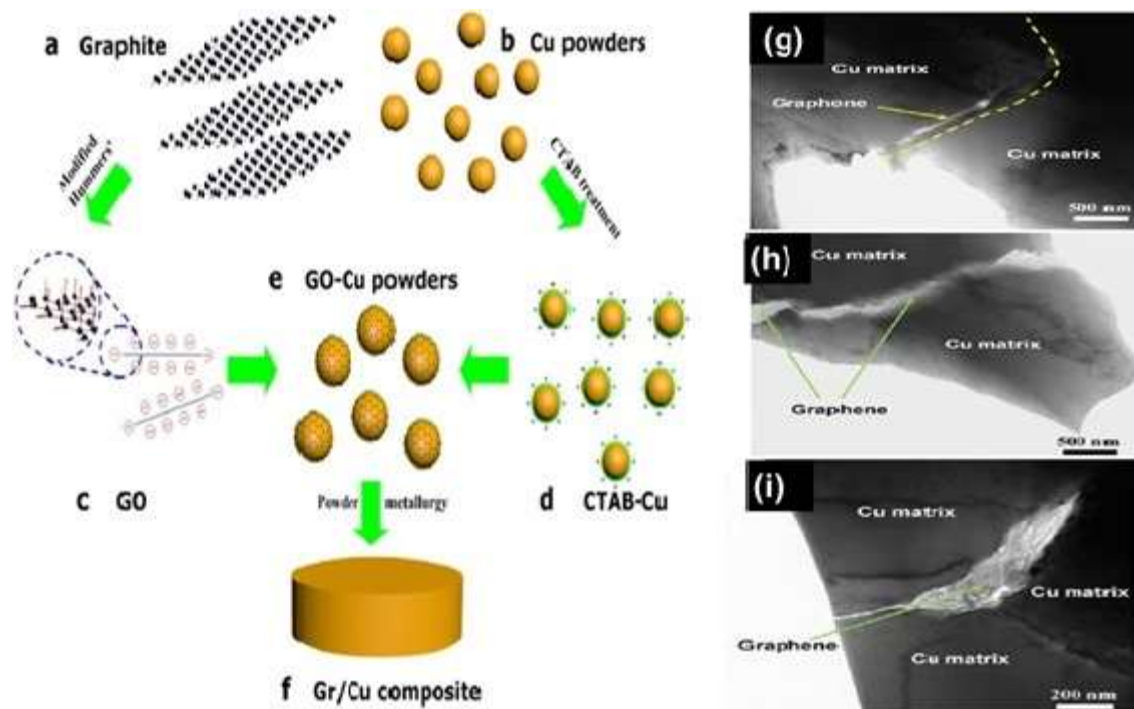


Figure 2.9: Schematic of the fabrication process of Cu-Gr composite by cold pressing and sintering (a) Graphite, (b) Cu powders, (c) GO with the negative charge, (d) CTAB modified Cu powders (CTAB\Cu) with the positive charge, (e) GO-Cu powders, (f) Cu-Gr composite. and TEM images of 0.3 wt.% Cu-Gr composite, (g) 0.5 wt.% Cu-Gr composite, (h) TEM image of graphene at the boundary of Cu grains and (i) TEM image of graphene in the triple region of Cu grains Reprinted from Gao et al. [132]. Copyright (2016) with permission from Elsevier

2.3.2.1.1.2 Hot pressing and sintering

This route focuses on using high-temperature compaction of powder mixture followed by sintering by any of the methods mentioned above. Due to high-temperature compaction, the graphene concentration can be increased up to 10 vol.% inside the Cu matrix without significant agglomeration. Hence the properties of the as-synthesized composites are expected to be better than cold pressing and sintering routes.

Li et al. have reported Cu-Gr composite by a combination of sintering and hot pressing. The Cu-Gr composite was prepared with graphene concentrations of 2.5 vol.%, 5 vol.%, 7.5 vol.% and 10 vol.% and copper powder (99.98% purity and grain size of 25 μm) which was hot-pressed at 900 $^{\circ}\text{C}$ with 25 MPa pressure for more than 40 min. Figure 2.10 (a) shows the schematic image of the preparation of Cu-Gr composite. Figure 2.10 (b) shows the SEM image of graphene nano-sheet (GNS) used in the study, composites by

using (c) 2.5 vol.% GNS and (d) 10 vol.% GNS. Here in figure 2.10 (c) it can be seen that the GNS large sheets run along the grain boundaries of the copper matrix. Further, the pulling out of GNS demonstrates that they are firmly bonded with the matrix but with an increase in 10% Gr concentration as shown in figure 2.10(c) the agglomeration and clustering of the sheets were observed. The hardness of 7.5 vol.% Cu-Gr composite had increased from 67.8 HV to 97.4 HV which was 40% higher than the unreinforced copper matrix. When the graphene concentration increased from 7.5 vol.% to 10 vol.% the hardness of composite reduced to 56.8 HV which shows the degradation of strengthening effect. The bending strength of Cu-Gr composite had also decreased with an increase in Gr concentration as compared to that of the copper matrix.

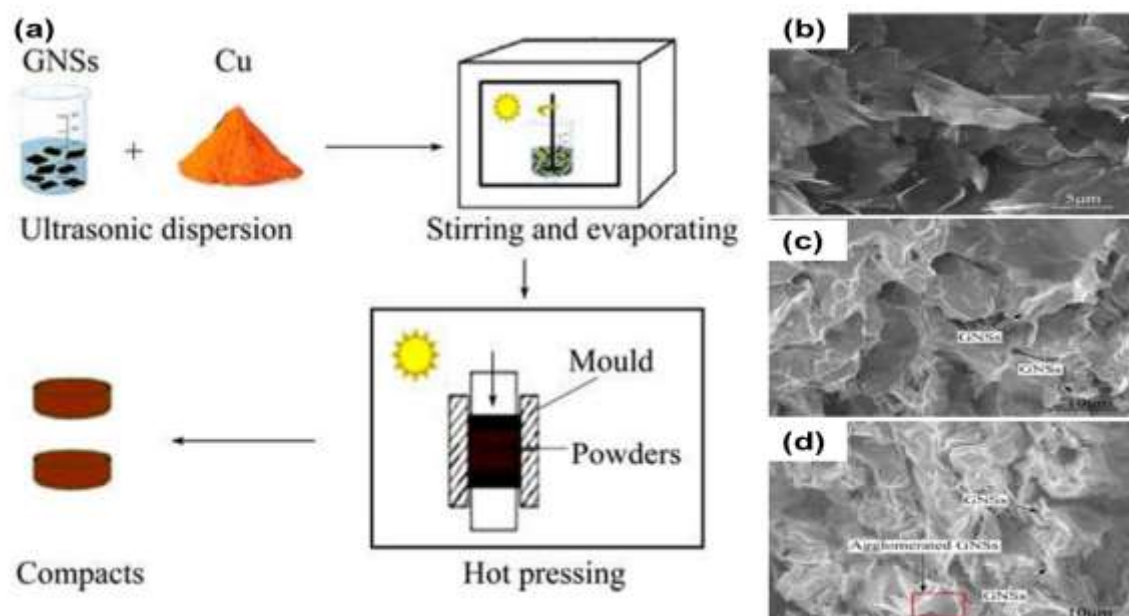


Figure 2.10: Schematic of the fabrication process of Cu-Gr composite by cold pressing and sintering (a) Graphite, (b) Cu powders, (c) GO with the negative charge, (d) CTAB modified Cu powders (CTAB\Cu) with the positive charge, (e) GO-Cu powders, (f) Cu-Gr composite. and TEM images of 0.3 wt.% Cu-Gr composite, (g) 0.5 wt.% Cu-Gr composite, (h) TEM image of graphene at the boundary of Cu grains and (i) TEM image of graphene in the triple region of Cu grains Reprinted from Gao et al. [132]. Copyright (2016) with permission from Elsevier

The coefficient of friction of Cu-Gr composite decreased from 0.24 to 0.16 and wear rate decreased from 13.6×10^{-4} to 2.3×10^{-4} mm³/m for GNSs concentration of 2.5 vol.% to 7.5 vol.% [83]. Chen et al. have also prepared Cu-Gr composite by hot press sintering process [136], where the samples were subjected to high vacuum ($< 10^{-4}$ MPa) with a pressure and temperature of 50 MPa and 800 °C respectively. Graphene concentrations of 0.4 and 0.9 wt% were added to the copper matrix (grain size of 30–40 μm). The hardness of

composite increased from 123 HV to 143 HV. Also other mechanical properties were found to increase such as yield strength of 52-144 MPa and tensile strength of 215-274 MPa with graphene concentration of 0.95 wt%. The electrical conductivity of 0.9 wt% Cu-Gr composite showed $57.5 \times 10^6 \text{ S}\cdot\text{m}^{-1}$ which is superior to pure copper $57.1 \times 10^6 \text{ S}\cdot\text{m}^{-1}$ [136]. Due to the good uniform distribution of graphene particles, the electrical conductivity was observed to be higher even at such high concentrations. In 2016 Wang et al. also prepared Cu-Gr composite by vacuum sintering and hot-pressing process [137]. Graphene and graphite (GP), each of 0.5 wt% was added separately to the copper matrix (99.9%, $<75 \mu\text{m}$) between room temperature and 600 °C. The hardness of Cu- 0.5 wt% Gr and Cu-0.5 wt% GP composites showed the same value between room temperature and 450 °C. The hardness of composites had however increased from 30 HV to 60 HV at a temperature of 600 °C which is twice of Cu-GP composite. The reinforced graphene particles are believed to have hindered the atomic diffusion over the grain boundary in Cu-Gr composite which in turn has improved the mechanical properties. Cu-Gr composite had a higher electrical conductivity than Cu-GP composite [137]. In the same year, Duda et al. synthesized Cu-Gr composite by sintering process [138]. The Gr mixed samples were pressed by hydraulic press mold and the molded samples were sintered at 800 °C. In this study 0.5 and 1 wt% of RGO (thermally reduced graphene oxide) were added with the copper matrix (grain size of 40 μm). The resistivity of composite increased with an increase in RGO concentration in the copper matrix. The coefficient of friction decreased from 0.76 to 0.22 for 1% RGO in metal matrix composite [138]. In 2017 Cao et al. reported Cu-Gr composite by in-situ fabrication through hot pressed and hot-rolled sintering. The graphene concentration of 1.6 vol.% and 2.5 vol.% was used as reinforcement with the copper matrix. The 2.5 vol.% Cu-Gr showed higher yield strength, tensile strength and Young's modulus of 200 MPa, 378 MPa and 135 GPa as compared to pure copper of 72 MPa, 218 MPa and 108 GPa respectively. The ductility of 2.5 vol.% Gr/Cu composite decreased and electrical conductivity was comparable to that of pure copper [139].

2.3.2.1.2 Powder metallurgy with ball milled graphene powders

Ball milling is a process in which a grinder with abrasive balls made up of different materials is used to drudge and blend the materials into nano-sized particles. It consists of a hollow cylinder partially filled with balls rotating about its own axis and size reduction occurs in the principle of impact and attrition as balls drop onto the material. In this

process, some control can be gained over the size of material by varying the rotation and speed of the ball, amount of material, milling time and size, process control agent and number of grinding balls. The materials' homogeneity depends mainly upon the ball to powder ratio (BPR). Most of the time, in this process different graphene concentrations that are used in the fabrication of Cu-Gr composites are synthesized during the process itself and then used in the composite as per the requirement. Further subclassification of the process along with a combination of other techniques is briefly discussed below.

Chu et al. have prepared Cu-Gr composite using a ball milling process to mix powders which in turn was fabricated using powder metallurgy route. A graphene concentration of 0-12 vol.% was dispersed with copper powder (99.9% pure, 15–20 μm) and was subjected to ball milling rotating at a speed of 1200 rpm for 3 h under argon atmosphere and BPR of 10:1. Later on, the obtained powder was first compacted and then sintered at 800 °C for 15 min to obtain the final Cu-Gr composite. The study showed that the composite gave enhanced yield strength and Young's modulus of 320 MPa and 105 GPa which was 114% and 37% higher than the copper sample of 150 MPa and 80 GPa respectively for 8 vol.% of GNPs content in the copper matrix. The mechanical properties got enhanced with the increment of graphene upto 8 vol.% but on further increment, the mechanical properties of the composite decreased. Agglomeration of GNP was found for a higher concentration (12 vol.%) where an overall decrease of the properties were observed [140]. In the same year, Chmielewski et al. reported preparation of Cu-Gr composite using ball milling and spark plasma sintering process. The graphene concentration of 3 wt%, 5 wt% and 10 wt% were mixed with copper matrix (99.8% purity and grain size of 3 μm) at 100 rpm for 4 h. Then the powder mixture was consolidated by SPS (950 °C, 50 MPa, 15 min). The hardness of Cu-Gr composite increased to 88.4 HV for Cu-3% graphene and 75.9 HV for Cu-10% graphene in comparison to pure copper (46.9 HV). The hardness of Cu-Gr composite decreased with further increase in graphene concentration of 5% graphene and 10% graphene as compared to 3% graphene reinforcement. The decrease in hardness was due to the increase in the number of pores in the carbon phase. The Cu-Gr composite showed a decrease in coefficient of friction from 1.21 to 0.46 (Cu-10% graphene) due to presence of graphene which acts as a solid lubricant in Cu-Gr composite [2]. In 2017 Yue et al. reported Cu-Gr composite prepared by high-energy ball-milling and hot-press sintering process. Graphene concentration of 0.5, 1 and 2 wt% were added with copper matrix and ball-milled at 400 rpm under argon

atmosphere for different times (1, 3, 5, and 7 h) with BPR 10:1. Figure 2.11(a) shows the schematic of the preparation of Cu-Gr composite by high-energy ball-milling and hot pressing sintering. The increase in ball milling time improved the uniform dispersion of GNSs sheets within the copper matrix but it also increased the defects and other inhomogeneity in GNSs. The longtime ball milling had caused serious damage to the GNSs. Less the amount of GNSs content (0.5 wt %) higher was the ultimate tensile stress of 230 MPa, which was 28% higher in comparison to pure copper (192 MPa). The said observation was due to the good interface bonding between Cu and GNSs.

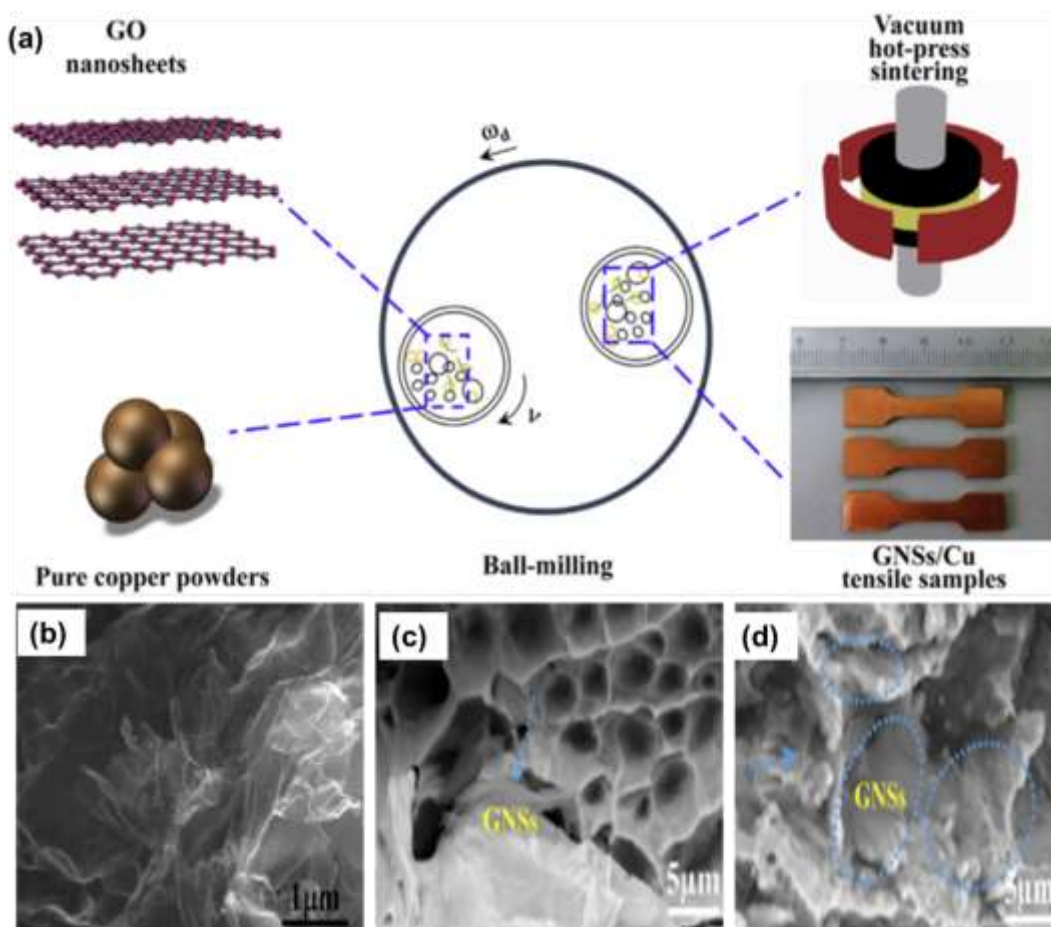


Figure 2.11: (a) Schematic of preparation of Cu-Gr composite by Powder metallurgy route with ball milled powder, (b) SEM images of Graphene Nano-sheets and Cu-Gr composite for concentration (c) 0.5 wt% GNSs and (d) 2.0 wt% GNSs. Reprinted from Yue et al. [141].

Copyright (2017) with permission from Elsevier

The strength of composite increased due to the multi-directional thermal stresses at Cu-Gr interface and the improvement of dislocation density. The GNSs concentration of 1 wt% and 2 wt% in Cu-Gr composite has deteriorated the mechanical properties in comparison to 0.5 wt% due to the aggregation of GNSs. It was explained that the agglomerated

graphene particles separated the Cu matrix and cracks were formed in the composite decreasing the tensile strength [141]. Figure 2.11 shows the SEM images of graphene and Cu-Gr composite. It can be seen in figure 2.11(b) that, for 0.5 wt% Cu-Gr composite, the fracture surface is characterized by small dimples and large tear ridges with GNSs around the boundary of copper grains. But with an increase in GNSs content, the Cu-Gr composites exhibit flat dimples with different sizes and many GNSs are observed on the fracture surface. Hence, with a high content of GNSs, the aggregation of GNSs is apparent which seriously separates the matrix, so the cracks preferentially form in graphene and had been extended into the copper matrix.

2.3.2.1.2.1 Ball milling and high-ratio differential speed rolling

This technique involves high-ratio differential speed rolling (HRDSR) combined with ball milling. High-ratio differential speed rolling is a modification of the asymmetric rolling process where deformation is due to the difference in the rotational speeds of lower and upper rolls. This results in qualitative and quantitative changes of imposed strain and hence new structural effects in comparison to a conventional rolling has been observed. The differential friction of the lower and upper surface helps in improving the properties of the synthesized composite materials. Kim et al. have reported the use of multi-layer graphene (MLG) with copper matrix to produce Cu-Gr composite by using high energy ball milling and high-ratio differential speed rolling technique. MLG platelets consisting of irregular shaped flakes (1-2 μm dia, 6-15 sheets) with concentrations of 0.5 and 1 vol.% and copper powder (99.5% in purity, 20–45 μm dia) were used in making the Cu-Gr composite powders. The high energy ball milling was carried out at a speed of 400 rpm for 4 h under an argon atmosphere and BPR was maintained at 15:1. The composite powder mixture was further consolidated to bulk composites during the successive multi-pass rolling process where during HRDSR the speed ratio between the upper and lower rolls was set at 2. The Cu-Gr composite showed an increase in the mechanical properties for HRDSR process. Composite with 1 vol.% MLG showed a yield strength of 316.2-360 MPa and ultimate tensile strength of 365.5-425.5 MPa respectively. The strength had increased due to the uniform distribution of MLG throughout the copper matrix thereby increasing the strength of the composite [81].

2.3.2.1.2.2 Ball milling and vacuum uniaxial hot pressing

Hot pressing is a technique in which powder consolidation is done under high-pressure and low-strain-rate and simultaneously it is subjected to a high temperature which helps in compaction as well as induces sintering. If the process is carried out under the combination of vacuum and load is applied only along the longitudinal direction, then it is referred to as vacuum uniaxial hot pressing. High-density product free of porosity is achieved by the simultaneous application of heat and pressure. In 2015 Dutkiewicz et al. reported Cu-Gr composite fabrication by vacuum uniaxial hot pressing and have used ball milling for mixing the powder. It consisted of copper powder (99.9% purity and 40-90 μm) and two different grades of coarse and fine graphene platelets (N006 of 10-20 nm and FLGPs of thickness 2-4 nm) which were mixed in the ball mill for 5h and a BPR 10:1 was maintained. The graphene concentration of 1 and 2 wt% of either N600 or FLGPs was used with copper matrix to synthesize the composite under uniaxial hot pressing of 550 MPa at a temperature of 510 $^{\circ}\text{C}$ at 10^{-2} bar vacuum and the uniaxial pressure. The addition of fine particles of graphene gave enhanced hardness of 615 MPa which was 50% higher than that of pure copper and 30% lower electrical resistivity than that of coarser graphene platelets of the composite. The fine graphene platelets had a homogeneous distribution with copper matrix but coarser one gave more defects and underwent agglomeration in the composite, hence giving inferior properties [142].

2.3.2.2 Accumulative roll bonding (ARB)

Accumulative roll bonding (ARB) is a severe plastic deformation (SPD) process where generally stack of metal sheets are rolled over and over due to which severe size reduction occurs; also it is sectioned into two halves, piled again and rolled. Metal materials with ultrafine grain microstructure are produced by this technique. To obtain a single slab of solid material, the rolling involves not only deformation but also roll bonding. Liu et al. have reported Cu-Gr composite fabrication by this method. Oxygen-free strips of copper (150 mm \times 25 mm \times 1 mm) were first annealed and GNSs (10 nm \times 15 μm) of 0.05 mg/mm² concentration was sprayed onto the Cu strips. Then two such strips were stacked on top of each other and rolled with 20 tons load and roll speed of 0.34 m/s per rolling cycle was maintained. After one cycle the reduced sheet was cut, stacked and rolled; this cycle was done for 8 cycles without any further addition of Gr particles. The tensile strength of the prepared Cu-Gr composite was found to be 496 MPa which is much higher than that of

annealed copper of 221 MPa and also from that of ARBed copper 463 MPa [143]. The composites showed a homogeneous dispersion of GNSs and a good interfacial bonding with extensive grain refinement.

Table 2.3: The development of copper-graphene composite synthesis and their main results

Fabrication Methods	Year	Graphene Concn.	Main results	Author	Ref. no
Direct Electrochemical Deposition	2011	Not provided	Thermal conductivity improved from 3.8 to 5.0 W/cm.K and electrical conductivity reduced from 2.031 to 1.699 $\mu\Omega\text{cm}$.	Jaganna dham et al.	[118] – [120]
	2012		Thermal conductivity 510 W/m.K at 250 K (-23°C) to 440 W/m.K at 350 K (77°C).		
	2014	Cu-0.1mg/L and 0.5mg/L Gr	Electrical resistivity decreased from 38.39 $\text{m}\Omega\cdot\text{m}$ to 31.2 $\text{m}\Omega\cdot\text{m}$.	Xie et al.	[144]
	2017	Cu-0.2, 0.5 and 0.8 g/L Gr	Tensile strength, elastic modulus and hardness increases at a temperature 25-40 $^\circ\text{C}$	Song et al.	[117]
	2017	Cu-0.125, 0.25 and 1 g/L Gr	Corrosion rate decreased from 62.76 (Cu) to 9.16 mil/year (Cu-Gr)	Raghupathy et al.	[122]
	2018	Cu-0 to 0.4 g/L Gr	Hardness increased by 30% and Cof decreases 35%-40% and wear rate decreases 10-18 times.	Mai et al.	[123]
	2018	Cu-0.1, 0.3 and 0.5 g/L Gr	Hardness increase up to 31%	Behera et al.	[42]
Pulse electrodeposition	2013	Cu-0 to 1 g/L Gr	Hardness increases by 96% and elastic modulus increase 30%	Chokkula et al.	[85]
	2016	Cu-0.1 to 0.75 g/L Gr	Hardness increases by 125% and elastic modulus increase 30%	Pavithra et al.	[124]
	2016	Cu-0.5 and	Young's modulus increased	Hwang	[125]

		300 mg/L Gr	by 172% (82.5 GPa) and also yield strength and breaking strength increased by 39.1% and 21.1%	et al.	
		2107 Cu-0 to 1 g/L Gr	Hardness increased by 40% and CoF decreased	Maharana et al.	[126]
Powder metallurgy	2016	Cu-0, 0.1, 0.3 and 0.5 wt% Gr	Max thermal conductivity 396 W.m ⁻¹ K ⁻¹ observed at 0.3 wt% Gr/Cu	Gao et al.	[20]
	2017	Cu-1 wt.% and 2 wt.% GNS	Compressive stress of 284 MPa, increased up to 10% of Cu	Ponraj et al.	[135]
Semi powder mixing + SPS	2016	Cu-0.5 vol.% Gr	Yield strength(164 MPa) increased by up to 49.1%	Zhang et al.	[145]
SPS (Powder metallurgy)	2016	Cu-0.2 wt% RGO	Yield strength increases from 95-172 MPa and 5% compression strength of 120-128 MPa as compared to pure copper	Jiang et al.	[133]
Microwave sintering + powder metallurgy	2017	Cu-0.9, 1.8, 2.7 and 3.6 vol.% Gr	Hardness increased 46 HV -89 HV and COF decreases	Ayyappa das et al.	[134]
Electrostatic self-assembly and powder metallurgy (PM)	2018	Cu-0 to 0.5 g/L Gr	Hardness increases by 18.6% and COF decrease up to 65%	Gao et al.	[146]
Electrochemical deposition method and powder metallurgy	2018	Cu-8, 12, 28 wt% Gr	Hardness(112 HV) increases 2.47 times than copper	Zhao et al.	[147]
Chemical synthesis and powder metallurgy	2018	Cu-0.2, 0.5 vol.% Gr	Yield strength increases 1.14 times	Jang et al.	[148]
	2013	Cu-1, 2, 2.5, 80 vol.% Gr	Elastic modulus and yield strength increase by up to 30% and 80 %.	Hwang et al.	[149]
Molecular-lever mixing (MLM)+ SPS	2015	Cu-0.6, 1.2, 2.4, 4.8 vol.% RGO	Yield strength increases three times than pure Cu	Wang et al.	[150]
	2016	Cu-0.2, 0.4, 0.6, 0.8, 2.4 vol.% GNP	Elastic modulus and hardness increases by 67% and 75% and COF decreases from 0.6 to 0.25	Chen et al.	[151]
	2016	Cu-2.4, 5	Tensile strength and hardness	Wang et al.	[152]

		vol.% Gr	increase up to three times as compared to copper(255-608 MPa) and (63-188.8 HV)	al.	
	2016	Cu-0.05, 1 vol.% Gr	Yield strength increases 136 MPa to 208MPa on 0.1 vol.% GNPs/Cu and 250 MPa on 0.1 vol.% RGO/Cu	Zhang et al.	[153]
	2018	Cu-2.5, 5, 7.5% RGO	Tensile strength(748 MPa) 32% higher	Yang et al.	[154]
Electroless + SPS	2014	Cu-1.3 wt% Gr	Young's modulus increases 85-104 GPa, Tensile strength 234-485 MPa	Zhao et al.	[155]
Chemical reduction method + SPS	2014	Cu-0.5,1 vol.% Gr	Young's modulus increases 82-132 GPa, Tensile strength 230-320 GPa, and Yield strength 138-268 MPa	Tang et al.	[156]
Ball milling and hot pressing	2014	Cu-0-12 vol.% Gr	Enhanced yield strength and Young's modulus of 114% and 37%	Chu et al	[140]
One-pot reduction method	2014	Cu-0.1 g/L and 0.4 g/L Gr	Improve the load-carrying capacity of the base oil by 50%	Li et al.	[131]
Ultrasound-assisted electroless plating	2014	Not provided	2D sandwich-like Cu/RGOS nanocomposites, large aspect ratio, high surface area	Peng et al.	[130]
Ball milling and high-ratio differential speed rolling (HRDSR)	2014	Cu-0.5 and 1 vol.% MLG	1% Yield strength increases 316.2 -360.5 MPa and Ultimate tensile strength 365.5-425.5 MPa	Kim et al.	[81]
Ball milling + spark plasma sintering(SPS)	2015	Cu-3, 5, 10 wt% Gr	Hardness increases 46.9 HV to 88.5 HV	Chmielewski et al.	[2]
Sintering +Hot pressing	2015	Cu-2.5, 5, 7.5 and 10 vol.% Gr	Hardness increases 67.8 HV to 97.4 HV coefficient friction decreases 0.28 -0.19 for Cu-Gr and 0.24-0.16 for Cu-GNS	Li et al.	[83]
Freeze-drying +SPS	2016	Cu-2.5, 5 wt% RGO	Hardness increases from 62.2-65.3HV and coefficient of friction decrease from 0.84 -0.38 and volume rate (1.17-0.64) $\times 10^{-4}$ mm ³ /Nm	Zhang et al.	[157]
	2016	Cu-2.5 wt% RGO	0.2%Yield strength increased to 121.2 MPa from pure Cu 33.5 MPa and as sintered Pure	Zhang et al.	[158]

				Cu 89.6 MPa		
Hot-press sintering	2016	Cu-0.4, 0.9 wt% Gr		Hardness increases 123 HV to 143 HV and yield strength 52 - 144 MPa and tensile strength 215 to 274 MPa.	Chen et al.	[136]
Vacuum sintering + hot-pressing	2016	Cu-0.5 wt% GN		Hardness increases at high temperature 600 °C	Wang et al.	[137]
Sintering	2016	Cu-0.5, 1 wt%		COF decreases from 0.75 to 0.24	Duda et al.	[159]
SPS + hot-rolling	2017	Cu-0.5, 1 and 2 vol.% Gr		Improved electrical conductivity	Yang et al.	[160]
Vacuum filtration +SPS	2018	Cu-20, 20, 40 vol.% Gr		Thermal conductivity increases by up to 50%	Chu et al.	[161]
Ball milling + hot press sintering	2017	Cu-0.5, 1,2 wt% GNSs		UTS strength increases 28% at 0.5 wt% of GNSs content	Yue et al.	[141]
	2015	Cu-1, 2 wt% Gr		Hardness increased by 50%	Dutkiewicz et al.	[142]
Ball milling	2015	Cu-1, 2 and 5 vol.%		At 1wt% of the HQG electrical conductivity increases by 8%	Li et al.	[162]
Ball milling + CVD	2016	Cu-0.4, 0.95 wt%		Yield strength and tensile strength increased up to 233.3% (290 MPa) and 35.7% (308 MPa)	Chen et al.	[136]
In-situ fabrication Hot rolled and hot pressed and sintering	2017	Cu-1.6, 2.5 vol.%		Yield strength and elastic modulus increases up to 177% and 25%	Cao et al.	[139]
Accumulative roll bonding(ARB)	2015	Not provided		Tensile strength increases 496 MPa than annealed copper of 221 MPa	Liu et al.	[143]
GO fill in 'brick-and-mortar'	2015	Cu-45 vol.% Gr		Increase in Young's modulus 97-109 GPa, yield strength 106-233 MPa, tensile strength 218-308 MPa	Xiong et al.	[163]
Electroless co-deposition	2017	Cu-0 to 7 mg/L		Hardness increases 1.47 GPa of copper to 2.33 GPa of Cu-Gr composite at 5 mg/L concentration	Zhang et al.	[128]
	2019	Cu-20, 60 and 100 mg/L		Hardness 3.4 GPa and elastic modulus 96.2 GPa	Li et al.	[129]

2.3.3 Mixed phase fabrication techniques

The mixed phase is the combination of dry and wet phases including processes such as molecular-level mixing (MLM) with SPS, electroless plating with SPS and in-situ chemical reduction with SPS. Further, these techniques can be briefly described as below.

2.3.3.1 Molecular-level mixing process with SPS

The molecular-level mixing process is a novel fabrication technique which is quite different from conventional mixing to synthesize composite materials. In this process, a slurry of the desirable powder mixture is prepared and from it the powder mixture is obtained by mixing at the molecular level. Bonding takes place between negatively and positively charged ions of the powder constituents in the slurry mixture. There is uniformity in the composite materials and it reduces the dispersion and thermal damage of materials in the copper matrix composite. The graphene sheets are homogeneously distributed throughout the metal matrix and develop strong interfacial strength by this process. In this process, due to the attached functional groups to graphene sheets, better interfacial chemical bonding between the graphene sheets and the metal matrix is achieved. This technique combined with SPS would avoid the dispersion and thermal damage of graphene sheets within the metal matrix. Further SPS process limits the grain growth and diffusion mechanism of powder particles. The advantage of this process is fast heating rate, fast cooling rate, short holding and material processing time. The above route was followed to synthesize Cu-Gr composite by Yang et al. The RGO concentration were in the range of 2.5, 5 and 7.5 vol.% in the copper matrix. In this case, NaOH was used to functionalize the graphene sheets at pH ranges of 6 to 9. Figure 2.12 (a) shows the schematic image of Cu-Gr composite by MLM and SPS method. The tensile strength of Cu-Gr composite has 748 MPa at 2.5 vol. % of RGO reinforcement which is up to 32% higher than copper (574 MPa). The mechanical properties of Cu-Gr composite increased without a decrease in electrical conductivity which shows a better dispersion of the reinforcement [154]. Figure 2.12 (b) shows the SEM image of Gr flake, and figure 2.12 (c), (d) show fractured surfaces of 2.5 vol.% Cu-Gr and 7.5 vol.% Cu-Gr. Looking at the fracture morphology of the 2.5 vol.% Cu-Gr composite, it can be observed that the composite is extremely homogeneous and the dimples are about 500 nm in size. As the volume fraction of graphene increases, the size of the dimples is not consistent and keeps increasing due to graphene agglomerations (marked by yellow circles) as shown in figure

2.12(d). Hwang et al. have also reported Cu-Gr nanocomposite prepared by this hybrid route. The graphene (RGO) concentration of 1 vol.%, 2 vol.% and 80 vol.% were added with the copper matrix. The 2 vol.% Cu-Gr nanocomposite resulted in an increase in tensile strength of 335 MPa which is 30% more than pure Cu of 255 MPa. The elastic modulus was 30% (131 GPa) and yield strength was 80% (284 MPa) as compared to pure copper of 102 GPa and 160 MPa respectively. The adhesion energy between graphene and copper was estimated to be around 164 Jm^{-2} which shows a strong interfacial bonding in graphene and copper [149].

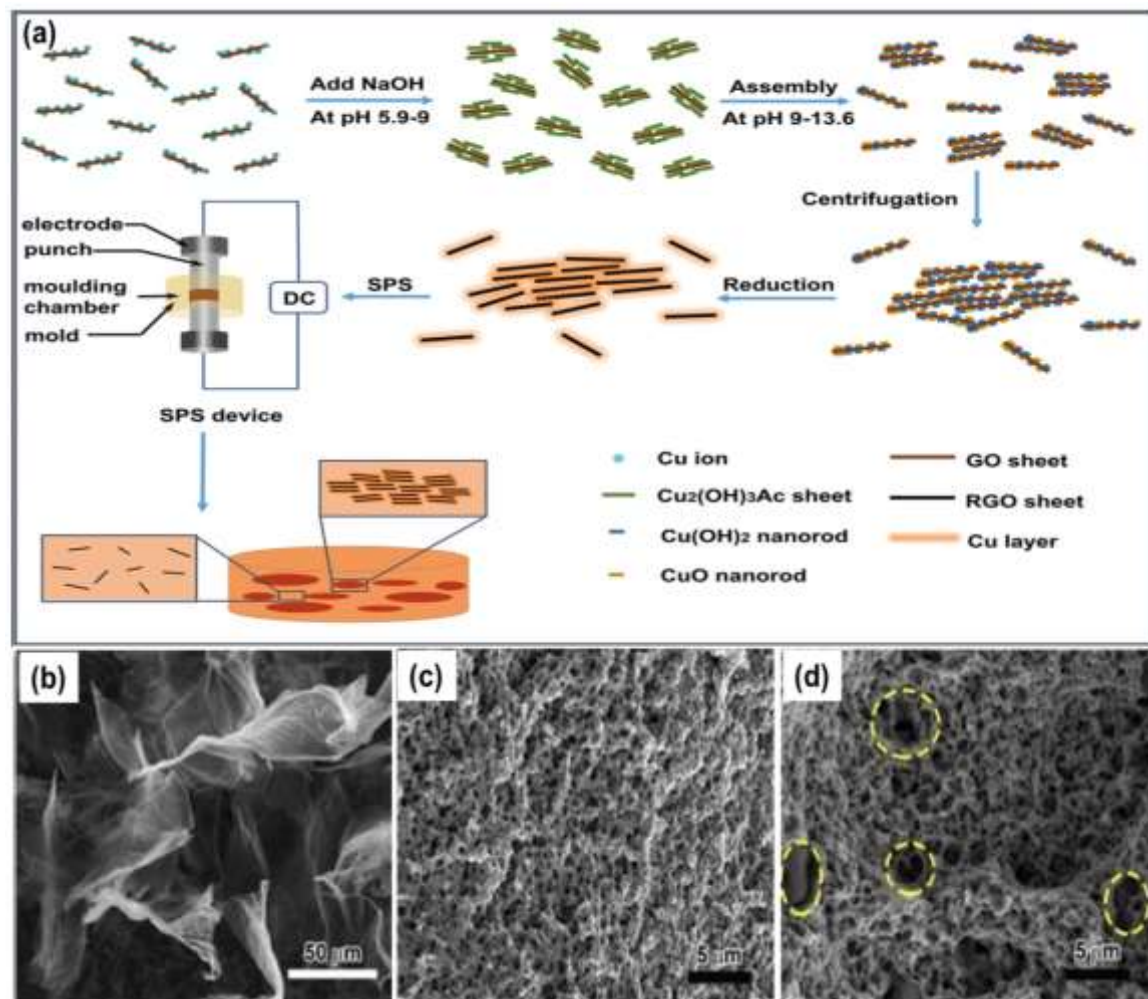


Figure 2.12: (a) Schematic image of Cu-Gr composite by MLM and SPS method and SEM image of (b) Graphene flake, fracture surface of Cu-Gr composites (c) 2.5 vol. % and (d) 7.5 vol.%.

Reprinted from Yang et al. [154]. Copyright (2018) with permission from Elsevier

In 2015 L. Wang et al. reported RGO in copper matrix composites produced by MLM and high-shear mixing with SPS technique [150]. The composite prepared by only MLM method was abbreviated as M whereas by high shear mixing and MLM as M-H. Graphene

concentrations of 0.6, 1.2, 2.4 and 4.8 vol.% were introduced with copper matrix to synthesize the composite. The RGO/Cu composite prepared by high-shear mixing gave higher mechanical properties than the magnetic stirring mixing process. In this process, yield strength of 2.4 vol.% Cu-Gr (M-H) composite (501 MPa) is three times higher than the copper matrix (150 MPa).

The RGO concentration of 4.8 vol.% (M-H) (395 MPa) in Cu-Gr gave lower mechanical properties as compared to 2.4 vol.% RGO content of yield strength 501 MPa. The decrease in mechanical properties was due to agglomeration of RGO sheets in solution during MLM process [150]. Chen et al. reported Cu-Gr composite by the same route. The GNP concentration of 0.2 vol.%, 0.4 vol.%, 0.6 vol.%, 0.8 vol.%, 2.0 vol.% and 4.0 vol.% were mixed with Cu matrix. The yield strength of 0.6 vol.% Cu-Gr composite showed 310 MPa which is higher than that of copper (142 MPa), but on a further increase of graphene concentration to 4.0 vol.% yield strength decreased to 200 MPa. The elastic modulus and hardness of 0.8 vol.% (Cu-Gr) composite have 147 GPa and 1.75 GPa as compared to pure copper of 89 GPa and 1.01 GPa which is 65% and 75% higher than pure copper. The coefficient of friction decreased from 0.6 (copper) to 0.25 (Cu-Gr) for composite which is 60% lower than copper. The wear depth of composite also decreased as compared to reference copper. The coefficient of friction of Cu-Gr composites varied with sliding time and profiles of the wear tracks. Also the electrical conductivity of 4.0 vol.% Cu-Gr composite increased up to 85% higher than reference copper. The mechanical properties of Cu-Gr composite increased with an increase in graphene concentration up to 0.8 vol.%. Further, it deteriorated with an increase in graphene concentration due to aggregation [151]. In the same year, Wang et al. also reported Cu-Gr composite following the route. Graphene concentration of 2.4 vol.% and 5 vol.% was added with copper matrix. The tensile strength of 5 vol.% Cu-Gr composite increased up to 608 MPa which is 2.4 times higher than pure Cu (255 MPa). The compressive strength increased up to 630 MPa for 5 vol.% Cu-Gr composite. The hardness also increased from a value of 63 HV of copper to 188.8 HV of 5 vol.% Cu-Gr composite which is three times higher than pure copper. The RGO concentration of 5 vol.% with the copper matrix in Cu-Gr composite resulted in enhanced properties without any agglomeration of GO sheets [152]. Zhang et al. have also reported fabrication of Cu-GNP and Cu-RGO composites by the same route. The GNP and RGO ranges of 0.05 vol.% to 1 vol.% were introduced as reinforcement with copper matrix. The 0.1 vol.% of both, Cu-GNPs and Cu-

Gr composite gave enhanced yield strength of 208 and 170 MPa which is 52.9% and 25% higher than pure copper of yield strength of 136 MPa respectively. The 0.1 vol.% of GNPs-Cu and RGO-Cu have higher strengthening efficiency of reinforcements i.e. 529 and 250 respectively. The strengthening efficiency of GNPs composite decreased with increase in reinforcement concentration of 0.1 vol.% to 1 vol.% but in Cu-Gr case it is the opposite. The strength of above Cu-Gr composites was lower than the Cu-Gr composite at a higher reinforcement concentration of 0.5-1 vol.% graphene. The difference may be due to graphene distribution, structural integrity, poor interfacial bonding, and agglomeration problem [153].

2.3.3.2 Freeze-drying and spark plasma sintering

Freeze drying is a low-temperature dehydration process in which the product is frozen and then subjected to low pressure, after which heat is added which results in the sublimation of the frozen water in the material. This is quite different from the conventional dehydration process where water is evaporated by heating it. This technique helps in giving a high-quality product hereby maintaining the original shape of the product. Along with this technique, SPS process described in the previous sections has been used which gave a highly consolidated composite of good quality. Zhang et al. have synthesized Cu-Gr composite by freeze-drying and subsequent sintering by SPS route [157]. Figure 2.13(a) shows a schematic of the fabrication process of Cu-Gr nano-composite. The RGO concentration of 2.5 wt% and 5 wt% was introduced as reinforcement with copper matrix to prepare Cu-Gr composite. Figure 2.13 shows SEM image of (b) dried CF/Gr/Cu composite powder, (c) CF/Gr/Cu-matrix composite where the dark and white arrows respectively show the agglomerated and dispersed rGO and (d) TEM image of Cu-Gr interface. The 0.2% yield strength ($\sigma_{0.2}$) of Cu-Gr composite is 121.2 MPa which is higher than both cast pure Cu (33.5 MPa) and sintered Cu (89.6 MPa). The compressive ductility of the composite decreased with an increase in RGO concentration of 5 wt% in composite [157]. The same group also fabricated hybrid Cu-Gr composite with short carbon fiber (CF) and RGO by the same method. The tribological properties of composite increased i.e. COF decreased from 0.84 (of copper) to 0.32 (of Cu-Gr composite) and wear rate also decreased from 1.17×10^{-4} mm³/Nm (Cu) to 0.64×10^{-4} mm³/Nm (Cu-Gr composite). The addition of CF/RGO to form the hybrid composite had reduced the material removal of surfaces during dry sliding with steel counter surface. The microhardness of composite increased from 62.2 HV (Cu) to 68.7 HV (Cu-Gr) [158].

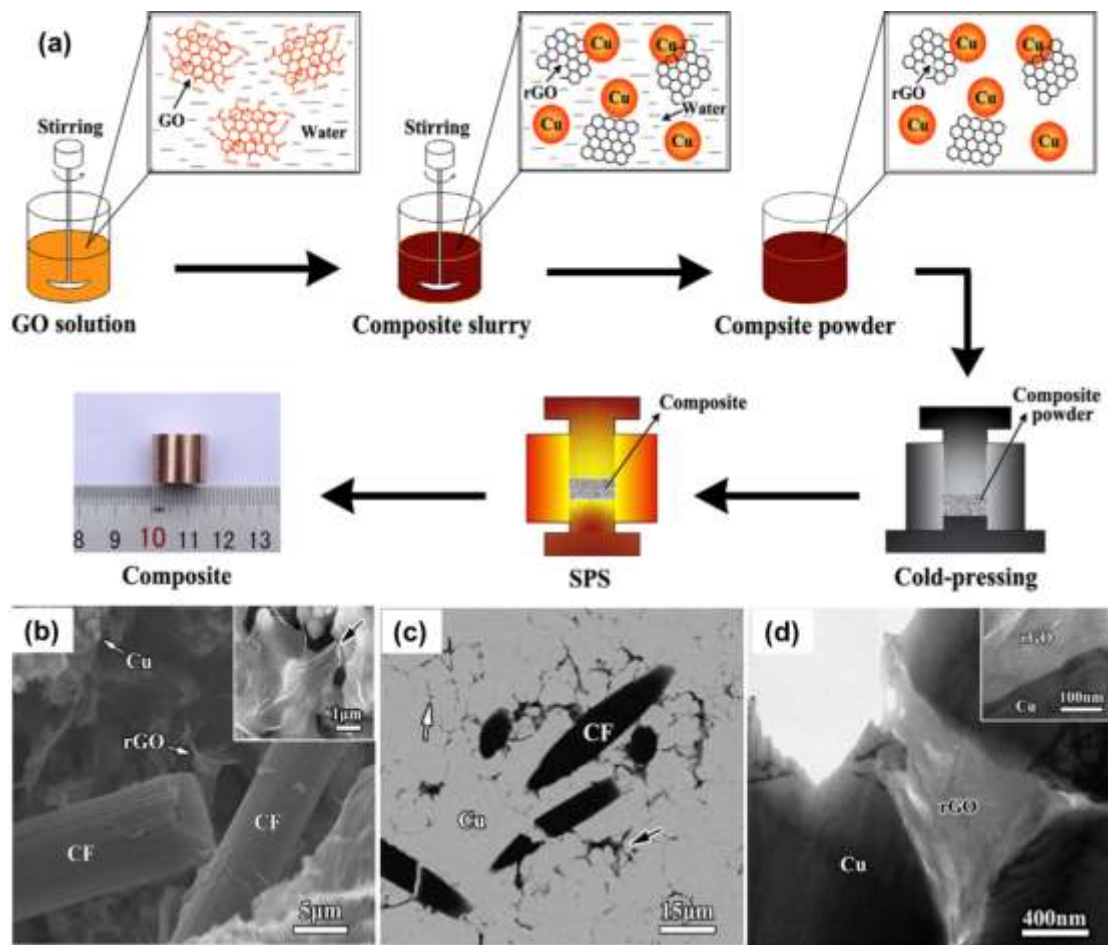


Figure 2.13: (a) Schematic illustration of the fabrication process of Cu-Gr composites by freeze-drying and spark plasma sintering route and SEM image of (b) dried CF/Gr/Cu composite powder, (c) CF/Gr/Cu-matrix composite where the dark and white arrows respectively show the agglomerated and dispersed rGO and (d) TEM image of Gr/Cu interface. Reprinted from Zhang et al. [157]. Copyright (2016) with permission from Elsevier

2.3.3.3 Electroless plating with SPS

This is a unique technique in which both electroless plating and spark plasma sintering (as described in the previous sections) is combined to give a highly consolidated and compact composite. Zhao et al. prepared Cu-Gr composite by the combination of electroless plating with SPS process [155]. Figure 2.14 shows the SEM image of (a) as-prepared GO, (b) as-prepared Cu-Gr powders and (c) Cu-Gr composites. Here, in figure 2.14(a) GO displayed a transparent sheet-like morphology with characteristically stacked, crumpled and folded structures, in (b) a great number of Cu nanoparticles were not only covered on the surface of GNPs (red arrows), but also embedded between neighboring GNPs to serve as spacers in order to prevent GNPs from aggregations and restacks. Figure 2.14 (c)

shows that the size of the ductile dimples decreased significantly in Cu-Gr composites. High magnification of the image (figure 2.14(c), inset) clearly shows the presence of GNPs (marked by circles) that were embedded in the dimple walls. The Young's modulus and tensile strength of 1.3 wt% Cu-Gr composite have increased to 85-104 GPa and 234-485 MPa respectively.

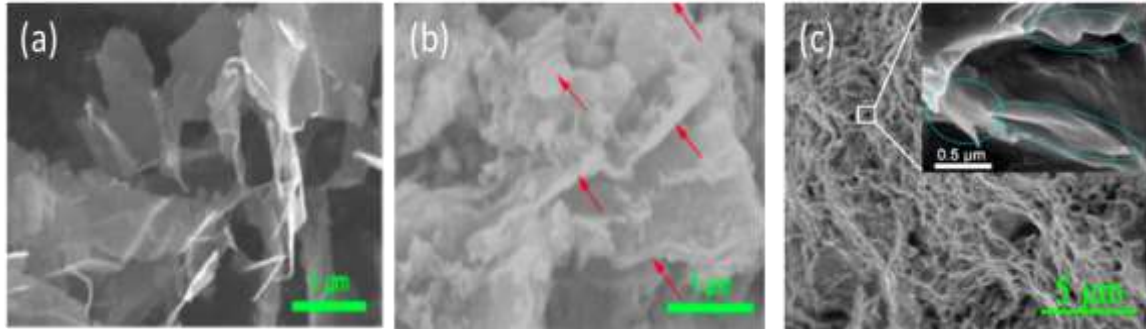


Figure 2.14: SEM image of (a) as prepared GO, (b) as-prepared Cu-Gr powders and (c) Cu-Gr composites (inset for high magnification) fabricated by Electroless plating with SPS Reprinted from Zhao et al. [155]

2.3.3.4 In situ chemical reduction and spark plasma sintering

In situ chemical reduction is another novel technique and as the name suggests it involves the insertion of a reductant or reductant generating material in SPS process. This is done for the purpose of reducing the undesired complex in the mixture to the desired one without going to the additional step of first reducing and then using it for the process. So, prior to the compaction of powder mixture the mixture undergoes chemical reduction by addition of suitable chemically reducing additives in liquid form which helps in giving the final desired composition of the powder mixture. And then the powder mixture is sent for final consolidation by the SPS process as described earlier to give a compact composite. In 2014, Tang et al. have reported GNS–Ni/Cu composite prepared by the combination of in situ chemical reduction and spark plasma sintering [156]. The GNS concentration of 0.5 and 1 vol.% were wet mixed with the copper matrix. This was done by introducing Gr-Ni hybrids (synthesized by in-situ chemical reduction) into the Cu matrix followed by spark plasma sintering. Figure 2.15 shows the (a) TEM images of GO nano-sheets, (b) SEM images of the fracture surfaces and (c) 1.0 vol.% GNS–Ni/Cu composites. Here figure 2.15(c) exhibits that isolated GNSs have been pulled out or tightly embedded in the Cu matrix (marked by arrows), suggesting that GNSs have stronger interfacial interaction with the Cu matrix. The choice of using Ni, stems from the fact that Cu and Ni phases

have homogeneity between them at any given temperature and thus it was expected to have higher Cu-Gr bonding between the planes. SPS played a key role in deoxygenating the RGO sheets and removing defects from the graphene structure. The 1.0 vol.% GNS-Ni/Cu composite shows higher Young's modulus and tensile strength of 132 GPa and 268 MPa respectively which is 61% and 94% higher than copper [156].

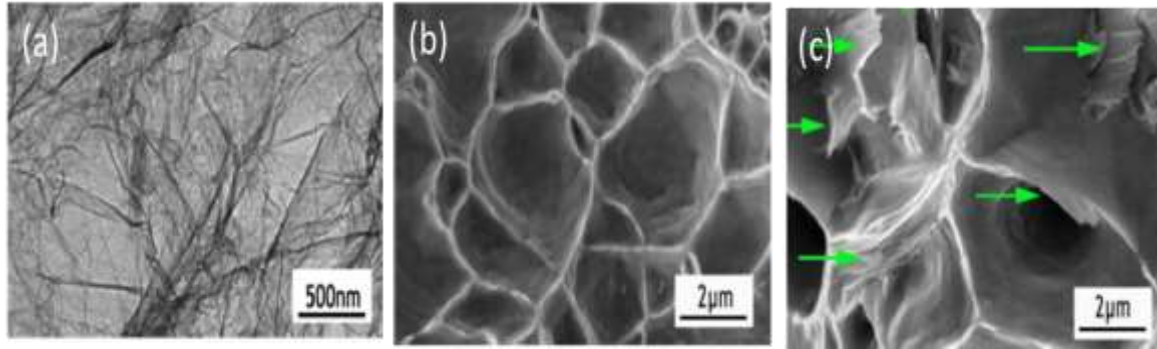


Figure 2.15: (a) TEM images of GO nanosheets, SEM images of the fracture surfaces of (b) Cu and (c) 1.0 vol.% GNS-Ni/Cu composites fabricated by In-situ chemical reduction and SPS technique Reprinted from Tang et al. [156]

2.3.3.5 Semi powder mixing and SPS route

Semi powder mixing method is quite similar to conventional molecular mixing methods but the conditions are different i.e. solution based powder method where the powder mixture is mixed in a suitable solvent like ethanol using a mechanical agitator. Also, there can be external addition of other materials during the operation so as to give a homogeneous mixture. Further, the powder is compacted and sintering is done through SPS for the final product. Zhang et al. have reported Cu-Gr composite fabrication by semi powder mixing and SPS route [145]. Graphene (5-10 nm thick) of 0.5 vol.% concentration was mixed with copper matrix (99.5% pure and grain size of 75 μm) in ethanol under mechanical stirred conditions for 2h to obtain the mixture. Then the mixture was finally consolidated by SPS at 600 $^{\circ}\text{C}$ and under uniaxial pressure of 45 MPa to obtain Cu-Gr composite. The yield strength of 0.5 vol.% graphene concentration composite showed an enhanced yield strength of 164 MPa which is 49.1% higher than that of copper (112 MPa). Figure 2.16 shows the SEM images of the fracture surface of (a) pure Cu, (b) 0.5 vol.% Cu-Gr and (c) 0.5 vol.% Cu-Gr.

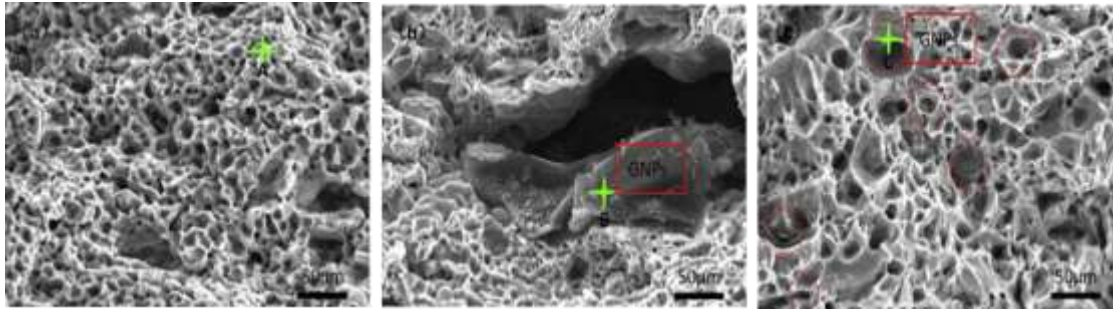


Figure 2.16: SEM images of the fracture surface of (a) pure Cu, (b) 0.5 vol.% Cu-Gr and (c) 0.5 vol.% Cu-Gr fabricated by Semi powder mixing and SPS technique. Reprinted from Zhang et al.[145]

2.4 Mechanism of property adaptations of Cu-Gr nano-composites:

In general, graphene and graphene derivatives when added to copper-based composites affect the properties of the as-obtained Cu-Gr composite. Mechanical, tribological, electrical, corrosion-resistant and thermal properties are some of the principal properties that are affected by graphene-based reinforcement in the composite. The said properties of Cu-Gr composites generally get increased with the increase in graphene concentration in the copper matrix. However, the properties do not improve indefinitely after a certain concentration, rather it is found to decline from higher values to values lower than parent Cu matrix properties. The underlying mechanisms for improvement and subsequently deterioration of the properties are briefly discussed below.

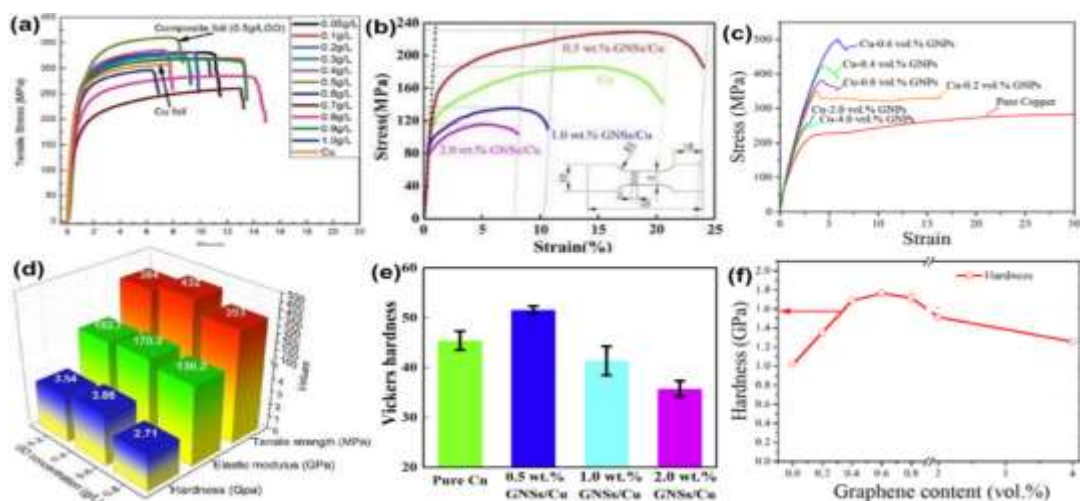


Figure 2.17: Variation of mechanical properties of Cu-Gr composites prepared by (a) and (d) wet method [117], (b) and (e) dry method [141], (c) and (f) mixed method [151]

The mechanical properties of Cu-Gr composites increase with an increase in graphene concentration in the copper matrix. Figure 2.17 shows alteration of the mechanical properties of the Cu-Gr composites fabricated through different routes. The uniform distribution of graphene sheets gave enhanced properties due to good interface bonding between the reinforcement and the matrix. However, it can be observed that in case of composites fabricated through either dry or wet method the maximum graphene concentration is 0.5 wt% which gave elevated properties and any further increase in concentrations resulted in a decrease of hardness and other mechanical properties. In the case of mixed-phase synthesis, up to 5 wt% shows an increase in properties. The said observation and limit of graphene percentage incorporation can be explained in the following discussion. A particular metal's mechanical properties can be controlled by varying the presence of dislocation impeding sources and increasing the density of dislocations. Although seemingly counter-intuitive, as the density of dislocations increases, there are more intersections created and consequently more anchor points. Similarly, as more obstructions to dislocation are created, more pinning points that impede the movements of dislocations are formed. As a result, higher the presence of anchor points, the harder the material will become. At low concentrations of graphene reinforcement, the Orowan strengthening mechanism was observed during synthesis of Cu-Gr composite. The graphene nano-sheets block the movement of dislocation motion at grain boundaries and its interfaces between graphene reinforcement and copper matrix leading to the dislocation pileups at the interface of Cu-Gr composite thereby increasing the overall strength of the composite. The restricted dislocation motion increased the critical stress for dislocation glide to the grain boundary, which leads to an increase in mechanical properties. At higher graphene concentrations, the main key issue was the agglomeration of graphene nano-sheets in Cu-Gr composite as they have high surface area and Van der Waals bonding between the sheets. Hence, excess amount of graphene sheets cause aggregation which in turn separates the copper matrix in the composite. This phenomenon creates voids and cracks in composite and thus decreases mechanical properties.

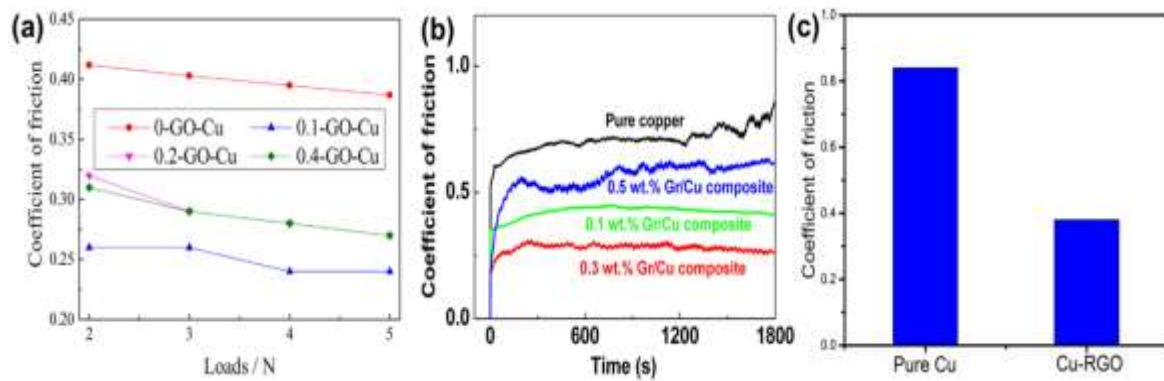


Figure 2.18: Variation of the coefficient of friction of Cu-Gr composite prepared by (a) wet method [123], (b) dry method [146] and (c) mixed method [158]

Graphene addition also affects the tribological characteristics like wear properties and coefficient of friction (CoF). Figure 2.18 shows the change in CoF values with graphene concentration. It can be observed that irrespective of the synthesis route there is a decrease in the values, hence improved lubrication and wear properties can be generally expected. Also, the wear scar analysis showed less intense plastic deformation in the composite when graphene was added to it. It results in a remarkably decreased friction coefficient as graphene could act as a solid lubricant in the Cu-Gr composite. Hence a small amount of graphene can significantly increase the wear resistance and decrease the coefficient of friction of the material.

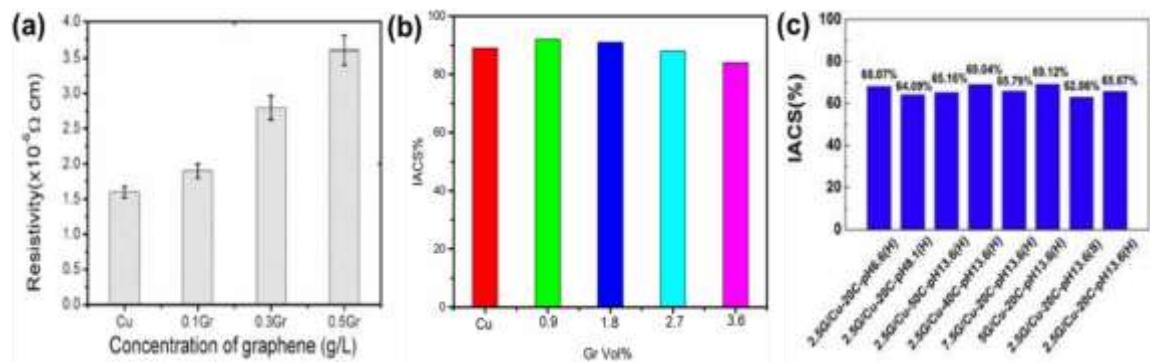


Figure 2.19: variation of electrical properties (a) wet method [42], (b) dry method [134] and (c) mixed method [154]

Graphene is considered as a highly conductive material due to the presence of free delocalized electron in each atom of its 2D hexagonal based structure that helps in carrying and passing on an electric charge. Hence, in general with an increase in the graphene concentration in the Cu-Gr composite the overall electrical conductivity was found to increase quite significantly in comparison to copper. However higher

concentration of graphene in the matrix may lead to agglomeration which may decrease the electrical resistance as shown in figure 2.19.

Table 2.4: The development of copper-graphene composite synthesis and their main results

Parameter	Wet method	Dry method	Mixed method
Thermal conductivity in W/m.K	Increased from 286.5 (Pure electroplated Cu) to 300.5 (Electroplated Cu-Gr composite) – 5% <i>increase</i>	Increased from 360 (Pure Cu) to 396 (Cu-Gr composite by powder metallurgy) – 10% <i>increase</i>	Increased from 350 (Pure Cu) to 525 (Cu-Gr composite by hybrid route) – 50% <i>increase</i>

Now focusing on thermal conductivity (TC) of any material, it can be primarily based on two directions, parallel (cross-plane thermal conductivity) and perpendicular (in-plane thermal conductivity). Thermal diffusivity (TD) and specific heat simultaneously determine the thermal conductivity of any material. It was observed that on incorporating graphene, the TC and TD of the Cu-Gr composites increased due to the decrease of voids (Shown in Table 4) and decreased due to the increased interfacial thermal resistance (ITR) with the increase of graphene contents. The decreased TC in the Cu-Gr composites could be attributed to the following factors. Firstly, with the incorporation of graphene, grain refinement and more dislocations in Cu matrix led to stronger electron scattering. ITR always existed in spite of good interface bonding between graphene and copper. Anisotropic thermal conductivities are observed in the laminated Cu-Gr composites. Due to graphene's 2D character, the scattering of phonons crossing the layers is stronger due to weaker interlayer Van der Waals force, leading to the fact that its cross-plane TC was lower than the in-plane TC. Moreover, there existed much more Cu-Gr hetero-interfaces in the cross-plane direction, while the in-plane direction was dominated by Cu grain boundary. All the facts resulted in higher interfacial thermal resistance and lower thermal conductivity in the direction perpendicular to the laminated structure.

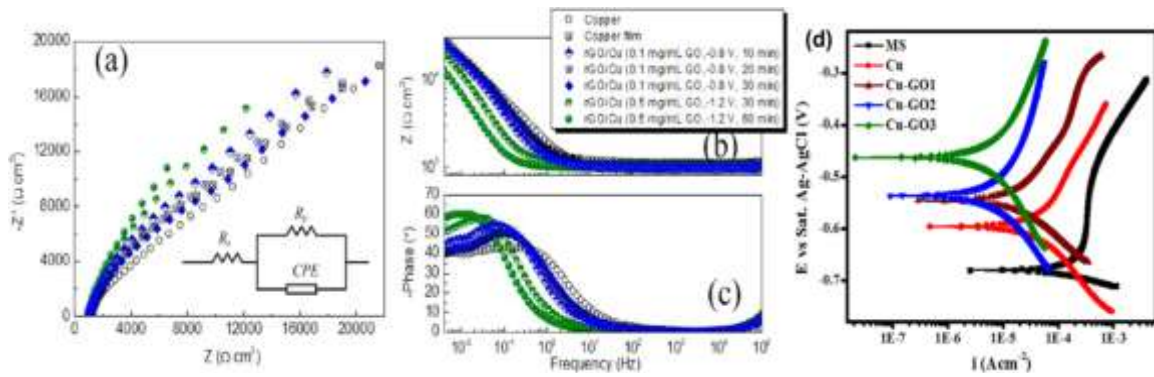


Figure 2.20: Variation of corrosion properties of Cu-Gr composites [164]

The corrosion resistance of the Cu-Gr composite was observed to be more than that of simple copper under suitable corrosive media e.g. in the presence of Cl^- ions. Figure 2.20 shows the corrosion resistance of composite films obtained through the wet phase synthesis route. Unfortunately, there are rare studies of corrosion on composites prepared through other routes. It can be seen that the films show enhanced corrosion resistance with the addition of graphene reinforcement. Now the enhanced corrosion resistance could be attributed to change in grain morphology and dense structure due to Gr sheets. In addition, the high impermeability of Gr served as corrosion protection barriers to impede the oxidation of Cu to Cu^+ ions. Further, there could be texture-induced passivity of the composite films if there is a growth in planes other than dense pack planes. Additionally, at the local sites of passivity breakdown, the passive layer could form easily and particularly within the defect sites (such as pits or cracks in the passive film) where Cu corrosion is most likely to occur. Hence, it can be concluded that, compared to pure Cu coatings, Cu-GO coatings are generally more stable owing to stable passive films that can heal up rapidly in the event of localized film damage.

2.5 Concluding remarks

Graphene has been gradually replacing other reinforcement materials in almost every engineering material matrix for its superior properties and capability to alter any physicochemical and other properties. One such category of nano-composites is Cu based composites, which has several applications ranging from electrical to anti-corrosion sectors. However, the principal challenge was to synthesize these composites with uniformly distributed graphene nano-sheets in the copper matrix. Hence in this section, we have briefly reviewed the synthesis techniques to produce graphene embedded copper composites and have also discussed the alteration in various properties of Cu-Gr

composite from its parent copper matrix. The salient points have been summarized and are mentioned below.

All the available synthesis processes have been categorized into three broad groups i.e. wet phase, dry phase and mixed/hybrid phase routes in the present review. During the process of synthesis, there could be two crucial points of concern: (i) phase of synthesis and (ii) maximum limit of graphene assimilation. The phase of synthesis has been determined based on the initial phase of the matrix in which the graphene has been dispersed for incorporation during the solid phase formation of the composites. In the wet phase, Cu matrix is in the form of dissolved ions in the solution where graphene nano-sheets are dispersed in solution. In dry phase, copper and graphene powders are mixed to get the distribution and in mixed/hybrid phase there is sequential transition of either wet to dry or dry to wet during the whole synthesis process. The maximum amount of graphene or its derivatives as reinforcement in the copper matrix was in the ranges of 1 wt%, 2 wt% and 10 vol.% for wet phase, dry phase and mixed/hybrid phase routes respectively. The optimum range was decided on the factor of uniform incorporation and distribution in the Cu matrix, as higher concentrations would result in agglomeration and will decide the optimal property alterations.

Direct electroplating and pulse reverse electrodeposition are the most common routes under the wet phase synthesis category where 0.5 g/L graphene concentration could be the ideal concentration for improved properties. In the case of dry route, powder metallurgy is believed to be the best in the lot with a maximum permissible limit of 0.5 wt% graphene in the matrix. In the case of hybrid route, there are many options available that may allow the reinforcement concentration up to 5 vol.% without affecting the synergistic property enhancement.

The properties of Cu-Gr composite including mechanical, electrical, thermal and chemical have been observed to be increased up to a certain increment of graphene reinforcement and after that, the values decreased mainly due to the agglomeration of graphene nano-sheets leading to void formation. Hence the present section has critically reviewed the development and up-gradation of synthesis methods to reduce agglomeration and increase uniform dispersion of graphene reinforcement with copper matrix to improve its properties.

Chapter 3

3: Materials, methods and characterization techniques of FLGPs, RFLGPs, Cu-FLGPs and Cu-RFLGPs

3.1 Introduction

Graphene is a single layer and two dimensional (2D) nano-material. This field of research has more demand in the industry due to its outstanding properties. The higher demand for graphene requires low-cost technology for the large production of graphene with high quality and low defect particles. The electrochemical exfoliation process is one of the simple, cost-effective route which produces high-quality few-layer graphene particles (FLGPs). This route follows the intercalation by cations and anions from the electrolytes to the graphite electrodes with a suitable applied potential. The materials and methodology used to prepare FLGPs and Cu-FLGPs nano-composites are discussed in the subsequent section along with their characterization.

3.2 Materials

Graphite used for preparing graphene particles were of commercial grade. The chemicals such as H_2SO_4 , HNO_3 , $\text{CuSO}_4 \cdot 5\text{H}_2\text{O}$, ascorbic acid and hydrazine hydrate were analytical grade and used without further processing. Double distilled water was used as solvent which was freshly prepared by the distillation unit. NaCl and borate buffer were used for the electrochemical behavior of synthesized films.

3.3 Synthesis of Few layer graphene particles (FLGPs)

The few-layer graphene particles (FLGPs) have been electrochemically exfoliated in various electrolyte conditions such as 1M H_2SO_4 and 1M HNO_3 electrolyte solutions. A graphite sheet of area 0.45 cm^2 ($1.0 \text{ cm} \times 1.5 \text{ cm} \times 0.3 \text{ cm}$) was used as a working electrode (WE). Another graphite rod was used as a counter electrode with a huge expressed surface area. The electrodes were placed in the electrolyte cell maintained at a 2 cm gap between them and facing vertically to each other. The experiment was completed at room temperature. Before anodic exfoliation, a cathodic treatment was completed by applying a negative DC bias of 3 V for 10 minutes and 10 V for 10 seconds. The cathodic treatment helps to clean the working area as well as to find the availability of internal lattice pores on the working electrode. Then the graphite electrode was connected as anode and graphite used as cathode. A positive bias of 0-8 V was applied to the electrode in a range of 0.5 V per 3 minutes. After electro exfoliation graphite flakes were collected and washed with distilled water to remove acidic and unwanted chemicals attached, if

any. The collected flakes were further centrifuged by sonication up to 1 h and centrifuged at 4500 rpm for 30 minutes. The centrifuged flakes have been dried by oven and collected as the few-layer graphene particles.

3.4 Synthesis of Reduced Few layer graphene particles (RFLGPs)

The FLGPs has been reduced by reducing agents such as hydrazine hydrate and ascorbic acid. 100 mg of FLGPs was dispersed in 100 mL of distilled water by sonication for 1 h. After dispersion, hydrazine hydrate (0.5 and 1ml) was added and the solution was heated in a water bath at 100 °C for up to 24 h. Then the reduced FLGPs became black solid powder. The obtained powder was washed with distilled water to remove unwanted materials. The washed powders were re-dispersed separately with 100 mL water. The dispersed graphene was centrifuged and dried in an oven at 60 °C. The dried powder is known as RFLGPs (RFLGPs-HY1(0.5 g) and RFLGPs-HY2(1 g)). Further ascorbic acid of (50 and 100 mg) was added with dispersed FLGPs (100 mg) and stirred for 2 h. Then the solution was filtered through filter paper (Grade 42, Retention 2.5 µm) and washed with water several times to remove unwanted materials. The same procedure of hydrazine was applied to ascorbic acid reduction and are collected as the RFLGPs powder known as RFLGPs-VC1 (50 mg) and RFLGPs-VC2 (100 mg).

3.5 Substrate preparation

The copper and Cu-Gr composite films are electrodeposited onto steel and copper substrates. The dimension of steel was circular in shape with a diameter of 12 cm² and copper cut piece of 15 mm × 10 mm × 2 mm. Both steel and copper samples were metallography polished by belt grinder with various grade emery papers. After emery paper polishing, samples were polished by cloth polish using diamond paste up to mirror polish. The polished substrates were washed with soap water and then by distilled water.

3.6 Electrolytic bath preparation, deposition setup and process parameters of Cu and Cu-FLGPs composite

The copper thin films were electrodeposited onto O₂ free and polished steel substrates of area 490.625 mm². The depositing bath had Cu(II) ions from 1M CuSO₄.5H₂O and H₂SO₄ was added to maintain the pH at 1 as well as to induce bath conductivity in double-distilled water. The electrodeposition was carried out by a two-electrode DC supply system where a graphite rod was used as a counter electrode (6 cm × 3 mm × 5 mm). The deposition was carried out at temperatures of 15, 20 and 25 °C and a potential of 2 V for 20 minutes to obtain a sufficient thick and uniform film. The ultrasound source used in the current study was an immersion type of high-density horn with an output frequency of 20 kHz and a power of 500 Watts (Sonics and materials, VCX 500). A double water-jacketed cell has been used to balance the temperature rise in the bath due to the application of ultrasound. Then the films were washed properly with distilled water to clean the reactant chemicals and dried and then placed in oxygen-free vacuum desiccators. The thin films were then peeled off from the steel substrate and were subjected to further characterization and analysis.

The as-synthesized FLGPs were grinded by mortar and pestle and are dispersed in the same electrolyte used for copper film deposition at concentrations of 0.1, 0.3 and 0.5 g/L. Cu-FLGPs composite films are synthesized by electro/sono-electroplating route onto O₂ free polished steel samples. The pH of the electrolyte was maintained at 1 which is sufficiently lower than the isoelectric point of second phase particles. The said pH was maintained to disperse the FLGPs particles uniformly in the electrolyte. Further, a polymeric surfactant like SDS (30 ppm for 0.5 g/L of FLGPs) was added in the electrolyte to avoid the agglomeration of graphene particles during electrodeposition. Moreover, to achieve uniform dispersion of graphene in the composite film as well as good quality film, ultrasound was applied during deposition process. Electrodeposition of the composite films was done with the same operating parameters as of Cu electroplating, however, the electrolyte temperature was maintained at 15-17 °C as the Cu films obtained were of the best in the lot at this temperature [85]. Then the films were washed and dried properly. The coated composite films were then peeled off from the steel substrate and were subjected to further characterization and analysis.

3.7 Nomenclature of the as-synthesized FLGPs and composites

The synthesized FLGPs obtained from various electrochemical intercalation conditions and composites are named as follows.

- (i) **H, HHY1, HHY2, HVC1 and HVC2:** The FLGPs exfoliated from 1M H₂SO₄ electrolyte bath(H), HHY1, HHY2 (H FLGPs reduced by hydrazine 0.5 and 1 mL) and HVC1, HVC2 (H FLGPs reduced by ascorbic acid 50 mg and 100 mg) respectively.
- (ii) **N, NHY1, NHY2, NVC1 and NVC2:** The FLGPs exfoliated from 1M HNO₃ electrolyte bath(N), NHY1, NHY2 (N FLGPs reduced by hydrazine 0.5 and 1 mL) and NVC1, NVC2 (N FLGPs reduced by ascorbic acid 50 mg and 100 mg) respectively.
- (iii) **Cu(s), Cu(US), 0.1Cu-FLGPs(S), 0.3Cu-FLGPs(S), 0.5Cu-FLGPs(S), 0.1Cu-FLGPs(US), 0.3Cu-FLGPs(US) and 0.5Cu-FLGPs(US):** the copper thin films at silent condition, ultrasonic condition, composite films of 0.1, 0.3 and 0.5 g/L Cu-FLGPs in silent condition, composite films of 0.1, 0.3 and 0.5 g/L Cu-FLGPs in ultrasonic condition respectively.
- (iv) **Cu-FLGPs, Cu-RFLGPs, Cu-RFLGPs(Hy) and Cu-RFLGPs(Vc):** The electrodeposited composites copper-FLGPs, copper-RFLGPs(Hy), and copper-RFLGPs(Vc) respectively.

3.8 Instrumentation

The research work is a full experimental approach to synthesize graphene particles and composite films and characterization. The prepared graphene particles and composite samples were characterized by different scientific instruments for their electrochemical synthesis, electrodeposition, structure, morphology and functional groups. The brief details of scientific equipment are given below.

3.8.1 Two electrode DC system

A two-electrode direct current (DC) bias system of Aplab make (Model No.7103) has been used for electrochemical synthesis of few-layer graphene particles and

electrodeposition of graphene-based composite samples. The maximum regulated voltage of the device is of 20 V and of 12 A maximum current output to two electrodes.

3.8.2 Particle size analyzer

The particle size distribution and the zeta potential of the prepared graphene particles have been analyzed by Malvern Zetasizer series with the help of dynamic light scattering techniques. In the process, a monochromatic light source is incident on the colloidal solution, and the obtained scattered light is collected by photomultiplier so as to get a speckle pattern. Brownian motion among the particles results in the variation of scattering distance with time. Using this dynamic study of the speckle patterns, particle size distribution was measured. Sample preparation was done by taking ~ 10 µl of exfoliated FLGPSs uniformly distributed in 15 ml of double-distilled water. A quartz cuvette was used to measure the particle size of the dispersed sample.

3.8.3 Thermo-gravimetric analysis (TGA)

The thermal stability of the samples was analyzed by TGA instrument with increasing heating temperature. The mass of the sample measured over time with a change in temperature is generally measured. In these analyses thermal reactions occur in various atmospheres such as argon gas, nitrogen gas, ambient air, vacuum, reducing gases and vapor of liquids. The TGA instrument measures continuously the mass losses of the material with increasing heating temperature. In this analysis, FLGPs was grinded by mortar and pestle. The graphene samples were put in TGA instrument in an alumina crucible and heated at a rate of 10 °C/min up to 800 °C. The TGA instrument of DTG-60H, Shimadzu was used for TGA analysis. After TGA analysis the mass loss and yield value were calculated through the following equation 3.1.

$$\text{Yield (Z)} = (\text{M/Y}) \times 100 \quad (3.1)$$

Where, M, Y and Z are in gm, M is X % of Z. X (in %) is the weight at 500 °C, Z is the weight of the FLGPs obtained and Y is the weight of the exposed graphite material.

3.8.4 X-ray diffraction (XRD)

X-ray diffraction (XRD) is an analytical technique mainly used for the characterization of the crystal structure and phase identification of the material. Amorphous and crystalline structures of the materials can also be distinguished with the help of this method. A

standard X-ray diffractometer consists of three basic elements: an x-ray tube, a sample holder and an x-ray detector. Generally, X-rays are generated by heating a filament so as to produce electrons which are accelerated towards a target material by applying a suitable voltage. When electrons have sufficient energy to dislodge an inner shell of electrons in target material then it results in the formation of characteristic X-ray and the spectra consists of major components like K_{α} and K_{β} . $K_{\alpha 1}$ and $K_{\alpha 2}$ radiations are a subpart of K_{α} and $K_{\alpha 1}$ has a slightly shorter wavelength and double the intensity as $K_{\alpha 2}$. The target materials have their specific wavelengths and monochromatic X-rays are filtered by using crystal monochromators. The intensity of the reflected X-ray is recorded with the rotation of the detector and the sample. Depending on the geometry of the incident x-ray constructive interference occurs showing a peak value. This X-ray signal gets recorded and processed by a detector and converts the signal to count rate versus 2θ value, which is then export to output devices such as a computer monitor or printer [104]. In this project, all the characterization of the samples has been carried out with the help of a multipurpose Rigaku Ultima-IV diffractometer by Bragg-Brentano (θ - 2θ) diffraction (XRD) using $Cu K\alpha$ ($\lambda = 0.15406$ nm) radiation. For all the graphene samples the data was taken in the 2θ range from $\sim 5^{\circ}$ to 60° and electroplated samples from $\sim 10^{\circ}$ to 80° .

3.8.5 Raman spectroscopy

Raman spectroscopy is an essential and efficient analysis technique which gives information about molecular vibrations and defect analysis of various nanomaterials. The spectroscopic technique works on the analysis of inelastic scattering of a monochromatic incident laser beam, which interacts with the sample molecules. The interactions between the incident, electromagnetic waves result in a small amount of the scattered light, i.e., 5-10% of the incident light intensity which is shifted in energy from the laser frequency and the vibrational energy levels of the molecules in the sample. The extent of disorder and presence of defects in the prepared FLGPs were evaluated using the Raman spectrum which usually consists of intensity versus Raman shifts (wavenumber in cm^{-1}). For the following project, the spectra were recorded by the Renishaw in via micro-Raman spectrometer with an excitation using a Nd:YAG laser source. All the spectra recorded at a wavelength of 532 nm and in a scan range of 1100 - 3100 cm^{-1} .

3.8.6 X-ray photoelectron spectroscopy (XPS)

X-ray photoelectron spectroscopy (XPS) is a quantitative technique which is used for surface analysis, elemental composition, empirical formula and electrochemical information of the surface material. It shows what all elements are present in a film and also other elements bonded in the film. It measures the elemental composition in the range of parts per thousand, chemical state, electronic state and empirical formula of the elements that present in a material. The spectra are obtained by irradiating the material with x-ray beams (Al K α or Mg K α) and the electronic transition state of the material was maintained within ~ 10 nm depth under high vacuum condition ($P \sim 10^{-8}$ millibar or $P < 10^{-9}$ millibar). XPS spectrum usually consists of a plot of the number of electrons detected (sometimes per unit time) or intensity in the arbitrary unit versus the binding energy of the electrons detected in the sample. For this project XPS of AMICUS 3400, Kratos Analytical Shimadzu Corporation has been used for the qualitative and quantitative analyses of the surface functional groups present in the FLGPs powdered sample and a monochromatic Mg K α (1253.6 eV) X-ray source has been used. The high-resolution C 1s spectrum has been used for the quantification of the functional groups present on the sample surface and for the quantitative analysis, Casa XPS software has been used for the purpose.

3.8.7 Fourier transmission infrared (FTIR) spectroscopy

FTIR spectroscopy is a technique used to observe infrared spectra of absorption or emission of samples. The goal of spectroscopy is to find how the sample absorbs light at each wavelength. The spectroscopy detects the molecular vibration, stretching and chemical bonds of the sample. The broadband light source of the beam containing a full spectrum of wavelengths and the light into a Michelson interferometer. The Michelson interferometer gives the configuration of transmitted and blocked each wavelength by wave interference. The functional groups of FLGPs have been analyzed by FTIR spectroscopy. The samples have been prepared by mixing of FLGPs with KBR powder in a ratio of 30:70 wt%. A pallet of 12 mm diameter has been produced from the mixed samples and tested at a range of 800-3500 cm^{-1} with the FTIR spectra (Shimadzu IR Prestige-21 instrument).

3.8.8 UV-Visible spectroscopy

Ultraviolet-visible spectroscopy generally is termed as absorption spectroscopy or reflectance spectroscopy in part of the ultraviolet and the adjacent visible spectral regions. Normally electromagnetic radiation ranging from 200 to 900 nm wavelength was incident onto the sample which in turn leads to the absorbance of certain radiations and transmittance of others. This absorbance of the incident radiation by the sample is used in the plotting of the absorption spectrum where the nature of the sample, functional groups, electronic transitions and optical bands are calculated. In order to obtain UV-visible spectra of the obtained FLGPs a colloidal sample of few microliters was taken in a glass cuvette keeping distilled water as the reference for analysis. The nature of functional groups and electronic transitions w.r.t. electromagnetic radiation has been noted from UV-Visible absorption spectra. For this project a highly calibrated scientific instrument from Perkin Elmer, model-Lambda 35 was used.

3.8.9 SEM, Field emission scanning electron microscope (FESEM) with EDS

SEM and FESEM are an electron microscopy technique used to produce a highly magnified image of the material for finding its morphology. The morphology of samples is scanned by a focused beam of electrons. The electrons interact with the sample and give various signals which contain information on the surface topography and composition of the material. The electron microscopy gives high magnifications up to 1,000,000 times higher than that of the optical microscope. The samples used to analyze by SEM and FESEM must be conducting and completely dry. The non-conducting samples were coated with a thin layer of conducting material like platinum or gold. FESEM gives 3 or 6 times better image than SEM. FESEM uses the field emission gun which gives a clean image and less electrostatic distortion than the SEM. In the present study FESEM of model Nova NanoSEM 450 by FEI has been used to analyze surface topography of graphene samples. SEM of model JEOL JSM-6480 LV has been used for analyzing surface morphology of Cu and Cu-Gr samples. The X-ray elemental mapping and an energy dispersive spectrometer (EDS) attached with SEM has been used for analyzing the composition of the sample.

3.8.10 Transmission electron microscope (TEM)

TEM is a microscopy technique in which an electron beam transmitted through a specimen or sample. The sample is ultrathin usually smaller than 100nm or copper grid or holey carbon copper grid. The electron beam transmitted through the sample and forms image of the specimen. TEM is capable of imaging a higher resolution image than the light microscope. The microscope covers the magnification range of 100X to 1000000X. A tungsten filament or needle used as an emission source or cathode. A high voltage source of 100-300 kV connected to the gun and the gun emit electrons either by field electron emission or thermoionic in a vacuum medium. In this study TEM and high resolution TEM was used for morphological study and number of layers of FLGPs and RFLGPs. The crystallinity of FLGPs and RFLGPs has been analyzed by selected diffraction pattern (SAED) analysis. The FLGPs and RFLGPs samples dispersed with acetone solvent by bath sonicated and drop cast on to holey carbon Cu grid in room temperature. Then the grid is dried by using the halogen lamp before analysis. Transmission electron microscopy (TEM) of FEI Tecnai G2 TF30-ST at an acceleration voltage of 200 kV was used for layer structure and SAED pattern of graphene particles.

3.8.11 Atomic force microscope (AFM)

Atomic force microscope (AFM) is a very high-resolution microscope which is 1000 times better than the optical microscope. In this microscope, the resolution goes up to a nanometer level. A silicon-based material like a micro cantilever probe used for scanning the sample surface. The probe cantilever interacts with the sample with a raster motion. The side motion of AFM tip scans along the surface laser beam reflected with the AFM continuous tip. The deflection of the laser beam was tracked by the position-sensitive photodiode and the deflection sensor analyzed to give a topography image of the sample. The AFM analysis of the prepared Cu and Cu-Gr samples were analyzed by Veeco di Innova model. The contact mode of AFM was applied to the samples to observe the image of samples. The samples loaded with the sample holder and scanned at an area of $20 \times 20 \mu\text{m}^2$ in different places. The force-displacement curves of samples were also analyzed by point spectroscopy of AFM in contact mode. The conducted data of the samples were analyzed by Nanoscope Analysis of version 1.20 software.

3.8.12 Surface profilometer

Stylus profilometer is a measuring instrument used to measure accurate surface roughness, thickness, curvature and flatness of the surface. It gives 2D surface roughness and steps height of the surface material with residual stress analysis. A stylus of diameter 12.5 μm has been used to measure the properties of the surface. The stylus is moved vertical in contact with the material and crosses the sample distance with a contact force. The electrodeposited samples were measured by a 2D stylus covering a 2 μm distance with an applied force of 2 mg. All the roughness and thickness of current samples are average of 3 data measured at different locations of the electrodeposited samples.

3.8.13 Microhardness measurement

It is the measure of the resistance to localized plastic deformation induced by either mechanical indentation or abrasion. Being a fundamental physical property it is characteristic of the material and is defined as the resistance to indentation and determined by measuring the permanent depth of the indentation. The Vickers microhardness tester is mostly used for thin sections, small parts, coatings, and case depth work. The hardness test can be used for all metals. The unit of hardness by the test known as Vickers Pyramid Number (HV) or diamond pyramid number (DPH). The unit can be converted to pascals and not confused with pressure. It follows the optical measurement system. It specifies a range of light loads by using a diamond indenter and the indenter makes an indentation. The indentation is measured and converted to Vickers hardness value (HV). We have applied loads of 5, 10, 15, 20 and 25 gf to find the proper indentation for hardness calculation. An applied load of 25 gf has been found to give the proper indentation to calculate hardness value. The indentation was taken at 10 different locations to calculate the average hardness value for the samples. Finally, 25 gf was chosen for reporting and experimentation.

3.8.14 Wear testing

The damaging, gradual removal, deformation and erosion of material at a solid surface is known as wear. Wear tests carried out for the samples were studied for wear performance and wear mechanism. The test evaluates the wear property of material whether it can be applicable for wear application. Wear rate depends upon various factors such as loading, lubrication, temperature and types of motion (sliding, rolling).

A ball-on-plate type wear tester (DUCOM TR-208-M1) was used for wear and friction test at room temperature with dry sliding conditions for thin films. The wear tests were done with 0.5 N load at a speed of 10 rpm up to 5 minutes at 1.05 mm/s sliding speed.

3.8.15 Electrical conductivity

Electrical conductivity is a fundamental property of a material which quantifies how a strongly electric current can flow. A low electrical resistivity indicated materials allows electric current through it. The resistivity is represented by ρ (rho) and its SI unit is ohm-meter ($\Omega\cdot\text{m}$). The electrical resistivity of electrodeposited composites films were measured by fore-probe method at ambient temperature. A four-probe setup (KEITHLEY 6221 current source combined with 2182 A nano-voltmeter) was used for electrical conductivity measurement at room temperature. The values reported in this report are the average value of three measurements.

3.8.16 Electrochemical/Corrosion study

The corrosion behavior of a composite sample was then studied in a potentiostat (Corr Test, CS 350) with a standard three-electrode system. In the electrochemical cell, composite films with exposed areas of 0.6 mm^2 were used as a working electrode, a platinum rod as a counter electrode and a saturated calomel electrode (SCE) as a reference electrode. The corrosion behavior of composites was analyzed in 3.5% sodium chloride solution and borate buffer solution at room temperature. The open-circuit potential (OCP) was recorded up to 30 minutes. The potentiodynamic polarization was carried out in the range of potentials of -0.4 V to 0.4 V w.r.t OCP at a scan rate of 5 mV/s and 0.1667 mV/s. The corrosion rate was analyzed by using Tafel plot analysis through the supplied software of CS studio 5. EIS studies have also been carried out to critically analyze the corrosive mechanism.

Chapter 4

4: Physicochemical properties of electrochemically synthesized FLGPs and RFLGPs

4.1 Introduction

This section describes the detailed analysis of as-synthesized FLGPs and RFLGPs. The synthesis procedure for both FLGPs and RFLGPs has been given in section 3. Here the mechanism will be described briefly. The FLGPs were reduced by chemical reduction method using hydrazine hydrate and ascorbic acid as the reducing agents. The prepared graphene particles were characterized by different characterization route to confirm crystallinity, structure and topography properties.

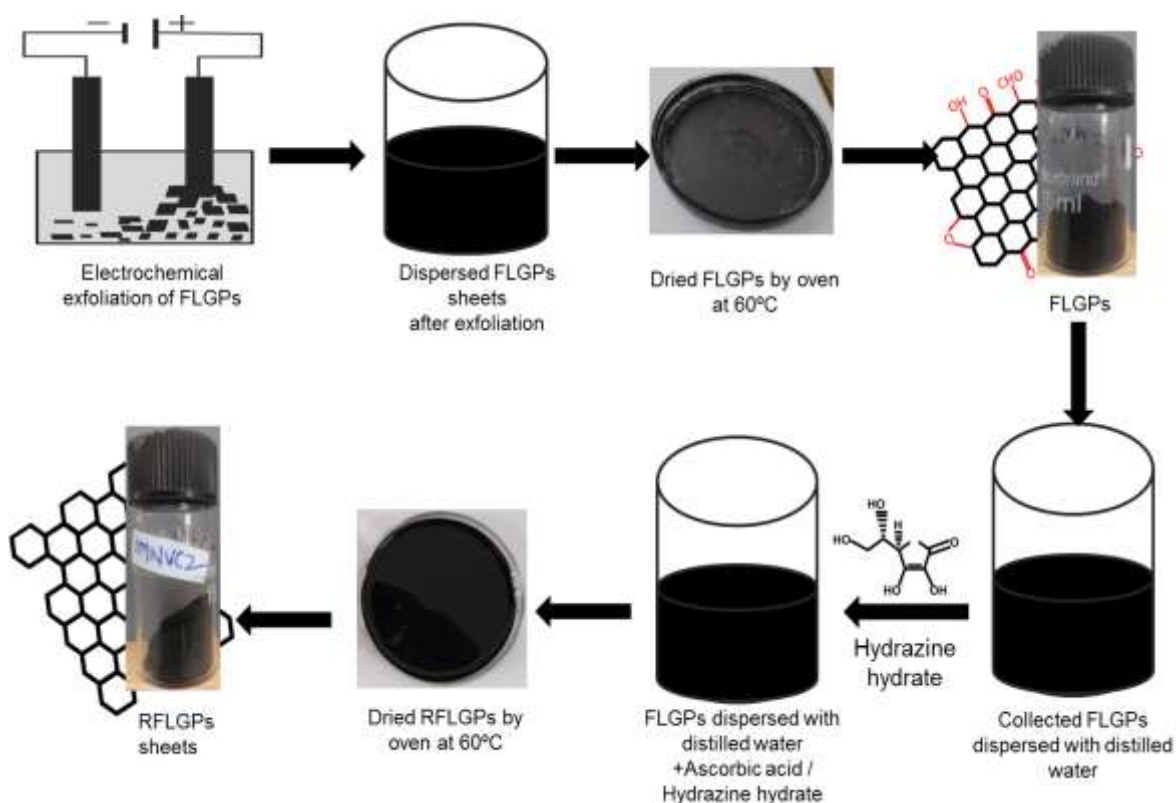


Figure 4.1: Schematic diagram showing the steps for the synthesis of graphene particles (FLGPs and RFLGPs)

4.2 Methodology

The electrochemical exfoliation of graphene particles was done by two step process i.e (i) cathodic pre-treatment and (ii) anodic treatment. In cathodic treatment, H₂ gas bubbles were found to be formed on the WE surface and released from the working electrode. During this treatment, the WE gets expanded which may help in better intercalation. Further, it may also help in removing the impurities from the surface [165].

The expanded WE electrode was then used as an anode during anodic treatment. During anodic treatment, anions including (SO₄²⁻, HNO₃⁻) ions with hydroxyl (OH⁻) anions intercalate the working electrode. There is also simultaneous release of O₂, CO, and CO₂ gases during intercalation. In anodic intercalation, oxidation occurs at the anode and attachment of some functional groups such as carboxyl, hydroxyl, and alkoxide groups may occur [54]. The intercalated graphite particles are known as FLGPs and are found to consist of several functional groups.

After anodic treatment, FLGPs were reduced by chemical reduction method using hydrazine hydrate and ascorbic acid. In chemical reduction method ascorbic acid was added to disperse FLGPs and then the solution stirred up to 2 h at room temperature. During reduction, hydrazine hydrate and ascorbic acid gave electron and proton to easily detach the OH group. The OH group was dehydrated and hereby get detached from the graphene particles [41,66,166]. Other functional groups also are reduced during the reduction of FLGPs. The mechanism of reduction can be explained as followed. Ascorbic acid is a mild reducing agent and antioxidant. It is oxidized with the loss of one electron to form a radical cation and then the loss of the second electron to form dehydroascorbic acid [166–168]. It reacts with oxidants of the reactive oxygen species, such as hydroxyl radicals and separates it from the parent graphene network. Hydrazine is a convenient reducing agent and gives the by-product of nitrogen gas and water [62,169–171]. The mechanism by which ascorbic acid and hydrazine reduce graphene oxide to reduced graphene oxide is presented below in figure 4.2.

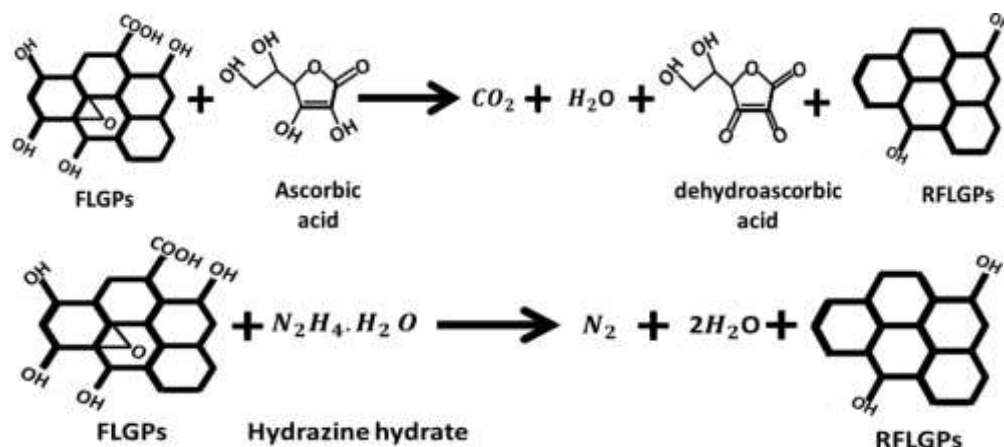


Figure 4.2: Mechanism of reduced FLGPs (a) Ascorbic acid and (b) Hydrazine hydrate

4.3 Thermal stability and yield in FLGPs and RFLGPs synthesis

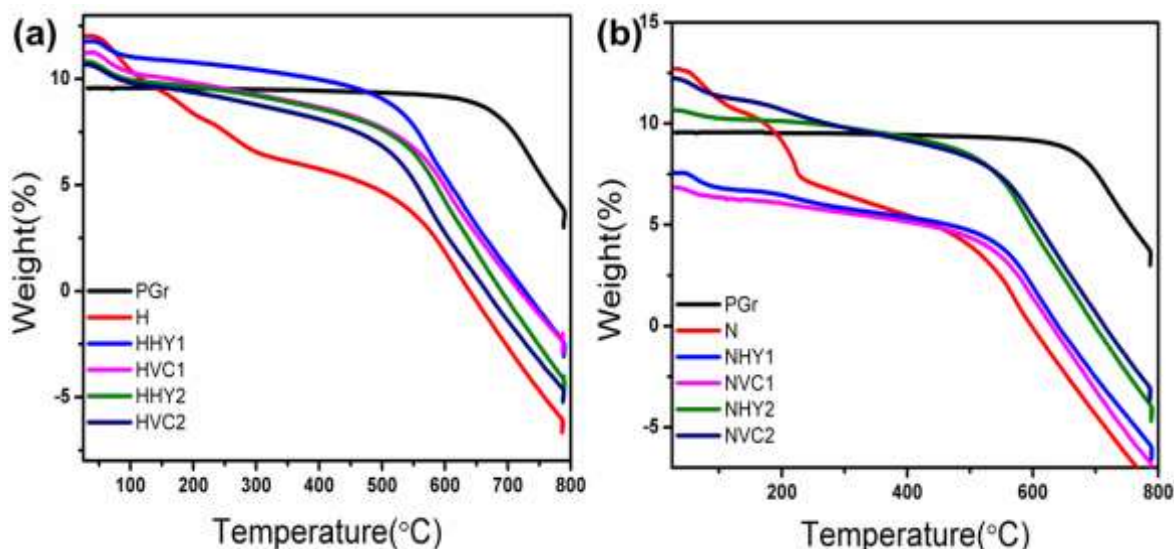


Figure 4.3: TGA analysis of (a) PGr, H, HHY1, HHY2, HVC1 and HVC2 RFLGPs and (b) PGr, N, NHY1, NHY2, NVC1 and NVC2 RFLGPs

The thermogravimetric analysis (TGA) shows the thermal stability of prepared FLGPs. It gives the mass loss of FLGPs at various temperatures. Figure 4.3(a) shows the TGA analysis image of H, HHY1, HHY2, HVC1 and HVC2. The TGA analysis of graphite powder shows high resistance and shows only 3% weight loss up to 660 °C. The FLGPs have showed a ramped up 35% weight loss at 250 °C. This may be due to the evaporation of moisture content and removal of gases like CO and CO_2 present in the FLGPs. Then a slow and steady weight loss after 400 °C is observed in FLGPs due to high temperature of thermal reactions of functionalized FLGPs. The weight losses of FLGPs have been

observed to be around 62% near the temperature of 500 °C. The weight loss of HHY1, HHY2, HVC1, and HVC2 shows a slow and steady mass loss of 23%, 29%, 29% and 35% respectively. The weight loss of RFLGPs is not that significant compared to FLGPs. Further HHY1 and HVC1 have high thermal stability than FLGPs, HHY2 and HVC2. This may be due to defect structure induced in the graphene lattice by applying more amounts of reducing agents. The yields of FLGPs were calculated from the weight loss data and are presented in Table 4.1. Figure 4.3(b) shows the TGA image of N group FLGPs where it shows the thermal stability and yield of N, NHY1, NHY2, NVC1 and NVC2 RFLGPs respectively. A significant weight loss of 41% on N FLGPs occurred at 250 °C. The weight loss occurs due to the absorbance of moisture content on FLGPs. Various oxygen functional groups as CO, CO₂ and carbon radical elements were decomposed at temperature 250 °C. Then a slow and steady weight loss of 30% observed in the temperature range of 500 °C due to the decomposition of oxygen functional groups (CO, CO₂, and COOH) of FLGPs. The FLGPs have a total thermal and yield loss of 68% at a temperature of 500 °C. The weight loss of NHY1, NHY2, NVC1 and NVC2 are 37%, 22%, 37% and 30% in the range of 500 °C respectively. The weight loss of RFLGPs is shown to be less as compared to FLGPs. Table 4.1 shows the mass loss of graphene particles by TG analysis. The ascorbic acid reduces up to 50% of the oxygen functional groups present in FLGPs. The mass loss of RFLGPs confirms the reduction of most stable functional groups by applying reducing agents. Table 4.1 Yield of graphene particles after TGA analysis

Graphene particles	Wt of Graphene particles (mg)	TGA wt. (mg) yield at 500 °C	Yield (%)
H	12.7	4.23	62
HHY1	11.75	8.52	23
HVC1	10.30	7.21	30
HHY2	10.79	6.9	29
HVC2	10.64	6.5	35
N	12.69	3.02	68
NHY1	7.61	4.45	37
NVC1	6.87	4.03	37
NHY2	10.63	7.87	22
NVC2	12.26	7.94	30

4.4 Structural analysis of FLGPs

4.4.1 XRD studies

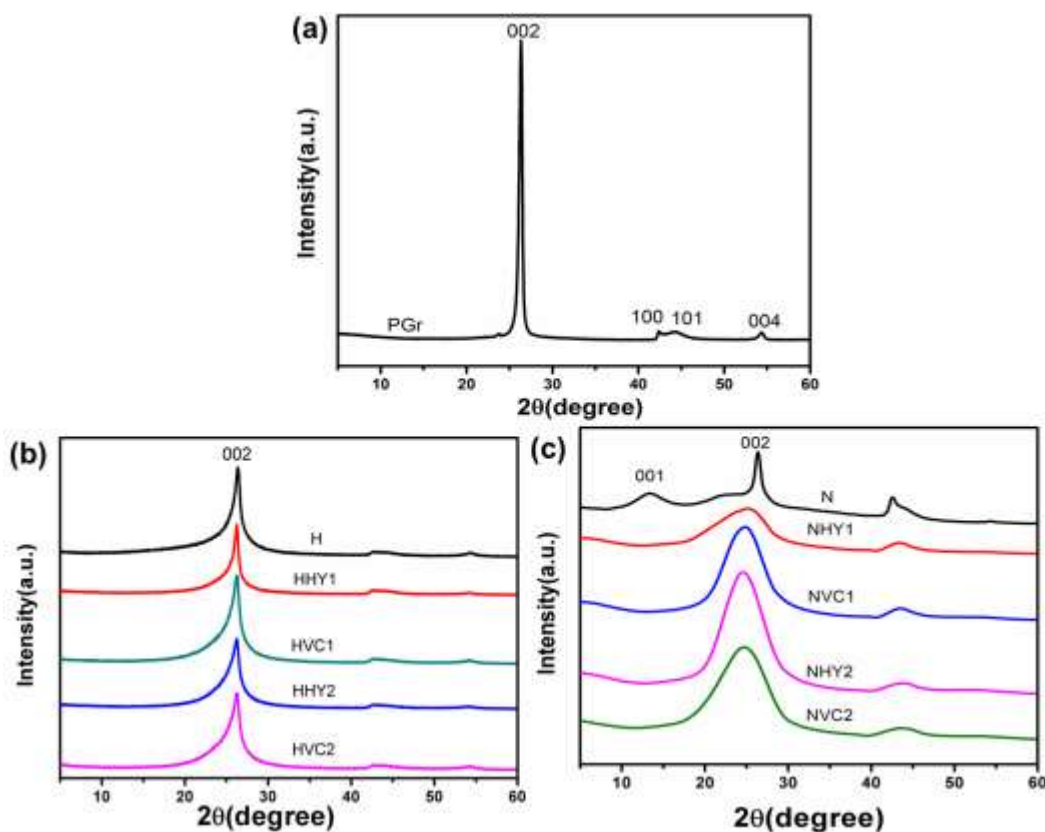


Figure 4.4: XRD analysis of (a) PGr, H group (b) (H, HHY1, HHY2, HVC1 and HVC2) and (c) N Group (N, NHY1, NHY2, NVC1 and NVC2)

Figure 4.4(a) shows the XRD image of PGr. (002) plane of PGr shows at $2\theta=26.37^\circ$. Figure 4.4(b) represents the XRD pattern of H, HHY1, HHY2, HVC1 and HVC2 respectively. The figure shows 2θ of (002) for H (26.38°), HHY1 (26.17°), HVC1 (26.10°), HHY2 (26.25°) and HVC2 (26.23°). (001) plane of GO peak was absent in H FLGPs which may be due to the small amount of oxygen functional groups present in the graphene network. The intensity of FLGPs has decreased and broadness increased and interlayer spacing of graphite structure increase as compared to PGr sheet. This configuration of flakes confirms the presence of graphene [57, 172]. The intensity of HHY1, HHY2, HVC1 and HVC2 has decreased and broadening increases as compared to H FLGPs.

Figure 4.4(c) shows the XRD analysis of graphene particles of N, NHY1, NHY2, NVC1 and NVC2. From XRD analysis it was confirmed that prepared FLGPs contain graphene

oxide (GO) peak of (001) plane at 13.26° and graphene peak at 26.33° of 2θ value. The (002) shows the crystalline structure of carbon particles and confirms the presence of few layers of graphene particles. The NHY1, NHY2, NVC1 and NVC2 show the representing crystal structure (002) plane at 25.15° , 24.91° , 24.61° , 24.7° . It can also be observed that (001) peak was absent in reduced FLGPs. The peaks have been broadened for RFLGPs as compared to FLGPs.

4.4.2 Raman studies

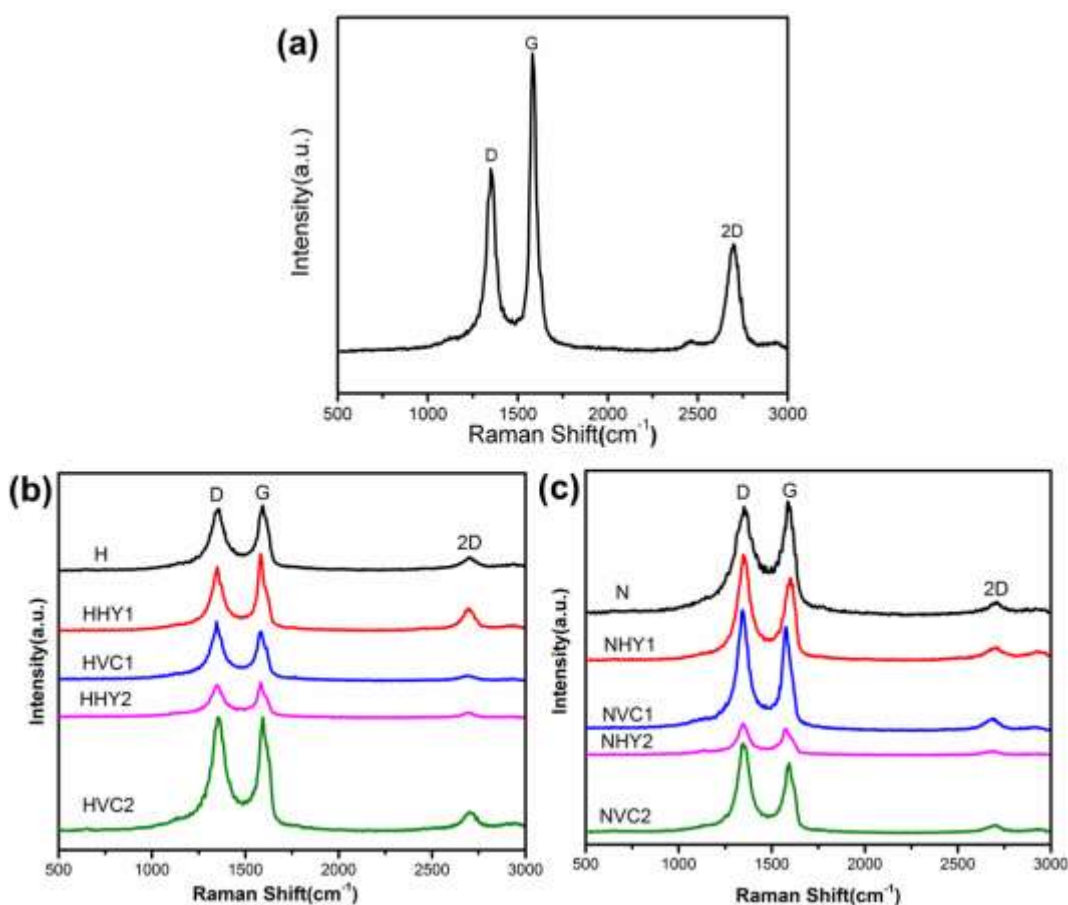


Figure 4.5: Raman spectra of (a) PGr, (b) H group FLGPs (H, HHY1, HHY2, HVC1 and HVC2) and (c) N group FLGPs (N, NHY1, NHY2, NVC1 and NVC2)

Raman spectroscopy is one of the fast, most common and nondestructive techniques for analyzing the structure of graphene particles for defects, disorder and structure of sp^2 hybridized carbon atoms of graphene particles. Figure 4.5(a) shows the Raman spectra of PGr. Figure 4.5(b) shows the Raman spectra analysis of H groups FLGPs and RFLGPs (HHY1, HHY2, HVC1 and HVC2). Raman spectra show the crystallinity structure of graphene particles prepared by electro exfoliation and reduced subsequently by chemical reduction. The Raman spectra analysis of FLGPs contains D, G, and 2D band at 1341,

1572 and 2675 cm^{-1} respectively. The D band signifies the presence of defects or disorder in sp^2 network due to the defects at the edges. The G band shows the sign of hexagonal carbon ring structure of plane C-C band stretching motion and shows the first-order scattering of the E_{2g} phonon of the Brillouin zone center. The 2D band shows the frequency dependent laser energy corresponding to second-order Raman scattering of two phonon scattering processes [173]. The defect density of carbon sp^2 structure can be measured by I_D/I_G ratio. The ratios for PGr and FLGPs were found to be 0.73 and 0.99 respectively. The defect density of reduced FLGPs HHY1, HHY2, HVC1 and HVC2 were 0.97, 1.03, 0.99 and 1.00 respectively. The intensity of disorderness in RFLGPs has linearly increased as compared to FLGPs with the increasing content of the reducing agents. Figure 4.5(c) shows the Raman spectra of N Group FLGPs (N, NHY1, NHY2, NVC1, and NVC2). The Raman spectrum of N FLGPs contains D, G, and 2D band peak observed at 1352, 1589 and 2714 cm^{-1} . The defect density of N FLGPs has been observed to be around 0.99. After reduction of FLGPs by hydrazine hydrate and ascorbic acid had similar intensity peaks but different in the intensity ratio of D to G band (I_D/I_G). The intensity ratios of RFLGPs (NHY1, NHY2, NVC1, and NVC2) were 1.07, 1.06, 1.03 and 1.17 respectively. This may indicate that the reduction process needs further optimization with the FLGPs.

4.5 Functional analysis

4.5.1 FTIR studies

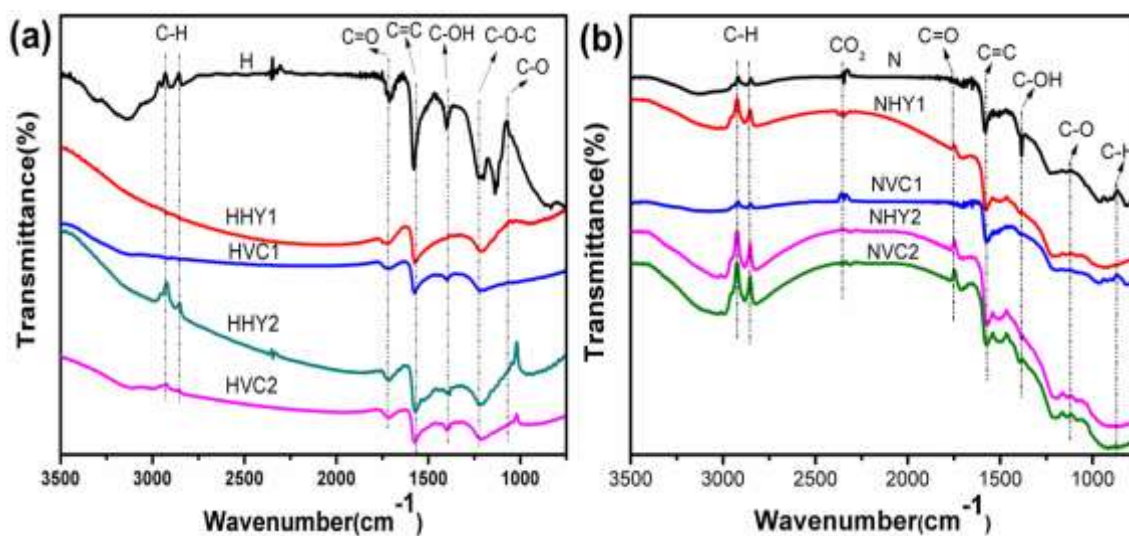


Figure 4.6: FTIR analysis of (a) H Group FLGPs (H, HHY1, HHY2, HVC1 and HVC2) and (b) N Group (N, NHY1, NHY2, NVC1 and NVC2)

The prepared FLGPs and RFLGPs were synthesized by various chemical processes. Therefore, various functional groups are expected to be attached during electro-chemical exfoliation process of FLGPs. The functional group and carbon structure of FLGPs have been analyzed by Fourier transform infrared spectroscopy. Figure 4.6(a) shows the FTIR spectra of H FLGPs and HHY1, HHY2, HVC1, HVC2 RFLGPs. FTIR spectroscopy confirms the oxygen functional groups attached to FLGPs. The stretching vibration peak of OH and C-H groups have been observed at 3138.66 cm^{-1} and 2896.23 cm^{-1} . The aromatic sp^2 carbon ring structure of the C=C stretching peak has been observed at 1577.8 cm^{-1} . The oxygen functional groups were observed at 1712.89 cm^{-1} (C=O), 1137.07 cm^{-1} (C-O aloxy group) and 618 cm^{-1} (CH). The observed intensity of peaks for RFLGPs particles were 1214.21 cm^{-1} (C-O alkoxy group), 1574 cm^{-1} (C=C) and 1713.0 cm^{-1} (C-O-C) respectively. The Intensity of oxygen functional groups RFLGPs decreased as compared to that of FLGPs which indicates that the reducing agents have reduced some of the oxygen functional groups. The observed peaks of C=C stretching at 1574 cm^{-1} confirms the aromatic ring structure of carbon of RFLGPs. In RFLGPs some functional groups have disappeared but the intensity of C-H bond has increased at 2936 and 2851 cm^{-1} . It was confirmed that intensity associated with oxygen functional groups have strongly decreased by reducing agent hydrazine hydrate and ascorbic acid as compared to unreduced FLGPs. The highly reduced FLGPs still contain some functional groups that cannot be totally reduced by the chemical reduction method.

The functionalization study of N series FLGPs are shown in Figure 4.6(b). The C-H bond stretching vibration of sp^3 hydroxylation arises at 2918 and 2856 cm^{-1} . The carboxylation and oxygen functional groups such as alkoxy/alkoxide (C-O), ether/epoxide (C-O-C), carboxyl (C-OH) and carbonyl (C=O) stretching vibrations of the FLGPs have been observed at 1045 , 1150 , 1400 and 1740 cm^{-1} respectively. The sp^2 hybridized graphene sheet formation of aromatic C=C bond stretching vibration appeared at 1584 cm^{-1} . The reduced FLGPs NHY1, NHY2, NVC1 and NVC2, the aromatic (C=C) signal observed at 1569 - 1577 cm^{-1} . The intensity of oxygen functional groups has been decreased and some of the functional groups vanished due to the reduction of FLGPs.

4.5.2 XPS studies

XPS analysis studied the surface composition and elemental analysis of electrochemically exfoliated FLGPs and RFLGPs. It indicates the intensity of emitted photoelectrons of

various atoms and provides evidence of the reduction of graphene oxide. Figure 4.7 shows the XPS spectra of H group (H, HHY1, HHY2, HVC1 and HVC2 RFLGPs) graphene particles.

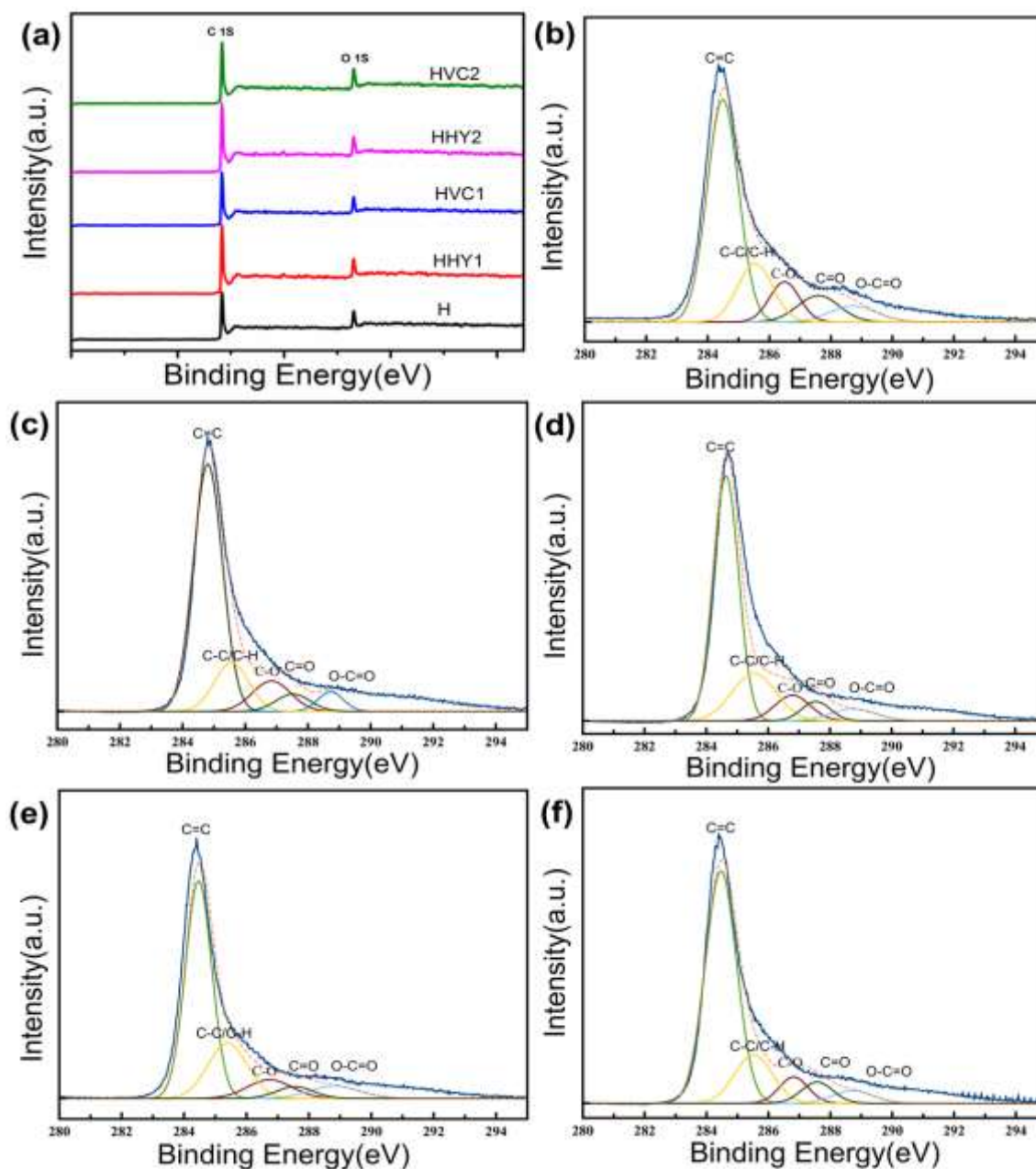


Figure 4.7: XPS spectrum of (a) survey scan of graphene sheets and high resolution C 1s spectrum of (b) H, (c) HHY1, (d) HHY2, (e) HVC1 and (f) HVC2 RFLGPs

Figure 4.7(a) shows the survey scan of graphene particles which has two peaks at ~ 284.5 and ~ 533 eV corresponding to the core level C1s and O1s of the H group graphene particles. Table 4.2 shows the ratio of carbon (C) and oxygen (O) elemental composition

of H group graphene particles. It shows the carbons to oxygen ratio (C/O) are 6.1, 6.5, 8.5, 6.4 and 8.3 for the H, HHY1, HHY2, HVC1 and HVC2 RFLGPs respectively.

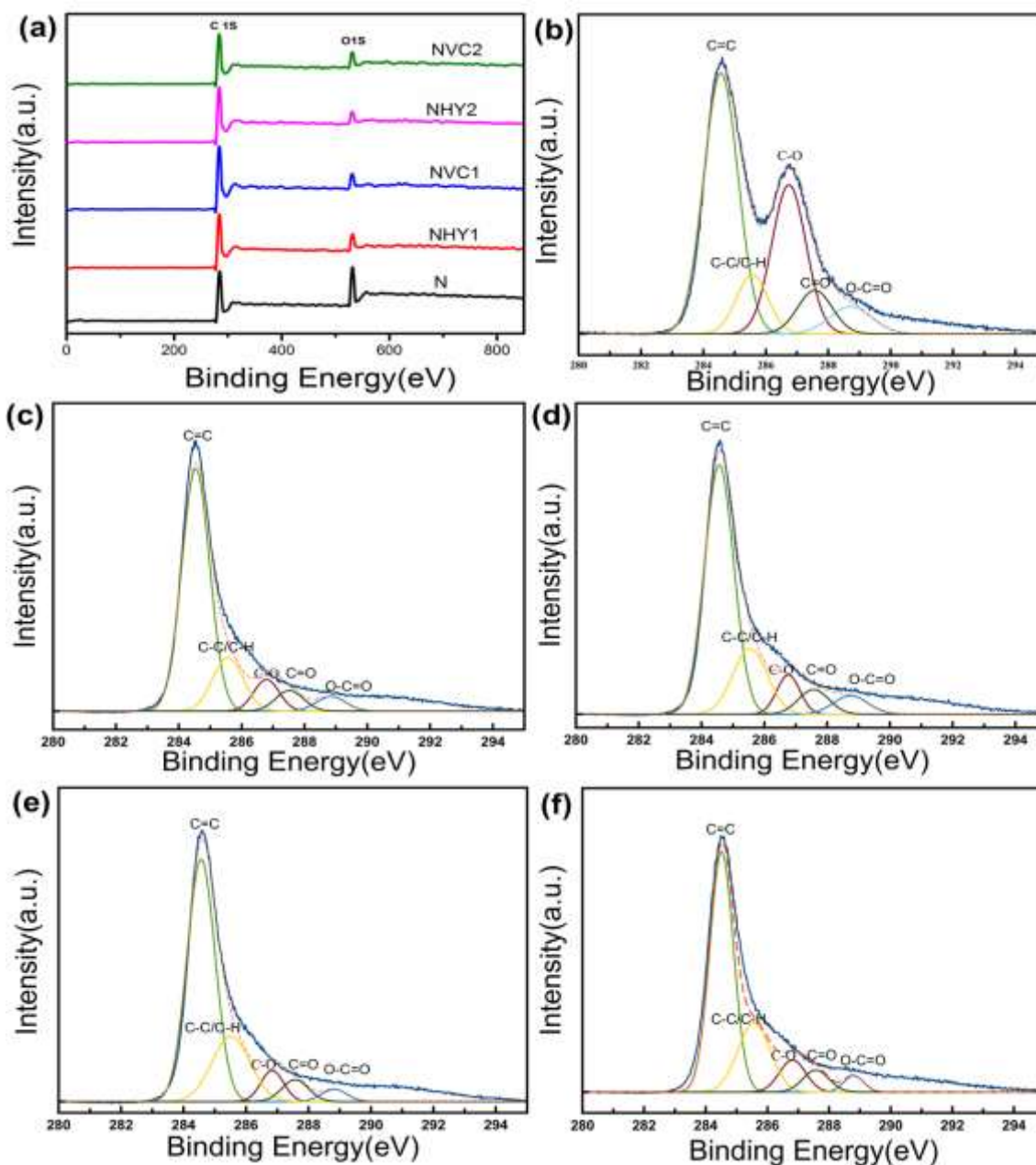


Figure 4.8: XPS spectrum of (a) survey scan of graphene sheets and high resolution C 1s spectrum of (b) N, (c) NHY1, (d) NHY2, (e) NVC1 and (f) NVC2 RFLGPs

The H FLGPs contain more carbon to oxygen ratio due to the slow electrochemical intercalation of PGr sheets by the impact of SO_4^{2-} anions of H_2SO_4 electrolyte. The carbon to oxygen ratio of RFLGPs has gradually increased with the increase of reducing agents. The de-convoluted high-resolution C1s peaks of XPS spectra are shown in figures

4.7(b-f) for the H, HHY1, HHY2, HVC1 and HVC2 RFLGPs respectively. The deconvoluted C1s peak has multi fits with various carbon-oxygen groups such as C=C (hydrocarbons, sp^2), C-C/C-H (sp^3), C-O (hydroxyl and epoxy), C=O (carbonyl groups), and O-C=O (carboxyl groups). The peak positions of carbon-oxygen functional groups are around 284.5, 285.5, 286.8, 287.6 and 288.7 eV of sp^2 , sp^3 , hydroxyl and epoxy, carbonyl groups and carboxyl groups of the deconvolution fits of C1s peaks as shown in figure 4.7.

Table 4.2 XPS analysis of FLGPs and RFLGPs

Name of sample	Percentage proportion (at%) of FLGPs and RFLGPs		
	C	O	C/O ratio
H	85.88	14.12	6.082
HHY1	86.76	13.29	6.528
HHY2	89.54	10.41	8.49
HVC1	86.45	13.55	6.38
HVC2	89.27	10.73	8.31
N	75.36	24.64	3.05
NHY1	86.65	11.35	7.63
NHY2	91.01	8.99	10.12
NVC1	87.51	12.49	7.00
NVC2	91.03	8.97	10.14

Figure 4.8(a) shows the survey scan of graphene particles which has two peaks at ~ 284.5 and ~ 533 eV corresponding to the core level C1s and O1s of the N group graphene particles. Table 4.2 shows the ratio of carbon (C) and oxygen (O) elemental composition of N group graphene particles. It shows the carbons to oxygen ratio (C/O) are 3.1, 7.6, 10.1, 7 and 10.14 for the N, NHY1, NHY2, NVC1 and NVC2 RFLGPs respectively. The N FLGPs contain more carbon to oxygen ratio due to the slow electrochemical intercalation of PGr sheets by the impact of NO_3^- anions of HNO_3 electrolyte. The carbon to oxygen ratio of RFLGPs has gradually increased with the increase of reducing agents.

The de-convoluted high-resolution C 1s peaks of XPS spectra are shown in figures 4.8(b-f) for the N, NHY1, NHY2, NVC1 and NVC2 RFLGPs. The de-convoluted C1s peak has multi fits with various carbon-oxygen groups such as C=C (hydrocarbons, sp^2), C-C/C-H

(sp^3), C-O (hydroxyl and epoxy), C=O (carbonyl groups) and O-C=O (carboxyl groups). The peak position carbon-oxygen functional groups are around 284.5, 285.5, 286.8, 287.6 and 288.7 eV of sp^2 , sp^3 , hydroxyl and epoxy, carbonyl groups and carboxyl groups of the deconvolution fits of C1s peaks as shown in figure 4.8.

4.5.3 UV-Visible studies

Figure 4.9(a) shows the UV-visible spectra of H series synthesized FLGPs. The FLGPs were dispersed in double distilled water using a bath sonicator. The absorbance peaks are observed at 259, 261, 263, 266, 266 nm for samples H, HHY1, HVC1, HHY2 and HVC2 respectively. A strong absorbance peak of $\pi-\pi^*$ electronic transition of the aromatic ring of C=C bond observed between 259 to 266 nm [174]. It can be observed that the peaks have been shifted to higher wavelengths (blue shift) values after reduction. The red shift of the peak can be mainly due to the reduction of FLGPs. The concentration of hydrazine hydrate and ascorbic acid changes the maximum blueshift of spectra from 259 to 266nm.

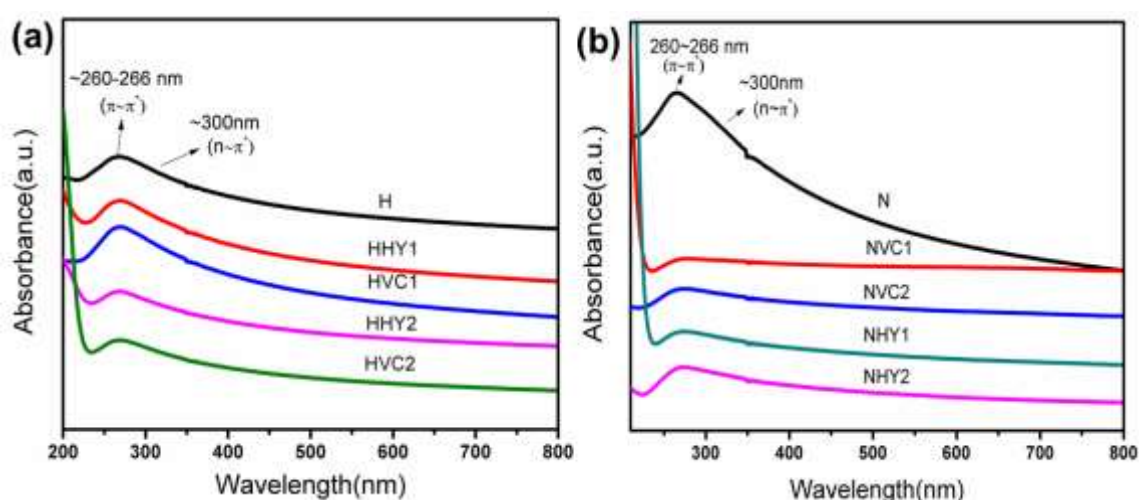


Figure 4.9: UV analysis of (a) H Group (H, HHY1, HHY2, HVC1 and HVC2 RFLGPs) and (b) N Group (N, NHY1, NHY2, NVC1 and NVC2 RFLGPs)

Figure 4.9(b) shows the image of UV-visible analysis of N group (N, NHY1, NHY2, NVC1 and NVC2 RFLGPs) graphene particles respectively. Graphene particles were dispersed in distilled water solvent. A strong absorbance peak of $\pi-\pi^*$ electronic transition of the aromatic ring of C=C bond observed at 266 nm. In RFLGPs (N group) aromatic ring structure of C=C bond of $\pi-\pi^*$ has been red shifted to 272-274 nm. The concentration of hydrazine hydrate and ascorbic acid changes the maximum redshift from 266 to 274

nm. The redshift of peaks confirms the reduction of functional groups present on RFLGPs.

4.6 Morphological analyses

4.6.1 FESEM studies

Figure 4.7 shows the FESEM image of the PGr sheets. This was used to synthesize FLGPs. Figure 4.10(a) shows the low-resolution FESEM image of PGr sheet which contains a large number of layers and many cleavage sites. Figure 4.10(b) shows the magnified image of PGr and shows the graphite crystal plane. Figure 4.10(c and d) show the less porous and layer stacking of the graphite crystal structure.

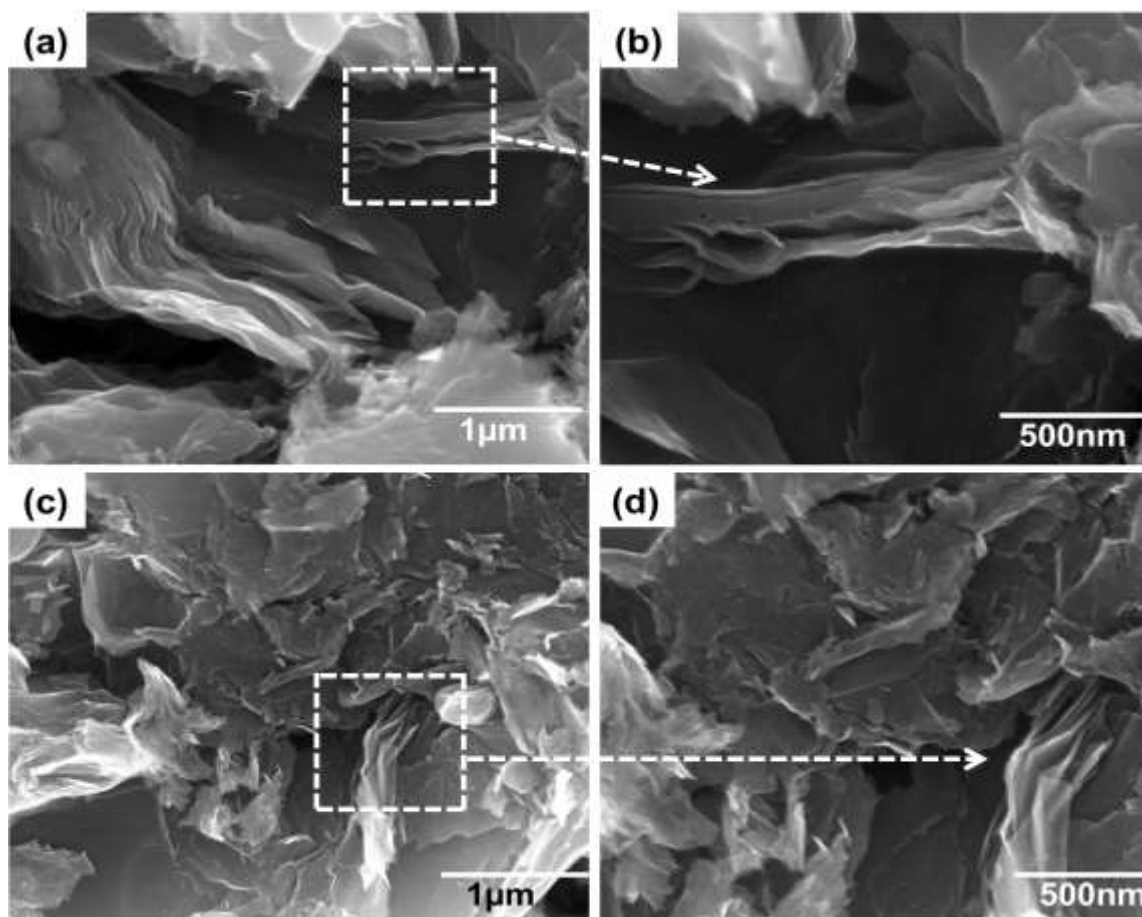


Figure 4.10: FESEM image of PGr sheets (a) and (c) magnified structure, (b) and (d) high magnified surface view

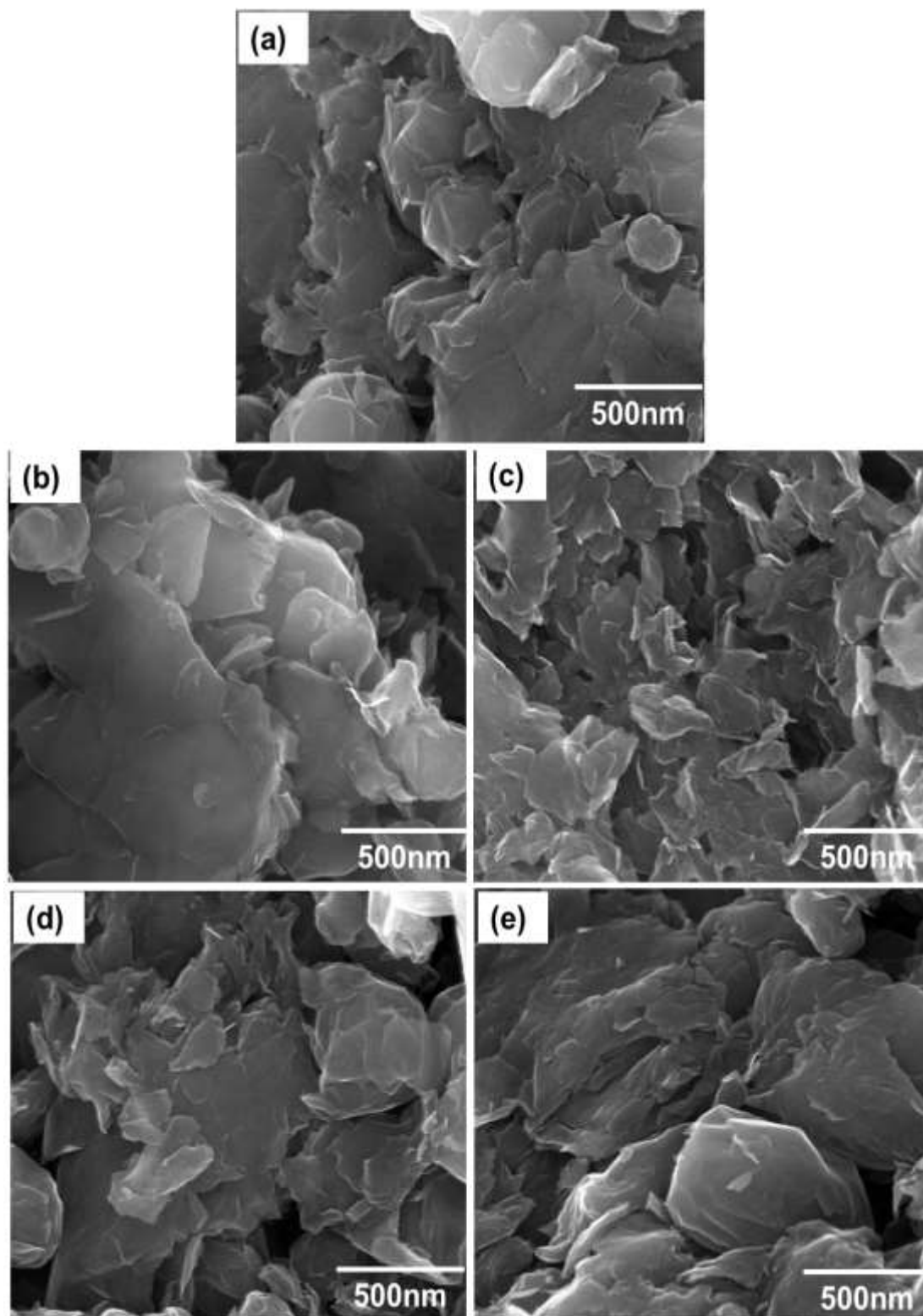


Figure 4.11: FESEM image of graphene particles (a) H, (b) HHY1, (c) HHY2, (d) HVC1 and (e) HVC2

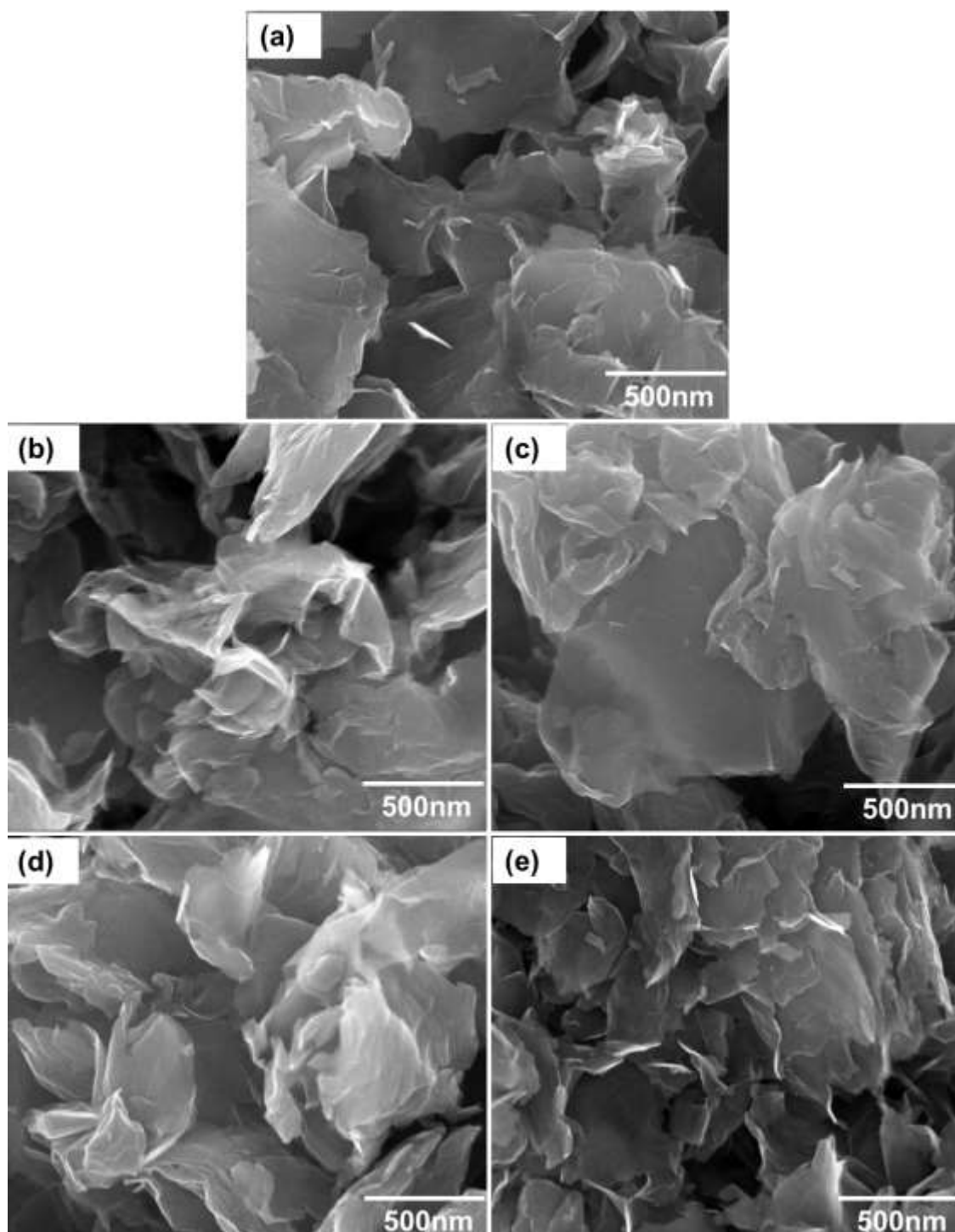


Figure 4.12: FESEM image of graphene particles (a) N, (b) NHY1, (c) NHY2, (d) NVC1 and (e) NVC2

Figure 4.11 shows the FESEM image of H group graphene particles, (a) H, (b) HHY1, (c) HHY2, (d) HVC1 and (e) HVC2. Figure 4.11(a) shows the image of FLGPs, electrochemically exfoliated by using aq H_2SO_4 as an electrolyte. The H FLGPs shows less crumpled graphene particles. It shows the multilayer of graphene particles. Figures

4.11(b) and (c) shows the layer structure of reduced graphene particles with folded and wrinkled structure whose intensity has decreased as compared to FLGPs. The layer structure of FLGPs is found to be decreased with the application of the reducing agent during chemical reduction. Figure 4.10(d and e) shows the wrinkled structure by sheet folding of graphene particles as compared to FLGPs.

Figure 4.12 shows the FESEM image of N group graphene particles, (a) N, (b) NHY1, (c) NHY2, (d) NVC1 and (e) NVC2. Figure 4.12(a) shows the image of FLGPs which was electrochemically exfoliated by using aq. HNO_3 as the electrolyte. The N FLGPs show a platelet like crystal structure of carbon. Figures 4.12(b) and (c) shows the layer structure of reduced graphene particles with less folded and wrinkled structure as compared to that of FLGPs. Figure 4.12 (d and e) shows the thin, crumpled, wrinkled structure by sheet-like pristine reduced graphene sheet folding of edges.

4.6.2 TEM studies

Figure 4.13 shows the TEM analysis of electrochemically exfoliated FLGPs and RFLGPs of H series. It shows the structure of graphene particles. The partial transparent structure and stacking of few-layer graphene particles of prepared FLGPs also can be observed. The HRTEM image shows the 7-12 layers stack of FLGPs flakes which were peeled from PGr sheet. The SAED pattern confirms the crystallinity and hexagonal structure of the synthesized FLGPs. It shows a ring structure due to the presence few-layer of graphene in place of single layer in that selected area. The RFLGPs further gives partial transparency and stacking of few-layer graphene from FLGPs. The number of layers has been reduced by applying reducing agents, hydrazine and ascorbic acid. With increasing concentration of hydrazine hydrate and ascorbic acid the layer structure has been decreased. The functional groups present with FLGPs were reduced and it has reduced the layers to 3-5 layers for HHY1, HVC1, HHY2 and HVC2 graphene sheets.

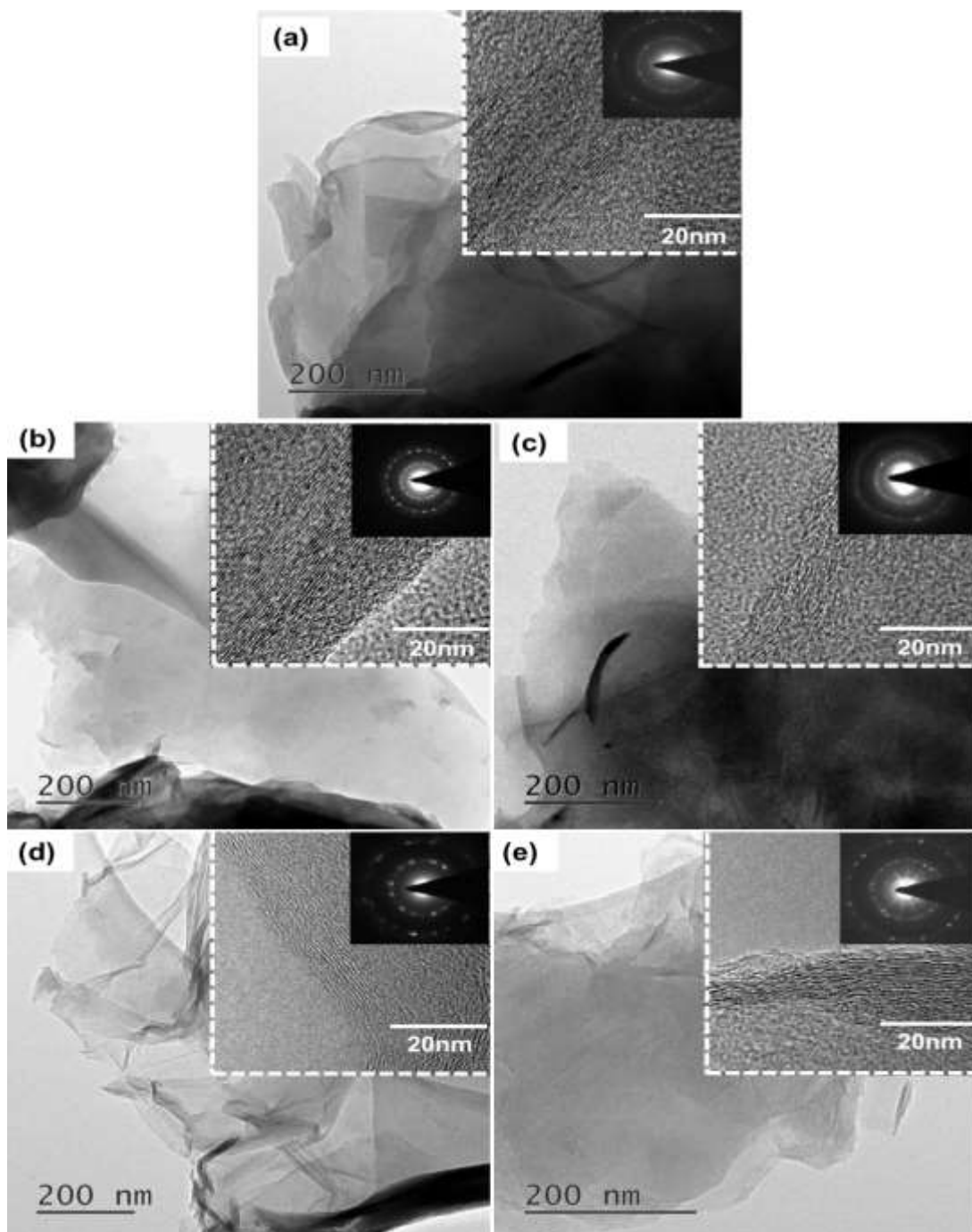


Figure 4.13: TEM image of graphene particles (a) H, (b) HHY1, (c) HHY2, (d) HVC1 and (e) HVC2

Figure 4.14 shows the TEM image of N series exfoliated FLGPs and RFLGPs. Where figure 4.14(a) shows N FLGPs and figure 4.14(b- e) shows the reduced FLGPs of NHY1, NHY2, NVC1 and NVC2 respectively. The FLGPs were intercalated from 1M nitric acid concentration. The NO_3^- anions intercalated the PGr sheets which are smaller than SO_4^{2-} ion. The electrochemical reaction of FLGPs is very slow than the electrochemical reaction of H series FLGPs.

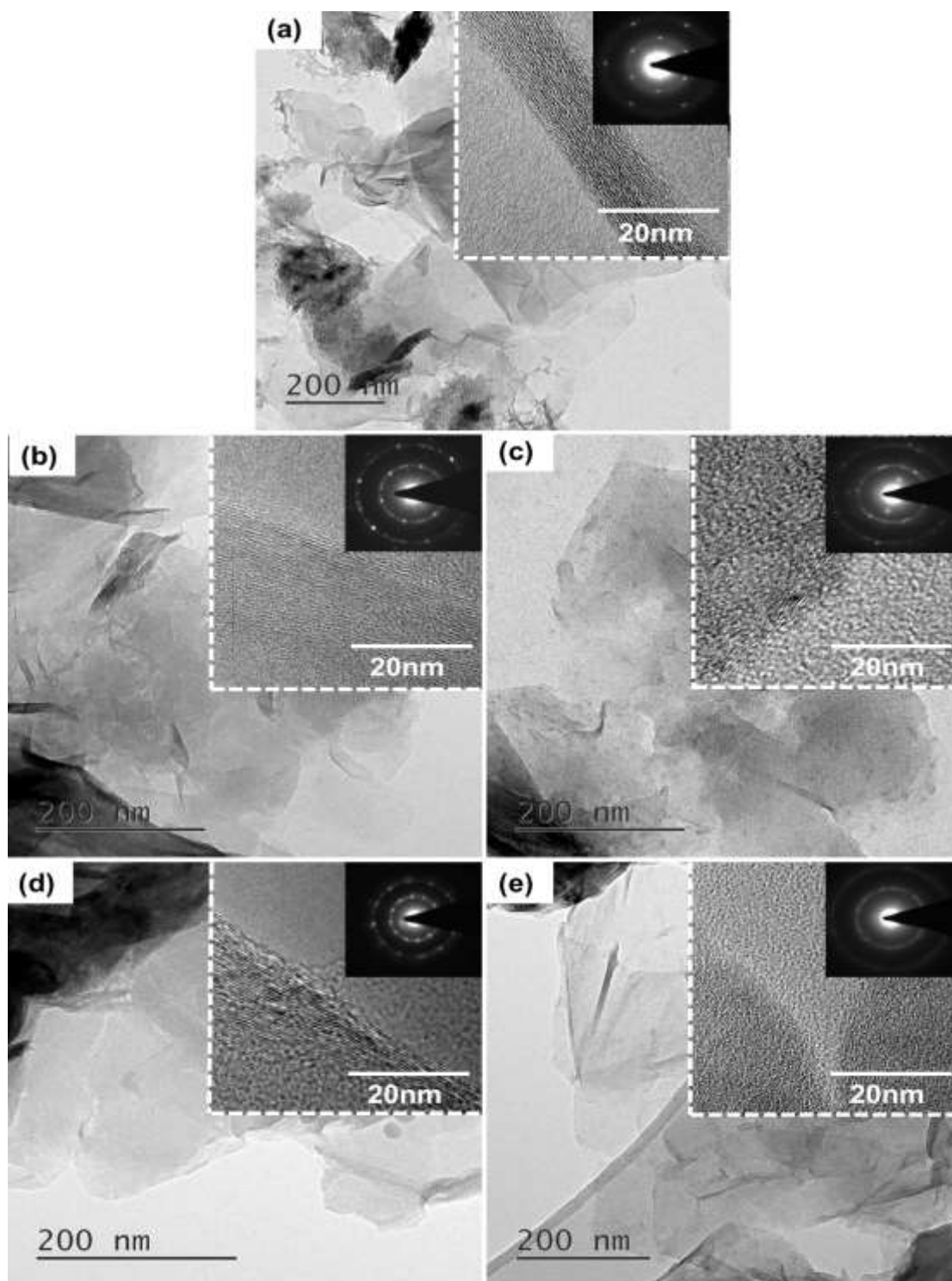


Figure 4.14: TEM image of graphene particles (a) N, (b) NHY1, (c) NHY2, (d) NVC1 and (e) NVC2

It contains bigger domain and layer structure than the H series FLGPs. The TEM image of N series FLGPs also shows the partial transparent structure (shown in figure 4.14). The HRTEM image of FLGPs and RFLGPs has also been included in figure 4.14. HRTEM image of FLGPs confirms the layer structure of 7-10 layers. The HRTEM image confirms

the reduction of layer structure up to 3-6 layers. The SAED pattern of N FLGPs shows the hexagonal structure of carbon particles and the crystal structure of graphene sheets.

4.7 Concluding remarks

FLGPs have been synthesized successfully by the electrochemical exfoliation method. The FLGPs have been reduced by chemical methods using ascorbic acid as a reducing agent. From XRD analysis of HHY2, HVC2, NHY2 and NVC2, it was confirmed that FLGPs peak of (001) plane completely vanished and shows only (002) plane. Raman spectroscopy shows the D and G peak of graphene particles. The FTIR study analysis confirms that the intensity of oxygen functional groups strongly decreased and some functional groups vanished due to reduction as compared to that of unreduced FLGPs. The UV spectroscopy shows the redshift of π - π^* transition band for FLGPs from (266 nm) to NVC2 (274 nm) and confirms the reduction of FLGPs. The layer structure of FLGPs decreases from 10 layers to 3-5 layer by reduction. The crystallinity and hexagonal ring structure of graphene particles have been confirmed by SAED pattern. From the above analysis, it was confirmed that some of the oxygen functional groups are still present even after reduction and need further optimization by other reducing agents.

Chapter 5

5: Micro and nano-mechanical Properties of Cu-FLGPs and Cu- RFLGPs composites

5.1 Ultrasound-assisted electroplating of nano-composite thin film of Cu matrix with electrochemically in-house synthesized few-layer graphene nano-particles as reinforcement

5.1.1 Introduction

The present section deals with electrodeposition of Cu and Cu-FLGPs on-to polished steel substrate by simple DC electrodeposition method at low bath temperatures in both presence and absence of ultrasound. The main is to monitor the distribution of the graphene flakes in the films and the evolution and variation of the properties associated with. Initially, copper is electrodeposited at different temperatures (15, 20 and 25 °C) to investigate the best temperature to work with for a well-metalized film. The structures of the composite films were then characterized by different analysis techniques to extract the effect of graphene as reinforcement.

5.1.2 Electrodeposition of copper and Cu-FLGPs films



Figure 5.1.1: (a) Experimental setup of pure copper deposition with sonication at a temperature of 15 °C and (b) Experimental setup of copper-FLGPs electrodeposition with sonication

Figure 5.1.1(a) shows the experimental setup of copper electrodeposition with sonication at a temperature of 15 °C in an ice bath at a potential of 2 V for 20 minutes. After deposition, copper samples were up peeled from the steel substrate for further

characterization. Figure 5.1.1(b) shows the experimental setup for electrodeposition of Cu-FLGPs with sonication, maintained with the same experimental parameters as that of Cu film deposition.

5.1.3 Analysis of Copper thin films

The thickness and roughness of the electro-deposited copper thin films is measured by the stylus profiler by applying a load of 2 mg on 3mm length as shown in figure 5.1.2(a). The thicknesses of electroplated copper films at different temperatures of 15, 20 and 25 °C were found to be 20.2, 19.7 and 19.7 μm and 20, 19.8 and 19.87 μm in silent and ultrasound conditions respectively. The root mean square (RMS) roughness values of the deposited films decreased from 793 to 410 nm with a decrease in temperature measured by the stylus surface profilometer. The visual appearance of the films can be observed in figure 5.1.2 (b). Which indicates that the smoothness of copper thin films has increased with a decrease in temperature. Figure 5.1.2(c) and (d) represent the X-ray diffractogram of copper thin films at different temperatures at a constant deposition time in silent and ultrasonic bath conditions respectively. It was observed that the deposition temperature and sonication has a definite impact on the structure of deposited thin films. The diffraction peaks at $2\theta = 43.62^\circ, 50.76^\circ, 74.34^\circ$ and 90.21° can be indexed as (111), (200), (220) and (311) planes respectively which confirms the FCC Cu lattice structure (JCPDS File No. 04-0836). The height of the peaks decreases and broadens as the temperature decreases from 25 °C to 15 °C. The average crystallite sizes and the associated strain of thin films were then calculated by Williamson-Hall formula (equation 5.1).

$$\beta \cos\theta = \frac{k\lambda}{D} + 4\varepsilon \sin\theta \quad (5.1)$$

Where k is the Scherrer constant, λ is the wavelength of the radiation source, β is the full width half maximum (FWHM), θ is the Bragg's angle, D is the grain size and ε is the internal strain respectively.

The crystallite sizes of copper thin films are found to vary in the range of 31 to 40 nm in both silent and sonication conditions. The deposits obtained at 15 °C have the finest crystal size in both silent and ultrasonic bath conditions. Figure 5.1.3 shows the surface structure of copper thin films deposited at 15 °C in both silent and ultrasonic stirring conditions respectively. The grains are either spherical or faceted structures in appearance

and show more roughness hence complimenting the profilometry data and visual appearance. Now comparing the deposits in ultrasonic conditions, the deposits are compact in nature and the individual grain morphology is hard to interpret. And of course the smoothness has been increased at all temperatures as compared to their silent counterpart films. The 3D height mode topographical AFM image of scan area $20 \times 20 \mu\text{m}^2$ for copper thin film of bath temperature 15°C are shown in figure 5.1.5 at silent and ultrasonic stirring conditions respectively.

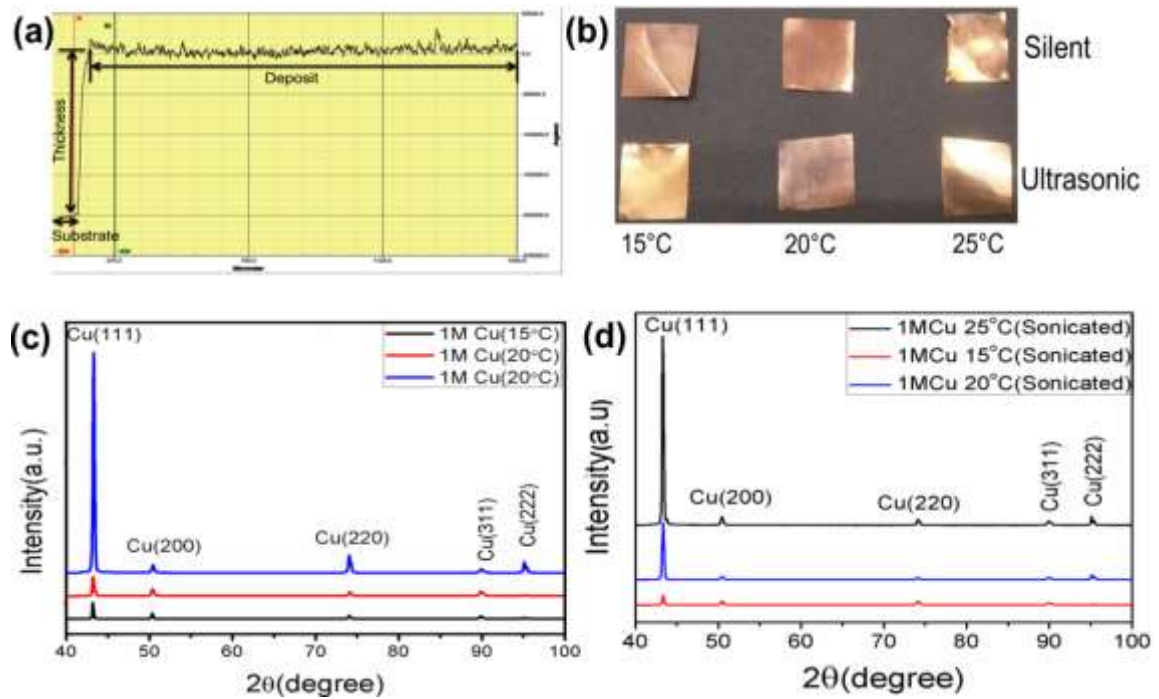


Figure 5.1.2: (a) Thickness measurement of Cu thin film by surface profiler, (b) Photography images of as-deposited Cu thin films, XRD pattern for Cu deposited in (c) silent and (d) sonication condition

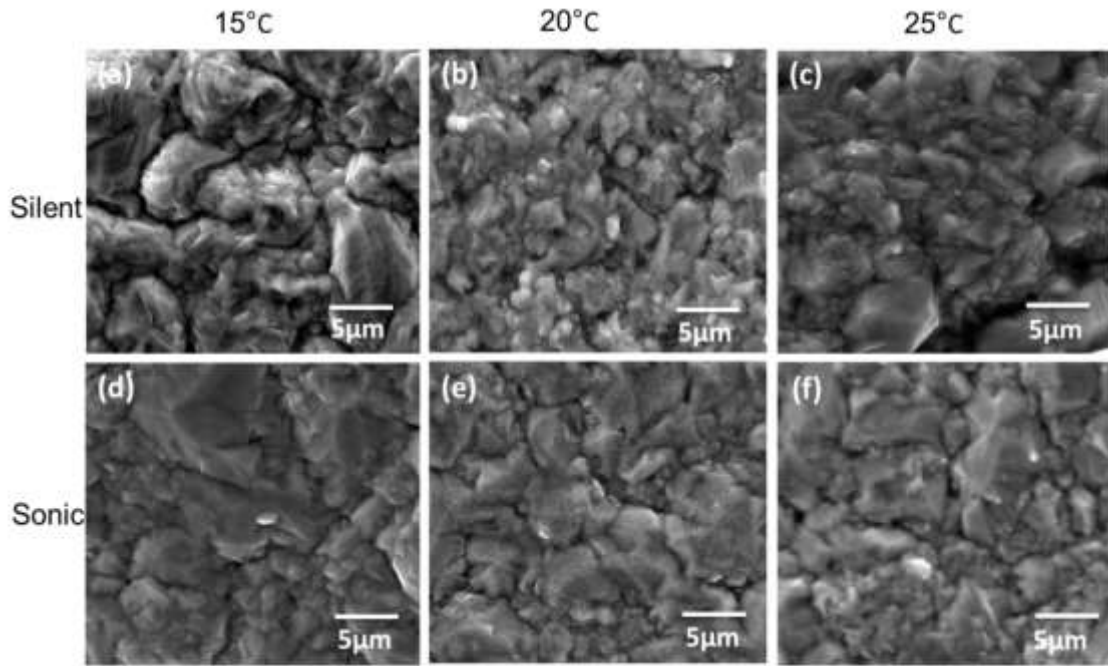


Figure 5.1.3: SEM images of Copper samples at different temperature

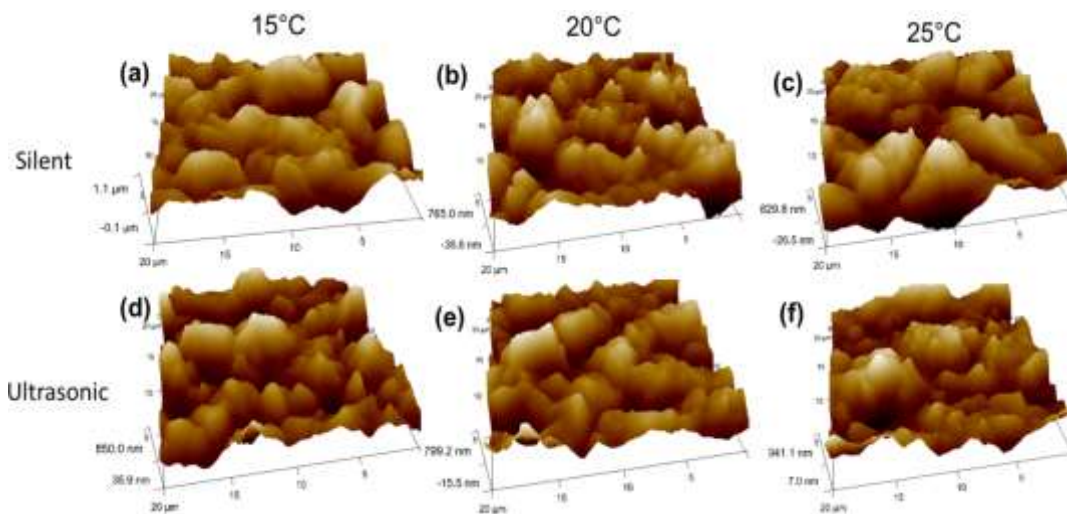


Figure 5.1.4: AFM images of Copper samples at different temperature

The extent of coalescence and grain architecture can further easily be examined with greater clarity from the above figures. The grains are observed to be primarily faceted with nearly mono-dispersive in nature. The roughness of the films is again verified by this technique and was found that it has decreased from high temperature (25 °C) to low temperature (15 °C) from 218 nm to 181 nm (the detailed study is presented in Table 5.1.1). The above findings, that the grain size and roughness of the deposits have been reduced with temperature and application of ultrasound, can be explained reasonably with the following justifications. The level of solution supersaturation has been increased with

the decrease of temperature which might have favored the formation of smaller nuclei but in a random fashion of discharging in the absence of ultrasound. Hence finer-grained deposits were obtained in silent conditions which are not so compact. As the application of ultrasound will homogenize the solution as well as increase the rate of mass transportation, the rate of nucleation is compelled to be increased and hence leading to finer, smoother and compact deposits [175]. Hence these results indicated that the highest surface finish of the deposit was at 15 °C among other bath temperatures. As compared to silent conditions, the ultrasonic bath condition shows the highest surface finish. So the lowest temperature (15 °C) was chosen for electroplating of Cu-FLGPs nano-composite for further studies.

5.1.4 Structural analysis of Cu-FLGPs

The thickness of Cu-FLGPs composites were measured by the surface profiler and are shown in figure 5.1.5 (a). The thicknesses of composites are found to be around ~20 µm on both silent and sonic conditions. The roughness of composites increased from 324 nm to 500 nm with an increase in graphene content from 0.1 to 0.5 g/L. Figure 5.1.5 (b) shows the photography images of as-deposited Cu-FLGPs thin films, indicating metalized and uniform films irrespective of deposition conditions. Figures 5.1.5(c) and (d) shows the XRD pattern of the Cu-FLGPs composite with graphene concentrations of 0.1 g/L, 0.3 g/L and 0.5 g/L in silent and ultrasound-assisted baths respectively. We observed that in silent condition there is no peak from graphene, but the increase of graphene percent has eventually decreased the intensity and increased the FWHM of copper peaks in the composite films. On the contrary, the reverse has been observed in case of ultrasonic conditions. The intensity of copper peak at $2\theta = 43.42^\circ$ of index (111) has been increased with an increase in the graphene percentage in the depositing solutions but the intensity of copper peak at $2\theta = 50.76^\circ$ of index (200) was found to be decreased. The above argument has further been complemented by a thorough and critical analysis by EDS study as presented later on. The texture co-efficient was then studied to analyze the above results as per equation 2.

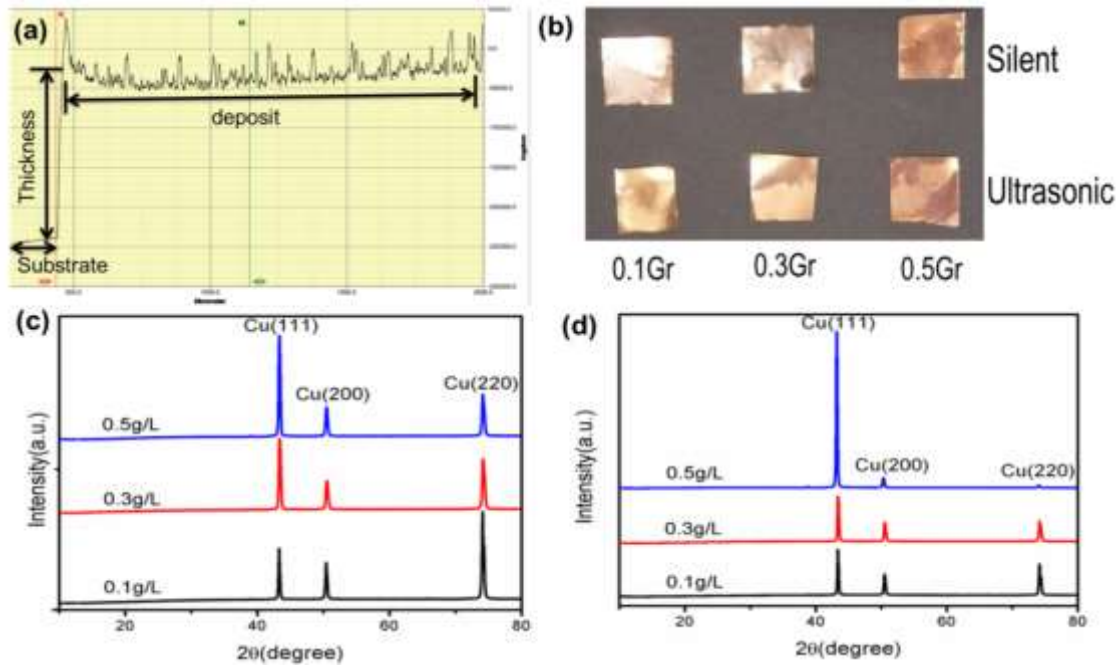


Figure 5.1.5: (a) Thickness measurement of Cu-FLGPs thin film by surface profiler, (b) Photography images of as-deposited Cu-FLGPs thin films, XRD pattern for Cu-FLGPs deposited (c) silent and (d) sonication

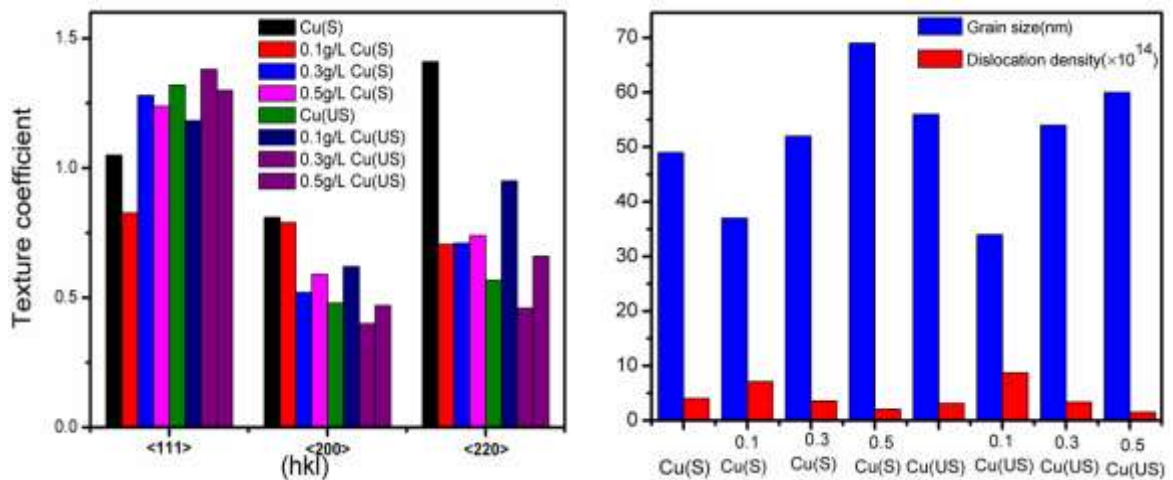


Figure 5.1.6: (a) Texture coefficient of Cu-FLGPs composite (b) grain size and dislocation density of films on silent and ultrasound conditions

$$T_c(hkl) = \left(\frac{I_{hkl}}{\sum I_{hkl}} \times \frac{\sum I_{0\ hkl}}{I_{0\ hkl}} \right) \quad (5.2)$$

Where T_c is the texture coefficient, $I_{(hkl)}$ is the intensity of prepared coating samples and $I_{0(hkl)}$ is the reference intensity of Cu (JCPDS No. 004-0836). Figure 5.1.6 shows the texture coefficient of Cu-FLGPs composite on silent and ultrasound conditions along with

grain size and dislocation density. The texture coefficient of randomly oriented planes is observed in the present study. The calculations for dislocation density and other parameters are done by equations 5.3 and 5.4.

$$\delta = \frac{1}{D^2} \quad (5.3)$$

Where δ is the dislocation density and D is the grain size.

$$N = \frac{t}{D^3} \quad (5.4)$$

Where N is the number of crystallites per unit area and t is the thickness of the composite film. Grain size has been increased and dislocation density has decreased with incorporation of FLGPs. Now focusing on the morphological variations of the composite films, figure 5.1.7 shows the SEM images of Cu-FLGPs nano-composites with graphene content of 0.1, 0.3 and 0.5 g/L in silent and sonication conditions deposited at 15 °C for 20 minutes. The overall appearance of the topography has a close resemblance with their counterpart Cu films in both the conditions at all graphene concentrations. However, the grain size of Cu-FLGPs composite has increased with an increase in graphene percent i.e. 0.1, 0.3 and 0.5 g/L in silent condition. The same trend is observed for sonicated samples too, but the films appear to be compact, void-free and adherent to the substrates. Moreover from the topography micrograph of Cu-FLGPs composite, it is difficult to determine the graphene from the matrix due to the intense mixing of the reinforcement with the matrix. Figure 5.1.8 displays the 3D AFM images of the films on some selected areas of $(20 \times 20) \mu\text{m}^2$ from both the depositing conditions. The roughness of composite thin films was then also measured by AFM analysis. The addition of graphene with Cu matrix gives surface roughness in the range of 200 nm. However in both the conditions the roughness was observed to be increased with increase in graphene content, whereas sonicated films have smoother surface finish. Because of ultrasonic stirring the graphene particles are expected to get distributed uniformly in the matrix. Hence the addition of graphene can decrease the voids of thin-film; the interphase boundary will be closely bonded between reinforcement and matrix in Cu-FLGPs composite. Also the uniform distribution of graphene can arrest the copper grain growth during electrodeposition to prepare the Cu-FLGPs composite. Hence the topography of copper thin film can readily be changed by addition of graphene in to copper electrolyte. The thin films thus produced

could be polished by micro-polishing to get high co-planarity and surface finish for use in electronic industries.

Table 5.1.1: Variation of average roughness of electroplated Cu and Cu-FLGPs thin films

Deposition Conditions	Average roughness, Ra	
	Silent	Sonicated
1MCu, 15 °C	181	176
1MCu, 20 °C	200	198
1MCu, 25 °C	218	205
1MCu, 15 °C, 0.1 g/L	201	198
1MCu, 15 °C, 0.3 g/L	213	230
1MCu, 15 °C, 0.5 g/L	254	235

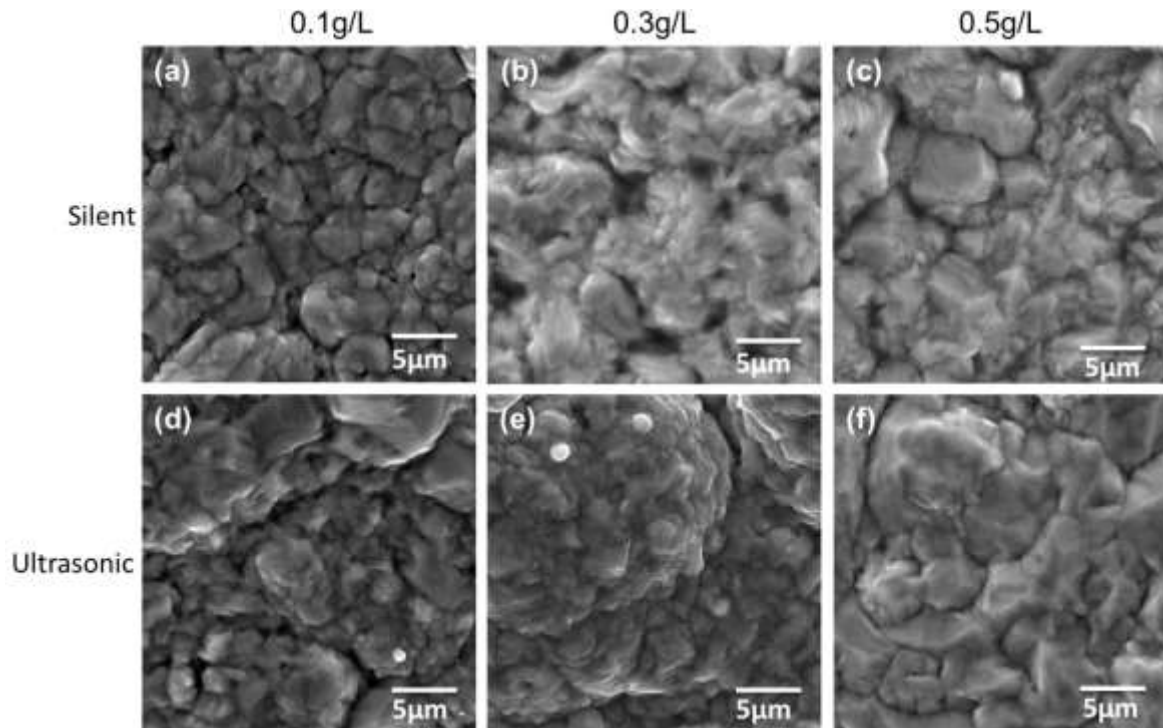


Figure 5.1.7: SEM images of electroplated Cu-FLGPs composites prepared with varying graphene concentrations

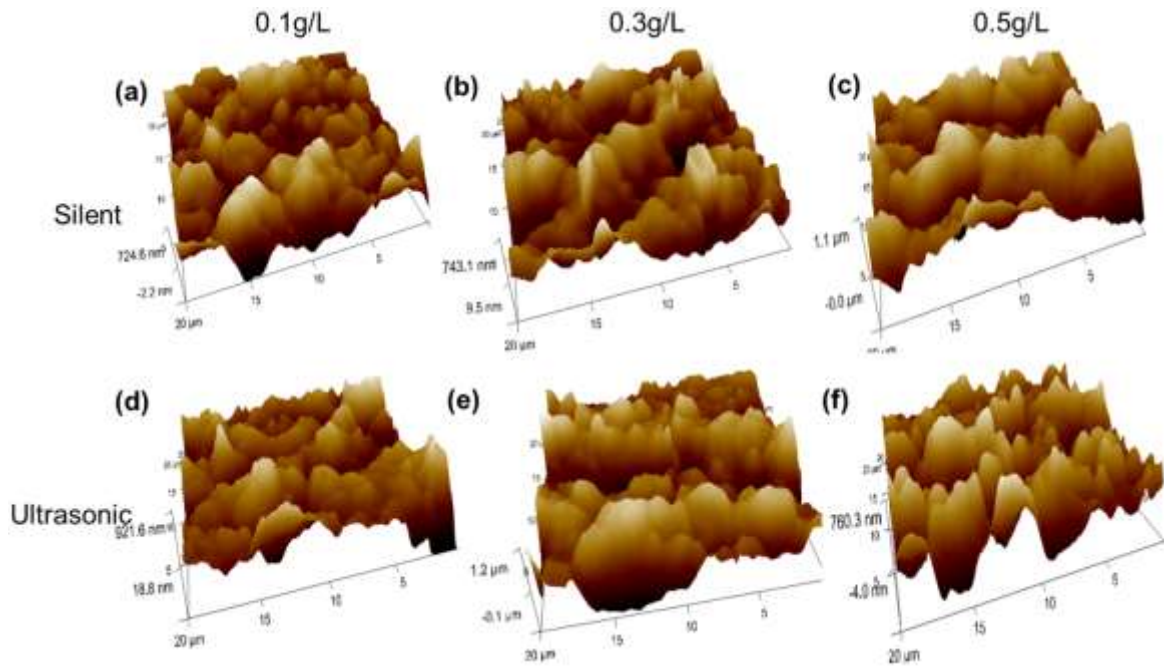


Figure 5.1.8: 3D AFM images of electroplated Cu-FLGPs composites prepared with varying graphene concentrations

5.1.5 Compositional analysis by EDS elemental mapping study

The EDS analysis of the composite films prepared in both silent and ultrasonic conditions are given in Figure 5.1.9. Figure 5.1.10 and 5.1.11 shows the elemental mapping of carbon and copper in composite thin films prepared from both silent and ultrasonic stirring conditions with an increase in graphene content of 0.1 g/L, 0.3 g/L and 0.5 g/L in the electrolyte respectively. The EDS analysis has been done on the entire selected area of SEM images presented in the next section. The spectrum contains strong carbon (C) and copper (Cu) peaks. The carbon peak of EDS analysis hence confirms the evidence of presence and incorporation of graphene nano-flakes into the copper matrix in the Cu-FLGPs composite thin film. However, there could be various other sources of carbon incorporation in the films which may manipulate the inference made from the above observations. Hence EDS analysis of pure copper films were also done and compared (not shown here) and it was found that the films are free from any carbon or other elements when obtained from baths without the addition of graphene. Henceforth the carbon intake in the films must be solely from the graphene. Furthermore, it was also observed that the carbon weight percentage in the matrix has been increased from 3.29, 6.54 and 8.7 with an

increase in graphene content from 0.1 g/L, 0.3 g/L and 0.5 g/L respectively. The carbon weight percentage hence increased with an increase in graphene content. The carbon signal shows uniform distribution of graphene on copper matrix. In ultrasonic conditions the variation of carbon weight percentage is from 8.55, 16.65 and 18.60 with increase in graphene from 0.1 g/L, 0.3 g/L and 0.5 g/L respectively. From X-ray mapping it was observed that more no of graphene particles have been uniformly distributed due to ultrasonic stirring as compared to silent bath condition. Hence ultrasound has assisted the distribution of graphene into the composite during deposition period. This observation should also reflect during the physical property analysis as presented in the next section.

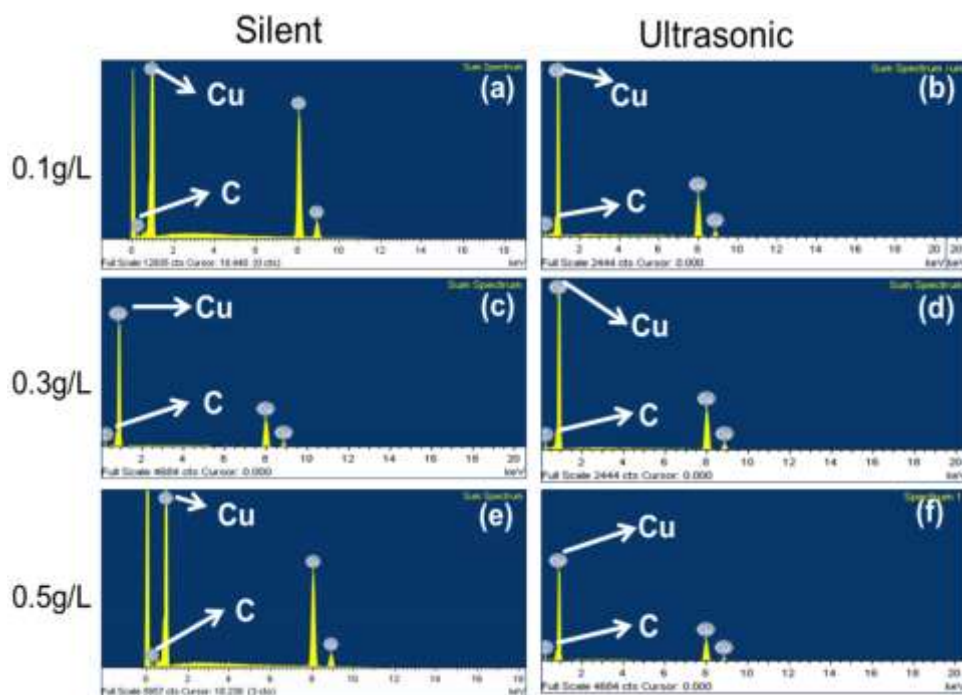


Figure 5.1.9: EDS image of Cu-FLGPs samples at various graphene concentration

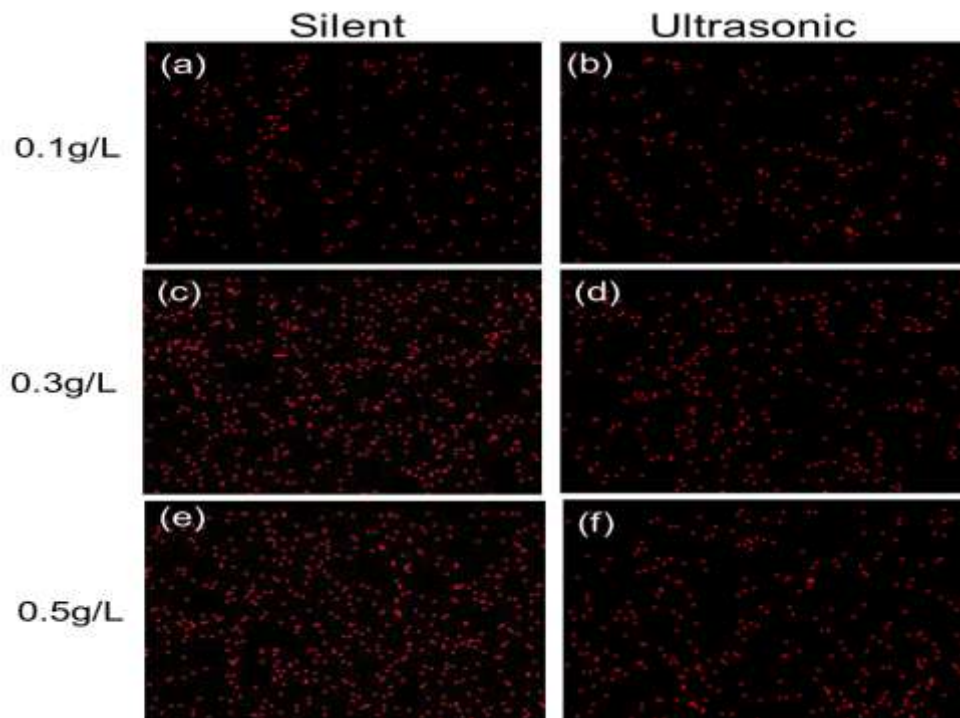


Figure 5.1.10: Elemental mapping for carbon in electroplated Cu-FLGPs composites prepared with varying graphene concentrations

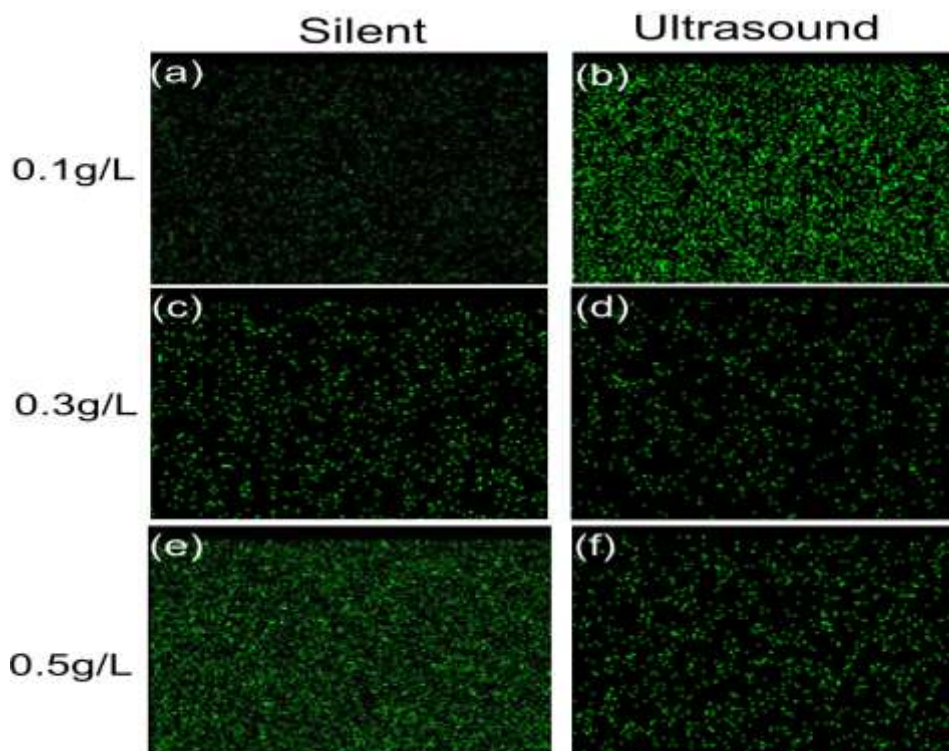


Figure 5.1.11: Elemental mapping for copper in electroplated Cu-FLGPs composites prepared with varying graphene concentrations

5.1.6 Surface micro and nano-mechanical properties

As the synthesized films are aimed for the use of hard electronic applications, the knowledge of mechanical properties mainly hardness becomes essential and hence is studied in the current sections by micro-hardness and force-displacement studies (FD analysis) by AFM. Figures 5.1.12(a) and (b) shows the hardness values measured on the coated Cu thin film (deposited at 15 °C) as well as of surfaces of nano-composites. The observed hardness value is 1.61 GPa for electroplated Cu films which are higher than the pure bulk copper [50] and matching with other reported values in the literature [85]. For composite thin films with different concentrations of graphene of 0.1, 0.3 and 0.5 g/L in silent and ultrasonic stirring conditions, the obtained hardness values are 1.96, 2.0 and 2.05 GPa and 1.99, 2.05 and 2.11 GPa respectively. It was observed that the hardness has increased with the addition of graphene up to 0.5 g/L Gr. However further increase of graphene concentration (e.g. 1 g/L Gr) may decrease the hardness due to agglomeration, non-uniform distribution and non-coherency of graphene particles in the copper matrix as reported by others [126]. The hardness value observed by the addition of 0.5 g/L in the ultrasonic stirring bath is 31% higher than pure copper thin films deposited at same criteria. The above observation is further micro-analyzed and complimented by force-displacement study by AFM. In this technique the cantilever and the tip are directly moved towards the sample by applying a load until they touch the surface, and when they are retracted, while the interaction between the tip and the sample is measured.

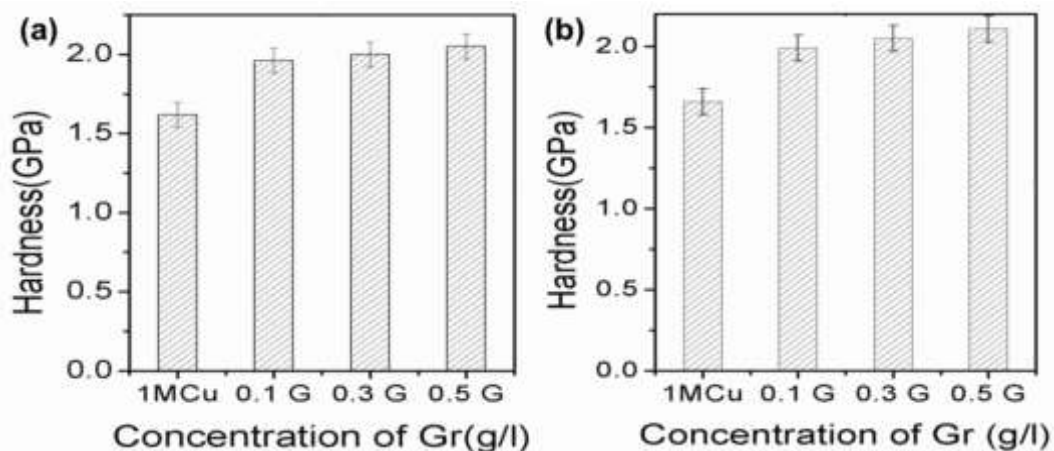


Figure 5.1.12: Hardness variation of Cu-FLGPs thin films deposited in (a) silent and (b) sonication conditions

This technique is explored by measuring the force in terms of level of deflection of the tip which decides the type of interaction between the tip and sample during the vertical interaction where essentially the lateral deflection is zero. The whole set of interactions could be grouped into three levels based upon the position of tip with respect to sample i.e. approach, at contact and retract. During approach the forces which are acted upon or can be measured are electrostatic, Van der Waals, magnetic and solvation forces, chemical potential and long range interactions. These interactions are marked as zero deflection in the graph. Then at the point of contact, where deflections can be observed, stiffness and viscoelastic properties can be measured [175]. Finally during retracting, where of course deflection is there, the adhesive nature of the surface atoms is primarily measured. Hence for the current study we have utilized the deflection portion of the FD curve to measure the stiffness or mechanical properties of the films. The FD graphs with an average of 10 readings at different locations on the composite films are obtained to map properly the interaction and are shown in Figure 5.1.13 for films deposited at various graphene concentration and 15 °C. Concentrating on the zero deflection lines, both the FD curves have irregularities which may be due to the long-range forces of interaction between the sample and the AFM tip. Now focusing on the deflections during the contact segment, the slope of the line would decide the mechanical properties; higher the slope, higher will be the sensitivity factor and hence better will be the mechanical properties. Comparing the FD graphs, it can be observed that the slopes of the deflection segment corresponding to contact region have decreased from 18.5 nm/V in ultrasonic condition to 11.3 nm/V in silent condition. The same has been observed for the other conditions of deposition (in figure 5.1.12), where deposits under sonication are found to be stiffer than the silent ones. Hence with an optimum concentration of 0.5 g/L, the Cu-FLGPs composite thin films deposited under sonication were found to be the best in the lot. To justify the above observation following arguments can be put forward: The hardness of a metal matrix composite generally depends on matrix and reinforcement structure and their distribution which essentially affects the mode of load distribution and mechanism of dislocation interaction. As has been pointed out before, in presence of ultrasound the graphene distribution was uniform, hence the load distribution might be even throughout the matrix and at the interfaces of matrix/reinforcement. Furthermore because of the reinforcement of the two dimensional partially functionalized graphene into the copper matrix, the dislocation motion and grain growth might have been arrested during electrodeposition leading to dispersion hardening mechanism. The uniform distribution of graphene

throughout the copper matrix might have also decreased the inter-particle distance of grains, hence further restraining the dislocation motion.

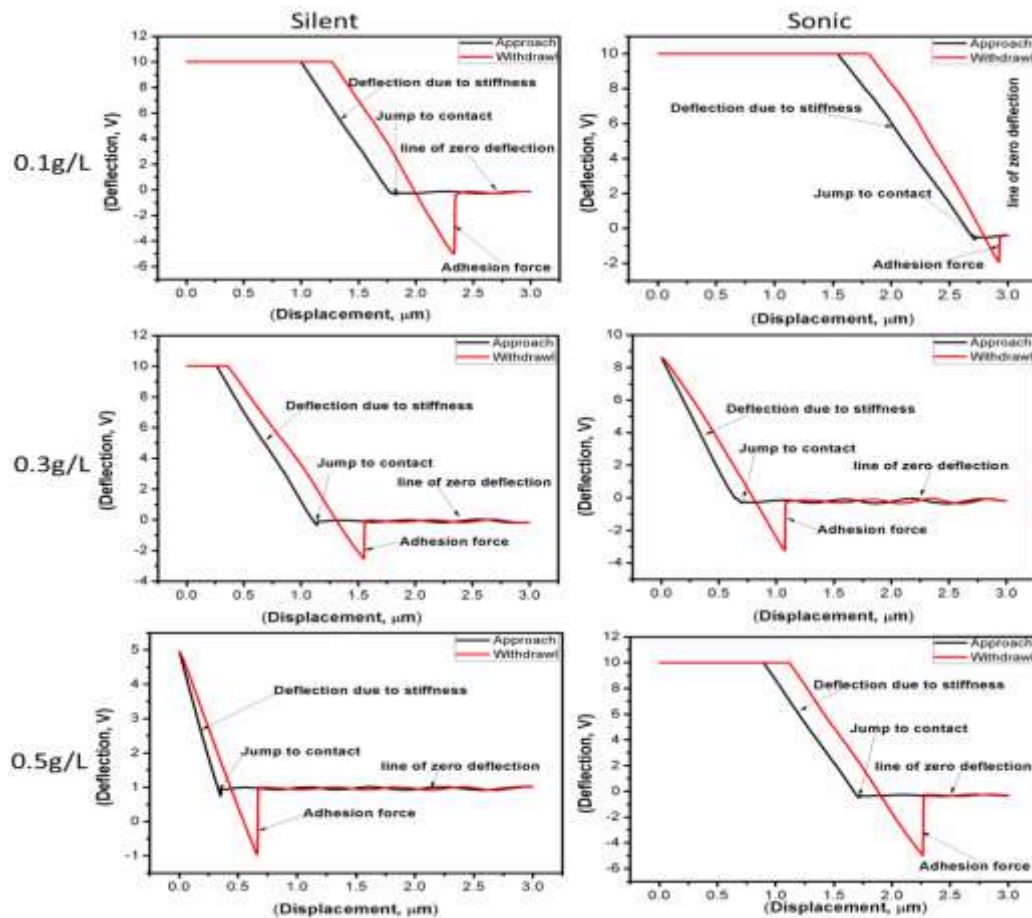


Figure 5.1.13: FD analysis image of Cu-FLGPs composite at various graphene concentration. The study can further be extended by analyzing the deflection in the withdrawal regions which are basically due to the interaction of surface particles with foreign atoms i.e. with the AFM tip. Maximum deflection will be observed in the case where the surface energy is high or to be derived specifically when the surface is chemically active. Hence the observation of the trend of the retracting forces suggests that the films are chemically unstable or reactive at low graphene percentage in the composite films deposited in silent conditions. Similar data were also obtained for the ultrasound-assisted electroplated films as well. The said observation can be justified with the fact that graphene has a highly chemically stable surface which must have contributed to the reduction of surface energy as the concentration and distribution of the same has been uniformly increased.

5.1.7 Electrical resistivity

The electrical resistivity of prepared Cu-FLGPs composite films was measured by the four-probe method at room temperature. The electrical resistivity of Cu-FLGPs composites is shown in figure 5.1.14(a) silent and (b) sonication. The electrical resistivity is observed in the range from $1.8\text{-}3.4 \times 10^{-6} \Omega\text{-cm}$ and $1.9\text{-}3.6 \times 10^{-6} \Omega\text{-cm}$ in silent and ultrasound conditions respectively. Irrespective of the deposition conditions, the Cu-FLGPs composites exhibited higher electrical resistivity ($3.6 \times 10^{-6} \Omega\text{-cm}$) than the bare Cu thin films ($1.6 \times 10^{-6} \Omega\text{-cm}$) which has also been observed in the other reported literature [85,176]. Furthermore, the resistivity of Cu-FLGPs composites increases with the graphene content. In both cases, the higher graphene content (0.5 g/L) exhibited the highest resistivity in the series we experimented with. Yet, Cu-FLGPs deposited at ultrasonic conditions showed an increase in electrical resistivity when compared to Cu-FLGPs deposited at silent conditions. The insignificant increase in the electrical resistivity due to the addition of graphene to the Cu matrix may be due to the presence of functionalized groups attached to the base hexagonal structure of graphene which may serve as the lattice impurity defect in the Cu structure. The incorporated graphene would also form small-range defects and might have increased the resistivity by affecting the flow of electrons. Moreover, the oxidation of Cu into oxides either by reacting with the atmospheric air or the oxygen groups of graphene might have escalated the resistivity further.

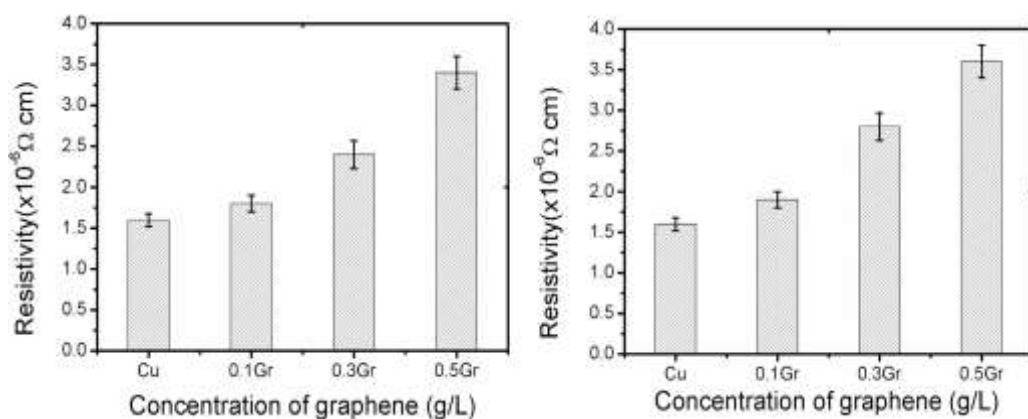


Figure 5.1.14: Electrical resistivity of Cu-FLGPs thin films deposited in (a) silent and (b) sonication conditions

5.1.8 Concluding remarks

In summary, the Cu-FLGPs nano-composite thin films were prepared by electrodeposition method from an electrolytic solution containing CuSO₄, H₂SO₄ and in-house synthesized FLGPs with varying concentrations. The investigation has three different sections comprising of synthesis and characterization of FLGPs, Cu thin films and Cu-FLGPs composite films. Metallic copper thin films were deposited onto steel substrates at different deposition temperatures (15, 20 and 25 °C) and ultrasound stirring to obtain the best operating temperature to study further with Cu-FLGPs composite films. It was found that with decreasing temperature and addition of ultrasound the film quality has improved remarkably and 15 °C was chosen for deposition of composite films. Then after Cu-FLGPs nano-composite thin films, sono-electroplated at 15 °C containing 0.1, 0.3 and 0.5 g/L concentrations of graphene, were characterized to analyze the effect of ultrasound on the distribution of graphene in the matrix and evolution of mechanical and electrical properties as the synthesized composites are aimed to find application in electro-friction materials. Elemental mapping studies of the composite showed the uniform dispersion of graphene and sonication has induced uniform the dispersion of graphene in the copper matrix. The composites containing 0.5 g/L graphene particles showed an increase of 31 % hardness value and electrical resistivity than the pure copper thin film.

5.2 An exploration of the use of in-house synthesized reduced few-layer graphene particles as reinforcement during sono-electroplating of Cu matrix composite films

5.2.1 Introduction

In this section, few-layer graphene particles synthesized by the electrochemical exfoliation method were reduced by chemical reduction method with hydrazine hydrate and ascorbic acid, and have been addressed as reduced few-layered graphene particles (RFLGPs). Hydrazine hydrate is more toxic than ascorbic acid whereas ascorbic acid is eco-friendly to the environment [55,58,177]. Furthermore, the synthesis of RFLGPs by hydrazine hydrate and ascorbic acid has similar properties. Hence ascorbic acid has been significantly used as a reducing agent in many researchers. However, in the present study both the reducing agents have been used to critically compare the evolution of properties. The reduced FLGPs are used as reinforcement with copper matrix to produce composites by electrodeposition technique. Figure 5.2.1 shows the various steps to synthesize, RFLGPs and Cu-RFLGPs composites.

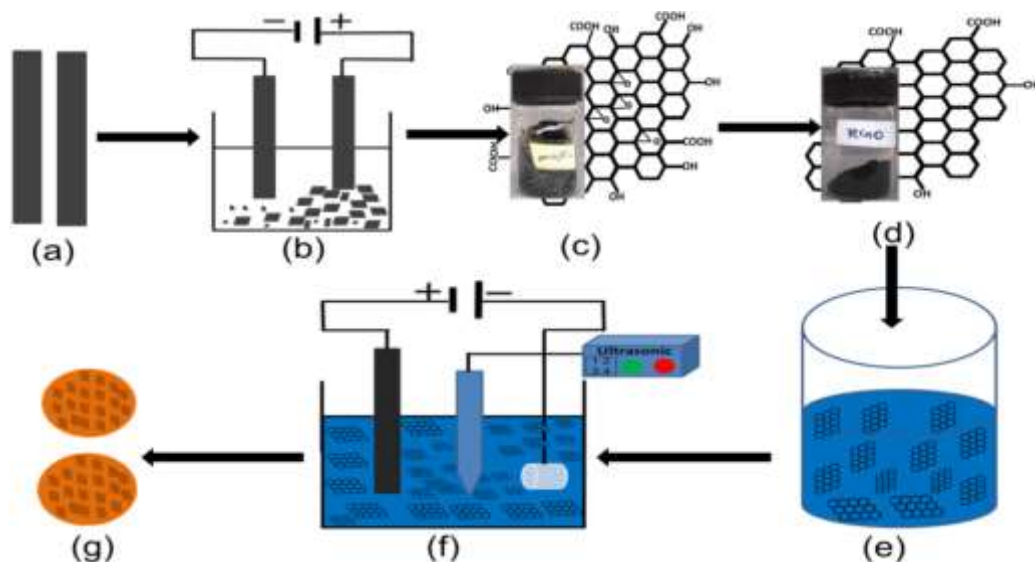


Figure 5.2.1: Schematic image of the synthesis route of RFLGPs and Cu-RFLGPs nanocomposite. (a) Graphite plates, (b) Electrochemical exfoliation setup, (c) & (d) reduced few layered graphene nano-particles, (e) electrolyte of Cu-RFLGPs composite synthesis, (f) Electrodeposition setup and (g) Cu-RFLGPs thin films

5.2.2 Analysis of Cu-RFLGPs composite films

Figure 5.2.2 shows the XRD analysis and texture coefficient of prepared copper Cu and Cu-RFLGPs films at different concentrations of 0.1 g/L, 0.3 g/L and 0.5 g/L RFLGPs(Hy) and RFLGPs(Vc). We observed that in Cu-RFLGPs(Hy) and Cu-RFLGPs(Vc) there are no RFLGPs peaks present, but with an increase in RFLGPs concentration, the intensity of the peaks has been decreased. The crystallite size of Cu and Cu-RFLGPs composite films were measured by using the Williamson-Hall formula and are presented in Table 5.2.1. The Table also includes the dislocation density and number of crystals calculated through equations 3 and 4.

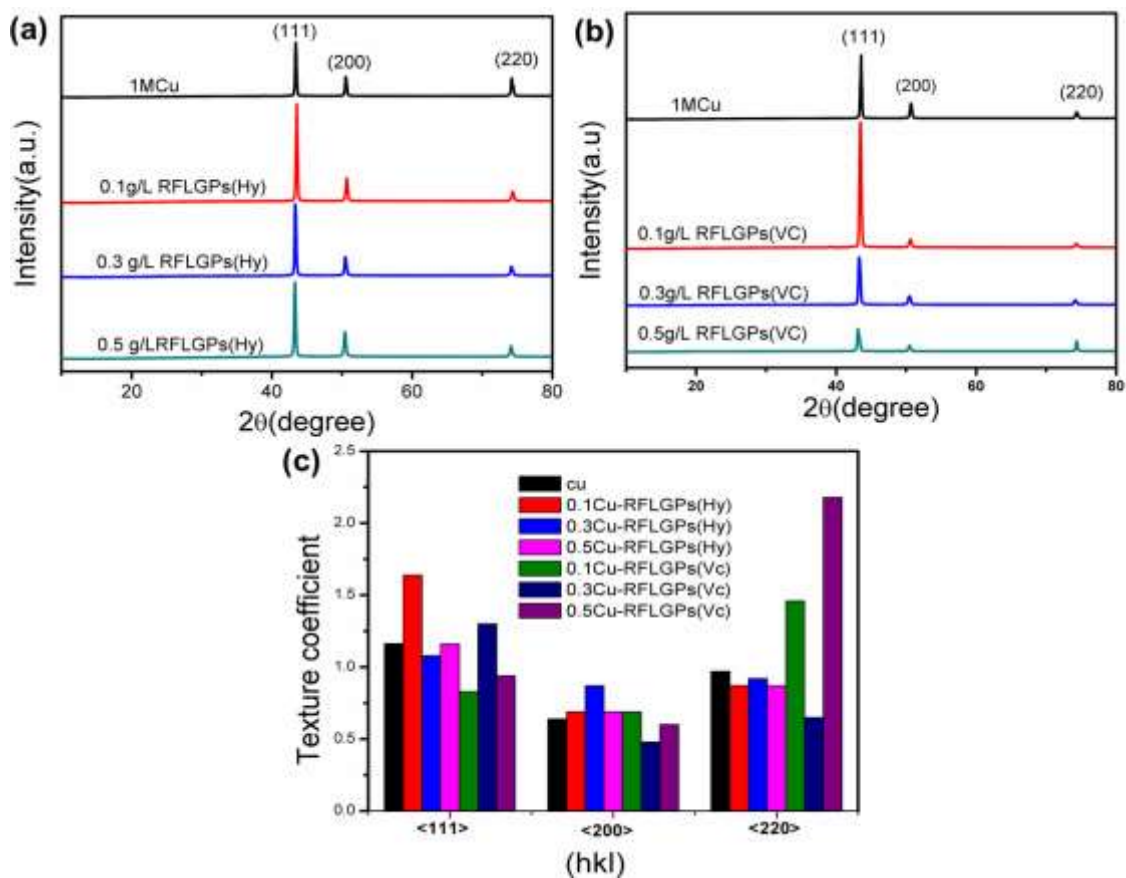


Figure 5.2.2: XRD analysis of (a) Cu-RFLGPs(Hy) composites, (b) Cu-RFLGPs(Vc) composites and (c) Texture coefficient of Cu-RFLGPs composites

The crystallite size of Cu and composites are in the range of 42–61 nm. Generally, the change in size due to incorporation of graphene may be due to the fact that it has not allowed the grain growth and has acted as a surfactant. Accordingly, the variation of dislocation density is also not significant. Furthermore, the intensity of (111) planes at 2θ

= 43.42° has been decreased with increase in RFLGPs concentrations in both Cu-RFLGPs(Hy) and Cu-RFLGPs(Vc) composite, and the intensity of peaks at $2\theta=74.23^\circ$ of the index (220) was found to be increased particularly for Cu-RFLGPs(Vc) films. The said observation indicates that there might have been textural growth of the copper metal matrix in a preferred direction i.e. (220) plane. The textural coefficient (T_c) of crystalline planes $\langle 111 \rangle$, $\langle 200 \rangle$ and $\langle 220 \rangle$ of crystal planes were calculated and the values have been reported in figure 5.2.2 (c).

Table 5.2.1 Thickness, crystallite size (D), dislocation density(δ) and the number of crystallites per unit area(N) of pure Cu, Cu-RFLGPs composite.

Sample	Thickness(um)	Crystallite size (μm)	$\delta \times 10^{15} (\text{m}^{-2})$	$N \times 10^{17} (\text{m}^{-2})$
Cu	23	42.3	5.53	3
0.1CuRFLGPs (VC)	24	33.5	5.27	1.4
0.3CuRFLGPs (Vc)	24.6	43.5	4.22	2.2
0.5CuRFLGPs (Vc)	27.5	61	6.63	5
0.1CuRFLGPs (Hy)	24.8	55.6	8.91	6.6
0.3CuRFLGPs (Hy)	26.8	48.6	2.85	1.3
0.5CuRFLGPs (Hy)	26.6	38.8	2.69	1.2

The relative texture coefficient data presented in figure 5.2.2(c) can infer the following observations: (i) the pure Cu coatings have the crystal growth in $\langle 111 \rangle$ direction and (ii) RFLGPs reinforcement in the Cu matrix has affected the crystal progression and has lead significant $\langle 200 \rangle$ and $\langle 220 \rangle$ directional growth simultaneously reducing the growth along the $\langle 111 \rangle$ direction. Also, it is interesting to note that graphene has strongly interfered with the crystal growth direction and has favored the crystal growth along $\langle 220 \rangle$. It can be due to the fact that the dispersed RFLGPs would have affected the

interfacial energy-driven phenomena in copper sulphate solution during electrodeposition which can modify the texture coefficient of electrodeposited thin films. This effect is expected to change the properties of electrodeposited Cu-RFLGPs composite films.

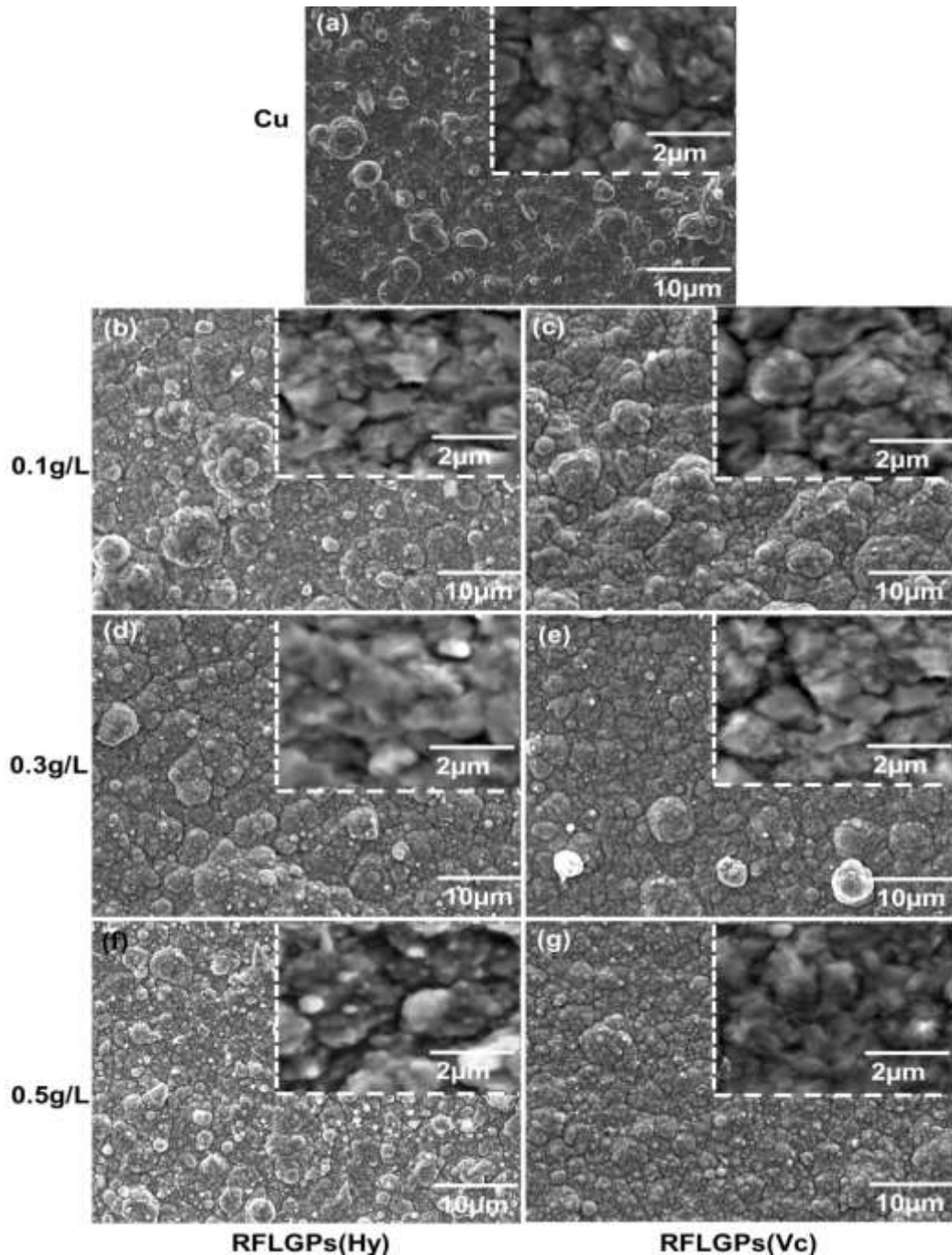


Figure 5.2.3: SEM image of (a) Cu thin film, (b) Cu-RFLGPs(Hy) and (c) Cu-RFLGPs(Vc) composite of RFLGPs concentration 0.5 g/L

Figure 5.2.3 shows the SEM images of copper thin film and Cu-RFLGPs composites with RFLGPs(Hy) and RFLGPs(Vc) content of 0.1 g/L, 0.3 g/L and 0.5 g/L respectively.

Figure 5.2.4 shows the 3D AFM images of Cu-RFLGPs(Hy) and Cu-RFLGPs(Vc) composite of RFLGPs concentration of 0.1, 0.3 and 0.5 g/L respectively. The grain size of Cu-RFLGPs(Hy) and Cu-RFLGPs(Vc) composite has been varied with an increase in graphene concentration. The composite films are also well compacted, void-free and adherent to the steel substrate. To establish further the above observation, 3D AFM images were taken. AFM analysis of Cu-RFLGPs composite was taken on some selected area of $(20 \times 20) \mu\text{m}^2$ of composites. The addition of RFLGPs reinforcement with copper matrix gives surface roughness in the range of 200-370 nm. The roughness of composite has increased with an increase in RFLGPs concentration in both cases of Cu-RFLGPs(Hy) and Cu-RFLGPs(Vc) composite. The introduction of RFLGPs as reinforcement with copper matrix might have decreased the voids of Cu-RFLGPs composite films and the interphase between reinforcement and copper matrix. However, it is difficult to find out RFLGPs on Cu-RFLGPs composite from the topography image due to a small amount of reinforcement in the Cu matrix. To confirm the presence of graphene particles, EDS and elemental mapping of Cu-RFLGPs(Hy) and Cu-RFLGPs(Vc) were done and the results are given in Figures 5.2.5- 5.2.7. The EDS spectrum analysis has been done on the $5 \mu\text{m}^2$ area of Cu-RFLGPs(Hy) and Cu-RFLGPs(Vc) composite. The EDS spectrum of Cu-RFLGPs(Hy) and Cu-RFLGPs(Vc) of RFLGPs concentration 0.5 g/L contains a strong signal of carbon (C) and copper (Cu) peaks. The carbon peak of EDS spectrum confirms the presence of RFLGPs in Cu-RFLGPs composite. The X-ray mapping of Cu-RFLGPs composite gives the signal of carbon and copper. From elemental mapping, it was observed that more number of RFLGPs was uniformly distributed with the copper matrix of Cu-RFLGPs composite.

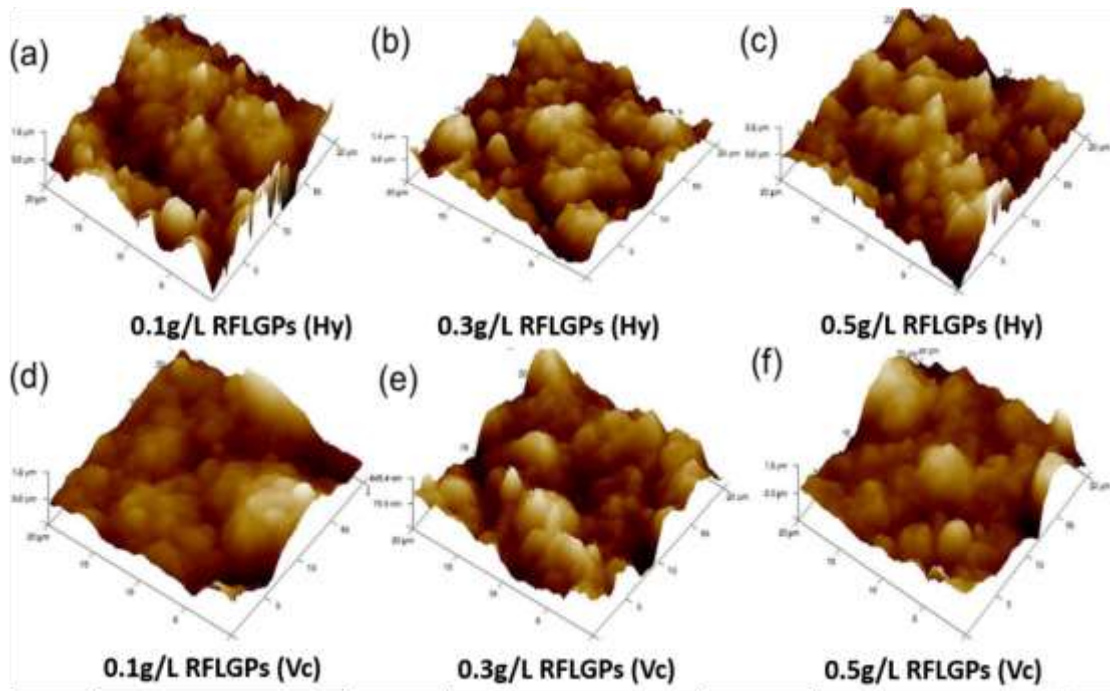


Figure 5.2.4: AFM image of Cu-RFLGPs composite with various RFLGPs concentration

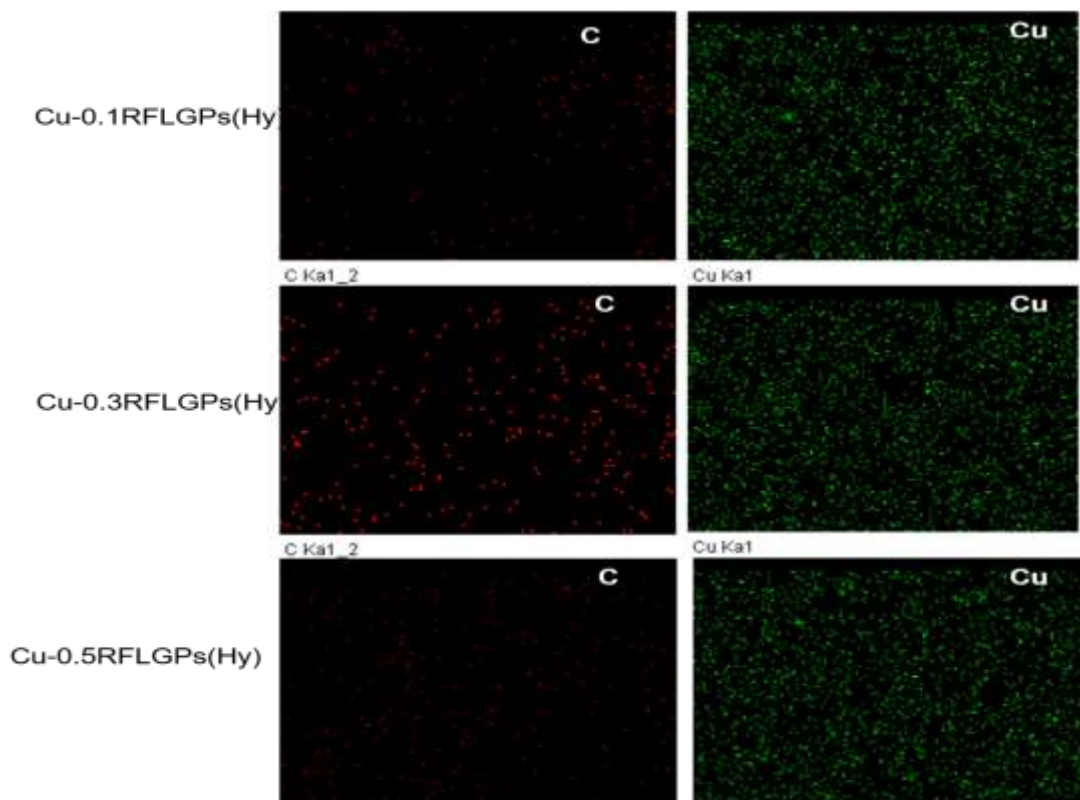


Figure 5.2.5: EDS mapping of Cu-FLGPs composite thin films of different concentrations of RFLGPs

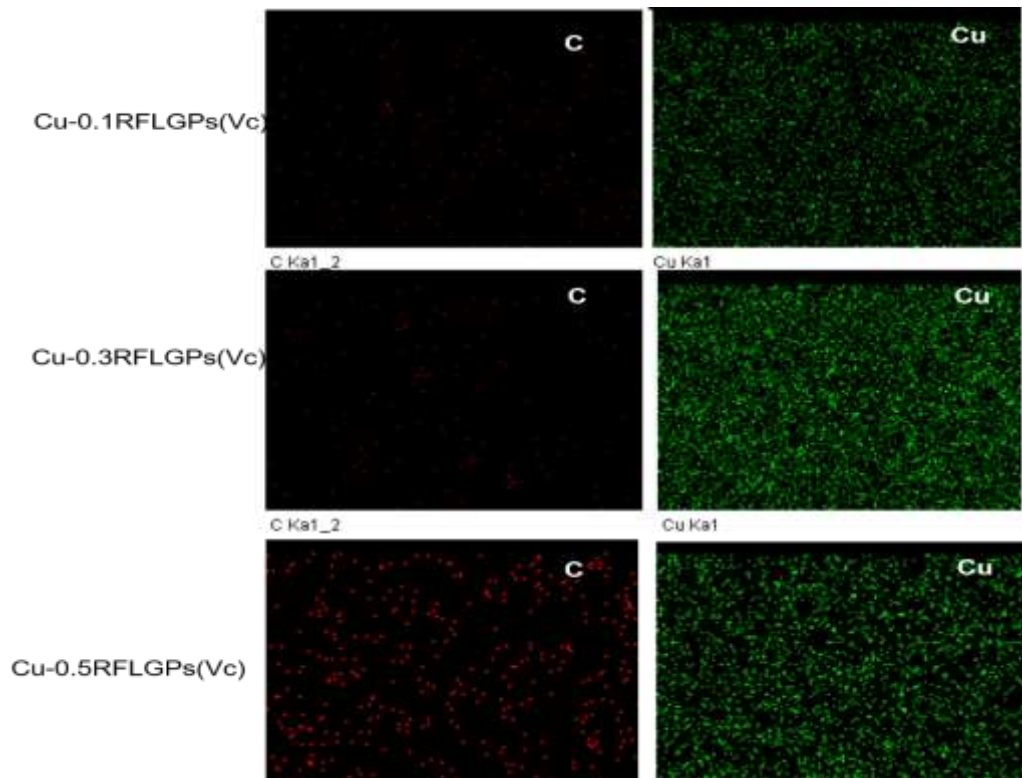


Figure 5.2.6: EDS mapping of Cu-FLGPs composite thin films of different concentrations of RFLGPs

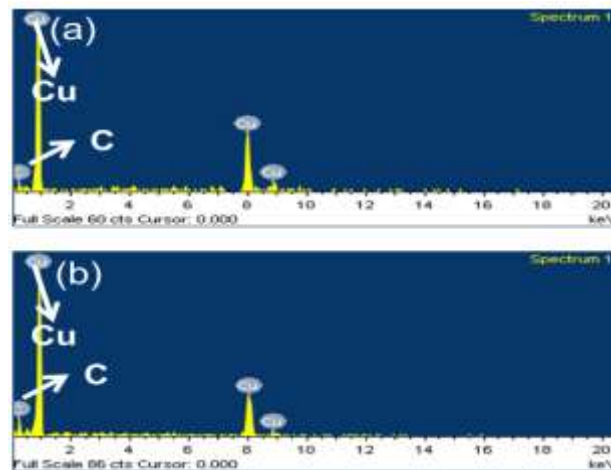


Figure 5.2.7: EDS image of (a) Cu-0.5RFLGPs(Hy) and (b) Cu-0.5RFLGPs(Vc)

Then the samples were subjected to hardness, electrical conductivity and corrosion analysis studies. The micro-hardness of electrodeposited composite films has been measured by Vickers microhardness tester. Figure 5.2.9 shows the micro-hardness of Cu and Cu-RFLGPs composite films at various RFLGPs concentrations. The hardness of electroplated copper film was 1.61 GPa which is higher than pure bulk copper and nearly matched the reported values [42]. The obtained hardness values were 1.96, 2.05 and 2.16

GPa and 1.98, 2.09 and 2.17 GPa of RFLGPs concentration of 0.1, 0.3 and 0.5 g/L for Cu-RFLGPs(Hy) and Cu-RFLGPs(Vc) composites deposited in ultrasonic conditions respectively. The hardness for 0.5 g/L RFLGPs concentration of composite showed 2.16 and 2.17 GPa as compared to the copper film of 1.61 GPa. The hardness value of composites increases with an increase in RFLGPs concentrations. The hardness value observed by the addition of 0.5 g/L RFLGPs concentrations is 38% higher as compared to the pure copper thin film. The hardness value of the composite probably has increased, due to the blocking of dislocation motion by RFLGPs during electrodeposition of Cu-RFLGPs composite. Furthermore, deposition in the presence of ultrasound might have helped the uniform distribution of RFLGPs particle and hence has improved the hardness values. To further micro-analyze the hardness values, FD analysis was carried out for all the samples and all are presented in figure 5.2.8. FD analysis is a module in AFM and the curves obtained are used to study the stiffness and micro-mechanical properties of the film. The FD analysis was studied by AFM in contact mode. The results presented in figure 5.2.8 are the average of 50 readings at different locations. In this case, the cantilever and the probe move towards the composite sample by applying a load until they touch the sample surface and then they are retracted. The interaction between the probe and the sample surface is measured by AFM software. The deflections of the probe in contact segment and the slope of the deflection line decides the mechanical properties of the composite. If the slope of the deflection line is higher, then higher will be the sensitivity factor and mechanical properties mainly stiffness of the materials under study will be higher. It can be observed that as the concentration of graphene has increased the stiffness value also has increased. Further, the slope of 0.5Cu-RFLGPs(Vc) is higher than that of 0.5Cu-RFLGPs(Hy). Hence, the stiffness of 0.5Cu-RFLGPs(Vc) composite is marginally higher than 0.5Cu-RFLGPs(Hy) composite, which is complimentary to micro-hardness analysis. The increase in stiffness may be due to the reinforcement of the two-dimensional graphene into the copper matrix which causes the arrest of the dislocation motion and restriction of grain growth during electrodeposition leading to dispersion hardening. Figure 5.2.9(b) shows the electrical resistivity of Cu and Cu-RFLGPs composites. The electrical resistivity of films shows in the range of $4.34\text{-}4.8 \times 10^{-6} \text{ }\Omega\text{-cm}$ and $3.6\text{-}4.4 \times 10^{-6} \text{ }\Omega\text{-cm}$ in Cu-RFLGPs(Hy) and Cu-RFLGPs(Vc) respectively. The prepared composite films exhibited higher electrical resistivity than the bare Cu thin films ($1.64 \times 10^{-6} \text{ }\Omega\text{-cm}$) which has also been observed in our previous work [42]. The electrical

resistivity of 0.1 g/L concentration shows higher value than other concentrations of RFLGPs in Cu-RFLGPs composite. The electrical resistivity of Cu-RFLGPs composites has also been found to be decreased with an increase in RFLGPs concentration in composite. Though the observed results may not make the composites a suitable candidate for electrical applications but maybe good towards development of a corrosion resistance coating which is presented in the next section.

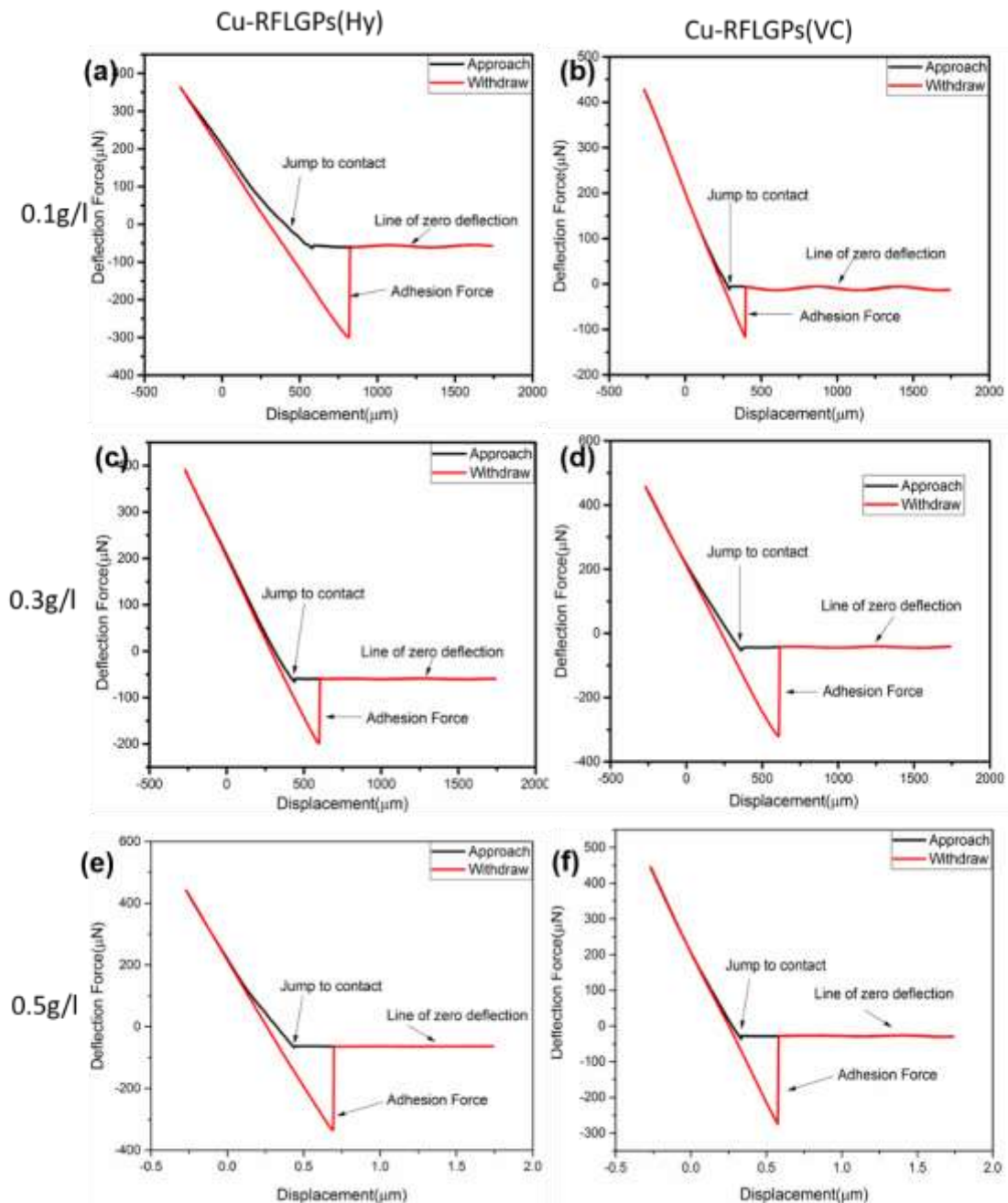


Figure 5.2.8: FD image of (a) 0.1Cu-RFLGPs(Hy), (b) 0.1Cu-RFLGPs(VC), (c) 0.3Cu-RFLGPs(Hy) and (d) 0.3Cu-RFLGPs(VC), (e) 0.5Cu-RFLGPs(Hy) and (f) 0.5Cu-RFLGPs(VC)

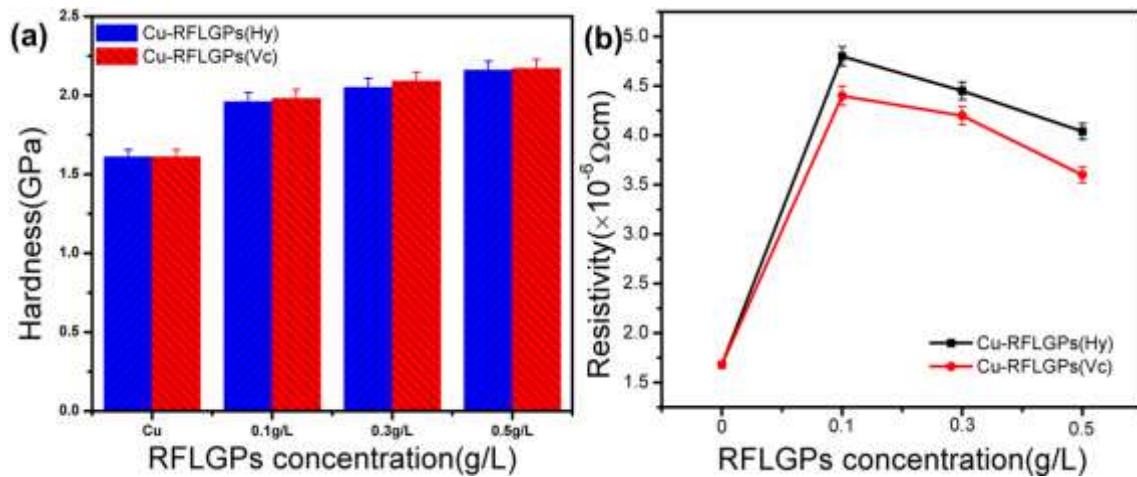


Figure 5.2.9: (a) Micro-hardness analysis of Cu-RFLGPs(Hy) and Cu-RFLGPs(Vc) composite, (b) electrical resistivity of Cu-RFLGPs(Hy) and Cu-RFLGPs(Vc)

5.2.4 Concluding remarks

In the present investigation composites with copper matrix (Cu-RFLGPs) have been synthesized by electrodeposition route with the addition of 0.1 g/L, 0.3 g/L and 0.5 g/L RFLGPs concentrations in acidic CuSO_4 solution. The RFLGPs used in the study have been produced in-house through electrochemical intercalation and exfoliation and then reduced by a chemical method using agents, hydrazine hydrate and ascorbic acid. The reduction of oxygen functional groups has been confirmed by XRD, FTIR spectroscopy and TEM. The composite films were electrodeposited at 15°C under the ultrasonic condition for the smooth surface finish as well as for uniform distribution of the graphene particles. The structural and morphological variation of the composites has been critically analyzed through various techniques. The presence of RFLGPs in Cu-RFLGPs composite was confirmed by EDS elemental mapping. The composites show a textured crystal growth towards $\langle 220 \rangle$ plane which has resulted in some significant property improvements. The reinforcements of graphene have also improved the grain distribution, morphology and hardness of the films. The RFLGPs concentration of 0.5 g/L shows 38% higher hardness as compared to the pure copper thin film.

5.3 Wear performance and nano-mechanical behaviour of sono-electroplated Cu-graphene nano-composite thin films

5.3.1 Introduction

In this section, Cu-Gr composites have been prepared by DC electrodeposition route in the presence of the ultrasonic environment. The graphene particles used in these composites were prepared by the electrochemical intercalation and exfoliation method. The structure and other property evaluations were done by the respective methodologies as explained in the next section. Then after a comprehensive analysis of wear performance of the composites has been done with an aim to explore the materials for electro-friction applications.

5.3.2 Deposition of Cu-graphene onto copper

Here the films were electroplated onto Cu instead of steel to imitate the practical application area i.e electro-friction and heat spreader etc. FLGPs and RFLGPs were dispersed in acidic copper sulfate solution added with SDS as a surfactant and was used as an electrolyte for the DC electrodeposition of Cu- FLGPs and Cu-RFLGPs nano-composite films onto copper substrates. A graphite rod was used as a counter electrode (anode) and a well-polished copper strip (substrate) as the cathode. The composite films were deposited at a temperature of 15-17 °C, this temperature was chosen from our previous work where the deposit was observed to be the best in the lot. The pH of the electrolyte was maintained at 1 by adding sulfuric acid. Three different concentrations of graphene particles (0.1, 0.3 and 0.5 g/L) were added to the electrolyte and sonicated up to 30 minutes for better dispersion. The polymeric surfactant (conc. 300 ppm for 0.5 g/L of reinforcement) was added to avoid agglomeration of graphene particles during electrodeposition. The electrodeposition was done up to 30 minutes at a potential of 2 V. Then the prepared films were analyzed for further characterization.

5.3.3 Analysis of Cu-FLGPs and Cu-RFLGPs composite films

The thickness of prepared copper, Cu- FLGPs and Cu-RFLGPs films were measured by surface profilometer and the thickness was approximately 20 µm. Figure 5.3.1 represents the XRD pattern of Cu-FLGPs and Cu-RFLGPs nano-composite with various graphene

concentrations of 0.1 g/L, 0.3 g/L and 0.5 g/L FLGPs and RFLGPs. The XRD spectra shows there were no FLGPs observed in composites which may be due to the fact that the concentration of graphene particles was apparently less to be detected by the XRD studies. Three characteristic peaks of Cu corresponding to (111), (200) and (220) planes can be observed in the XRD graphs. The intensity of Cu (111) has been found to be decreased with incorporation and increase of graphene concentration in the film. The intensity of other characteristic peaks has also been affected by graphene concentrations. To analyze it further, the texture coefficient (T_c) of planes (111), (200) and (220) of coated films were calculated by the equation 1 and the results are shown in figure 5.3.1(c).

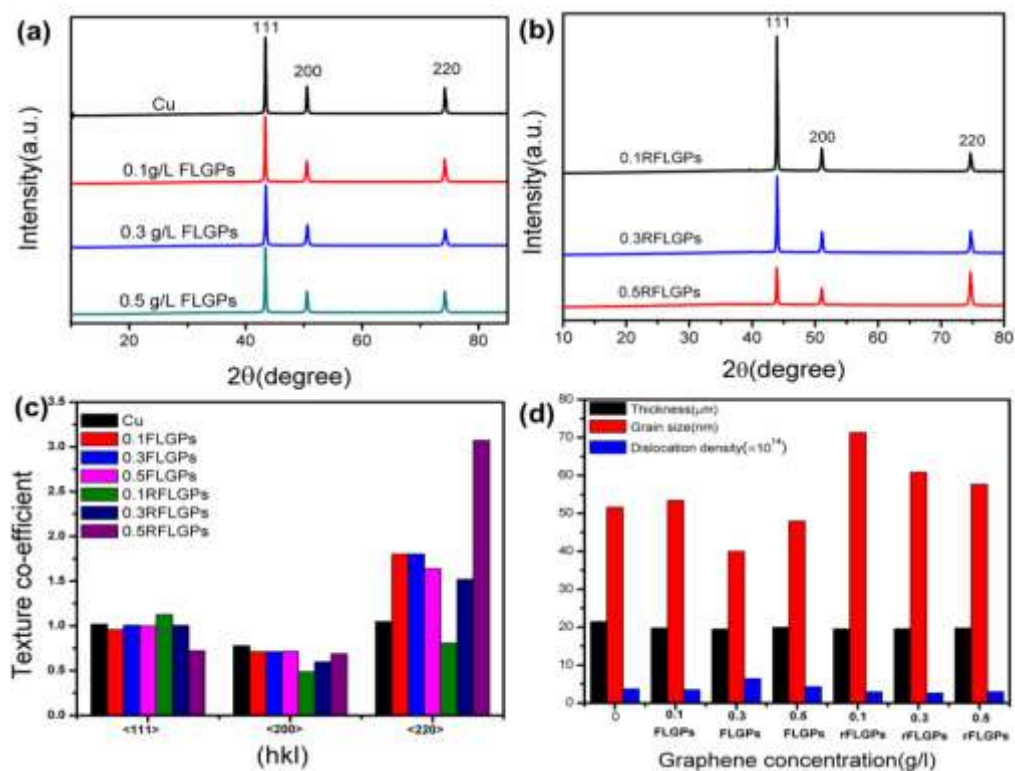


Figure 5.3.1: XRD analysis of Copper and Copper-FLGPs thin film: (a) Cu-and Cu- FLGPs films, (b) Cu-RFLGPs films, (c) Texture coefficient of films and (d) comparison of dislocation density, grain size and thickness with various graphene concentrations

The texture coefficient of coated samples shown in figure 5.3.1(c) gives the observation to quantify that the texture coefficient of $T_c(111)$ decreases and randomly oriented with an increase in graphene concentration. The $T_c(200)$ of composite films slightly decreases with an increase in graphene concentration. The $T_c(220)$ of the coated composite film increases randomly as compared to copper thin film but has increased relatively for all the composite films indicating a directional growth in (220) planes. The calculated grain size

of Cu, 0.1FLGPs, 0.3FLGPs, 0.5 FLGPs, 0.1RFLGPs, 0.3RFLGPs and 0.5RFLGPs were 51, 53, 39, 48, 71, 60, and 57 nm respectively. It can be observed that the grain size of composite films has marginally decreased with an increase in FLGPs and increased with an increase in RFLGPs concentration inserted within copper matrix.

To see the effect of reinforcement incorporation in the matrix, the dislocation density (δ) of the electrodeposited films was calculated by Williamson-Smallman relation through equation 3 and is presented in figure 5.3.1 (d). The dislocation density of composite films firstly increased with an increase in graphene concentrations and then slowly decreased.

The said observation on the effect of type of graphene particles on the phase transformations of Cu matrix could be due to the level of defects and crystallinity of the reinforcements. Because of the attached functional groups and better crystallinity, the incorporation of FLGPs might have been better than RFLGPs leading to grain refinement and hence higher dislocation density in the matrix. Figure 5.3.2 represents the SEM image of Cu-FLGPs and Cu-RFLGPs nano-composite with reinforcement concentration of 0.1, 0.3 and 0.5 g/L FLGPs and RFLGPs respectively. The SEM images of composite show triangular, pentagonal, hexagonal and leaf platelet like structures. The morphology of Cu-FLGPs composite particles was less compact than Cu-RFLGPs composites. Figure 5.3.3 represents the 3D AFM image of Cu-FLGPs and Cu-RFLGPs nano-composite with reinforcement concentration of 0.1, 0.3 and 0.5 g/L FLGPs and RFLGPs respectively. The 3D AFM image confirms that with the increase in graphene concentration the grain size of the composites has been decreased. The roughness values (obtained through AFM) of the composite were decreased as graphene concentration increased. The roughness of copper thin film was 0.635 μm . The roughness of Cu-FLGPs and Cu-RFLGPs composite films were in the range of 0.38-0.211 and 0.49 - 0.294 μm of graphene concentration (0.1, 0.3 and 0.5 g/L) respectively. The elements present in Cu-FLGPs and Cu-RFLGPs composite were characterized by high resolution XPS and EDS spectra.

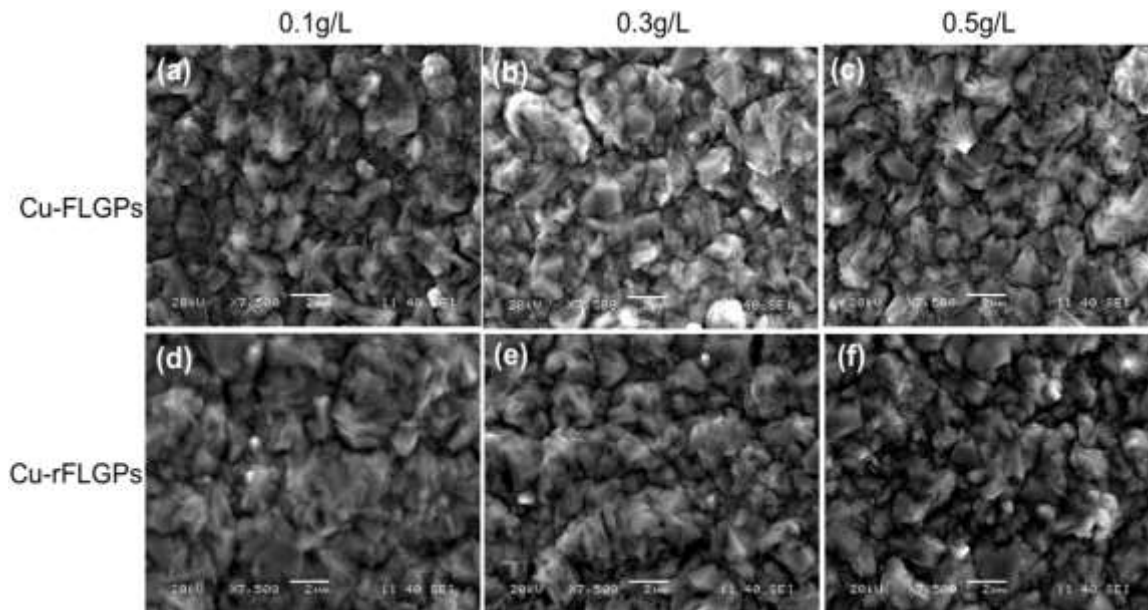


Figure 5.3.2: SEM images of Cu-FLGPs and Cu-RFLGPs at various graphene concentrations

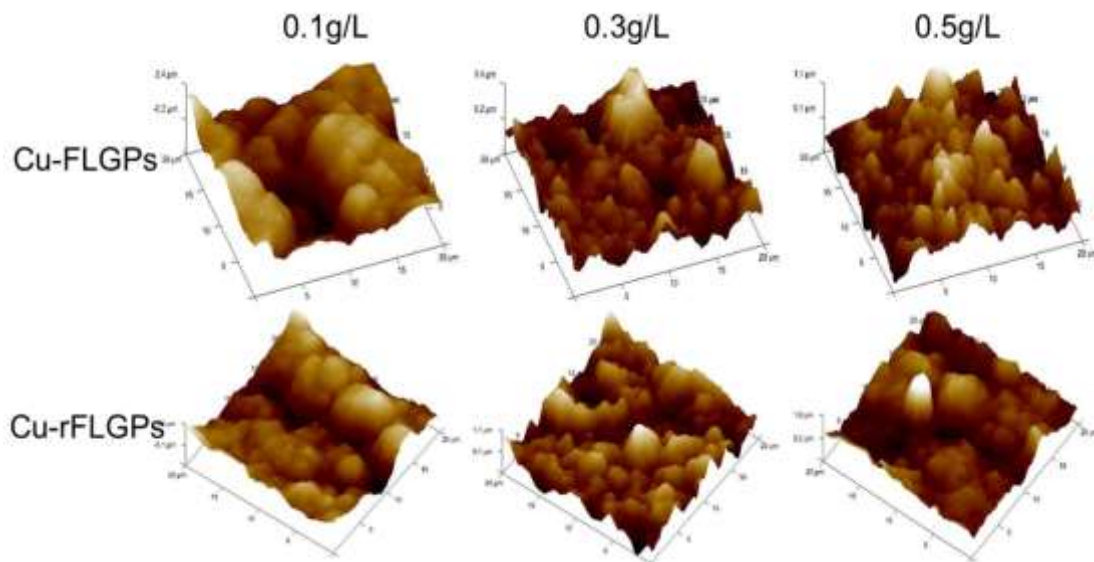


Figure 5.3.3: AFM images of Cu-FLGPs and Cu-RFLGPs at various graphene concentrations

Figure 5.3.4 shows the XPS spectra of Cu-0.5FLGPs and Cu-0.5RFLGPs composites. The C1s spectra of composite films were fitted by using Gaussian-Lorentzian peak shape with background correction. The C1s spectrum of carbon bond is located at 284.513 eV, 286.32 eV and 288.29 eV for sp² hybridized carbon atoms where C-C, C-O, and C=O bonds present. Hence the XPS spectra confirm the presence of graphene in Cu-FLGPs and Cu-RFLGPs composites. The XPS spectra of Cu shows (figure 5.3.4(c)) some oxygen functional groups present in composite which may be because of copper oxide formation due to contact with atmospheric air. In the elemental mapping by EDS (figures 5.3.5 and

5.3.6), it can be observed that carbon along with copper is present in the entire selected area of reported SEM images of composites. Both XPS and EDS elemental mapping confirm the presence of graphene in composite films. Moreover, the elemental mapping of composite gives a signal of uniform distribution of graphene particles in the copper matrix.

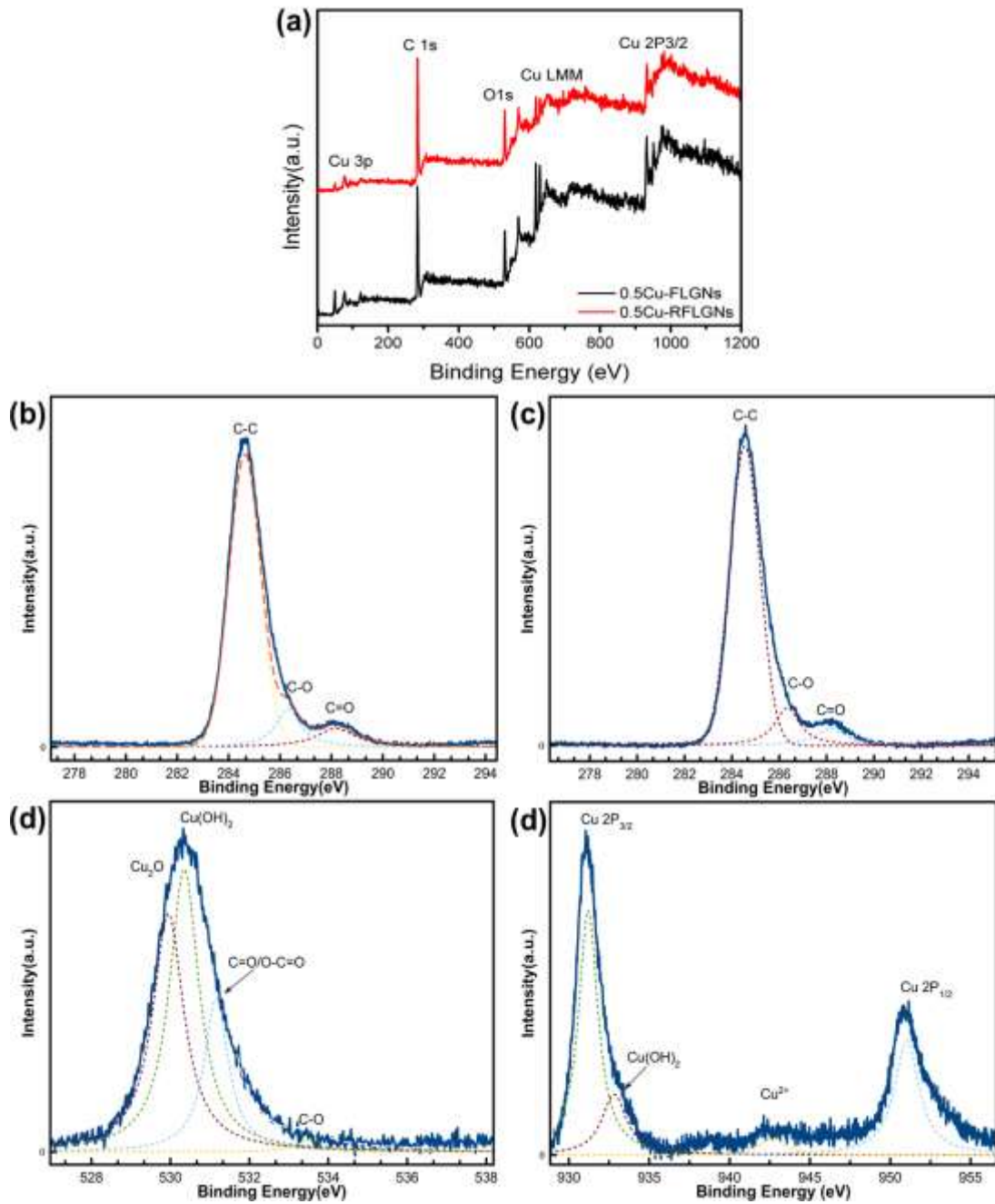


Figure 5.3.4: XPS spectra of 0.5FLGPs and 0.5RFLGPs composite films

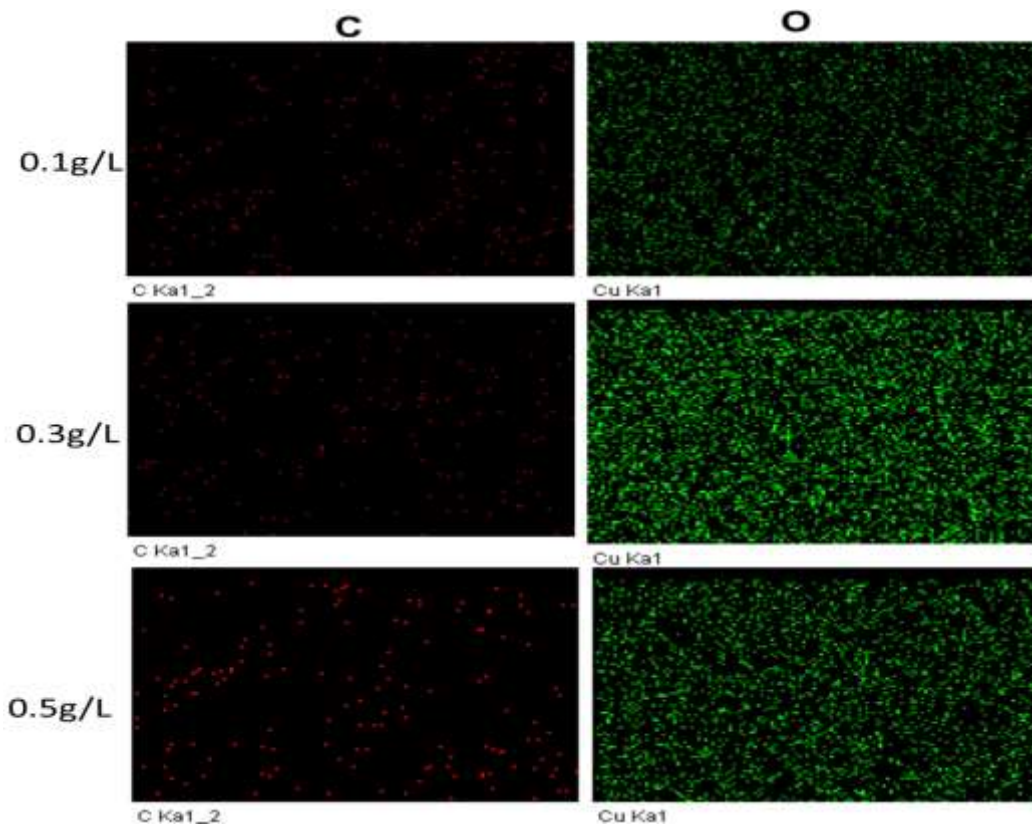


Figure 5.3.5: X-ray elemental mapping of Cu-FLGPs composite

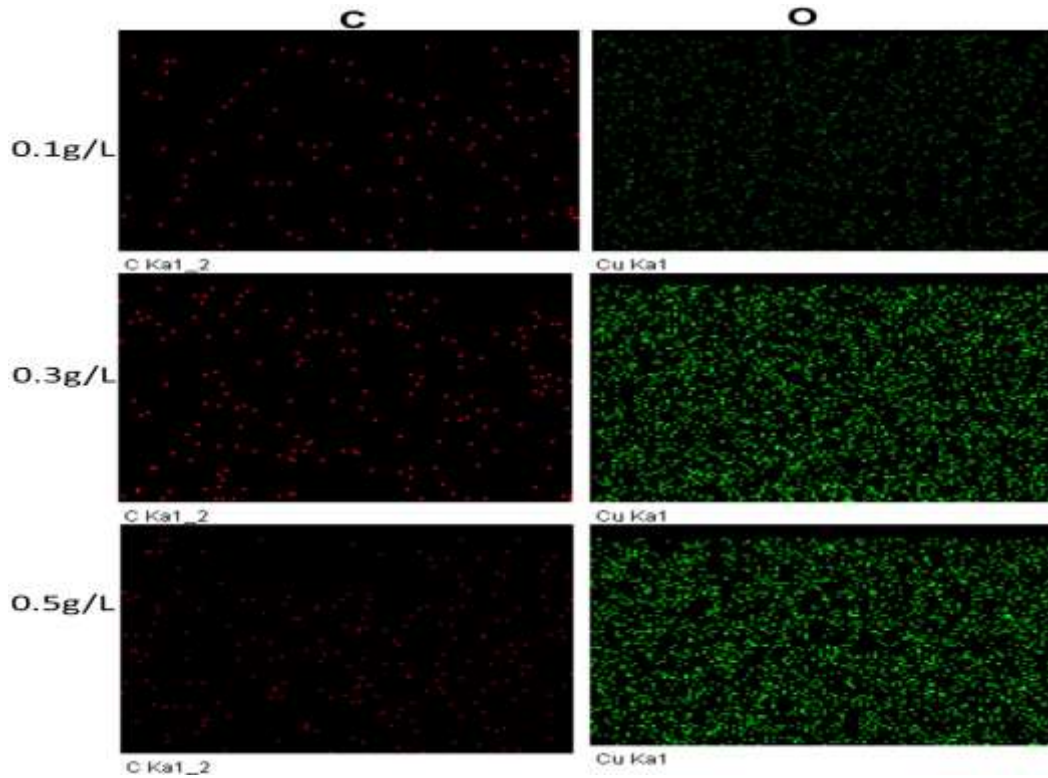


Figure 5.3.6: X-ray elemental mapping of Cu-RFLGPs composite

5.3.4 Wear behaviour of Cu-FLGPs and Cu-RFLGPs films

Wear and tear of a surface can be evaluated primarily by analyzing the following parameters: (i) width of the wear track, (ii) wear track depth, (iii) The calculated CoF and (iv) microscopic analysis of worn surfaces of the materials. Depending on the material properties, the above parameters generally vary and decide the wear type performance of the material of interest including adhesive, abrasive, diffusive, corrosive, fatigue or fretting wear.

The wear performance observed in the pure copper thin film and Cu-FLGPs and Cu-RFLGPs composites by a ball-on-plate type wear tester at room temperature are shown in figures 5.3.7 and 5.3.8.

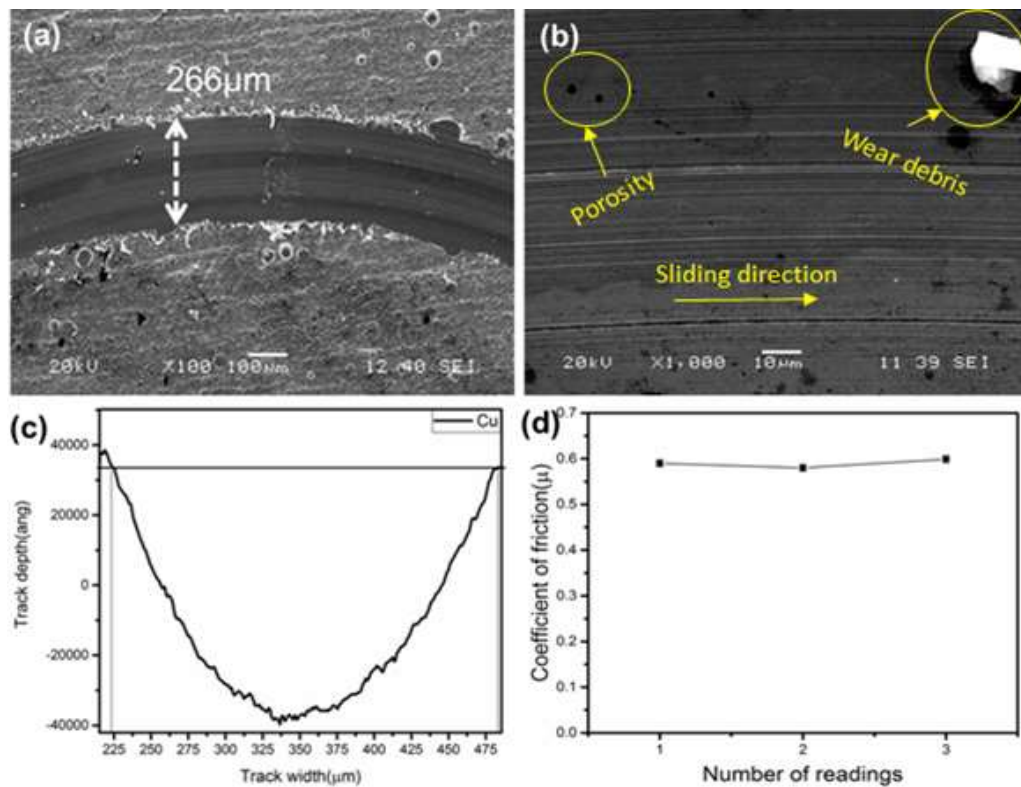


Figure 5.3.7: SEM image of (a), (b) wear track of Cu, (c) wear depth of Cu and (d) coefficient of friction of Cu

The variations of the four wear parameters for the pure electrodeposited copper film is shown in figure 5.3.7. The width and depth of the wear track at an applied load of 0.5 N are around 225 and 35 μm for pure copper which almost matches the values reported by Zhang et al.[25]. The wear depth and width were analyzed by stylus surface profilometer where a diamond stylus with compatible aspect ratio at a stylus tracking force of 2 mg

moved vertically in contact with the sample and moved laterally across the sample for the whole worn surface. The wear track and depth analysis show a smoother surface with few wear debris and microgroove marks indicating mild plastic deformation of the pure electroplated Cu. The track has only rubbing and grinding marks indicating comparatively well wear properties of the freshly deposited Cu films. The calculated CoF of 0.6 is also in the reported range of pure copper synthesized by other routes [25]. In the case of pure Cu films, the wear type was found to be of abrasive type. To compare these values and evaluate any alterations in the wear performances, the analysis was carried out for the two types of composites and the results are shown in figure 5.3.8 and Table 5.3.1. Figure 5.3.9 shows the width and depth profile of the worn region, observed by stylus surface profilometer, of the composite films containing various concentrations of graphene. The general convention is lower the wear depth and width better is the wear resistance properties of the material under study. For all the composites the wear depth varies in the range of 3–7 μm (shown in Table 5.3.1) which is quite below the coating thickness, hence a good comparison of the tribological behavior can be evaluated. It can be seen from the figure that with the increase of graphene concentration the wear depths as well as width of composites were observed to get decreased. The wear resistance of composites increased with increase in graphene concentration (0.1, 0.3 and 0.5 g/L) as reinforcement in the copper matrix. Moreover Cu-RFLGPs composites have lower wear width and varying depth as comparison to Cu-FLGPs composites hence have better wear properties. The Cu-FLGPs and Cu-RFLGPs composites of 0.5 g/L graphene concentration gave less wear depth and width as compared to pure copper thin film. The enhancement in wear resistance with increase in reinforcement loading level from 0.1 to 0.5 g/L, can be attributed to the restriction of removal of material due to strengthening and lubricating effect of graphene reinforcement in the copper matrix. Further, it has been well established that, due to its excellent tribological performance graphene is emerging as one of the novel solid lubricants. To confirm the above logic, CoF values of Cu, Cu-FLGPs and Cu-RFLGPs thin films were calculated and are shown in figure 5.3.12. The CoF values observed on Cu-FLGPs and Cu-RFLGPs were 0.18-0.4 and 0.15-0.36 respectively which is quite less than pure copper thin film (0.6). Though the graphene used in the present study consists of few layers, there was no observation of stick-slip phenomenon; rather formation of extremely adherent and continuous graphene layers at the sliding surfaces has taken place and thus reducing the CoF values. In addition to the above parameters the roughness and local microstructure of surface would affect the sliding wear

properties. The worn surfaces of Cu-RFLGPs composites are smooth; hence the wear properties are better than other films. After wear tests the micrographs of worn surfaces of composites are shown in figure 5.3.9. It can be perceived that Cu-FLGPs composites are showing only abrasive type of wear behavior and Cu-RFLGPs films are showing a combination of abrasive and adhesive wear. The worn surfaces have parallel grooves with varying shallow depth and narrow width in the direction of sliding, and the scuffing and spalling phenomena were observed in all samples. However, there are no noticeable micro-cracks that can be seen in the tracks indicating good wear properties of the composites. Yet, some wear debris can be observed in Cu-FLGPs composites. In case of Cu-RFLGPs composites the wear track appears quite smooth but delamination of copper layers yielding flake like debris can be observed. The delamination of surfaces is a hint of adhesive wear and generally involves initiation and propagation of cracks and a final fracture of the material in the near-surface region. The presence of second phase particles like graphene may create voids and other imperfections in the near-surface region during plastic deformation, hence providing favorable sites for the initiation of cracks. The crack propagation is determined by the competing effect of the hydrostatic stress (which suppresses crack propagation) and the shear stress (which promotes crack). Cracks may finally reach upto the surface thereby delaminating metal layers or flake-like wear debris.

To summarize, the major mechanism which has guided the reduced wear rate in the composite films is the presence of second phase particle i.e. the FLGPs and RFLGPs. After removal of the first layer of composite these second phase particles might lead to; (i) interlayer shearing of the graphene-based composite would act as a solid lubricant and prevent the further removal of the material, hence preventing the metal to metal contact resulting in low wear rate. (ii) Adsorption at the wear track – may lead to the formation of a surface-protective layer of graphene or graphene oxide at the interface allowing very easy shear and acts as a slider between the wear surfaces, by getting incorporated into the voids of composites improving the lubricating film continuity which would result in a reduction of CoF. The said hypothesis can be followed from the elemental analysis of worn surface as shown in figures 5.3.10 and 5.3.11. (iii) The increased induced hardness of the composite - According to Archard's wear equation, wear resistance increases with an increase in hardness [179]. Figure 5.3.12 shows the micro-hardness value of electrodeposited Cu, Cu-FLGPs and Cu-RFLGPs thin films. The hardness value of pure copper thin film was found to be around 1.56 GPa.

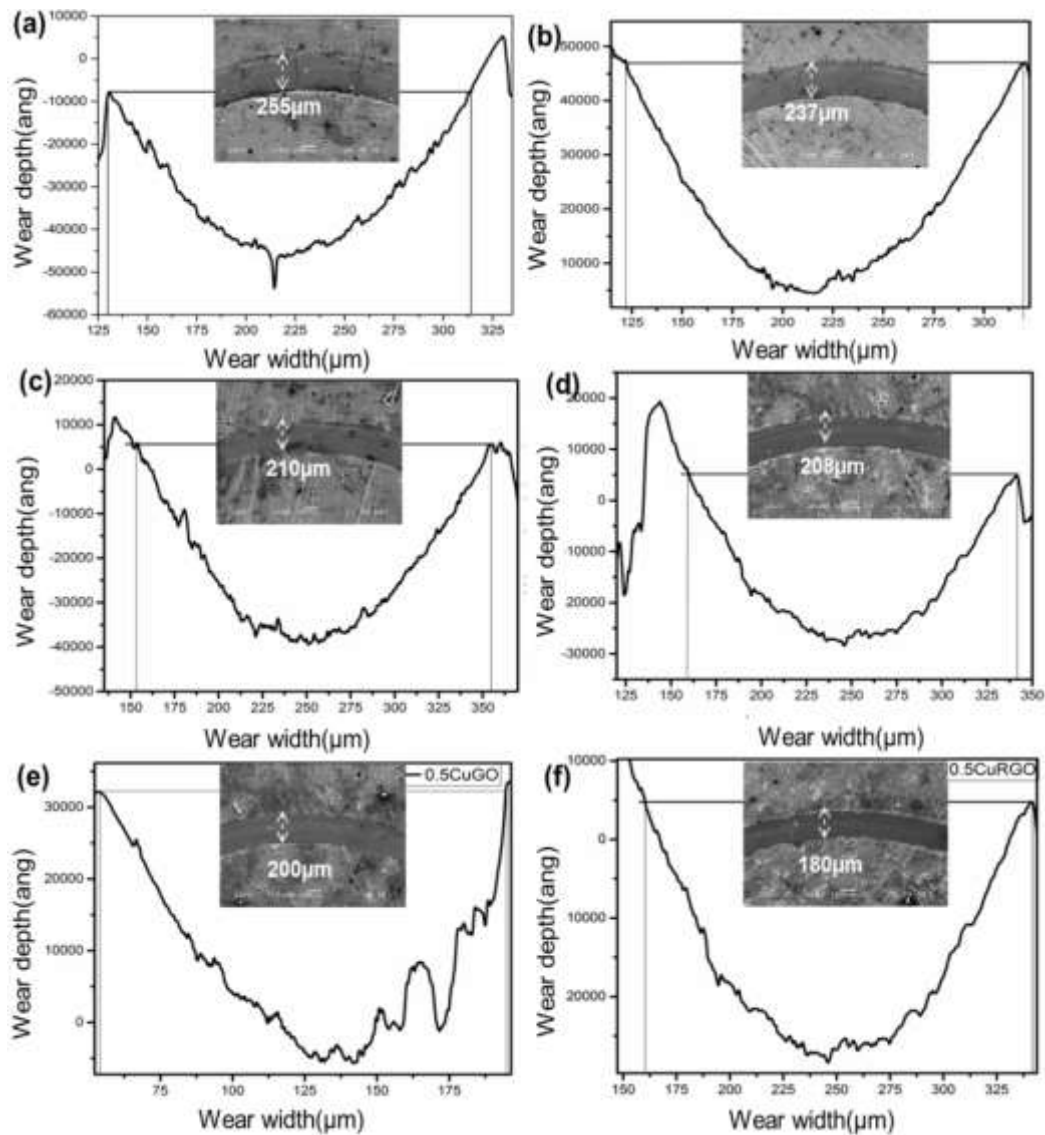


Figure 5.3.8: SEM image of wear track with wear depth and width of wear track of composites with various FLGPs concentration of (a) 0.1 g/L, (c) 0.3 g/L, (e) 0.5 g/L and RFLGPs concentration of (b) 0.1 g/L, (d) 0.3 g/L and (f) 0.5 g/L

The hardness value observed at different graphene concentrations (0.1, 0.3 and 0.5 g/L) with a copper matrix of Cu-FLGPs and Cu-RFLGPs composite are 1.76, 2.01, 2.1 and 1.77, 2.05, 2.15 GPa respectively. The graphene concentrations of 0.5 g/L on both Cu-FLGPs and Cu-RFLGPs have the highest hardness as compared to other concentrations. The hardness value increased by 38% higher than pure copper thin film deposited in the same condition. The increased hardness is mainly due to the blocking of the dislocation motion of grains as the dislocation density is not altered much by incorporating graphene (figure 5.3.1(d)). The graphene particles blocked the movement of dislocation motion in grain boundaries and its interfaces between graphene reinforcement and copper matrix

leading to the dislocation pileup at the interface of composite hereby increasing the overall strength of the composite. The impendent dislocation motion increased the critical stress to dislocation glide to the grain boundary which gave an increase in mechanical properties. Further, there could be the possibility of the presence of twin boundaries which might have changed the crystal orientation across the interface resulting in strengthening the composite by the discontinuity of slip systems. Hence the reinforcements can hinder the deformation of the matrix and hinder the propagation of the micro-cracks and wear debris during the sliding process enhancing the enduring ability to sustain the external pressure during a sliding process. (iv) Increased stiffness of the composites – stiffer the material, harder it will be to get worn. Stiffness analysis of the composites by the force-displacement studies (FD) by AFM is shown in figures 5.3.12(c) and (d) for 0.1 g/L FLGPs and RFLGPs respectively. In the force-displacement analysis, the cantilever and the probe of AFM have moved towards the sample to touch the surface and then retracted. The interaction between probe and sample is measured by the slope of the deflection segment. It means higher the slope, higher the sensitive factor and mechanical properties. The values obtained for slope vary in the range of 0.932 N/m to 1.00 N/m for the composites. It can be observed that, with the increase of the graphene concentration, the stiffness value increased. Again the increase in stiffness may be due to the reinforcement of the two-dimensional graphene into the copper matrix which causes the arrest of the dislocation motion and grain growth during electrodeposition leading to dispersion hardening. As the Cu-RFLGPs composites are stiffer than Cu-FLGPs, the wear properties are found to be better.

Table 5.3.1 Average wears depth, wears width and wear rate of composites

Sample	Average width (μm)	Depth(μm)	Wear rate ($\times 10^{-2}$ mm^3/Nm)
Cu	266	7.2	11.8
0.1FLGPs	255	6	4.7
0.3FLGPs	210	3.8	6
0.5FLGPs	200	3.5	3.8
0.1RFLGPs	237	4.2	7.2
0.3RFLGPs	208	4	4.6
0.5RFLGPs	180	3.2	6.1

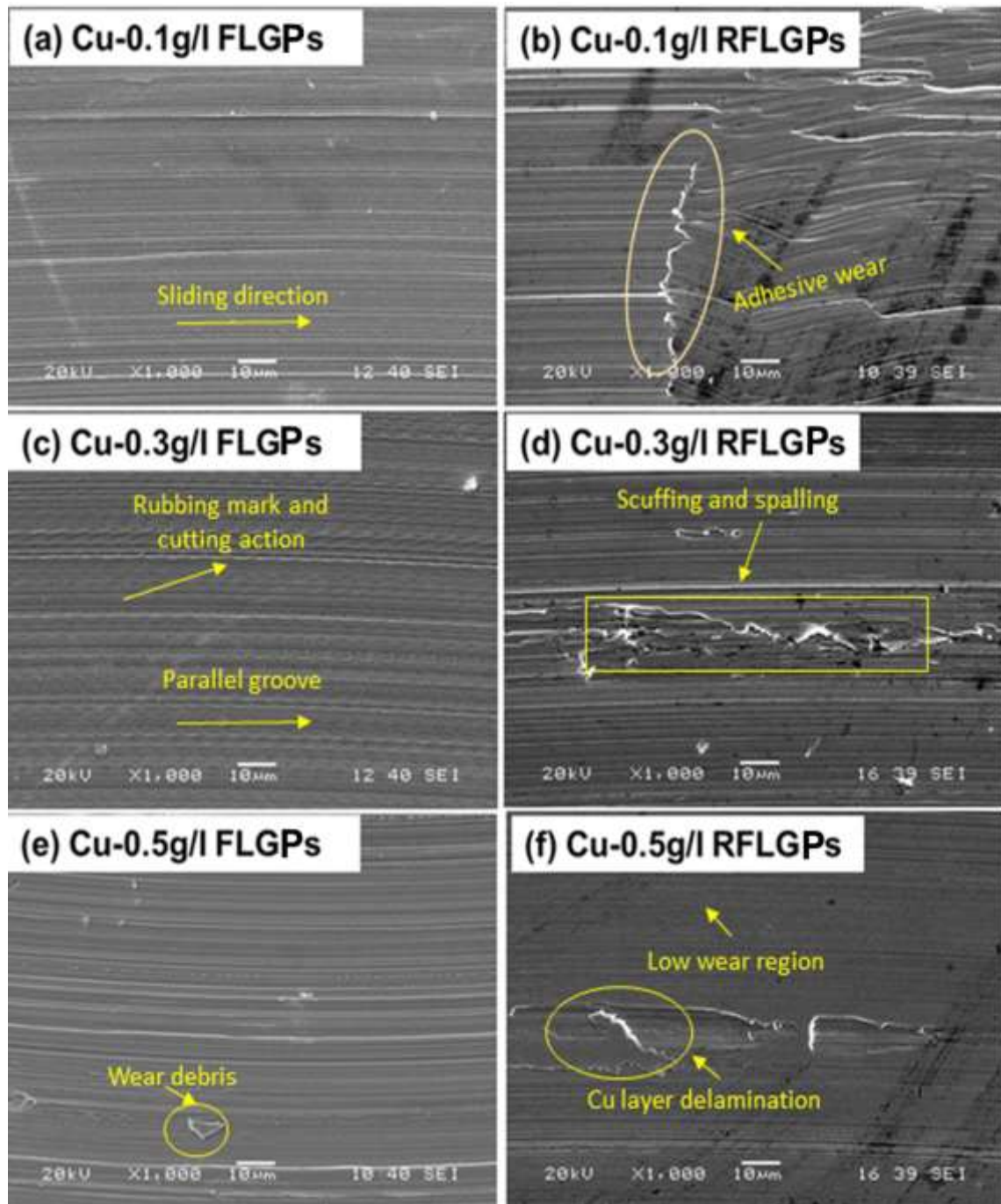


Figure 5.3.9: SEM image of worn wear track surface of composites with various FLGPs concentration of (a) 0.1 g/L, (c) 0.3 g/L, (e) 0.5 g/L and RFLGPs concentration of (b) 0.1 g/L, (d) 0.3 g/L and (f) 0.5 g/L

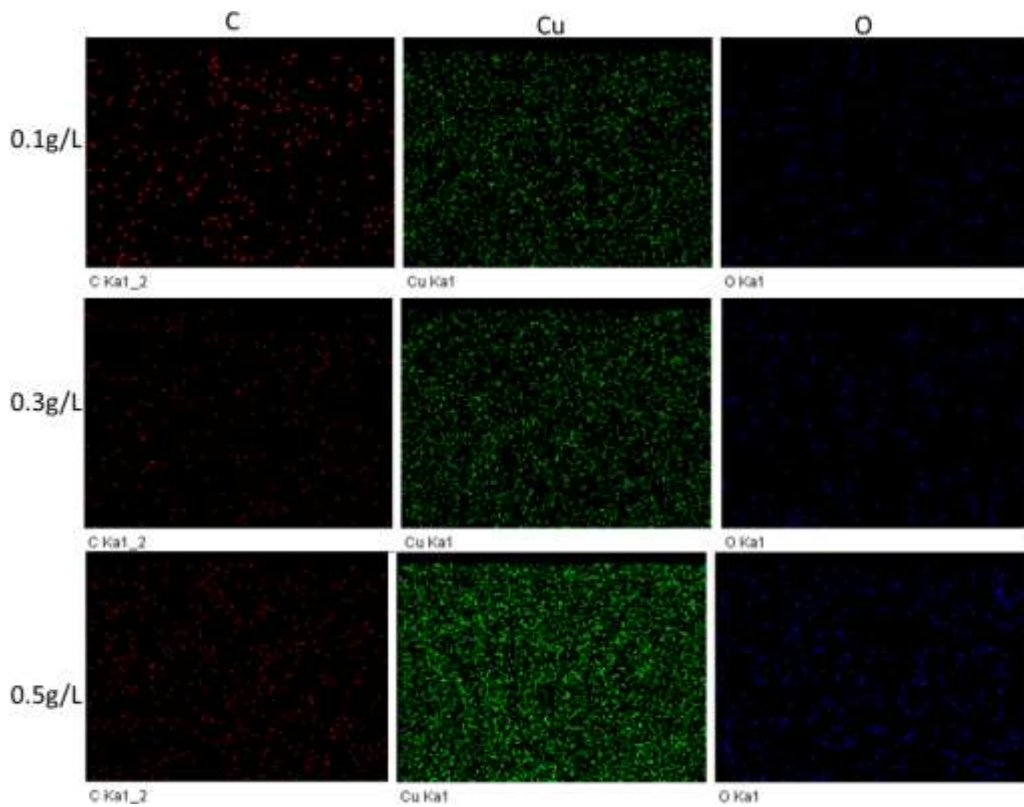


Figure 5.3.10: X-ray elemental mapping on the worn surface of composites (Cu-FLGPs)

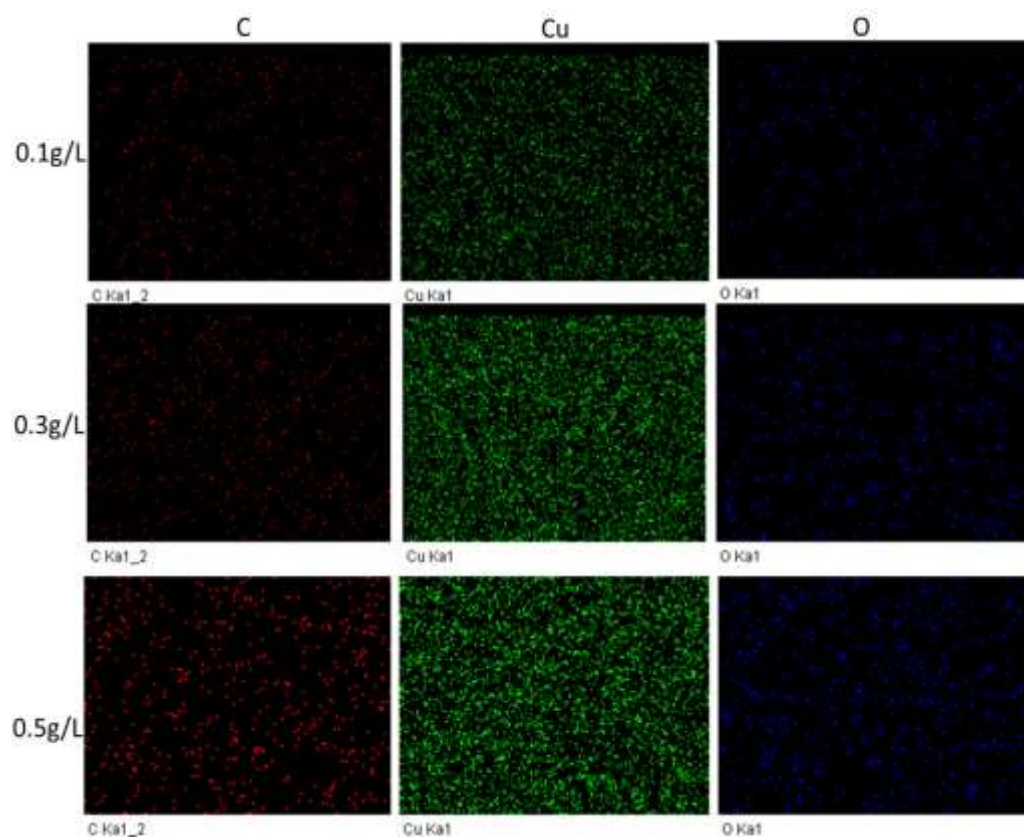


Figure 5.3.11: X-ray elemental mapping on the worn surface of composites (Cu-RFLGPs)

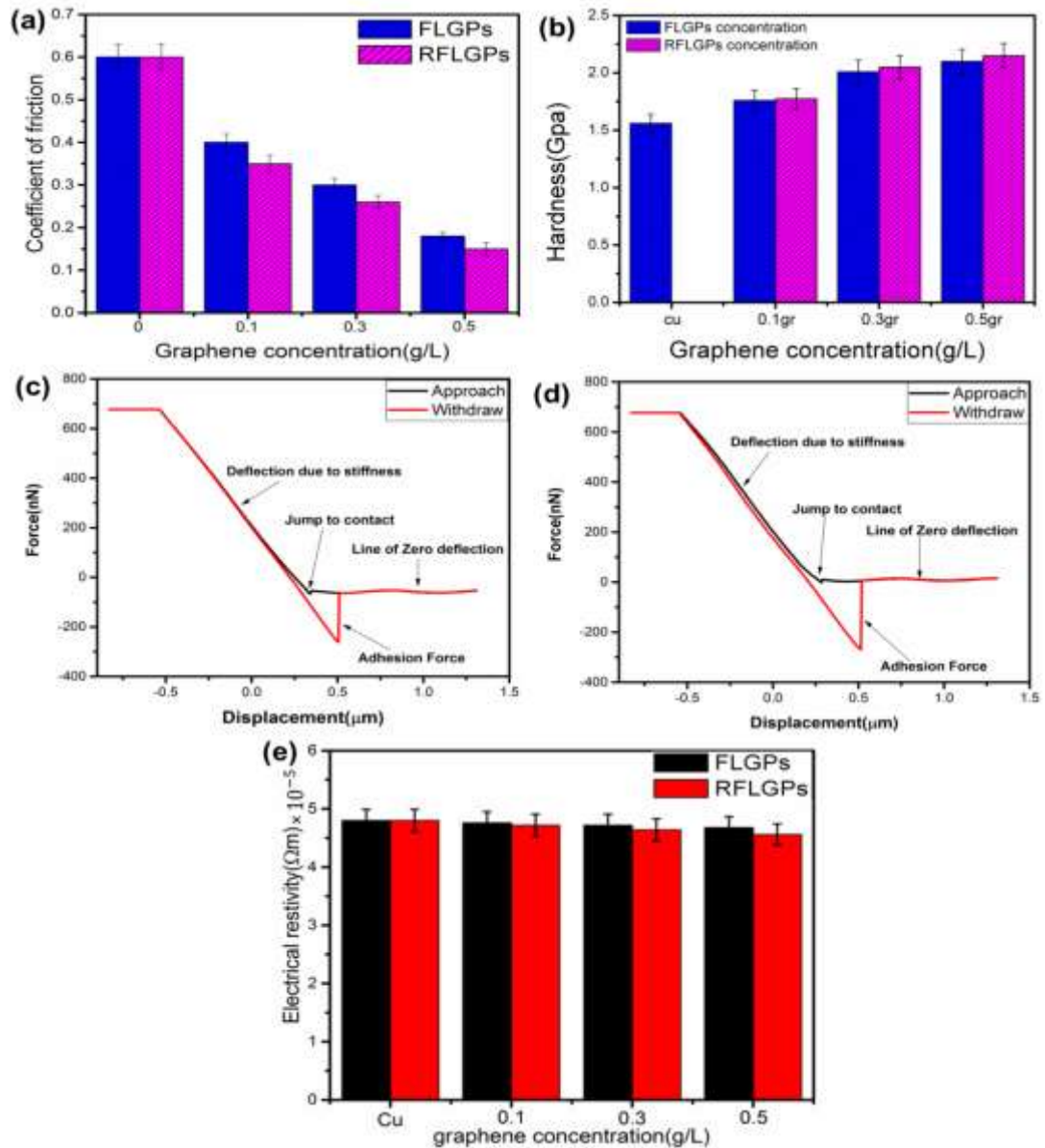


Figure 5.3.12: Coefficient of friction (a) and hardness (b) of Cu and composite films with various graphene concentrations, FD image of (c) 0.1 g/L FLGPs and (d) 0.1 g/L RFLGPs concentration and (e) Electrical resistivity of Cu, Cu-FLGPs and Cu-RFLGPs thin films

Figure 5.3.12(e) represents the electrical resistivity of Cu, Cu-FLGPs and Cu-RFLGPs films measured by four probe method. The electrical resistivity of Cu-FLGPs and Cu-RFLGPs composite films were $4.68\text{-}4.76 \times 10^{-5} \Omega\text{m}$ and $4.56\text{-}4.72 \times 10^{-5} \Omega\text{m}$ respectively, which are marginally low than pure copper ($4.8 \times 10^{-5} \Omega\text{m}$) thin film deposited in the same condition. This is due to the reduction of functional groups of FLGPs by reducing agent ascorbic acid. The electrical resistivity of the composite is higher as compared to pure copper thin films. Graphene being highly electrical conductive material due to the presence of the free ‘delocalized’ electron in each atom of its 2D hexagonal based

structure helps in carrying and passing on an electric charge. Hence in general with an increase in the graphene concentration in the composite the overall electrical conductivity was found to increase in comparison to pure copper.

5.3.5 Concluding remarks

In the present section, copper matrix nano-composites were obtained through sono-electroplating technique by incorporating graphene based reinforcements. The synthesized composite films were of 20 μm thickness and were subjected to various characterization techniques with a focus on wear performance of the films to explore the materials in electro-friction applications. Following are the salient features of the current investigation:

- An analysis of wear behavior of the films suggests that the wear mechanism is abrasive, for pure copper and Cu-FLGPs composites and a combination of abrasive and adhesive wear for Cu-RFLGPs composites. The wear width, wear depth and coefficient of friction of Cu films are 266 μm , 7.2 μm and 0.6 respectively. The values for Cu-FLGPs decreased from 255 μm , 4 μm and 0.4 to 200 μm , 3.5 μm and 0.18 whereas Cu-RFLGPs composites witnessed decreased values from 237 μm , 4.2 μm and 0.36 to 180 μm , 3.2 μm and 0.15 correspondingly. These improved wear properties are believed to be due to the combination of graphene-induced effects including interlayer shearing, the formation of a protective layer by graphene on wear surfaces that reduces the material wear and increased hardness and stiffness of the composites. Additionally, the values signposts that Cu-RFLGPs composites show better wear properties in the lot. However, in case of Cu-RFLGPs delamination of Cu layers was observed signifying the presence of harder phases and voids in the matrix for nucleation and propagation of cracks in the matrix. Apart from mechanical properties, the electrical resistivity of the sono-electroplated films was found to be improved as well and Cu-RFLGPs composites are better in this front.

Hence it can be concluded that despite the specific wear behavior, the prepared composite films can be explored for electrical and wear friction applications as a substitute for copper components.

Chapter 6

6: Electrochemical corrosion behaviour of sono-electroplated Cu-graphene nanocomposites in simulated standard and aggressive environment

6.1 Introduction

In the present metal-based civilization, corrosion of metals has been an inevitable phenomenon in domestic as well as commercial sectors. Worldwide, the cost of corrosion has seen a quantum jump to 840 Bn USD in United States of America (USA) and around INR 2 lakh crores per annum in India [180,181]. Hence protection of metals from corrosion has always been a great concern in this modern era, not only from economy point of view but also from the concerns of life threats [182]. Henceforth there have been several proactive developments to combat corrosion of metallic structures which primarily include alloying, incorporation of reinforcements, organic coatings, polymeric coatings and metallic coatings. These methods, no doubt, are expected to change the physical, thermal and electrical properties of metal in lieu of the enhanced corrosion resistance. However, amongst the lot, formations of composites with different reinforcements have been found to offer maximum corrosion protection without affecting much of the other inherent properties of the base metal.

Out of the many excellent metals in use, copper has seen many significant applications ranging from electrical to thermal and from electronics to water purification units due to its remarkable electrical, thermal, anti-corrosion and anti-fouling properties. However, the domain of its application has not experienced remarkable progress as it is prone to corrosion media, specifically in seawater applications, leading to pitting corrosion. To overcome this limitation, even though Cu has been coated with various polymer layers and has been explored in various applications [13,14], but the outcome shows that the coating would affect the thermal as well as the electrical conductivity of the base Cu. Hence composite formation does seem to be the best option left out for property alteration.

In recent years, research has been focused on the use of graphene, either as a coating or as reinforcement for corrosion protection of metals like Al, Cu, Ni and steel [15–23] due to its excellent anti-corrosion properties and chemical inertness. Uniform and single-layer graphene grown on a metal substrate has given enhanced corrosion resistance as compared to pure metals. But, several issues have cropped up, which have prevented the use of graphene as a corrosion protection material of metals. Among several reasons, one such reason is the defects (cracks and grain boundary) of graphene particles which can attract corrosion media and affect the metal substrates. This has resulted in limited progress in use

of bare graphene coating on metals for corrosion protection. Hence, gradually research focused on graphene base-metal matrix composite to protect metals from corrosion. Graphene particles introduced as reinforcement in metal matrices to produce composites such as Gr-Cr, Gr-Ni, Gr-Sn, Gr-Mg, Gr-Zn and Gr-Cu, have enhanced anti-corrosion properties as compared to the base material [27–34]. However, the main drawback of graphene to prepare Cu-Gr composite is its uniform dispersion and interfacial bonding with the copper matrix. Few studies have been reported about Cu-Gr composite in the field of corrosion protection of steel in 3.5% NaCl solution. Kamboj et al. have reported corrosion behavior of nano-crystalline Cu-Gr composite and steel metal [34, 37]. In the concerned study graphene particles were synthesized by electrochemical exfoliation route and Cu-Gr composites had been fabricated by electrodeposition route. The corrosion rate of uncoated mild steel, copper and Cu-Gr composite are 135.15, 57.53 and 32.26 mm/year respectively. The results indicate that corrosion resistance is 4 times higher than mild steel and 1.7 times higher than pure copper film. There are few more such attempts, which stimulate an urge to deepen the research in the coveted area. Hence a need of extensive study on the corrosion behavior of these composites is required to establish the emergence of graphene as corrosion resistant materials.

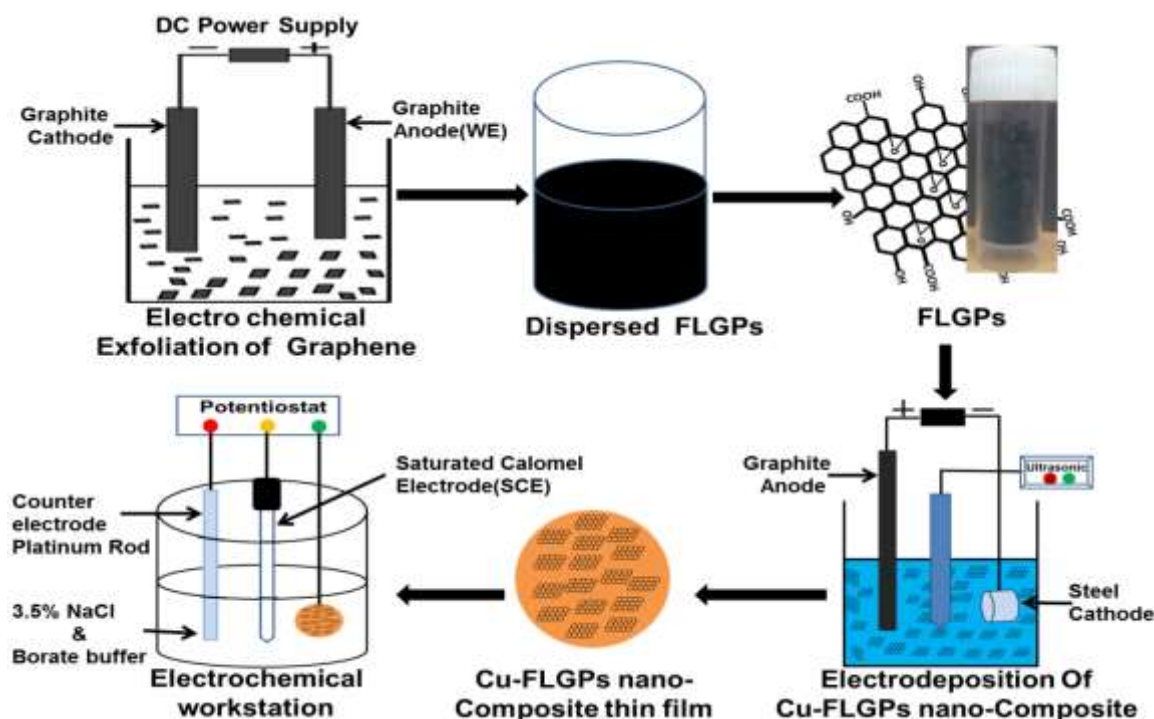


Figure 6.1: Schematic image of synthesis of graphene particles, electrodeposition of Cu-FLGPs composite and Corrosion setup of Cu-FLGPs composite

In this section, in-house synthesized graphene particles have been used to synthesize the composite films and the corrosion behavior of the films have been studied along with other physico-chemical properties.

6.2 Experimental details

6.2.1 Electrodeposition of Copper-FLGPs nanocomposite films

The graphene particles were synthesized by the electrochemical exfoliation route. The prepared FLGPs and RFLGPs were introduced as reinforcement in the copper matrix to synthesize Cu-FLGPs and Cu-RFLGPs composite on to polished O₂ free steel substrate of area 0.5 mm² by electrodeposition route in presence of an ultrasonic environment. Ultrasonic stirring was carried out during electrodeposition for uniform dispersion of FLGPs/ RFLGPs with copper matrix. The FLGPs/ RFLGPs of different concentrations of 0.1, 0.3 and 0.5 g/L were added with 1M CuSO₄.5H₂O at a maintained pH of 1 by adding H₂SO₄ with double distilled water. A polymeric surfactant of SDS (30 ppm for 0.5 g/L FLGPs) was added into the electrolyte to avoid agglomeration of FLGPs during electrodeposition. The electrodeposition was done with a potential of 2 V up to 20 minutes at a temperature of 15-17 °C by using a water jacket [42,183]. After finishing electrodeposition the films were washed with distilled water and dried. The prepared films were peeled from the steel substrate for further characterization and corrosion study. The composite films were tested in standard borate buffer, Cl⁻¹ ion modified buffer and 3.5% sodium chloride solutions to study the general and pitting corrosion behavior. The scheme of reaction is shown in figure 6.23.

6.2.2 Corrosion and other characterization techniques:

The potentiodynamic polarization testing was performed by using a standard three-electrode cell with a potentiostat/galvanostat system (Corr test). The electrodeposited Cu-FLGPs nano-composite film with an exposed area 0.6 cm² was used as working electrode, platinum (Pt) as the counter electrode and saturated calomel electrode (SCE) as a reference electrode. The corrosion testing was carried out with an aqueous solution of standard borate buffer solution of pH=8.4, standard borate buffer solution with 3.5% NaCl of pH=8 and 3.5% NaCl solution of pH=7.0 at ambient temperature. Then open circuit potential (OCP) was done up to 60 minutes to obtain a potential. Linear sweep

voltammetry (LSV) test was carried out in the potential range of -0.4 to 0.4 V at a scan rate of 0.1667 mV/s and 5 mV/s. The corrosion potential and current were measured from Potentio-dynamic curves. The electrochemical impedance spectroscopy (EIS) measurements were carried out at the corrosion potential or OCP over a frequency range of 0.01 Hz to 10000 Hz with AC amplitude of 10 mV. The scheme of the materials and methods is shown in figure 6.1.

6.3 Results and discussion

Then after the electrodeposited thin films prepared both in presence and absence of ultrasound were analyzed by a profilometer, XRD and SEM with EDS spectra and AFM. These analyzed results have been given in section 5.1. The thickness of Cu and composite films was found to be around $\pm 20 \mu\text{m}$.

6.3.1 Electrochemical corrosion studies

The electrochemical studies of Cu and Cu-FLGPs samples were carried out as per the ASTM G5-94 in the solutions.

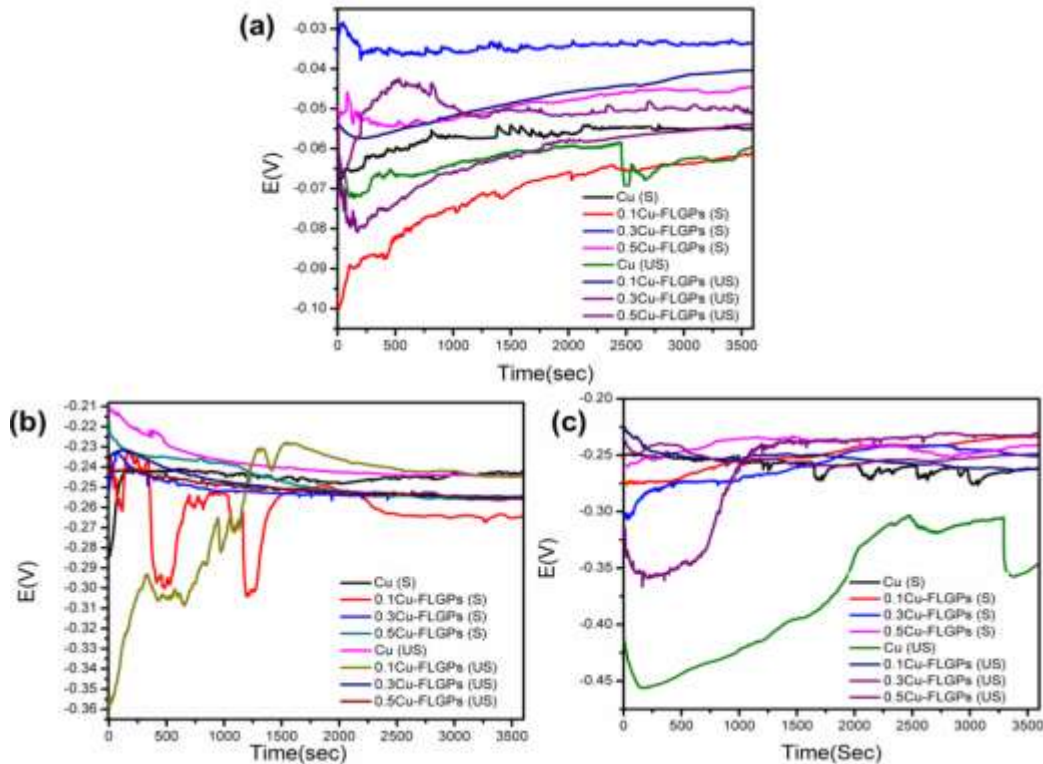


Figure 6.2: OCP of Cu-FLGPs composites deposited in silent and ultrasonic conditions in (a) borate buffer, (b) borate with 3.5% NaCl and (c) 3.5% NaCl solution

Borate buffer testing will be equivalent to the form of general/uniform type and 3.5% NaCl solution for pitting corrosion as Cl^- ions are the main factors which contribute towards breakdown of the passive layers formed on Cu surfaces. Hence the aim of the present section is to analyze whether the addition of graphene has altered both the general and pitting corrosion behavior of copper. Further, it is to be noted that the analysis of corrosion data in stable and potentiodynamic polarization are different. Modern theory of aqueous corrosion is based on the kinetics of the process as presented by Butler-Volmer relation (in equation 6.1) on the basis of mixed potential theory at stable polarization condition:

$$i = i_{corr} \left\{ \exp \left[\frac{2.303(E - E_{corr})}{\beta_a} \right] - \exp \left[\frac{-2.303(E - E_{corr})}{\beta_c} \right] \right\} \quad (6.1)$$

Where E is applied potential to polarize the system undergoing corrosion, i is the external current density, E_{corr} is corrosion potential, I_{corr} is corrosion current density, β_a is anodic Tafel slope and β_c is cathodic Tafel slope. When E is far away from E_{corr} , the relationship is presented by Tafel law and is presented below in equation 6.2:

$$E = a \pm b \log|i| \quad (6.2)$$

From the equation the corrosion current density can be determined by the method of Tafel extrapolation. For corrosion experiments, generally the corrosion parameters are first extracted at stable polarization condition i.e. open circuit potential (OCP) determination. Then potentiodynamic polarization are done at suitable scan rates. In this case, corrosion parameters are determined based on the assumption that the current response is coming from only corrosion phenomena. However, in a real situation there will always be interference of charging current during the potentiodynamic scan. Hence, the corrosion parameters thus extracted has to be carefully handled to give realistic information of corrosion phenomena. One approach to avoid the error is to run the scan at a very low rate i.e. 0.1667 mV/s. In the present study OCP as well as potentiodynamic scans have been performed both at high and low scan rates to evaluate the potential and current density values at meeting point of cathodic and anodic polarization curves which are leveled as E_0 and I_0 . These values are potentiodynamic corrosion values which is different from stable polarization value i.e. potential at zero current density. Accordingly, tests have been carried out to get the stable as well as potentiodynamic values for comparison.

To determine the stable polarization values, tests were done to measure the potential at OCP (E_{op}) after stabilization for 2 h. The E_{op} of the film gives the equilibrium potential of the corrosion system and has been presented in figure 6.2. The stable E_{op} values were in the range of -0.22 to -0.42 V for different films. Figure 6.3 shows the polarization curve of composite samples deposited in both silent and ultrasonic conditions and tested in borate buffer, borate buffer with 3.5% NaCl as well as in 3.5% NaCl solution at a scan rate 0.1667 mV/s. The potentiodynamic polarization curves have the typical shape with anodic and cathodic wings, including three distinct regions; (i) corrosion, (ii) passivation region and (iii) film dissolution. The effect of solution type, graphene concentration and ultrasound on the corrosion behavior of samples can be observed clearly.

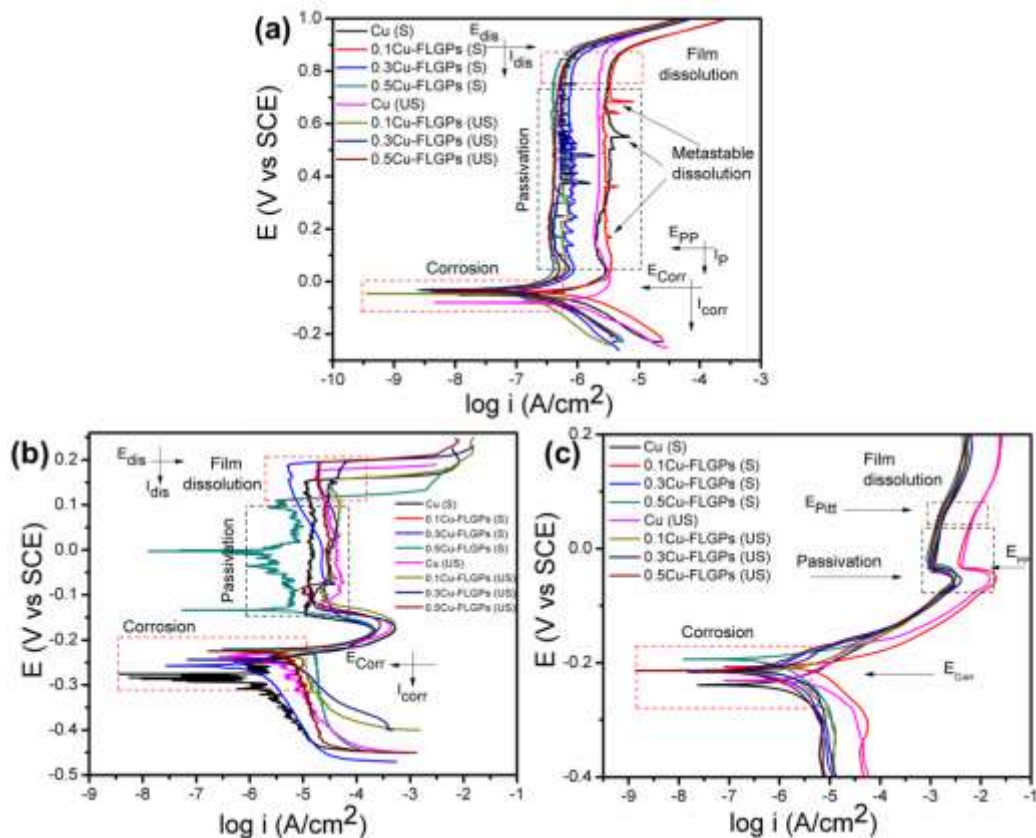


Figure 6.3: Potentiodynamic polarization curves of Cu-FLGPs composites deposited in silent and ultrasonic conditions in (a) borate buffer, (b) borate buffer with 3.5% NaCl and (c) 3.5% NaCl solution at a scan rate 0.1667 mV/s

The corrosion parameters i.e. potentiodynamic corrosion potential (E_0) and current density (I_0) extracted from the corrosion analysis are shown in Tables 6.1-6.3 along with other parameters, obtained from individual curve fitting of Potentiodynamic plots, such as Tafel constants, corrosion current and corrosion rate.

In borate buffer solutions, it can be observed that corrosion potential is almost invariable and noble as compared to the other two solutions. Further, the passivation region has been well developed and elongated. The passive films formed onto composite films prepared in ultrasonic conditions are quite stable and metastable dissolution of other films has been observed during the testing. Moreover, passivation current is quite less in composite films. This may indicate that graphene has been uniformly distributed in the composite films due to application of ultrasound which might have improved the anti-corrosion properties. Then the studies were carried out in NaCl modified buffer as well as in 3.5% NaCl to imitate the real operating conditions. The effect can readily be observed in these baths. The corrosion potential values have become active as compared to borate buffer and the values are nobler with increase in graphene concentration in both silent and sonic conditioned films. The passivation regions have been truncated in 3.5% NaCl borate buffer. Again composite films are showing better passivation properties. In the tests, proper pitting can be observed. The pitting potentials of sonicated composite films are nobler than films prepared in silent conditions. Films tested in 3.5% NaCl show quite active corrosion potentials as compared to other two solutions. However, composite films do show very feeble passivation which we are addressing as pseudo-passivation in the current study. To sum up the above observations: In general, the corrosion potential (E_0) of the process would indicate the corrosion tendency of the samples under observation. Nobler the potential is, lesser is the tendency of corrosion. Hence resistance of composite material has been increased with an increase in graphene concentration as compared to copper film. The corrosion rates of prepared samples were then calculated following the general equation (equation 6.3) of rate expression in mm/year.

$$CR = 0.00327 \frac{ai}{nD} \left(in \frac{mm}{yr} \right) \quad (6.3)$$

Where a is the atomic weight in gram, i is the current density in $\mu\text{A}/\text{cm}^2$, n is the number of electrons involved and D is the density in g/cm^3 . Corrosion rates are quite less in borate buffer solution. The graphene concentration of 0.5 g/L Cu-FLGPs composite of silent and sonicate conditions shows the corrosion rate of 0.004 mm/yr and 0.002 mm/yr, as compared to pure copper of 0.018 mm/yr in both the conditions.

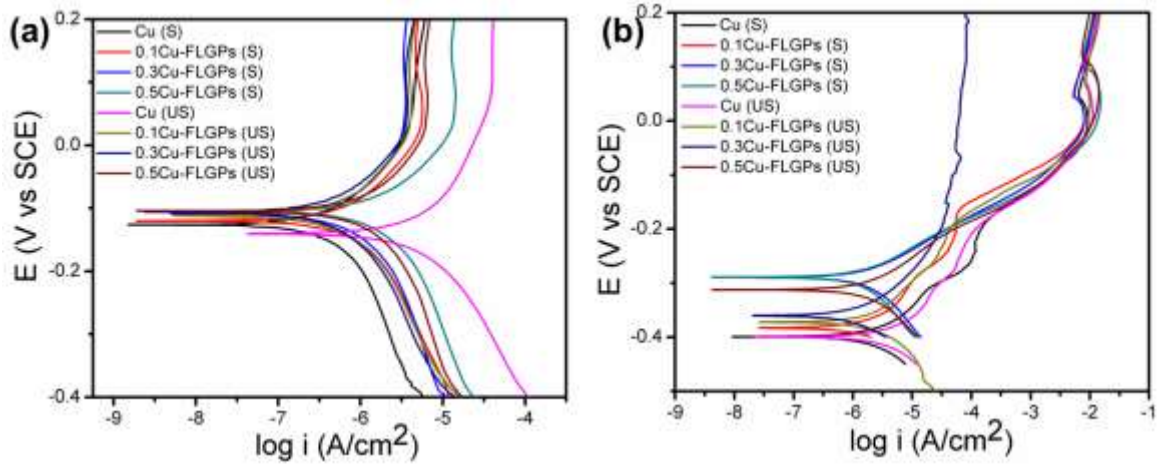


Figure 6.4: Potentio-dynamic polarization curves of Cu-FLGPs composites deposited in silent and ultrasonic conditions in (a) borate buffer, (b) 3.5% NaCl solution at a scan rate 5 mV/s

Similarly, the composites show decreased corrosion rates in other solutions which can be followed by Tables 6.1-6.3. The corrosion rate of 0.5 g/L Cu-FLGPs composite prepared in silent and sonicate condition are 50% and 59% less than pure copper. The above corrosion rate of composites can further be validated with the co-relation of corrosion rate, Tafel constants and potential as per the Tafel law presented in following equation 6.4.

$$\eta_{cor a} = \beta_{cor a} \log \frac{i_{cor a}}{i_0} \quad (6.4)$$

Where $\eta_{cor a}$ and $\beta_{cor a}$ are either cathodic or anodic over potential and Tafel constants, $i_{cor a}$ is either applied cathodic or anodic current and i_0 is the exchange current density at E_{corr} , $\eta_c = \eta_a$. The corrosion tendency of a system can be dependent on the observed Tafel constants. The variation of Tafel constants of corrosion of Cu-FLGPs composites with varying concentrations of FLGPs can be observed in Tables 6.1-6.3. Unfortunately, the Tafel constants are not varying systematically as that of corrosion potential and currents for the films. Hence a definite conclusion may not be drawn from Tafel constant values however from other results it can be concluded that both the thermodynamic and kinetics factors complement each other with the fact that increase in FLGPs concentration has generally improved the corrosion resistance of the composite films. The above studies have also been done at a scan rate of 5 mV/s to investigate the dominance of kinetic factors if any. The results show similar behavior as that of low scan rate studies and have been presented in figure 6.4 and Tables 6.4 and 6.5.

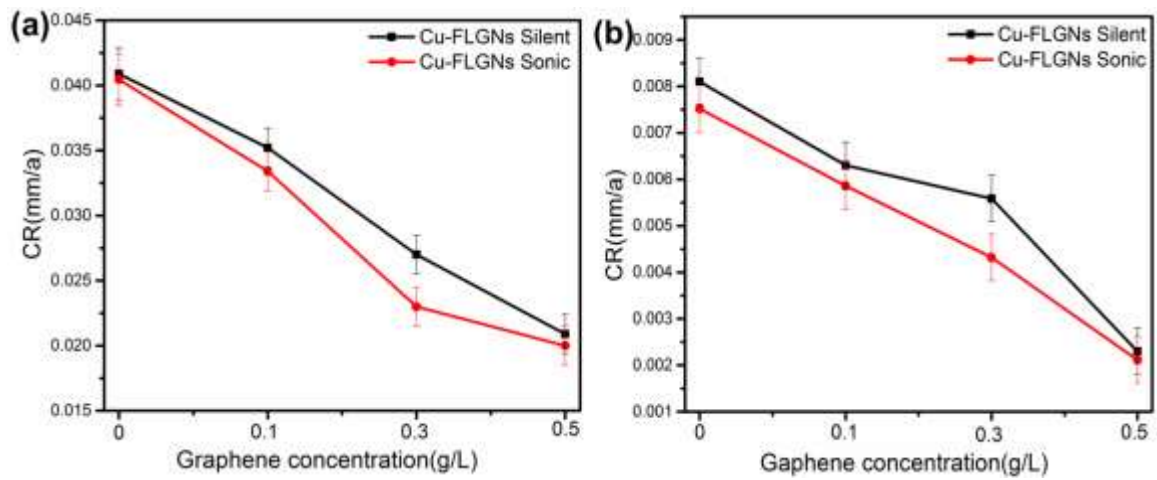


Figure 6.5: Corrosion Resistance of Cu-FLGPs nanocomposites (a) 3.5% NaCl and (b) Borate buffer solution

Table 6.1 Electrochemical corrosion parameter in borate buffer solution by Potentio-dynamic polarization curve at a scan rate 0.1667 mV/s

Sample	β_a (mV)	β_c (mV)	I_0 (Amp/cm ²)	E_0 (Volt)	CR(mm/a)
Cu (S)	101	151	1.025×10^{-6}	-0.045	0.018
0.1Cu-FLGPs (S)	53.5	86	8.47×10^{-7}	-0.038	0.015
0.3Cu-FLGPs (S)	160	167	3.45×10^{-7}	-0.045	0.005
0.5Cu-FLGPs (S)	191	121	2.56×10^{-7}	-0.03	0.004
Cu (US)	56	116.6	1.02×10^{-6}	-0.08	0.018
0.1Cu-FLGPs (US)	94.5	307	1.588×10^{-7}	-0.05	0.0024
0.3Cu-FLGPs (US)	99	85	1.98×10^{-7}	-0.031	0.003
0.5Cu-FLGPs (US)	81	80	1.3×10^{-7}	-0.04	0.002

Table 6.2: Electrochemical corrosion parameter in NaCl with borate buffer solution by Potentio-dynamic polarization curve at a scan rate 0.1667 mV/s

Sample	β_a (mv)	β_c (mv)	I_0 (Amp/cm ²)	E_0 (Volt)	CR(mm/a)
Cu (S)	53.8	106	1.3×10^{-6}	-0.25	0.025
0.1Cu-FLGPs (S)	17	80	2.2×10^{-6}	-0.23	0.046
0.3Cu-FLGPs (S)	47	155.7	1.56×10^{-6}	-0.26	0.024
0.5Cu-FLGPs (S)	13.3	181.7	4.29×10^{-6}	-0.22	0.064
Cu (US)	22	135.4	2.2×10^{-6}	-0.24	0.025
0.1Cu-FLGPs (US)	8.4	164	5.6×10^{-6}	-0.23	0.066
0.3Cu-FLGPs (US)	14.4	109.4	3.3×10^{-6}	-0.23	0.039
0.5Cu-FLGPs (US)	9.2	44.2	2.2×10^{-6}	-0.22	0.033

Table 6.3: Electrochemical corrosion parameter in 3.5% NaCl solutions by Potentio-dynamic polarization curve at a scan rate 0.1667 mV/s.

Sample	β_a (mv)	β_c (mv)	I_0 (Amp/cm ²)	E_0 (Volt)	CR(mm/a)
Cu (S)	51	101	2.05×10^{-6}	-0.238	0.03
0.1Cu-FLGPs (S)	20	83	5.65×10^{-6}	-0.206	0.097
0.3Cu-FLGPs (S)	51.2	60	9.05×10^{-7}	-0.216	0.016
0.5Cu-FLGPs (S)	17.4	62.8	7.8×10^{-7}	-0.193	0.015
Cu (US)	49	17	2.2×10^{-6}	-0.231	0.038
0.1Cu-FLGPs (US)	30.5	124	2.23×10^{-6}	-0.215	0.034
0.3Cu-FLGPs (US)	20.4	30.6	1.48×10^{-6}	-0.215	0.034
0.5Cu-FLGPs (US)	50	77	6.94×10^{-7}	-0.213	0.015

Table 6.4: Electrochemical corrosion parameter in borate buffer solution by Potentio-dynamic polarization curve at a scan rate 5 mV/s

Sample	β_a (mv)	β_c (mv)	I_0 (Amp/cm ²)	E_0 (Volt)	CR(mm/a)
Cu (S)	181	298	6.832×10^{-7}	-0.138	0.008
0.1Cu-FLGPs (S)	1103	88	5.48×10^{-7}	-0.120	0.006
0.3Cu-FLGPs (S)	67.86	97	4.73×10^{-7}	-0.108	0.006
0.5Cu-FLGPs (S)	102.81	140	1.972×10^{-7}	-0.095	0.002
Cu (US)	36.028	26	2.3033×10^{-6}	-0.141	0.007
0.1Cu-FLGPs (US)	89.33	149	4.98×10^{-7}	-0.106	0.006
0.3Cu-FLGPs (US)	96.49	143	1.33×10^{-6}	-0.103	0.004
0.5Cu-FLGPs (US)	117.3	87	6.532×10^{-7}	-0.098	0.002

Table 6.5: Electrochemical corrosion parameter in 3.5% NaCl solutions by Potentio-dynamic polarization curve at a scan rate 5 mV/s

Sample	β_a (mv)	β_c (mv)	I_{corr} (Amp/cm ²)	E_0 (Volt)	CR(mm/a)
Cu (S)	158.15	206.7	1.254×10^{-5}	-0.390	0.041
0.1Cu-FLGPs (S)	103.56	158	3.001×10^{-6}	-0.375	0.035
0.3Cu-FLGPs (S)	76.87	137	2.304×10^{-6}	-0.289	0.027
0.5Cu-FLGPs (S)	65.38	144.2	1.78×10^{-6}	-0.288	0.021
Cu (US)	111.39	139.9	1.25×10^{-5}	-0.399	0.041
0.1Cu-FLGPs (US)	138.69	73.3	2.8589×10^{-6}	-0.372	0.034
0.3Cu-FLGPs (US)	111.74	114.3	1.89×10^{-6}	-0.360	0.023
0.5Cu-FLGPs (US)	74.61	78.3	1.699×10^{-6}	-0.313	0.02

6.3.2 Corrosion study of Cu-RFLGPs

The corrosion studies were carried out as per the ASTM G5-94 standard with 3.5% NaCl solution. Open circuit potential (OCP) was measured for 30 minutes to obtain a stable corrosion potential as well as to reach the state of equilibrium in the present corrosion system as shown in figure 6.6 where the stable values are in the range of -0.2 to -0.4 V. Then after, the samples were tested in the potential range of 0.4 V to -0.4 V versus open circuit potential with a scanning rate of 5 mV/s.

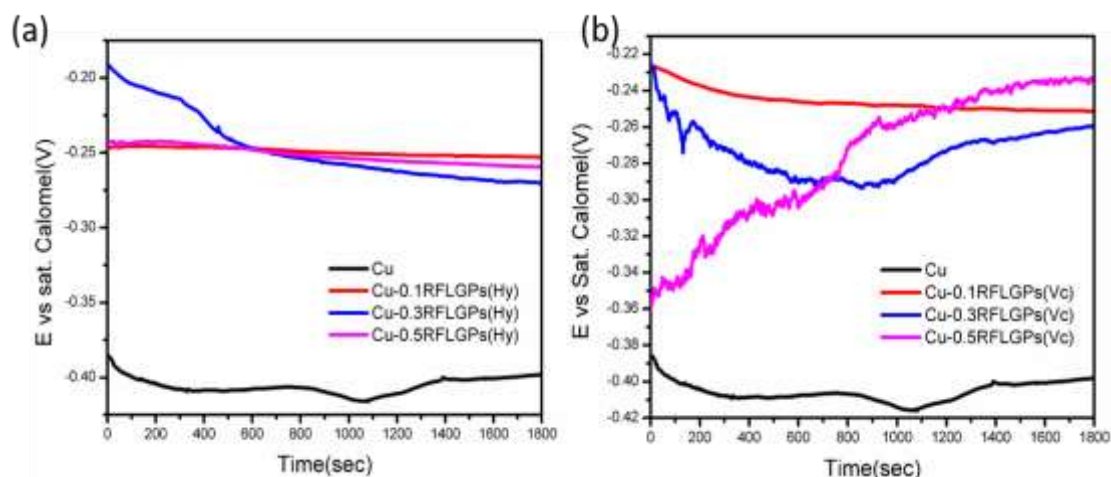


Figure 6.6A: OCP of Cu-RFLGPs composite

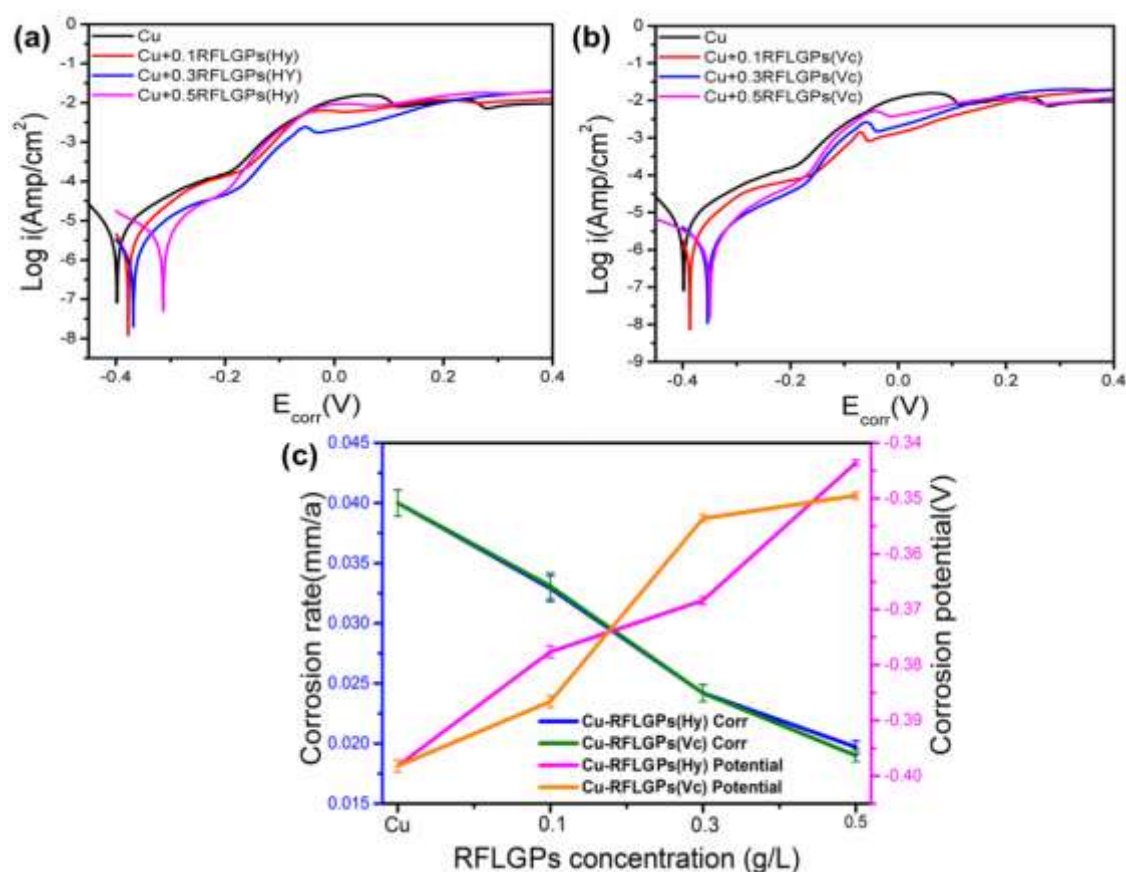
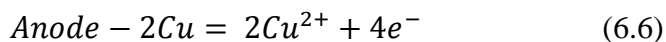
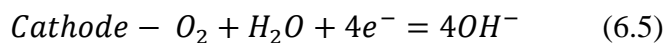


Figure 6.6B: Potentio-dynamic polarization curves (a) Cu-RFLGPs(Hy), (b) Cu-RFLGPs(Vc) nano-composites and (c) corrosion rate and variation of corrosion potential vs RFLGPs concentration

Figures 6.7 (a) and (b) shows the potentio-dynamic polarization curve for the samples performed in 3.5% sodium chloride solution. Thermodynamic and kinetic parameters including corrosion rate, corrosion current, corrosion potential and Tafel constant values

obtained through individual curve fitting of Potentio-dynamic plots are shown in Table 6.6. The corrosion in the Cu based samples are believed to have followed the following half-cell reactions: 6.5 and 6.6



E_0 values obtained on Cu, 0.1 g/L Cu-RFLGPs(Hy), 0.3 g/L Cu-RFLGPs(Hy) and 0.5 g/L Cu-RFLGPs(Hy) composite were -0.398 V, -0.3776 V, -0.3684 V and -0.343 V respectively. The E_{corr} values of 0.1Cu-RFLGPs(Vc), 0.3Cu-RFLGPs(Vc) and 0.5Cu-RFLGPs(Vc) composite were -0.386 V, -0.353 V and -0.349 V respectively which were nobler than the pure copper values. The general trend of the corrosion potential values indicates that the composites are resistant to corrosion as compared to pure copper films, also with an increase of RFLGPs concentration, the corrosion tendency has decreased. However, the kinetics factor of the corrosion system will decide the corrosion behavior. Hence it was necessary to evaluate the behavior of the corrosion rate of the films. The corrosion rate was calculated as per equation 6.3:

Table 6.6: Corrosion parameters of Potentio-dynamic polarization curves in 3.5% NaCl solution of Cu-RFLGPs.

Sample	β_a (mv)	β_c (mv)	I_0 (Amp/cm ²)	E_0 (Volts)	CR (mm/a)
Cu	90	78.94	1.2447×10^{-5}	-0.3982	0.0404
0.1CuRFLGPs (Hy)	97.194	137.6	1.01×10^{-5}	-0.3776	0.0329
0.3CuRFLGPs (Hy)	107.323	239.05	7.4×10^{-6}	-0.36	0.0242
0.5CuRFLGPs (Hy)	103.4	210.2	6.057×10^{-6}	-0.34	0.0197
0.1CuRFLGPs (Vc)	78.941	119.61	2.824×10^{-6}	-0.386	0.0331
0.3CuRFLGPs (Vc)	103.41	139.38	2.19×10^{-6}	-0.3536	0.0257
0.5CuRFLGPs (Vc)	111.0	281.94	5.88×10^{-6}	-0.3495	0.0195

The corrosion behavior of 0.5 g/L Cu-RFLGPs(Hy) and 0.5Cu-RFLGPs(Vc) shows a decrease of corrosion rate with values of 0.0197 mm/yr and 0.0195 mm/yr as compared to the pure copper thin film of 0.0404 mm/yr. The corrosion rate of 0.5 g/L RFLGPs concentration composite is 50% less than the corrosion rate of the pure copper thin film

prepared by the same method. The above agreements need to be further validated through the co-relation of Tafel constants with corrosion rate and potential as per equation 6.2.

Hence the variation of the Tafel constants also decides the corrosion tendency of the system. The variation of corrosion potential and corrosion rate of Cu-RFLGPs composites with varying concentrations of RFLGPs and Tafel constants can be seen in Table 6.6 and figure 6.8.(c). Unfortunately, the Tafel constants are not varying systematically as that of corrosion potential and currents for the films in 3.5% NaCl solution except for cathodic Tafel constants for Cu-RFLGPs. Hence a definite conclusion may not be drawn from Tafel constant values however from other results it can be concluded that both the thermodynamics and kinetics factors complement each other with the fact that an increase in RFLGPs concentration has generally improved the corrosion resistance of the composite films. It can be observed from Table 6.6 that with an increase of graphene concentration in the films, the extent of oxidation has decreased.

6.3.2.1 EIS Analysis.

The electrochemical behavior of Cu and Cu-FLGPs composite films in borate buffer, borate buffer with 3.5% NaCl and 3.5% NaCl solution were further analyzed by EIS to understand the copper dissolution mechanism in presence of graphene and chloride ions.

At this juncture a brief introduction and capability of EIS need to be enumerated as it is one of the most powerful tool of an electrochemist. It has significant applications ranging from corrosion, biosensors, battery development, fuel cell development, paint characterization, sensor development, and physical electrochemistry solid-state electrochemistry, non-aqueous and aqueous electrochemistry to electronics. Its application ranges from fundamental investigations to very applied uses such as product quality monitoring. EIS provides a more thorough understanding of an electrochemical system than any other electrochemical technique. The method consists in measuring the complex impedance $Z = Z' + iZ''$ as a function of frequency of an AC perturbation given to the system. The data is then analyzed and the tools used to interpret impedance data fall into two classes: (i) analogs, and (ii) physical models. Analogs, which almost always take the form of electrical equivalent circuits (EECs), do not pretend to describe the physico-electrochemical properties of the system, but simply reproduce the properties. On the other hand, physical models aim at not only reproducing the phenomenon of interest (in this case, $Z(j\omega)$), but of also accounting for the mechanism of the processes occurring at

the interface. Analog mode of analysis is more convenient as computer algorithms are now available that will assign an electrical analog to account for almost any impedance data provided that the locus is restricted to the right side of the complex plane. The analogs are almost always assigned without regard to the physics of the system. The main difficulty is the prior choice of the equivalent circuit (numbers of elements, impedance form) that can reliably represent the physical phenomena. Testing the integrity of measured data is therefore a crucial part of the analysis. However, mechanistic analysis by physical model proposal through identifying the set of different possible reactions and analysis of kinetics of reactions is essentially an exercise in pattern recognition, with recognition being performed by inspection. These functions would be better performed using artificial neural networks coupled with extensive libraries of reaction mechanisms. One such extensive mechanistic analysis by using EIS has been made by Macdonald and his group [184,185] to study the passive film characteristics grown on various metals and alloys showing active-passive behavior. The group has proposed the mechanism of point defect model for the passive film growth by analyzing the rate of various reactions occurring at the two interfaces. However, these kind of analysis is not very common for any kind of electrochemical phenomena analysis, due to the fact that in developing a reaction mechanism, it is necessary to recognize certain caveats. The first is that the reactions that comprise the mechanism must be elementary in nature; that is, they must not be of an order higher than two and no more than a single electron must be exchanged in the case of a charge transfer reaction. Unfortunately, these caveats are not widely recognized amongst electrochemists with the result many proposed mechanisms are not as fundamental as they might otherwise be. In the present case, because of the unavailability of the set of the neural network analysis setup, we followed an analog mode of analysis of the data where the power of the technique arises from: (i) It is a linear technique and hence the results are readily interpreted in terms of Linear Systems Theory (LST); (ii) If measured over an infinite frequency range, the impedance (or admittance) contains all of the information that can be gleaned from the system by linear electrical perturbation/response techniques; (iii) experimental efficiency (amount of information transferred to the observer compared to the amount produced by the experiment) is extraordinarily high; and (iv) The validity of the data is readily determined using integral transform techniques i.e. the Kramers-Kronig transforms (KK) that are independent of the physical processes involved. Accordingly data were generated and validate by KK transform.

One of the great advantages of EIS is that an independent check of the validity of impedance data (that is, compliance with the constraints of LST) is possible through the use of the Kramers-Kronig transforms. The KK transforms were originally developed in the 1920s to treat optical data and they were not applied to electrochemical and corrosion problems until many years later.

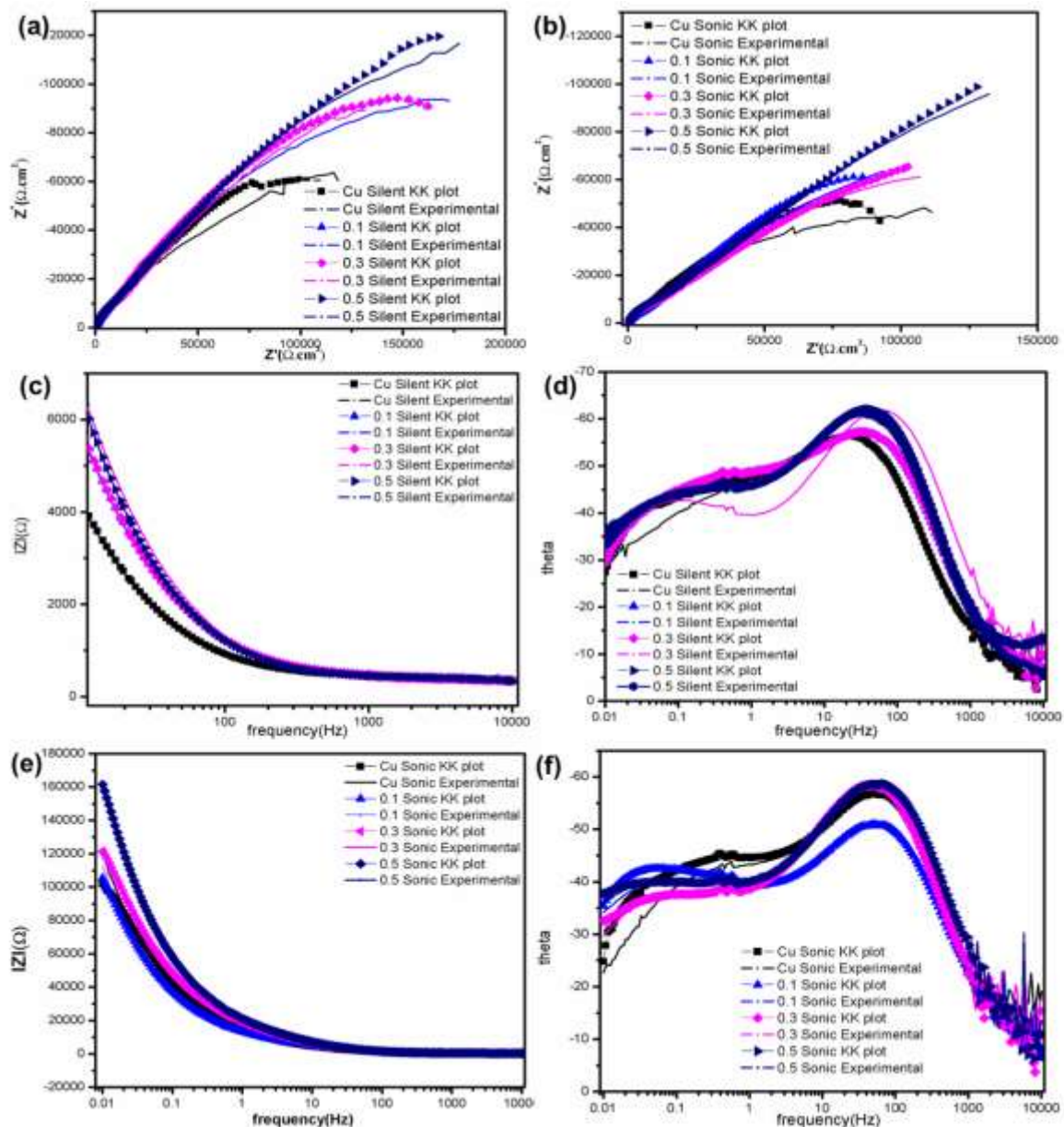


Figure 6.7: KK plot of Nyquist (a) silent, (b) sonic and Bode plots in (c, d) silent and (e, f) sonic condition of Cu and Cu-FLGPs sample with borate buffer solution

The KK transforms stem from Cauchy's theorem that provides the mathematical basis for causality, which is not only one of the constraints of LST but has been the mainstay of

scientific philosophy since the ancient Greeks. In their most popular form, the transforms are written as:

$$Z'(w) = Z'(\infty) + \frac{2w}{\pi} \int_0^{\infty} (xZ''(x) - wZ''(w))/(x^2 - w^2)dx \quad (6.7)$$

$$Z'(w) = Z'(0) + \frac{2w}{\pi} \int_0^{\infty} ((w/x)Z''(x) - Z''(w))/(x^2 - w^2)dx \quad (6.8)$$

$$Z' = -\frac{2w}{\pi} \int_0^{\infty} (Z'(w) - Z'(x))/(x^2 - w^2)dx \quad (6.9)$$

Where ω is the frequency of transform and x is normal frequency. Equations 6.7-6.9 and provide imaginary axis to real axis transformations, while Equation 6.9 yields the real axis to imaginary axis transform. In this technique, plotting of the measured data Z' and Z'' are checked against the calculated data from the above integrals. Of course, full precision cannot be attained because infinite frequency as in the integral is not accessible. However, the direct calculation of the KK integral yields an approximately correct result if the measured frequency range is sufficiently large, in the sense that semi-circles or semi-arcs in the Nyquist plot (Z' vs Z'') are completed. A deviation between experimental data and Kramers-Kronig fit, and an error statistic more than two orders of magnitude higher than the data with no drift, suggests the baseline drift data is not valid impedance.

The electrochemical behavior of Cu and Cu-FLGPs composite films in borate buffer, borate buffer with 3.5% NaCl and 3.5% NaCl solution were validated by Kramers-Kronig Transformations before analysis. Figure 6.7 shows the KK plot of composite films in borate buffer solution for both silent and sonic condition. The KK plot of films matched with experimental plot of borate buffer solution with. Figure 6.8 shows the KK plot of composite films in 3.5% NaCl solution in silent and sonic condition. Figure 6.9 shows the KK plot of composite films on borate buffer with 3.5% NaCl solution in silent and sonic condition. The fitted plots have no drift and have minimal intrusion, and it can be observed that there is almost full agreement with KK calculation. Hence the EIS data are stable and acceptable at this point.

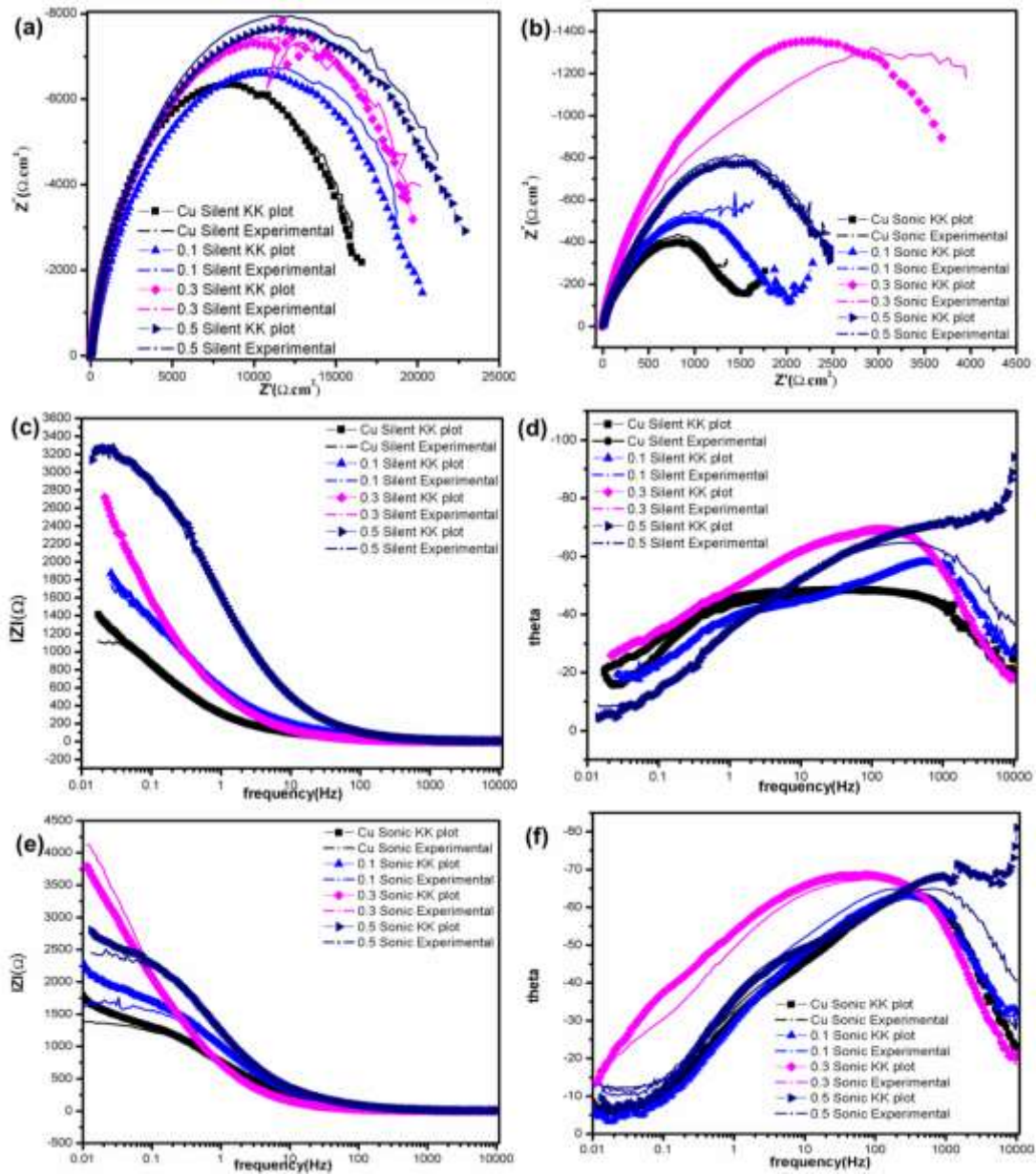


Figure 6.8: KK plot of Nyquist (a) silent, (b) sonic and Bode plots in (c, d) silent and (e, f) sonic condition of Cu and Cu-FLGPs sample borate buffer with 3.5% NaCl solution

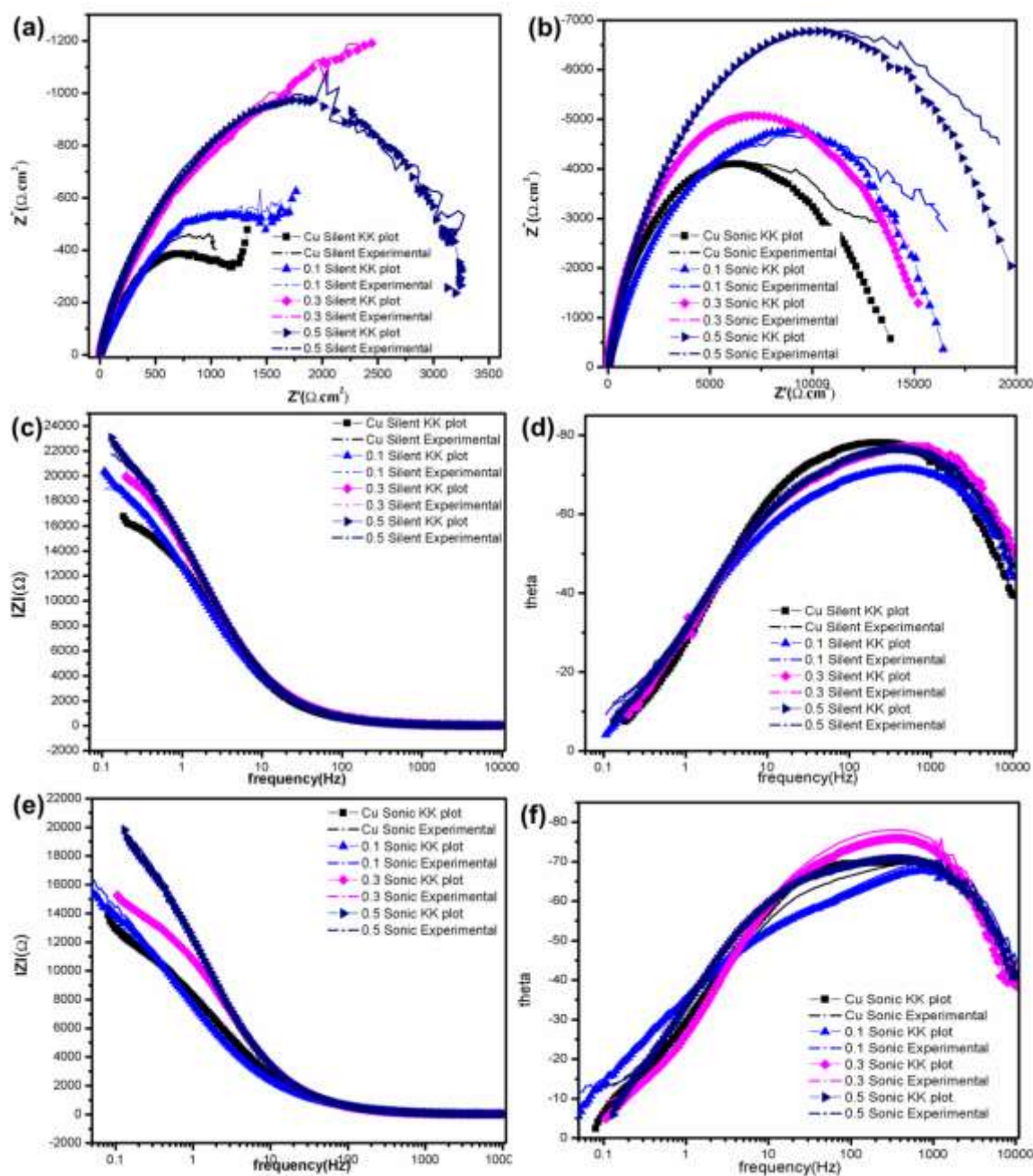


Figure 6.9: KK plot of Nyquist (a) silent, (b) sonic and Bode plots in (c, d) silent and (e, f) sonic condition of Cu and Cu-FLGPs sample with 3.5% NaCl solution

Figures 6.10-6.12 shows the Nyquist and Bode plots of films corroded in different conditions. Data for borate buffer with 3.5% NaCl is presented in figure 6.10 and Table 6.9 as it has the same varying trend as that of borate buffer. The data analysis can be followed by analyzing the Nyquist plot, impedance Bode and phase Bode plots along with the obtained fitted parameters from the plots. The Nyquist plot in borate buffer solution

has incomplete semicircle with capacitive loop at high and medium frequency (HF/MF), followed by extended linearity at low frequency (LF). This may indicate a pure resistance i.e. solution resistance at high frequency and the faradic charge transfer process in the low frequency range along with some diffusion impedance, which could be due to 45° linear tail or beginning of an overlapping third capacitive loop at very low frequency. It was observed that the diameter of the HF arc increased for the composite films as the graphene concentration in the film increased.

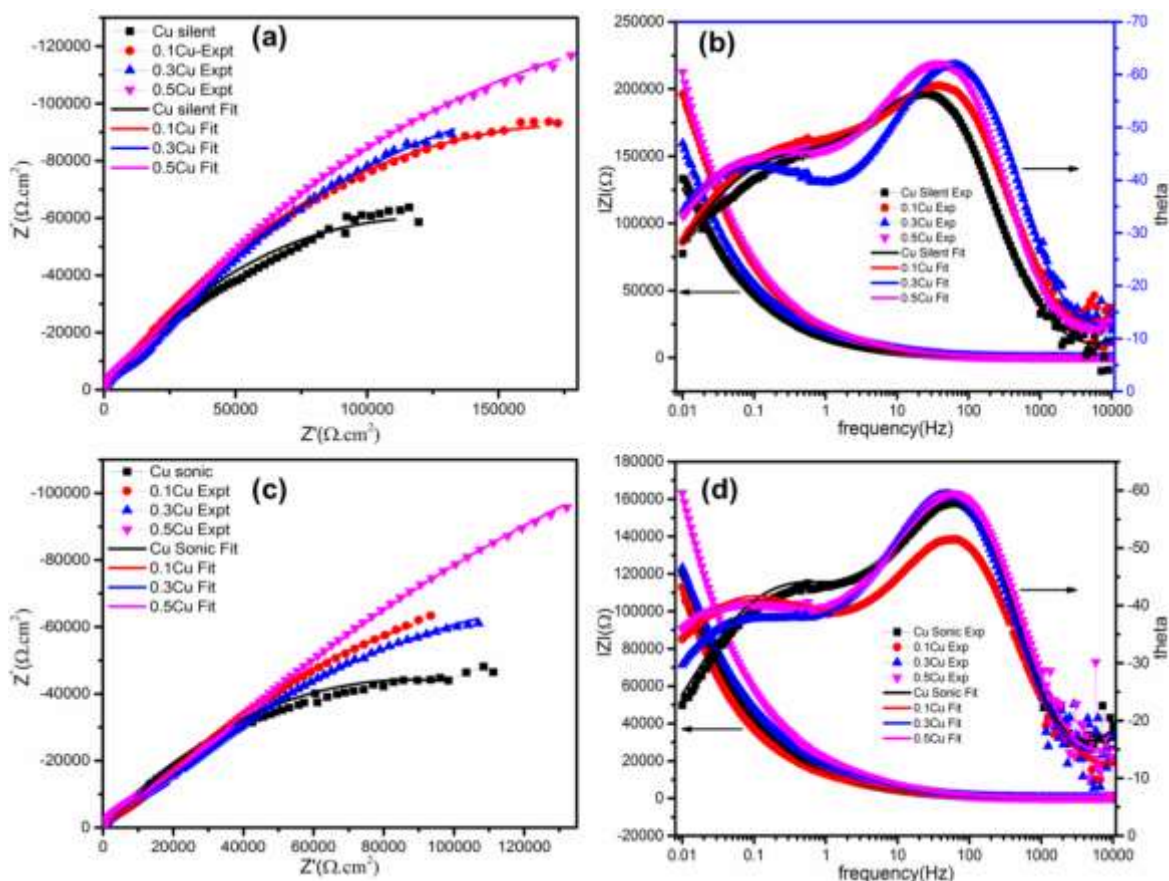


Figure 6.10: Nyquist and Bode plots of Cu and Cu-FLGPs sample in borate buffer solution and deposited in (a), (b) silent condition and (c), (d) ultrasonic condition

A better comprehensive analysis can be inferred by analyzing the Bode plots which would specify the type of impedance elements, number and nature of capacitance loops, presence/absence of diffusion impedances etc. The Bode plots in the present study exhibit pure resistance at high frequency and Warburg resembling impedance at low frequency, as the phase angle of the impedances are varying in between -20° to -45° . Further, the phase plot also shows two imperfect capacitances with phase angles of around -50° to -60° . Unlike borate buffer solutions, in NaCl solution, the Nyquist plot demonstrates

almost a semicircular arc with multiple resistances at LF along with indefinite Warburg impedances.

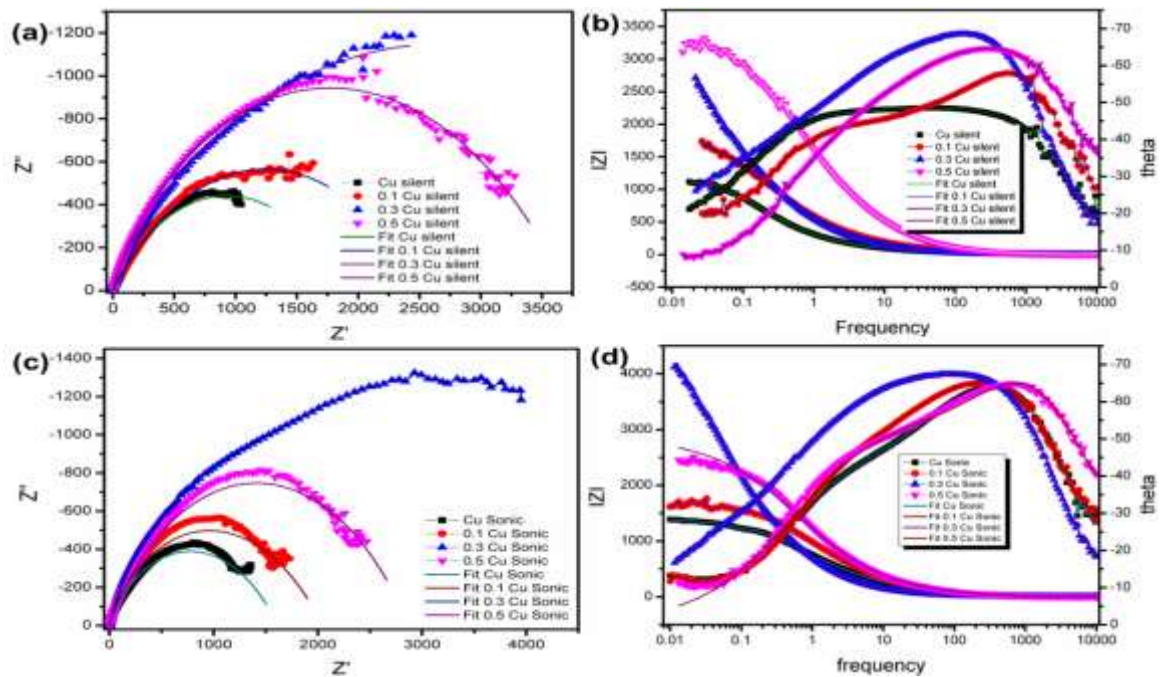


Figure 6.11: Nyquist and Bode plots of Cu and Cu-FLGPs sample in borate buffer with 3.5% NaCl solution and deposited in (a), (b) silent condition and (c), (d) ultrasonic condition

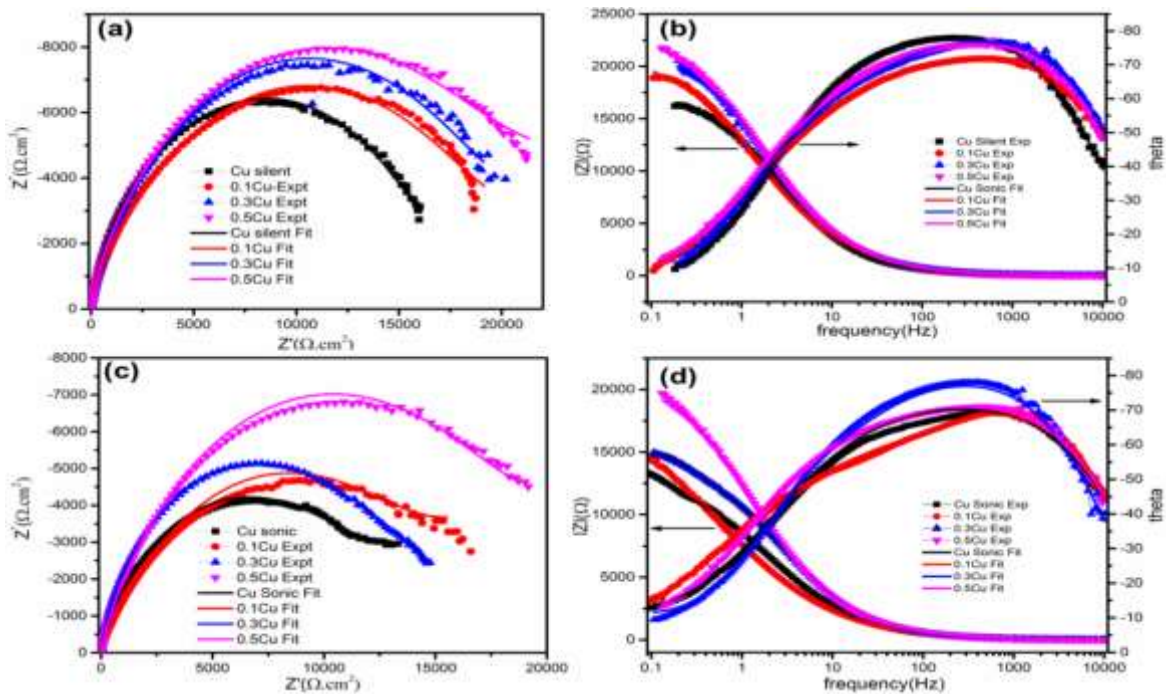


Figure 6.12: Nyquist and Bode plots of Cu and Cu-FLGPs sample in 3.5% NaCl solution and deposited in (a), (b) silent condition and (c), (d) ultrasonic condition

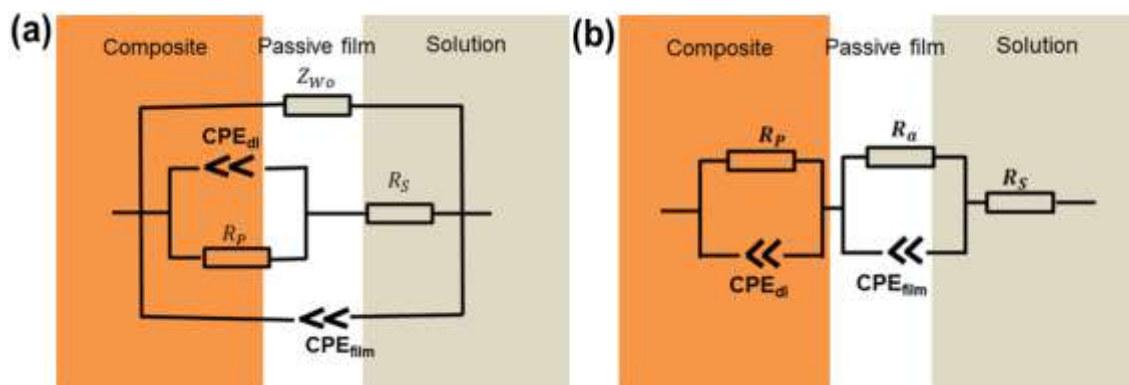


Figure 6.13: Circuit diagram of EIS analysis on (a) borate buffer and borate buffer with 3.5% NaCl and (b) 3.5% NaCl solutions

The corresponding Bode plots further compliment the observations. The above observation indicates that the corroding systems might be under mixed kinetics and diffusion control. The EIS spectra fitting were then carried out by using Z view software (CS studio 5) supplied by CorrTest and are presented in figures 6.10-6.12 along with the experimental curves to extract various physical parameters describing the impedance of the system. The fitted parameters along with the error values mentioned as (%E) are given in Tables 6.7- 6.9.

The proposed complete and best fitted models used in the present study to analyze the impedance data, in both the solutions, are presented in figure 6.13. The circuits essentially contain the components of R_s , R_p , R_a , Z_{wo} , CPE_{film} and CPE_{dl} , where R_s represents solution resistance at HF, R_p represents polarization resistance at MF and LF corresponding to corrosion tendencies, R_a is resistance offered by adsorbed Cl ions in the films at low frequency, Z_{wo} is the film resistance at LF offered by oxide film formed on the surface due to corrosion, CPE_{film} and CPE_{dl} are constant phase element corresponding to double layer charging and oxide / oxide + chloride film capacitance at HF and MF ranges. As proposed in the circuit, it is assumed that the surface is covered with either a well-developed passive layer (in borate buffer solution) or Cl impregnated passive layer (in Cl containing solution) which is not so protective. Hence we have two CPEs and three resistances assigned to the substrate/film and film/solution interfaces. Also it has been proposed that the passive layers are porous in Cl solutions as discussed later. In this case, the capacitances have been replaced by a CPE due to the fact that the reactions are taking place at non-uniform surfaces. In borate buffer solution the introduction of CPE was done to validate the assumption that there are numerous active sites which do vary dynamically

while the corrosion phenomena is progressing due to presence of graphene in the copper matrix. This also might have led to an improper double layer charging. In case of solution where Cl ions are present, CPE signifies varying composition of the films due to incorporation of these Cl ions in the film and subsequent formation of chloride bearing compounds. Since the impedance data obtained in the current study are quite complex, so in order to obtain the best fit parameters, the co-efficient of the constant phase element CPE has been fixed between 0.8 – 0.9. Referring to the error values, it can be safely presumed that the proposed circuits are the best fitted ones.

Table 6.7: Electrochemical parameters of Cu and Cu-FLGPs composites in borate buffer solution

Sample	R_s (Ω/cm^2) (%E)	R_p (Ohm/cm^2) (%E)	C_{dl} ($\mu\text{F}/\text{cm}^2$)	C_{film} ($\mu\text{F}/\text{cm}^2$)	n (Cdl)	n (C_{film})	Z_{film} (Ω/cm^2) (%E)
Cu (S)	876 (0.5%)	494960 (3.13%)	3.22	2.3E-3	1	0.84	52672 (5.16%)
0.1Cu- FLGPs (S)	870 (0.43%)	728100 (2.2%)	2.06	0.014	0.85	0.92	56918 (3.6%)
0.3Cu- FLGPs (S)	718 (0.36%)	796880 (2.63%)	0.017	7.5E-4	0.91	0.69	76714 (2.1%)
0.5Cu- FLGPs (S)	872 (0.05%)	1046780 (0.81%)	0.56	0.021	0.9	0.84	71846 (0.71%)
Cu (US)	652 (0.5%)	346860 (1.91%)	2.3	0.062	0.89	0.75	36530 (3.24%)
0.1Cu- FLGPs (US)	934 (0.5%)	588560 (3.44%)	1.56	0.012	0.83	0.60	46804 (2.44%)
0.3Cu- FLGPs (US)	878 (0.75%)	610500 (6.4%)	1.72	0.168	0.88	0.60	78954 (5.82%)
0.5Cu- FLGPs (US)	832 (0.87%)	1340760 (13%)	1.42	0.084	0.87	0.65	74164 (6.47%)

In order to calculate the capacitance values from the corresponding CPE used in the equivalent circuits, Brug's relationship was used as presented in equation 6.10:

$$C_{dl} = Q^{\frac{1}{n}}(R_s^{-1} + R_p^{-1})^{\frac{n-1}{n}} \text{ or } C_{film} = Q^{\frac{1}{n}}(R_{film}^{-1})^{\frac{n-1}{n}} \quad (6.10)$$

Where C_{dl} , Q , n and R_{film} are double layer capacitance, the capacitance value of CPE, constant of CPEs and resistances of film respectively. To begin with, at very high frequency the impedance may be assigned to the resistance of the electrolyte in series with the capacitance. From the Tables 6.7-6.9, it can be observed that R_s values are quite high for samples treated in buffer solutions, as compared to NaCl ones. Also, with increasing graphene concentration, the values have been higher for both the conditions as well.

Table 6.8: Electrochemical parameters of Cu and Cu-FLGPs composites in 3.5%NaCl solution

Sample	$R_s(\text{Ohm/cm}^2)$ (%E)	$R_p(\text{Ohm/cm}^2)$ (%E)	C_{dl} ($\mu\text{F/cm}^2$)	C_{film} ($\mu\text{F/cm}^2$)	n (Cdl)	$n C_{film}$	R_{film} (Ohm/cm^2) (%E)
Cu (S)	18.04 (0.5%)	9152 (4.2%)	8.76	22.4	0.91	0.89	24568 (1.4%)
0.1Cu- FLGPs (S)	16.72 (1.2%)	6090 (3.5%)	2.36	20.2	0.83	0.82	34564 (0.6%)
0.3Cu- FLGPs (S)	13.36 (1.39%)	4290 (21%)	5.98	13.34	0.89	0.88	36680 (0.5%)
0.5Cu- FLGPs (S)	15.4 (1.5%)	9148 (4%)	4.9	0.094	0.88	0.86	36568 (0.99%)
Cu (US)	14.48 (1.6%)	14434 (2.7%)	3.02	151	0.81	0.79	14670 (2.4%)
0.1Cu- FLGPs (US)	12.52 (3.2%)	3176 (0.8%)	4.4	41	0.82	0.76	29682 (4.2%)
0.3Cu- FLGPs (US)	18.6 (1.38%)	8950 (5.2%)	5.24	29.8	0.89	0.87	20878 (2%)
0.5Cu- FLGPs	17.52 (1.3%)	6078 (6%)	4.82	2	0.82	0.82	35232 (0.95%)

(US)

Now, corresponding to the double layer capacitance values along with the parallel impedance due to polarization/charge transfer, an interesting observation can be made. The C_{dl} values for buffer solutions lie below $1 \mu\text{F}\cdot\text{cm}^{-2}$, whereas the values are a bit higher i.e. $8\text{-}10 \mu\text{F}\cdot\text{cm}^{-2}$. Now, comparing the R_p , the impedance level is quite high in borate buffer then the salt solution, which is complementary to the solution resistance values. Further, R_p values are high for composite films irrespective of testing solutions. The said observation signifies the decrease in electrochemical activity, i.e. corrosion of Cu in borate buffer solutions and in presence of graphene reinforcements.

Films prepared in sonication conditions are showing higher impedance values as compared to their silent counterparts, thereby, indicating better film properties. In addition to these three parameters, there are also film capacitances, where it can be observed that films formed in borate buffer solutions have almost non-varying capacitance values, indicating uniform films with fixed composition, whereas the capacitance values are higher and non-uniform for films formed in salt solutions, which may specify non-uniform films with varying composition.

The high capacitance values of the films in 3.5% NaCl could be due to the adsorption of Cl ions which might have been adsorbed as complex copper compounds (CuCl or CuCl_2 as mentioned in the mechanism section and Table 6.13) and has induced charge effects. Film impedance has been added in borate buffer corrosion, the value of which has been increased with increase in graphene concentration of the films, indicating the fact that a metal covered with an undamaged coating generally has very high impedance. In case of corrosion in NaCl solution, the film is expected to be porous due to adsorbed chloride ions. Accordingly, impedance due to pore as well as relaxation of Cl ions has been added, the values of which have been increased with increased graphene concentrations in the films. The reason for the observed varying impedances of solution resistance and capacitance, high polarization impedance and film resistance and capacitances for the two solutions has been discussed later while discussing the mechanism of corrosion.

However, the decreased capacitance value and increased polarization resistance of composite films as compared to Cu films in both the solutions indicate better anti-corrosion properties of composite samples. Also the prepared composite samples do have

better anticorrosion property for borate buffer solution as compared to 3.5% NaCl solution.

Table 6.9: Electrochemical parameters of Cu and Cu-FLGPs composites in borate with 3.5%NaCl solution

Sample	R_s (Ω/cm^2) (%E)	R_p (Ohm/cm^2) (%E)	C_{dl} ($\mu\text{F}/\text{cm}^2$)	C_{film} ($\mu\text{F}/\text{cm}^2$)	n (Cdl)	n (C_{film})	Z_{film} (Ω/cm^2) (%E)
Cu (S)	6.689 (3.2124)	1856 (1.2559)	2.9067E-2	11.5	0.58	0.92	26.51 (11.638)
0.1Cu- FLGPs (S)	5.397 (1.8452)	2487 (1.0696)	0.38	11.2	0.58	0.92	208.8 (6.8132)
0.3Cu- FLGPs (S)	1.986 (1.4196)	5763 (1.5514)	0.44	50.1	0.58	0.92	30.12 (179.44)
0.5Cu- FLGPs (S)	7.728 (1.3119)	3652 (0.39822)	3.35E-11	2.99	0.58	0.92	0.1014 (935.55)
Cu (US)	6.136 (2.9263)	1611 (1.0271)	4.18E-17	5.34	0.58	0.92	0.0979 (1542.2)
0.1Cu- FLGPs (US)	7.028 (7.2725)	2036 (1.3308)	0.204	7.07	0.85	0.92	0.26565 (3.1368)
0.31Cu- FLGPs (US)	2.359 (7.0797)	5132 (1.3386)	0.501	39.6	0.85	0.92	25.65 (114)
0.51Cu- FLGPs (US)	4.798 (5.1434)	2965 (0.78209)	1.031E-7	3.87	0.87	0.65	1.915 (275.41)

6.3.3 Phase and microstructure of samples after corrosion test

The structural study of corroded samples would give clearer and complimenting information about the mechanism of corrosion. After the corrosion test (upto passivation regions in respective films), the structural and morphology analysis were examined via XRD and SEM combined with EDS attachment. The corroded samples were then compared with the bare copper. Figure 6.14 shows the XRD images of the corroded composite films along with the un-corroded and as-deposited films for comparison.

Specific observations from the investigations are: (i) samples tested in NaCl solutions have CuCl, Cu₂O peaks in addition to the regular Cu peaks, whereas borate buffer solutions have no other peaks than pure copper structure, (ii) the intensities of the peaks has got increased and decreased in case of borate buffer and salt solutions respectively and (iii) corrosion has taken place dominantly in the directions of (111) and (220) in borate buffer and salt solutions respectively. Figure 6.15 shows the Texture coefficient for Cu-FLGPs after corrosion in (a) borate buffer, (b) borate with 3.5% NaCl and (c) 3.5% NaCl solutions. It can be observed from the figure that there is no definite directional corrosion.

The above observations are then coupled with the microscopic analysis to present the corrosion mechanism. Figures 6.16 and 6.17 show the SEM images of Cu and 0.5Cu-FLGPs in both silent and sonic conditions, which have been corroded in the tested solutions. For analysis of samples at a scan rate of 5 mV/s and other concentrations of graphene reinforcements, the images have been provided in figure 6.20. The bare images (not shown here) of samples tested with borate buffer solution shows patina colored spots present on surfaces of Cu as well as composite samples, which has got increased as graphene concentration increased upto 0.5 g/L FLGPs. Now looking at the SEM images it can be observed that after corrosion the corroded surface looks smoother as compared to their corresponding non-corroded surfaces. This may indicate the surface has been covered with well-developed passive films in borate buffer solutions. In the case of NaCl solution, the coating surfaces of composites have been observed to be covered with white corrosion products. The corrosion products appear to be smooth flakes like surfaces comprising of trigonal, pentagonal and hexagonal structures present all over the surfaces. Further sonication has found to have distinct effect, as the surfaces appear to be smooth in borate buffer treatment and rough in 3.5% NaCl solution. To tally the XRD analysis with SEM images, and EDS analysis of the corroded surface was also carried out and have been provided in figures 6.18- 6.19 and 6.21.

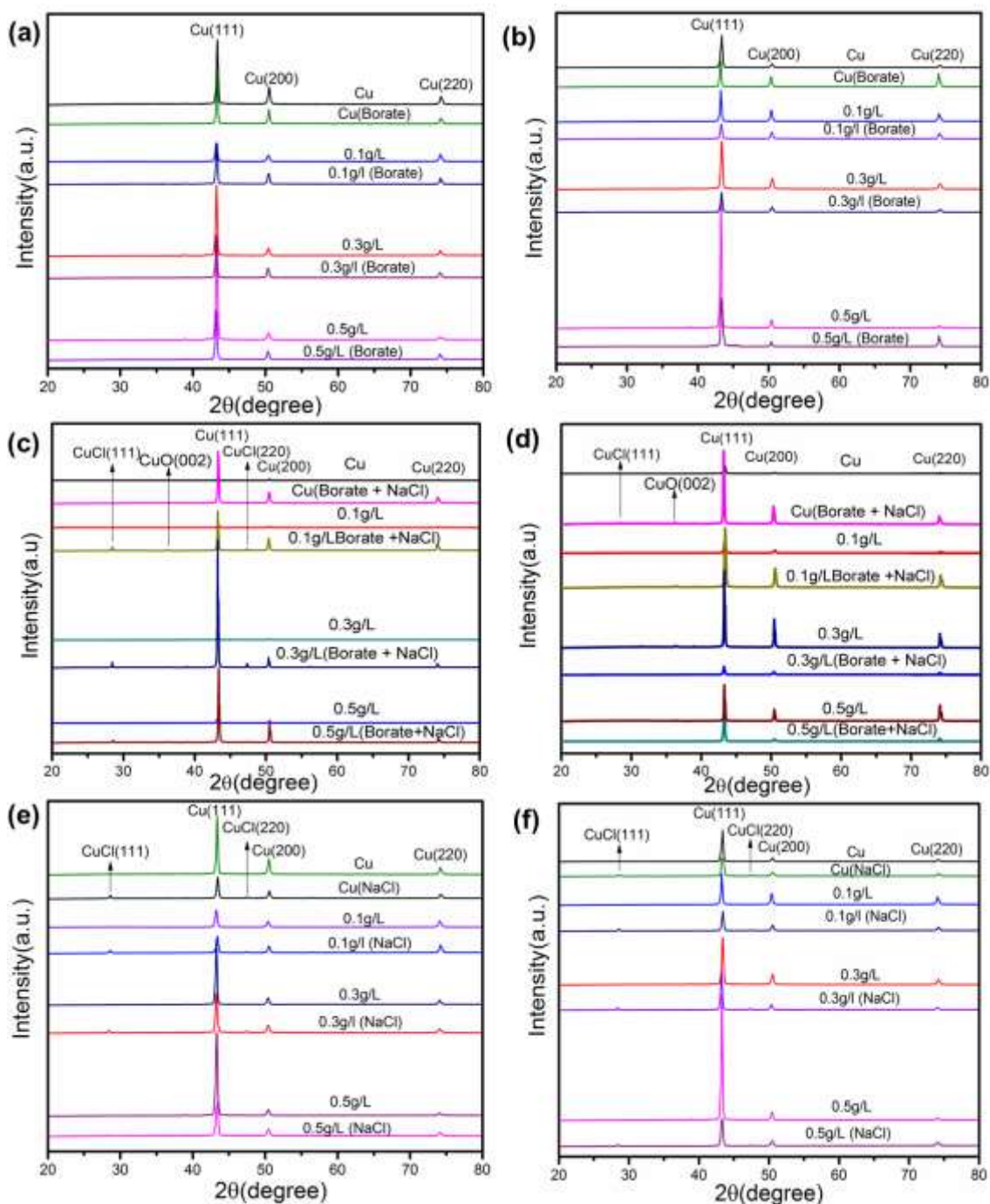


Figure 6.14: XRD pattern for Cu-FLGPs of before and after corrosion in borate buffer (a) silent, (b) ultrasonic condition films, borate buffer with 3.5% NaCl solution (c) silent, (d) ultrasonic condition films, (e) silent and (f) ultrasonic condition films in borate buffer solution and 3.5% NaCl

Figure 6.18 shows EDS analysis of corrosion samples in borate buffer solution, (a) Cu silent, (b) 0.5Cu silent, (c) Cu sonic and (d) 0.5 Cu sonic. Figure 6.19 shows the EDS analysis of corrosion samples in 3.5 % NaCl Cu silent, 0.5Cu silent, Cu sonic, 0.5Cu sonic. The EDS spectra of SEM analysis show the presence of chloride and oxygen in the salt solution treated films and only oxygen along with copper corroded in borate buffer

solution. Moreover, the patina and whitish color generally indicates Cu phases consisting of Cu_2O and $CuCl$ respectively.

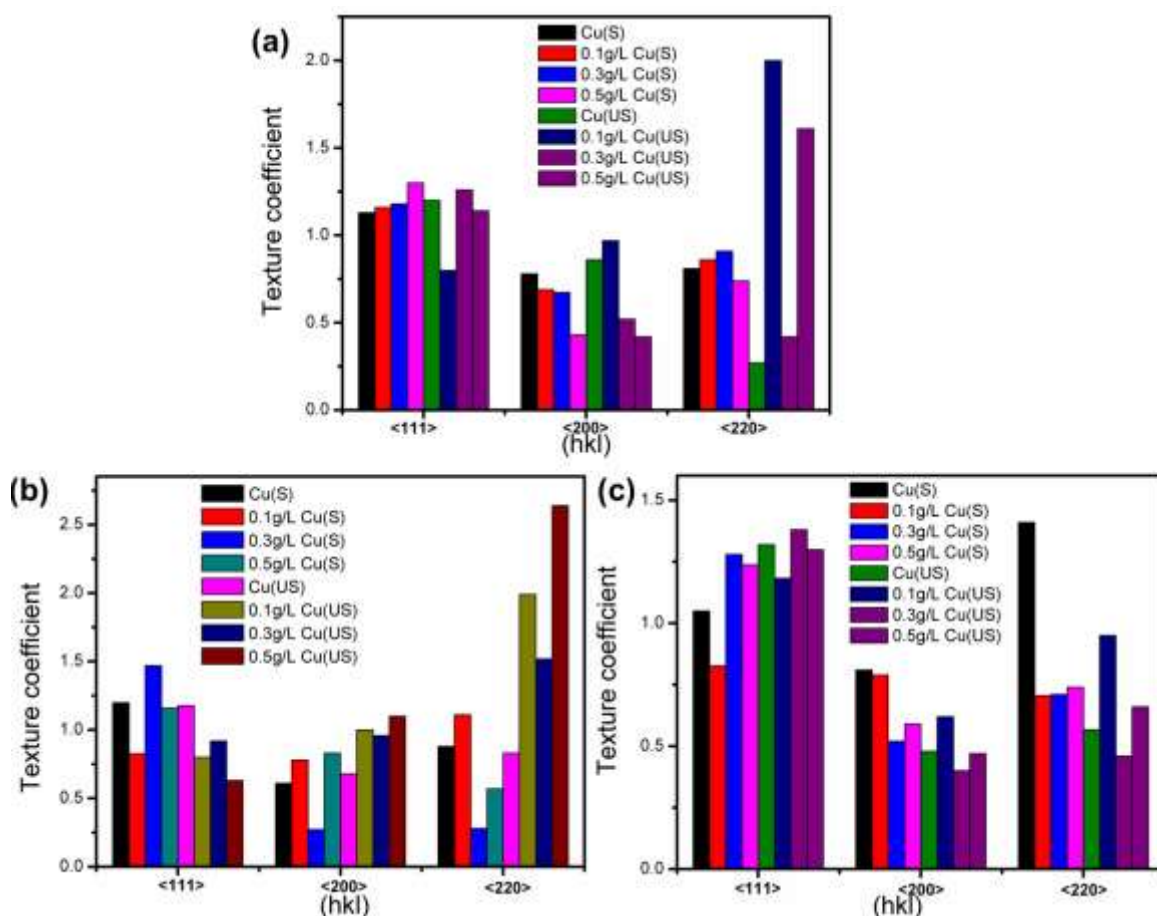


Figure 6.15: Texture co-efficient of composite samples after corrosion tests in (a) borate buffer, (b) borate buffer with 3.5% NaCl and (c) 3.5% NaCl solution

Table 6.10 shows the elemental analysis for composite samples treated in 3.5% NaCl solution. From the table it can be inferred that, Cl incorporation has been decreased with increase of graphene concentration. Hence it can be expected at this juncture that the corrosion products are copper oxide and a mixture of Cu_2O and $CuCl$ for borate and salt solution corrosion respectively, which has been well complemented by XRD analysis. However, Cu_2O phases are not present in XRD analysis, which may be due to the fact that the oxide layer is very thin to be detected by the technique and is non-porous and protective as comparison to the chloride and oxide layer mixture.

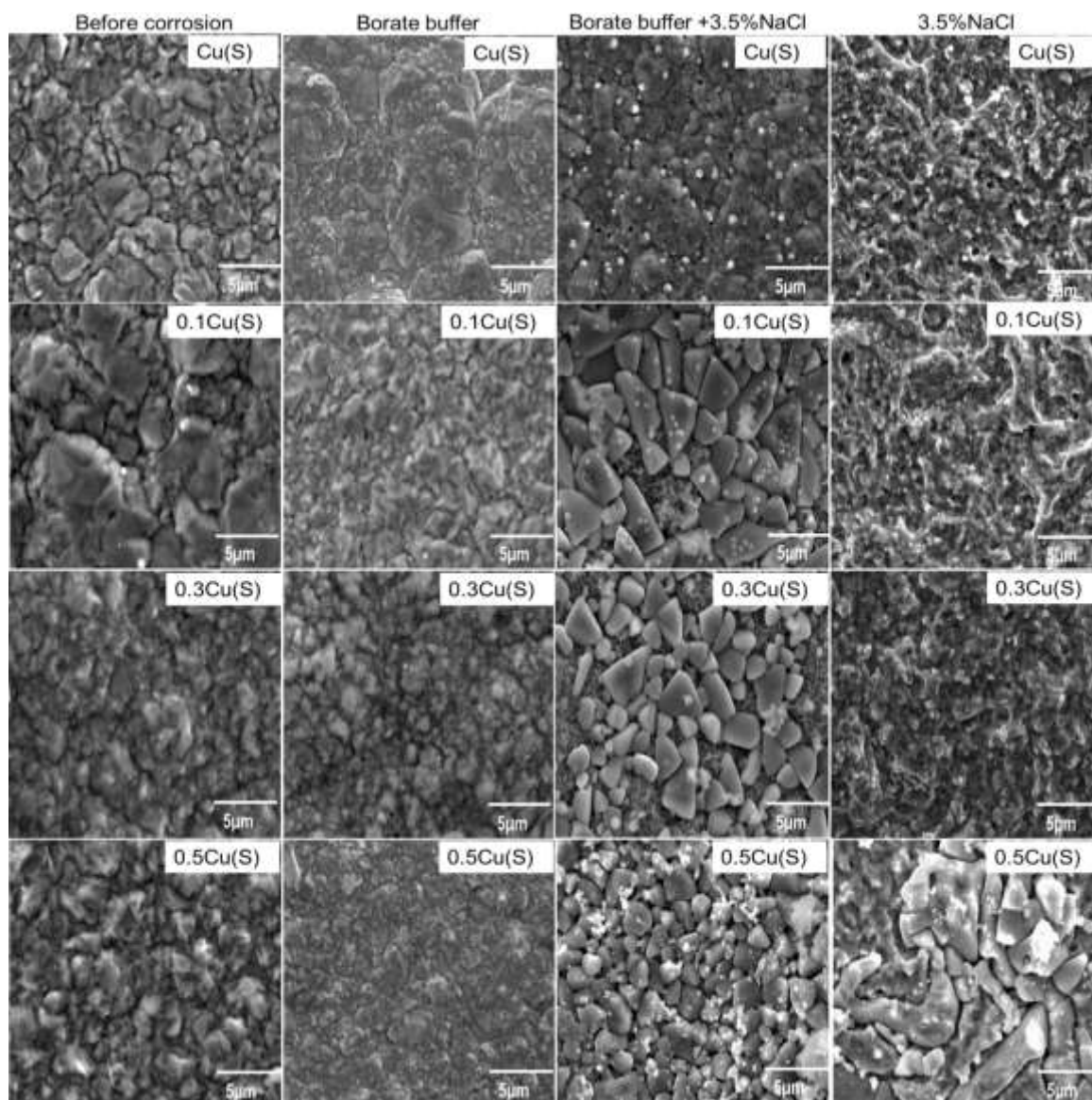


Figure 6.16: SEM image of Cu and Cu-FLGPs composite (silent condition) before and after corrosion of films in and borate buffer, borate buffer with 3.5% NaCl and 3.5% NaCl solution corroded at scan rate 0.1667 mV/s

To corroborate the above observation and propose a mechanism, the samples of Cu-RFLGPs were also analyzed and subjected to structural studies as well. Figure 6.21 shows the SEM images of sono-electroplated Cu, 0.5Cu-RFLGPs(Hy) and 0.5Cu-RFLGPs(Vc) composite films before corrosion (a), (c) and (e) and after corrosion (b), (d) and (f) along with representing EDS spectra of after corroded films. The microscopic analysis for all the samples has been done, however, is not presented to avoid voluminous data presentation and not shown here.

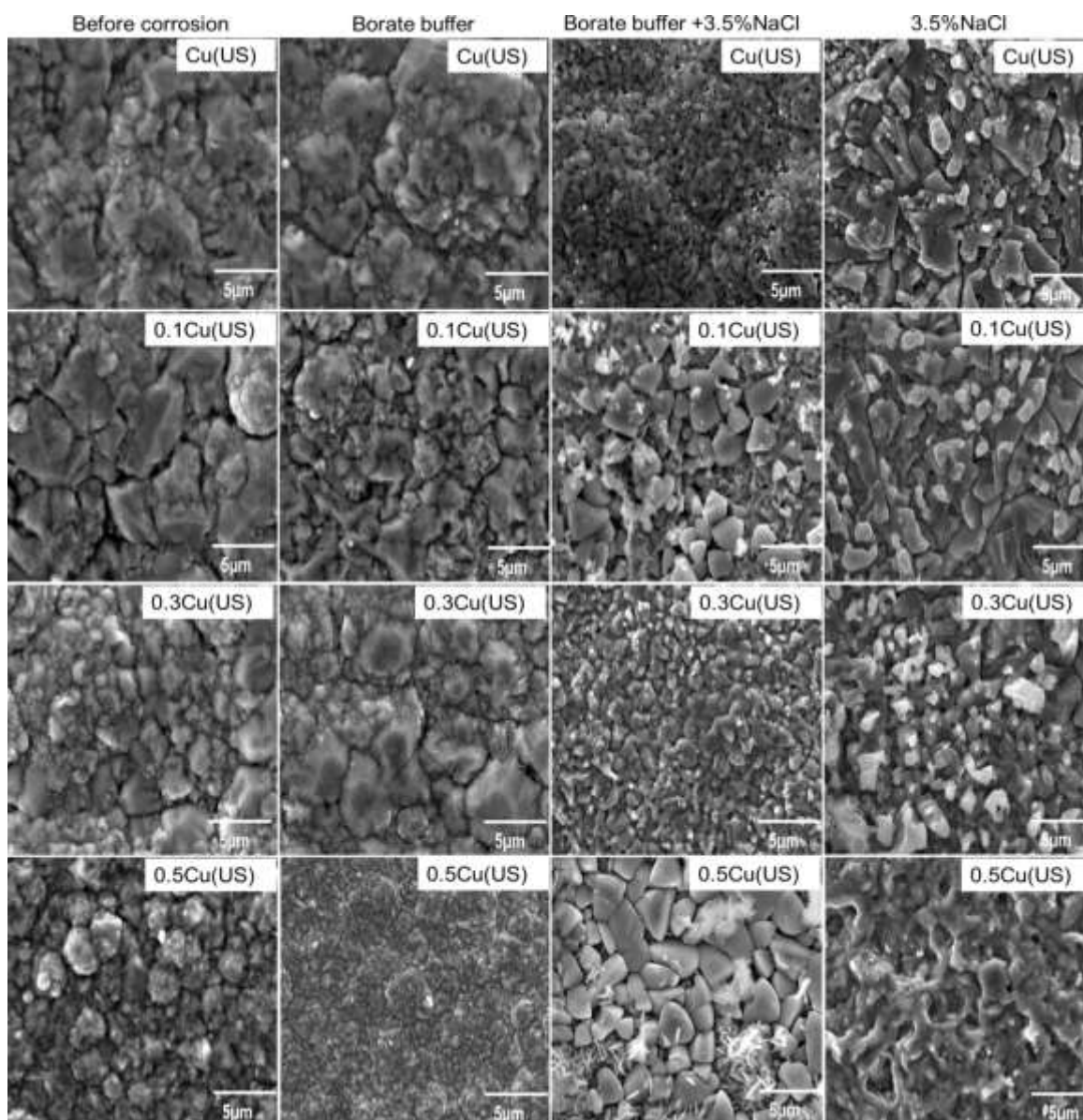


Figure 6.17: SEM image of Cu and Cu-FLGPs composite (Ultrasonic condition) before and after corrosion of films in and borate buffer, borate buffer with 3.5% NaCl and 3.5% NaCl solution corroded at scan rate 0.1667 mV/s

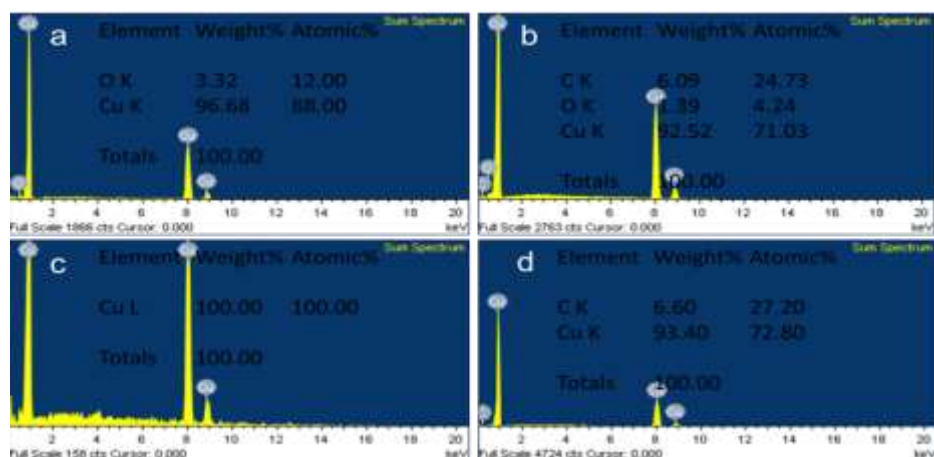


Figure 6.18: EDS analysis of corrosion samples in borate buffer solution (a) Cu (S), (b) 0.5Cu-FLGPs (S), (c) Cu (US) and (d) 0.5Cu-FLGPs (US)

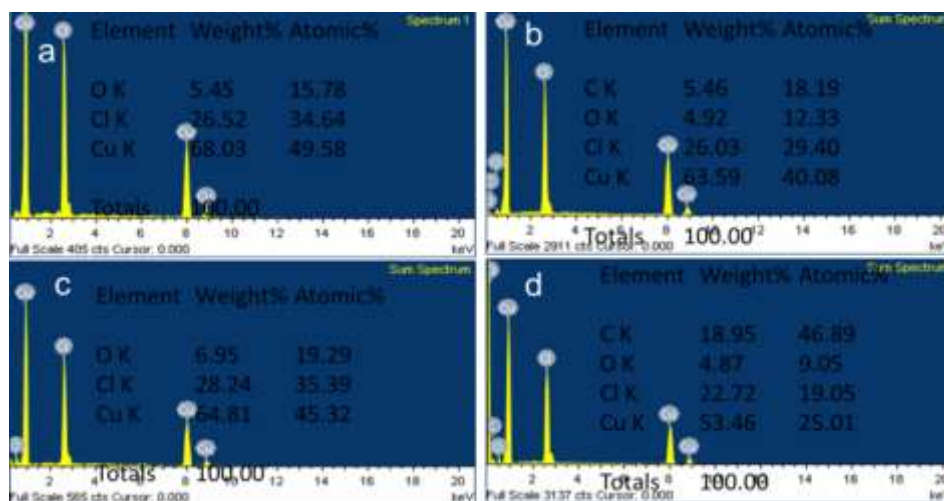


Figure 6.19: EDS analysis of thin films in 3.5% NaCl solution (a) Cu (S), (b) 0.5Cu-FLGPs (S), (c) Cu (US) and (d) 0.5Cu-FLGPs (US)

Table 6.10: EDS analysis of corroded samples of Cu and Cu-FLGPs treated in 3.5% NaCl

Sample	C%	O%	Cl%	Cu%
Cu (S)	-	5.45	26.52	68.03
0.1Cu-FLGPs (S)	6.11	2.55	27.97	63.37
0.3Cu-FLGPs (S)	9.04	12.92	16.90	60.78
0.5Cu-FLGPs (S)	14.80	7.98	10.09	67.12
Cu (US)	-	6.95	28.24	64.81
0.1Cu-FLGPs (US)	6	2.92	30.09	60.99
0.31Cu-FLGPs (US)	11.37	4.91	25.47	58.26
0.51Cu-FLGPs (US)	18.95	4.87	22.72	53.46

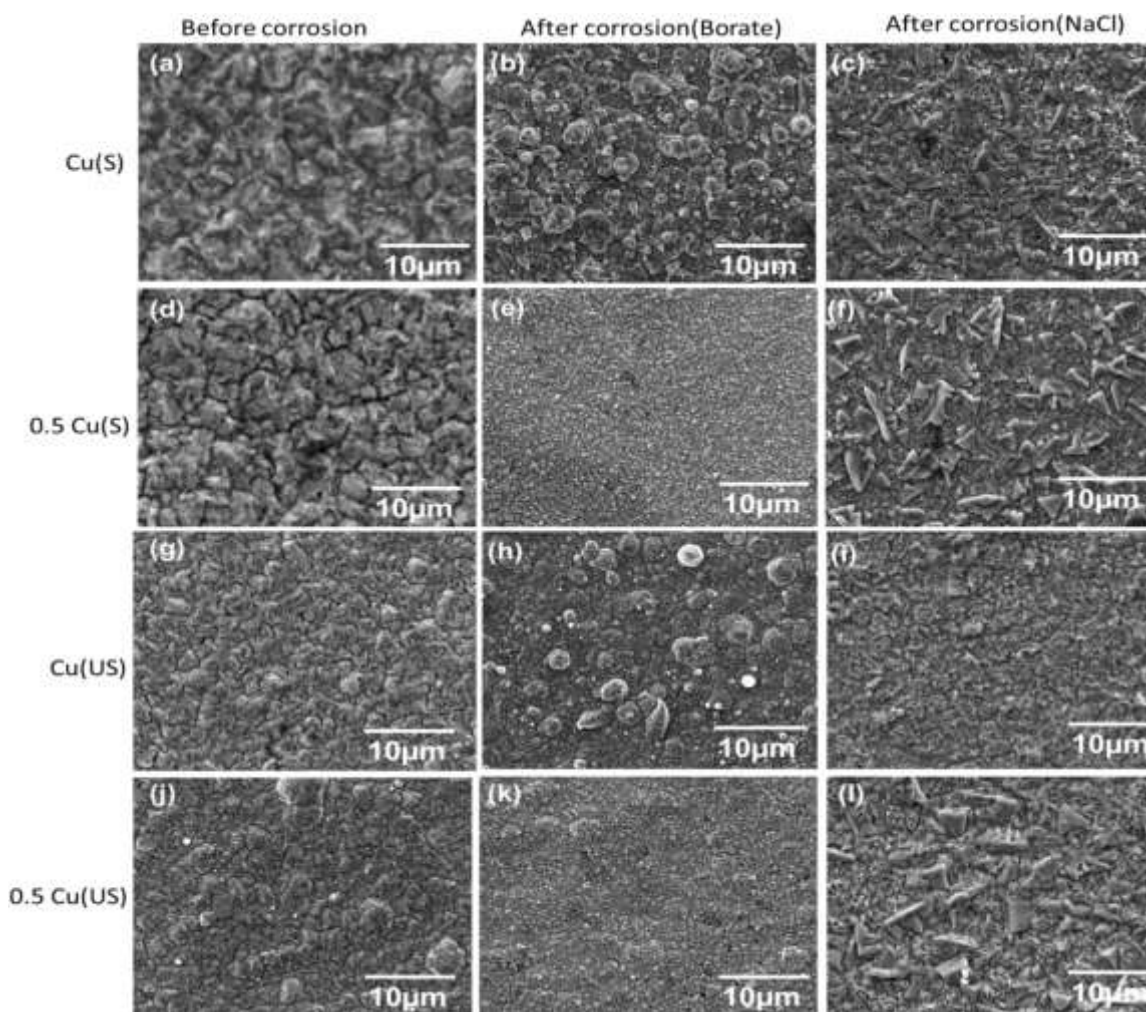


Figure 6.20: SEM image of Cu and Cu-FLGPs composite before and after corrosion of films in 3.5% NaCl solution and borate buffer solution corroded at a scan rate of 5 mV/s

The images have been taken for the corroded samples tested up to +0.4 V, where the samples have entered to the passivation region. SEM images of Cu and 0.5Cu-RFLGPs(Hy) before corrosion are having almost similar kind of appearances. Now focusing on the after corrosion images, the microstructure consists of faceted crystals which is a typical structure corresponding to $\text{Cu}_2\text{O}/\text{CuO}$ phases. This can be an acceptable logic as 400 mV potential at pH 7 is sufficient enough to form a passive layer on copper. The corroded SEM images of 0.5Cu-RFLGPs(Hy) and 0.5Cu-RFLGPs(Vc) films have also similar kinds of appearances signifying the fact that both have followed the same mechanism of corrosion. Table 6.11 shows the elemental analysis for composite samples treated in 3.5% NaCl solution. From the table it can be inferred that, Cl incorporation has been decreased with increase of graphene concentration.

Table 6.11: EDS analysis of corroded samples of Cu and Cu-RFLGPs treated in 3.5% NaCl

Thin film	C (wt%)	O (wt%)	Cl (wt%)	Cu (wt%)
Cu	0	8.29	32.8	58.9
Cu-0.1RFLGPs(Hy)	3.62	5.36	16.99	74.03
Cu-0.3RFLGPs(Hy)	27.89	7.15	2.74	62.22
Cu-0.5RFLGPs(Hy)	39.81	7.97	0.85	51.38
Cu-0.1RFLGPs(Vc)	5.38	2.55	28.82	63.25
Cu-0.3RFLGPs(Vc)	34.1	9.92	14.51	41.46
Cu-0.5RFLGPs(Vc)	45.71	4.53	0.18	49.58

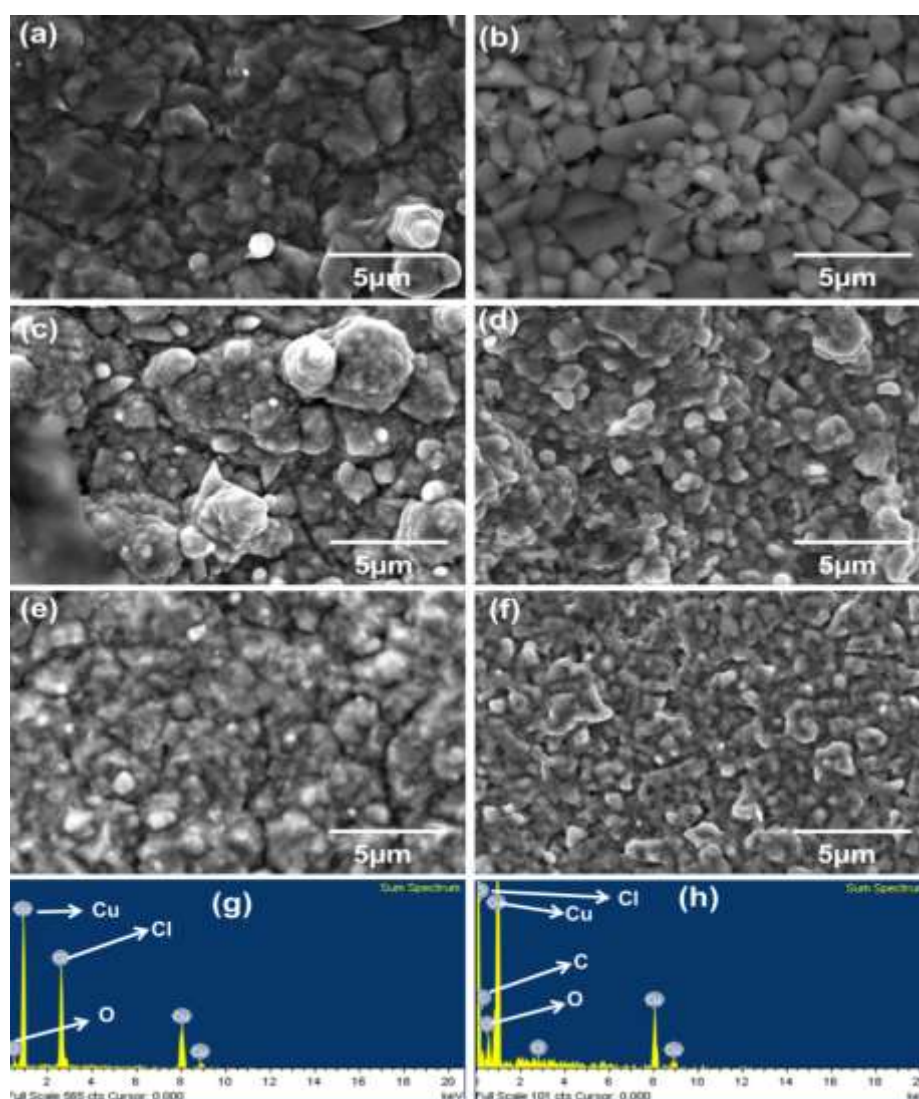


Figure 6.21: SEM image of (a) Cu, (c) 0.5Cu-RFLGPs(Hy) and (e) 0.5Cu-RFLGPs(Vc) before corrosion, (b) Cu, (d) 0.5Cu-RFLGPs(Hy) and (f) 0.5Cu-RFLGPs(Vc) after corrosion, EDS spectra of (g) Cu and (h) Cu-RFLGPs

6.3.4 Mechanism:

The observations can be summarized below by proposing the possible corrosion phenomena which might have occurred in the present investigation. The mechanisms of corrosion behavior of composite samples were proposed by equations given in Table 6.13. At OCP, i.e. at the equilibrium electrochemical point, copper dissolution takes place as per the equation 6.11 and 6.12 in all the solutions. However, the rate of dissolution would get affected by the fact that chloride ions (in 3.5% NaCl) will increase the rate by decreasing the pH of the solution near the vicinity of the electrode surface through the formation of HCl as per the reaction, $H^+ + Cl^- = HCl$. Simultaneously, there could be absorption of Cl ions inside the film, as the sizes of the ions are very small. The said logic can be explained through the observed impedance parameters. It can be noticed that due to absorption of Cl ions (R_a parameters and values) the polarization values (R_p) are low in NaCl solutions and high in borate buffer solutions. The said trend would testify the fact that dissolution/corrosion of copper is difficult in borate buffer but easy in NaCl solution due to absorption of Cl ions. With incorporation and increase of graphene fillers, the values are increasing in both the conditions of experimentation, hence corrosion is expected to be difficult then (follow figure 6.22). The presence of graphene fillers, being non-metallic phase, might have inhibited dissolution of copper from attack of HCl. Also graphene has higher electrical resistivity in the current study, hence might have imposed restrictions on the flow of electrons, thus not allowing channels for electron transfer through it to the copper phase for dissolution, which has been presented in the schematic image (figure 6.232). Furthermore, the R_a values are increasing with increase of graphene concentration, indicating restrictions to absorption of Cl ions which might lead to increase in corrosion resistance with higher percentage of graphene incorporation. After corrosion potential, initiation of passivation region onsets by formation of the passive layer with a composition of Cu_2O and CuO in borate buffer solution through equations 6.14 and 6.17, and in case of salt solution a mixed-phase comprising of Cu_2O/CuO and $CuCl + CuCl_2$ in chloride solution on the surface of the copper following equations 6.13 to 6.18. The $CuCl + CuCl_2$ phase would have formed as a singular layer or by dissolution of the copper oxide layer through equation 6.19.

Table 6.12: Comparison of MPY with Equivalent Metric-Rate Expressions [186]

Relative Corrosion Resistance	mpy	mm/yr	μm/yr	nm/h	pm/h
Outstanding	< 1	< 0.02	< 25	< 2	< 1
Excellent	1-5	0.02-0.1	25-100	2-10	1-5
Good	5-20	0.1-0.5	100-500	10-50	20-50
Fair	20-50	0.1-1	500-1000	50-150	20-50
Poor	50-200	1-5	1000-5000	150-500	50-200
Unacceptable	200+	5+	5000+	500+	200+

Table 6.13: List of reactions during corrosion, passivation and dissolution of composite films

Borate buffer	3.5% NaCl	Regions*
$2Cu + O_2 + H_2O = 2Cu^{2+} + 4OH^-$ (6.11)	$2Cu + O_2 + H_2O = 2Cu^{2+} + 4OH^-$ (6.11)	I
$2Cu + O_2 + H_2O = 4Cu^+ + 4OH^-$ (6.12)	$Cu^{2+} + 2H_2O + 2Cl^- = (CuOH)_2 + 2HCl$ (6.13)	
$4Cu + 2H_2O = 2Cu_2O + 4H^+ + 4e^-$ (6.14)	$2Cu + H_2O = 2Cu_2O + 4H^+ + 4e^-$ (6.15)	II
$2Cu + 2H_2O = 2CuO + 4H^+ + 4e^-$ (6.17)	$Cu^{2+} + 2Cl^- = CuCl_2$ (6.16)	
	$Cu^+ + Cl^- = CuCl$ (6.18)	
	$Cu_2O + H_2O + 4Cl^- = 2CuCl_2 + 2OH^- + 2e^-$ (6.19)	
$Cu_2O + H_2O = 2Cu^+ + 2OH^-$ (6.20)	$CuCl + H_2O + 0.5O_2 = Cu^+ + Cl^- + 2OH^-$ (6.21)	III
$CuO + H_2O = Cu^{2+} + 2OH^-$ (6.22)	$CuCl_2 + H_2O + 0.5O_2 = Cu^{2+} + 2Cl^- + 2OH^-$ (6.23)	

In the presence of graphene fillers, the weight percentage of oxygen, as well as chloride ions is observed to be less (Tables 6.10 and 6.11). It might be logical to argue that, graphene being chemically inert has not allowed the solid state diffusion of oxide ions to form thicker layer and chloride ions inside the copper oxide lattice to replace the oxygen

anion position and hence dissolve it. Hence, the thin oxide layer, with less chloride phase, would have provided better resistance as compared to pure copper coatings. The metastable dissolution of films prepared in silent conditions could be due to uneven distribution of graphene in the films which might have led to formation of micro-galvanic couples in these films. The dissolution of the films after entering into higher oxidizing power of the solution would have taken place following equations 6.20 and 6.21 in borate buffer solutions and 6.22 and 6.23 in salt solutions. In either case, films prepared under sonication are found to be better, which might be due to the directional growth of (220) plane. Hence, the thin oxide layer with less chloride phase would have provided better resistance as compared to pure copper coatings. Along with the above-proposed concept of formation of a mixed passive layer, chloride ions also can de-laminate the passive layer by getting absorbed at the anionic vacancy sites. However, in the potential range of experimentation, the dissolution of the passive layer has not been observed, hence it is expected that the passive layer is intact on the surface of the copper. The schematic of the above proposed has been presented in figure 6.22.

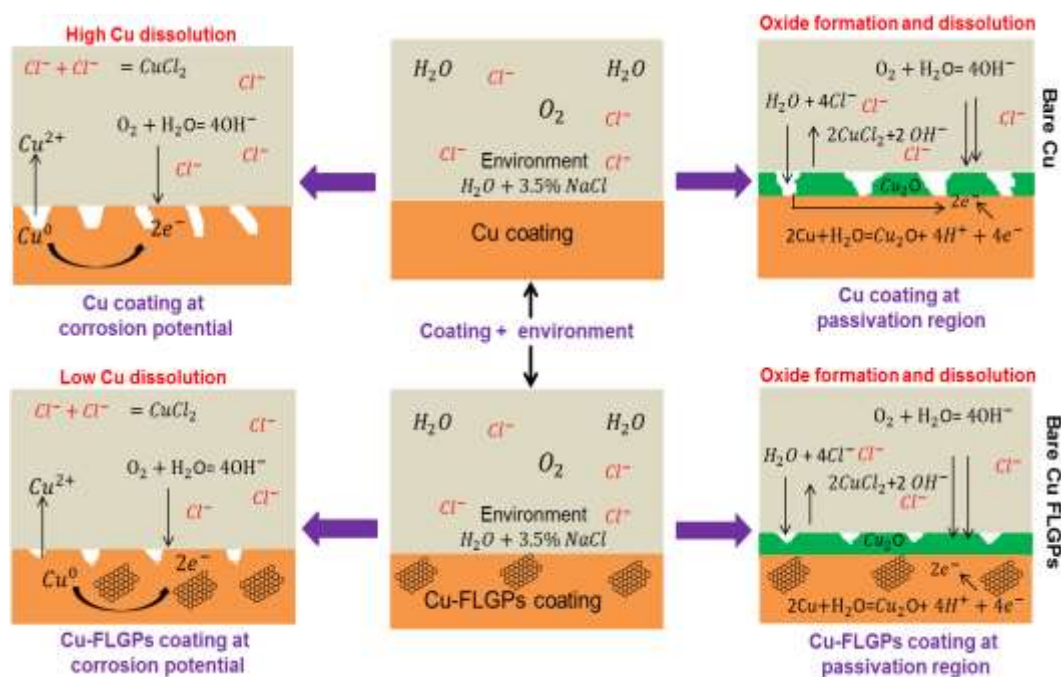


Figure 6.22: Schematic image of mechanism for corrosion resistance of Cu and Cu-FLGPs thin films

6.4 Concluding remarks

The corrosion mechanisms of composite films were explored by the electrochemical method using three solutions i.e. borate buffer, borate buffer with 3.5% NaCl and 3.5% NaCl. The following major results could be made to summarize the present investigation:

- The graphene used in the study has been synthesized in-house through electrochemical intercalation and exfoliation from an acidic solution. The graphene was found to be few layered and partially functionalized, which has been found to be beneficial for proper anchoring to the Cu matrix during electroplating of composite films.
- The composite films (of thickness around 20 μm) found to fall in the acceptable domain to experiment further for corrosion studies. Application of sonication has definitely improved the film properties due to its capability of uniform dispersion of the FLGPs reinforcements in the metal matrix.
- Borate buffer solution had been used to experiment for the general corrosion behavior of the films, whereas 3.5%NaCl was used for pitting corrosion studies of the films. The sono-electroplated films with FLGPs and RFLGPs have shown better anti-corrosion property than the pure and silent conditioned films. The E_{corr} value shifted towards positive values with increase in FLGPs/RFLGPs concentration and also demonstrated high polarization resistances. Corrosion products were found to be oxide and a mixture of oxide and chloride, in testing conditions of borate and salt solutions respectively. Composite films with 0.5 g/L concentration exhibited the best performing composite films in context of corrosion resistance.

Chapter 7

7: Conclusions

7.1 Concluding remarks

In the current research, few layer graphene particles (FLGPs) have been synthesized through electrochemical intercalation and exfoliation techniques by using two aqueous electrolytes i.e. 1M H₂SO₄ and 1 M HNO₃ and high quality graphite particles as the working electrode and counter electrode. The prepared FLGPs contain functional groups of hydroxylation (C-H), carboxyl (C-OH), epoxy (C-O-C) carboxylation such as carbonyl (C=O), and alkoxy (C-O). Further, the functional groups of FLGPs have been reduced by chemical reduction using reducing agents i.e. hydrazine hydrate and ascorbic acid and the obtained graphene has been termed as reduced FLGPs (RFLGPs). The prepared FLGPs and RFLGPs have been used as reinforcement to synthesize Cu-FLGPs and Cc-RFLGPs composite. The structure, phase and different properties of the composites have been studied elaborately. Further, the composites have been explored as an anti-corrosive coating. Hence, the concluding remarks of the detailed investigation of the current research work are summarized below:

- The structural studies of FLGPs and RFLGPs have been performed by XRD and Raman spectra. The XRD analysis confirms the (002) and (001) planes. FLGPs prepared by HNO₃ contains GO peak of (001) plane. After the chemical reduction of FLGPs, the (001) plane has vanished and confirms the reduction of FLGPs by the said reduction method.
- The maximum thermal reduction of FLGPs are 62% and 68% which were prepared by H₂SO₄ and HNO₃ electrolytes respectively. TGA analysis confirms the stability of HHY2, HVC2, NHY2 and NVC2 RFLGPs with maximum yields of around 29, 35, 22 and 30% respectively.
- The composite films (of thickness around 20 μm) have been successfully prepared by electrodeposition route and the distribution of the second phase particles i.e. FLGPs and RFLGPs of 0.1 g/L, 0.3 g/L and 0.5 g/L concentrations was achieved through sonication. Application of sonication has significantly improved the film properties due to its capability to disperse the FLGPs and RFLGPs reinforcements uniformly in the metal matrix.
- Cu-FLGPs, as well as Cu-RFLGPs composite with 0.5 g/L, have shown 31% and 38% higher hardness as compared to the pure copper thin film. The electrical resistivity of

composites has been increased as compared to pure copper due to the defects of FLGPs.

- The wear performance of electrodeposited Cu-FLGPs and Cu-RFLGPs composite films have also been evaluated. The composite shows higher wear performance as compared to pure copper films prepared by the same route.
- Borate buffer solution had been used to experiment with the general corrosion behavior of the films, whereas 3.5% NaCl was used for pitting corrosion studies of the films. The sono-electroplated films with FLGPs and RFLGPs have shown better anti-corrosion property than the pure and silent conditioned films. The E_{corr} value shifted towards positive values with an increase in graphene concentration and also demonstrated high polarization resistances. The corrosion of copper film was found to be decreased up to 50% on addition of the graphene reinforcements in the Cu matrix. Corrosion products were found to be oxide and a mixture of oxide and chloride, in testing conditions of borate and salt solutions respectively. Composite films with 0.5 g/L concentration exhibited the best performing composite films in the context of corrosion resistance.

The above results may provide a testimony for the prepared FLGPs and RFLGPs to explore in various useful functional areas including the field of electronics, sensor, supercapacitor, drug delivery etc. and the as-synthesized composite films may find huge applications as a heat spreader, electro-friction materials and as anti-corrosion coatings.

References

- [1] F. Chen, N. Gupta, R.K. Behera, P.K. Rohatgi, Graphene-Reinforced Aluminum Matrix Composites: A Review of Synthesis Methods and Properties, *Jom.* 70 (2018) 837–845. doi:10.1007/s11837-018-2810-7.
- [2] M. Chmielewski, R. Michalczewski, W. Piekoszewski, M. Kalbarczyk, Tribological Behaviour of Copper-Graphene Composite Materials, *Key Engineering Materials.* 674 (2016) 219–224. doi:10.4028/www.scientific.net/KEM.674.219.
- [3] Bethencourt M., F. Botana J., Calvino J., J.M. Marcos, Rodríguez-Chacón, M. A., Graphene based materials and their composites as coatings, *Corrosion Science.* 13 (1998) 1803–1819. doi:10.3144/expresspolymlett.2013.72.
- [4] G. Darabdhara, B. Sharma, M.R. Das, R. Boukherroub, S. Szunerits, Cu-Ag bimetallic nanoparticles on reduced graphene oxide nanosheets as peroxidase mimic for glucose and ascorbic acid detection, *Sensors and Actuators, B: Chemical.* 238 (2017) 842–851. doi:10.1016/j.snb.2016.07.106.
- [5] M.E. Turan, Y. Sun, Y. Akgul, Y. Turen, H. Ahlatci, The effect of GNPs on wear and corrosion behaviors of pure magnesium, *Journal of Alloys and Compounds.* 724 (2017) 14–23. doi:10.1016/j.jallcom.2017.07.022.
- [6] A. Mallik, B.C. Ray, Morphological study of electrodeposited copper under the influence of ultrasound and low temperature, *Thin Solid Films.* 517 (2009) 6612–6616. doi:10.1016/j.tsf.2009.04.054.
- [7] T.S. Koltsova, L.I. Nasibulina, I. V Anoshkin, V. V Mishin, E.I. Kauppinen, O. V Tolochko, A.G. Nasibulin, New Hybrid Copper Composite Materials Based on Carbon Nanostructures, *Journal of Materials Science and Engineering B.* 2 (2012) 240–246.
- [8] S.F. Bartolucci, J. Paras, M.A. Rafiee, J. Rafiee, S. Lee, D. Kapoor, N. Koratkar, Graphene-aluminum nanocomposites, *Materials Science and Engineering A.* 528 (2011) 7933–7937. doi:10.1016/j.msea.2011.07.043.
- [9] K. Pietrzak, N. Sobczak, M. Chmielewski, M. Homa, A. Gazda, R. Zyba??a, A. Strojny-N??dza, Effects of Carbon Allotropic Forms on Microstructure and Thermal Properties of Cu-C Composites Produced by SPS, *Journal of Materials Engineering and Performance.* 25 (2016) 3077–3083. doi:10.1007/s11665-015-1851-0.
- [10] C. Rouse, S. Beaufils, P. Fricoteaux, Electrodeposition of Cu-Zn thin films from room temperature ionic liquid, *Electrochimica Acta.* 107 (2013) 624–631. doi:10.1016/j.electacta.2013.06.053.
- [11] M. Ebrahimi, M.A. Par, Twenty-year uninterrupted endeavor of friction stir processing by focusing on copper and its alloys, *Journal of Alloys and Compounds.* 781 (2019) 1074–1090. doi:10.1016/j.jallcom.2018.12.083.

- [12] D.A. Simon, E. Bischoff, G.G. Buonocore, P. Cerruti, M.G. Raucci, H. Xia, H.S. Schrekker, M. Lavorgna, L. Ambrosio, R.S. Mauler, Graphene-based masterbatch obtained via modified polyvinyl alcohol liquid-shear exfoliation and its application in enhanced polymer composites, *Materials & Design*. 134 (2017) 103–110. doi:10.1016/j.matdes.2017.08.032.
- [13] 1 A K Geim, K. S. Novoselov, 1* S. V. Morozov, 2 D. Jiang, 1 Y. Zhang, 1 S. V. Dubonos, 2 I. V. Grigorieva, 1 A. A. Firsov, 2, Electric Field Effect in Atomically Thin Carbon Films, *Science*. 306 (2004) 666–670.
- [14] K.E. Whitener, P.E. Sheehan, Graphene synthesis, *Diamond and Related Materials*. 46 (2014) 25–34. doi:10.1016/j.diamond.2014.04.006.
- [15] K. Rajkumar, S. Aravindan, Tribological behavior of microwave processed copper-nanographite composites, *Tribology International*. 57 (2013) 282–296. doi:10.1016/j.triboint.2012.06.023.
- [16] K. Rajkumar, S. Aravindan, Tribological studies on microwave sintered copper-carbon nanotube composites, *Wear*. 270 (2011) 613–621. doi:10.1016/j.wear.2011.01.017.
- [17] L. Xu, C. Srinivasakannan, L. Zhang, M. Yan, J. Peng, H. Xia, S. Guo, Fabrication of tungsten-copper alloys by microwave hot pressing sintering, *Journal of Alloys and Compounds*. 658 (2016) 23–28. doi:10.1016/j.jallcom.2015.10.186.
- [18] F.C. Walsh, C.T.J. Low, A review of developments in the electrodeposition of tin-copper alloys, *Surface and Coatings Technology*. 304 (2016) 246–262. doi:10.1016/j.surfcoat.2016.06.065.
- [19] S. Ghosh, Electroless copper deposition: A critical review, *Thin Solid Films*. 669 (2019) 641–658. doi:10.1016/j.tsf.2018.11.016.
- [20] N.V. Sai, M. Komaraiah, a. V.S.R. Raju, Preparation and Properties of Sintered Copper-Tin Composites Containing Copper Coated or Uncoated Fly Ash, *Materials and Manufacturing Processes*. 23 (2008) 651–657. doi:10.1080/10426910802316617.
- [21] A. Hovestad, L.J.J. Janssen, Electrochemical codeposition of inert particles in a metallic matrix, *Journal of Applied Electrochemistry*. 25 (1995) 519–527. doi:10.1007/BF00573209.
- [22] C.R. Thurber, Y.H. Ahmad, S.F. Sanders, A. Al-Shenawa, N. D'Souza, A.M.A. Mohamed, T.D. Golden, Electrodeposition of 70-30 Cu-Ni nanocomposite coatings for enhanced mechanical and corrosion properties, *Current Applied Physics*. 16 (2016) 387–396. doi:10.1016/j.cap.2015.12.022.
- [23] S.F. Abbas, S.J. Seo, K.T. Park, B.S. Kim, T.S. Kim, Effect of grain size on the electrical conductivity of copper-iron alloys, *Journal of Alloys and Compounds*. 720 (2017) 8–16. doi:10.1016/j.jallcom.2017.05.244.
- [24] P.M. Hannula, A. Peltonen, J. Aromaa, D. Janas, M. Lundström, B.P. Wilson, K. Koziol, O. Forsén, Carbon nanotube-copper composites by electrodeposition on carbon nanotube fibers, *Carbon*. 107 (2016) 281–287.

doi:10.1016/j.carbon.2016.06.008.

- [25] A. Boden, B. Boerner, P. Kusch, I. Firkowska, S. Reich, Nanoplatelet size to control the alignment and thermal conductivity in copper-graphite composites, *Nano Letters*. 14 (2014) 3640–3644. doi:10.1021/nl501411g.
- [26] W.M. Daoush, B.K. Lim, C.B. Mo, D.H. Nam, S.H. Hong, Electrical and mechanical properties of carbon nanotube reinforced copper nanocomposites fabricated by electroless deposition process, *Materials Science and Engineering A*. 513–514 (2009) 247–253. doi:10.1016/j.msea.2009.01.073.
- [27] K.S. Novoselov, A.K. Geim, S. V. Morozov, D. Jiang, Y. Zhang, S. V. Dubonos, I. V. Grigorieva, A.A. Firsov, Electric Field Effect in Atomically Thin Carbon Films, *Science*. 306 (2004) 666–669. doi:10.1126/science.1102896.
- [28] A.K. Geim, Graphene : Status and Prospects, 324 (2009) 1530–1535.
- [29] K.S. Novoselov, V.I. Fal'ko, L. Colombo, P.R. Gellert, M.G. Schwab, K. Kim, A roadmap for graphene, *Nature*. 490 (2012) 192–200. doi:10.1038/nature11458.
- [30] B. Zhang, Y. Wang, G. Zhai, Biomedical applications of the graphene-based materials, *Materials Science and Engineering C*. 61 (2016) 953–964. doi:10.1016/j.msec.2015.12.073.
- [31] F. Torrisi, T. Hasan, W.P. Wu, Z.P. Sun, A. Lombardo, T.S. Kulmala, G.W. Hsieh, S.J. Jung, F. Bonaccorso, P.J. Paul, D.P. Chu, A.C. Ferrari, Inkjet-Printed Graphene Electronics, *ACS Nano*. 6 (2012) 2992–3006. doi:10.1021/nm2044609.
- [32] D.P. Wong, H.P. Tseng, Y.T. Chen, B.J. Hwang, L.C. Chen, K.H. Chen, A stable silicon/graphene composite using solvent exchange method as anode material for lithium ion batteries, *Carbon*. 63 (2013) 397–403. doi:10.1016/j.carbon.2013.06.095.
- [33] Z. Bo, X. Shuai, S. Mao, H. Yang, J. Qian, J. Chen, J. Yan, K. Cen, Green preparation of reduced graphene oxide for sensing and energy storage applications, *Scientific Reports*. 4 (2014) 1–8. doi:10.1038/srep04684.
- [34] C.A. Ubani, M.A. Ibrahim, M.A.M. Teridi, K. Sopian, J. Ali, K.T. Chaudhary, Application of graphene in dye and quantum dots sensitized solar cell, *Solar Energy*. 137 (2016) 531–550. doi:10.1016/j.solener.2016.08.055.
- [35] S.K. Sahoo, S. Ratha, C.S. Rout, A. Mallik, Physicochemical properties and supercapacitor behavior of electrochemically synthesized few layered graphene nanosheets, *Journal of Solid State Electrochemistry*. 20 (2016) 3415–3428. doi:10.1007/s10008-016-3304-6.
- [36] S. Ren, P. Rong, Q. Yu, Preparations , properties and applications of graphene in functional devices : A concise review, 44 (2018) 11940–11955. doi:10.1016/j.ceramint.2018.04.089.
- [37] V. Balaji, K. Lau, D. Hui, D. Bhattacharyya, Graphene-based materials and their composites : A review on production , applications and product limitations, *Composites Part B*. 142 (2018) 200–220. doi:10.1016/j.compositesb.2018.01.013.

- [38] M. Yi, Z. Shen, A review on mechanical exfoliation for the scalable production of graphene, *Journal of Materials Chemistry A*. 3 (2015) 11700–11715. doi:10.1039/c5ta00252d.
- [39] B. Deng, Z. Liu, H. Peng, Toward Mass Production of CVD Graphene Films, 1800996 (2018) 1–25. doi:10.1002/adma.201800996.
- [40] X. Chen, L. Zhang, S. Chen, Large area CVD growth of graphene, *Synthetic Metals*. 210 (2015) 95–108. doi:10.1016/j.synthmet.2015.07.005.
- [41] R.M.N.M. Rathnayake, H.W.M.A.C. Wijayasinghe, H.M.T.G.A. Pitawala, M. Yoshimura, H.H. Huang, Synthesis of graphene oxide and reduced graphene oxide by needle platy natural vein graphite, *Applied Surface Science*. 393 (2017) 309–315. doi:10.1016/j.apsusc.2016.10.008.
- [42] A.K. Behera, A. Mallik, Ultrasound assisted electroplating of nano-composite thin film of Cu matrix with electrochemically in-house synthesized few layer graphene nano-sheets as reinforcement, *Journal of Alloys and Compounds*. 750 (2018) 587–598. doi:10.1016/j.jallcom.2018.03.264.
- [43] S.T. Hossain, R. Wang, Electrochemical Exfoliation of Graphite: Effect of Temperature and Hydrogen Peroxide Addition, *Electrochimica Acta*. 216 (2016) 253–260. doi:10.1016/j.electacta.2016.09.022.
- [44] M. Alanyalıoğlu, J.J. Segura, J. Oró-Solè, N. Casañ Pastor, The synthesis of graphene sheets with controlled thickness and order using surfactant-assisted electrochemical processes, *Carbon*. 50 (2012) 142–152. doi:10.1016/j.carbon.2011.07.064.
- [45] V. Georgakilas, A.B. Bourlinos, E. Ntararas, A. Ibraliu, D. Gournis, K. Dimos, A. Kouloumpis, R. Zboril, Graphene nanobuds: Synthesis and selective organic derivatisation, *Carbon*. 110 (2016) 51–55. doi:10.1016/j.carbon.2016.09.003.
- [46] Graphene synthesis, *Diamond and Related Materials*. 46 (2014) 25–34. doi:10.1016/J.DIAMOND.2014.04.006.
- [47] R. Ramachandran, S. Felix, G.M. Joshi, B.P.C. Raghupathy, S.K. Jeong, A.N. Grace, Synthesis of graphene platelets by chemical and electrochemical route, *Materials Research Bulletin*. 48 (2013) 3834–3842. doi:10.1016/j.materresbull.2013.05.085.
- [48] S.K. Tiwari, A. Huczko, R. Oraon, A. De Adhikari, G.C. Nayak, Facile electrochemical synthesis of few layered graphene from discharged battery electrode and its application for energy storage, *Arabian Journal of Chemistry*. 10 (2017) 556–565. doi:10.1016/j.arabjc.2015.08.016.
- [49] K. Spyrou, L. Kang, E.K. Diamanti, R.Y. Gengler, D. Gournis, M. Prato, P. Rudolf, A novel route towards high quality fullerene-pillared graphene, *Carbon*. 61 (2013) 313–320. doi:10.1016/j.carbon.2013.05.010.
- [50] W. Guoxiu, Y. Juan, P. Jinsoo, G. Xinglong, W. Bei, L. Hao, Y. Jane, Facile synthesis and characterization of graphene nanosheets, *Journal of Physical Chemistry C*. 112 (2008) 8192–8195. doi:10.1021/jp710931h.

- [51] K. Parvez, Z. Wu, R. Li, X. Liu, R. Graf, Exfoliation of Graphite into Graphene in Aqueous Solutions, *Sup Info*. (2014). doi:10.1021/ja5017156.
- [52] M. Zhou, J. Tang, Q. Cheng, G. Xu, P. Cui, L.C. Qin, Few-layer graphene obtained by electrochemical exfoliation of graphite cathode, *Chemical Physics Letters*. 572 (2013) 61–65. doi:10.1016/j.cplett.2013.04.013.
- [53] M. Zhou, T. Tian, X. Li, X. Sun, J. Zhang, P. Cui, J. Tang, L.C. Qin, Production of graphene by liquid-phase exfoliation of intercalated graphite, *International Journal of Electrochemical Science*. 9 (2014) 810–820.
- [54] S.K. Sahoo, A. Mallik, Synthesis and characterization of conductive few layered graphene nanosheets using an anionic electrochemical intercalation and exfoliation technique, *Journal of Materials Chemistry C*. 3 (2015) 10870–10878. doi:10.1039/c5tc01893e.
- [55] M.J. Fernández-Merino, L. Guardia, J.I. Paredes, S. Villar-Rodil, P. Solís-Fernández, A. Martínez-Alonso, J.M.D. Tascón, Vitamin C is an ideal substitute for hydrazine in the reduction of graphene oxide suspensions, *Journal of Physical Chemistry C*. 114 (2010) 6426–6432. doi:10.1021/jp100603h.
- [56] H.M. Ju, S.H. Huh, S.H. Choi, H.L. Lee, Structures of thermally and chemically reduced graphene, *Materials Letters*. 64 (2010) 357–360. doi:10.1016/j.matlet.2009.11.016.
- [57] W. Chen, L. Yan, P.R. Bangal, Preparation of graphene by the rapid and mild thermal reduction of graphene oxide induced by microwaves, *Carbon*. 48 (2010) 1146–1152. doi:10.1016/j.carbon.2009.11.037.
- [58] T. Zhang, D. Zhang, M. Shen, A low-cost method for preliminary separation of reduced graphene oxide nanosheets, *Materials Letters*. 63 (2009) 2051–2054. doi:10.1016/j.matlet.2009.06.050.
- [59] T.V. Cuong, V.H. Pham, Q.T. Tran, J.S. Chung, E.W. Shin, J.S. Kim, E.J. Kim, Optoelectronic properties of graphene thin films prepared by thermal reduction of graphene oxide, *Materials Letters*. 64 (2010) 765–767. doi:10.1016/j.matlet.2010.01.009.
- [60] J. He, L. Fang, Controllable synthesis of reduced graphene oxide, *Current Applied Physics*. 16 (2016) 1152–1158. doi:10.1016/j.cap.2016.06.011.
- [61] X.Y. Peng, X.X. Liu, D. Diamond, K.T. Lau, Synthesis of electrochemically-reduced graphene oxide film with controllable size and thickness and its use in supercapacitor, *Carbon*. 49 (2011) 3488–3496. doi:10.1016/j.carbon.2011.04.047.
- [62] S. Stankovich, D.A. Dikin, R.D. Piner, K.A. Kohlhaas, A. Kleinhammes, Y. Jia, Y. Wu, S.B.T. Nguyen, R.S. Ruoff, Synthesis of graphene-based nanosheets via chemical reduction of exfoliated graphite oxide, *Carbon*. 45 (2007) 1558–1565. doi:10.1016/j.carbon.2007.02.034.
- [63] H. Feng, R. Cheng, X. Zhao, X. Duan, J. Li, A low-temperature method to produce highly reduced graphene oxide., *Nature Communications*. 4 (2013) 1539. doi:10.1038/ncomms2555.

- [64] J. Liu, Graphene-based Composites for Electrochemical Energy Storage, (2017) 39–51. doi:10.1007/978-981-10-3388-9.
- [65] A. Furst, R.C. Berlo, S. Hooton, Catalytic Hydrazine Reductions, Hydrazine as a Reducing Agent for Organic Compounds. 65 (1965) 51–68.
- [66] C. Xu, R. Yuan, X. Wang, Selective reduction of graphene oxide, *New Carbon Materials*. 71 (2014) 345. doi:10.1016/j.carbon.2014.01.048.
- [67] J. Wang, E.C. Salihi, L. Šiller, Green reduction of graphene oxide using alanine, *Materials Science and Engineering C*. 72 (2017) 1–6. doi:10.1016/j.msec.2016.11.017.
- [68] Q. Yan, Q. Liu, J. Wang, A simple and fast microwave assisted approach for the reduction of graphene oxide, *Ceramics International*. 42 (2015) 3007–3013. doi:10.1016/j.ceramint.2015.10.085.
- [69] J. Gao, F. Liu, Y. Liu, N. Ma, Z. Wang, X. Zhang, Environment-friendly method to produce graphene that employs vitamin C and amino acid, *Chemistry of Materials*. 22 (2010) 2213–2218. doi:10.1021/cm902635j.
- [70] R.A. Morton, Vitamins A and vision, *Br J Nutr*. 5 (1951) 100–104. doi:10.1079/BJN19510012.
- [71] J. Gao, F. Liu, Y. Liu, N. Ma, Z. Wang, X. Zhang, 39 Environment-Friendly Method To Produce Graphene That Employs Vitamin C and Amino Acid.pdf, (n.d.) 1–2.
- [72] J. Zhang, H. Yang, G. Shen, P. Cheng, J. Zhang, S. Guo, Reduction of graphene oxide via L-ascorbic acid, *Chem. Commun*. 46 (2010) 1112–1114. doi:10.1039/B917705A.
- [73] K. Jaroensil, V. Thongpool, S. Niamlang, Effect of Ascorbic acid Concentration on Electrical Conductivity of reduced Graphene Oxide, (2016) 44–47. doi:10.15242/iie.e0816026.
- [74] J. Zhang, H. Yang, G. Shen, P. Cheng, J. Zhang, S. Guo, Reduction of graphene oxide via L-ascorbic acid. Supporting Information, *Chemical Communications (Cambridge, England)*. 2 (2010).
- [75] H. Ding, S. Zhang, J.T. Chen, X.P. Hu, Z.F. Du, Y.X. Qiu, D.L. Zhao, Reduction of graphene oxide at room temperature with vitamin C for RGO-TiO₂ photoanodes in dye-sensitized solar cell, *Thin Solid Films*. 584 (2015) 29–36. doi:10.1016/j.tsf.2015.02.038.
- [76] J. Wang, Z. Li, G. Fan, H. Pan, Z. Chen, D. Zhang, Reinforcement with graphene nanosheets in aluminum matrix composites, *Scripta Materialia*. 66 (2012) 594–597. doi:10.1016/j.scriptamat.2012.01.012.
- [77] Y. Huang, P. Bazarnik, D. Wan, D. Luo, P. Henrique, R. Pereira, M. Lewandowska, J. Yao, B.E. Hayden, T.G. Langdon, Acta Materialia The fabrication of graphene-reinforced Al-based nanocomposites using high-pressure torsion, *Acta Materialia*. 164 (2019) 499–511. doi:10.1016/j.actamat.2018.10.060.

- [78] C.M.P. Kumar, T. V. Venkatesha, R. Shabadi, Preparation and corrosion behavior of Ni and Ni-graphene composite coatings, *Materials Research Bulletin*. 48 (2013) 1477–1483. doi:10.1016/j.materresbull.2012.12.064.
- [79] G. Cieślak, M. Trzaska, Preparation and properties of nanocrystalline Ni/graphene composite coatings deposited by electrochemical method, *Polish Journal of Chemical Technology*. 20 (2018) 29–34. doi:10.2478/pjct-2018-0005.
- [80] E. Cooling, Graphene Improves Copper Film Thermal Conductivity, (2014).
- [81] W.J. Kim, T.J. Lee, S.H. Han, Multi-layer graphene/copper composites: Preparation using high-ratio differential speed rolling, microstructure and mechanical properties, *Carbon*. 69 (2014) 55–65. doi:10.1016/j.carbon.2013.11.058.
- [82] W. Li, D. Li, Q. Fu, C. Pan, Conductive enhancement of copper/graphene composites based on high-quality graphene, *RSC Advances*. 5 (2015) 80428–80433. doi:10.1039/c5ra15189a.
- [83] J.F. Li, L. Zhang, J.K. Xiao, K.C. Zhou, Sliding wear behavior of copper-based composites reinforced with graphene nanosheets and graphite, *Transactions of Nonferrous Metals Society of China (English Edition)*. 25 (2015) 3354–3362. doi:10.1016/S1003-6326(15)63970-X.
- [84] H.S. Maharana, P.K. Rai, A. Basu, Surface-mechanical and electrical properties of pulse electrodeposited Cu–graphene oxide composite coating for electrical contacts, *Journal of Materials Science*. 52 (2017) 1089–1105. doi:10.1007/s10853-016-0405-7.
- [85] C.L.P. Pavithra, B. V. Sarada, K. V. Rajulapati, T.N. Rao, G. Sundararajan, A New Electrochemical Approach for the Synthesis of Copper-Graphene Nanocomposite Foils with High Hardness, *Scientific Reports*. 4 (2014) 1–7. doi:10.1038/srep04049.
- [86] K. Hu, D.D. Kulkarni, I. Choi, V. V Tsukruk, Progress in Polymer Science Graphene-polymer nanocomposites for structural and functional applications, *Progress in Polymer Science*. 39 (2014) 1934–1972. doi:10.1016/j.progpolymsci.2014.03.001.
- [87] X. Ji, Y. Xu, W. Zhang, L. Cui, J. Liu, Composites : Part A Review of functionalization , structure and properties of graphene / polymer composite fibers, *COMPOSITES PART A*. 87 (2016) 29–45. doi:10.1016/j.compositesa.2016.04.011.
- [88] H. Chang, C. Chang, Y. Tsai, Electrochemically synthesized graphene / polypyrrole composites and their use in supercapacitor, *Carbon*. 50 (2012) 2331–2336. doi:10.1016/j.carbon.2012.01.056.
- [89] Y. Liu, H. Wang, J. Zhou, L. Bian, E. Zhu, J. Hai, Electrochimica Acta Graphene / polypyrrole intercalating nanocomposites as supercapacitors electrode, *Electrochimica Acta*. 112 (2013) 44–52. doi:10.1016/j.electacta.2013.08.149.
- [90] M. Li, Q. Liu, Z. Jia, X. Xu, Y. Cheng, Y. Zheng, Graphene oxide / hydroxyapatite composite coatings fabricated by electrophoretic nanotechnology for biological

- applications, *Carbon*. 67 (2013) 185–197. doi:10.1016/j.carbon.2013.09.080.
- [91] Z. Fan, J. Wang, Z. Wang, H. Ran, Y. Li, L. Niu, P. Gong, B. Liu, S. Yang, One-pot synthesis of graphene / hydroxyapatite nanorod composite for tissue engineering, *Carbon*. 66 (2013) 407–416. doi:10.1016/j.carbon.2013.09.016.
- [92] S. Erakovic, M. Mitric, I.Z. Matic, Z.D. Juranic, G.C.P. Tsui, K. Yop, S. Jin, Bioactive hydroxyapatite / graphene composite coating and its corrosion stability in simulated body fluid, 624 (2015) 148–157. doi:10.1016/j.jallcom.2014.11.078.
- [93] H. Guo, X. Li, B. Li, J. Wang, S. Wang, Thermal conductivity of graphene / poly (vinylidene fluoride) nanocomposite membrane, *JMADE*. 114 (2017) 355–363. doi:10.1016/j.matdes.2016.11.010.
- [94] N. Theophile, H.K. Jeong, Electrochemical properties of poly (vinyl alcohol) and graphene oxide composite for supercapacitor applications, *Chemical Physics Letters*. 669 (2017) 125–129. doi:10.1016/j.cplett.2016.12.029.
- [95] Z. Cai, H. Xiong, Z. Zhu, H. Huang, L. Li, Y. Huang, X. Yu, Electrochemical synthesis of graphene/polypyrrole nanotube composites for multifunctional applications, *Synthetic Metals*. 227 (2017) 100–105. doi:10.1016/j.synthmet.2017.03.012.
- [96] A. Rose, K.G. Prasad, T. Sakthivel, V. Gunasekaran, T. Maiyalagan, T. Vijayakumar, Applied Surface Science Electrochemical analysis of Graphene Oxide / Polyaniline / Polyvinyl alcohol composite nanofibers for supercapacitor applications, *Applied Surface Science*. 449 (2018) 551–557. doi:10.1016/j.apsusc.2018.02.224.
- [97] P. Yu, R. Bao, X. Shi, W. Yang, M. Yang, oxide / chitosan composite hydrogel for bone tissue engineering, *Carbohydrate Polymers*. 155 (2017) 507–515. doi:10.1016/j.carbpol.2016.09.001.
- [98] K.T. Paula, G. Gaál, G.F.B. Almeida, M.B. Andrade, M.H.M. Facure, D.S. Correa, A. Riul, V. Rodrigues, C.R. Mendonça, Femtosecond laser micromachining of polylactic acid / graphene composites for designing interdigitated microelectrodes for sensor applications, *Optics and Laser Technology*. 101 (2018) 74–79. doi:10.1016/j.optlastec.2017.11.006.
- [99] M. Li, P. Xiong, F. Yan, S. Li, C. Ren, Z. Yin, A. Li, Bioactive Materials An overview of graphene-based hydroxyapatite composites for orthopedic applications, *Bioactive Materials*. 3 (2018) 1–18. doi:10.1016/j.bioactmat.2018.01.001.
- [100] Z. Guo, N. Liao, M. Zhang, W. Xue, Applied Surface Science Theoretical approach to evaluate graphene / PANI composite as highly selective ammonia sensor, *Applied Surface Science*. 453 (2018) 336–340. doi:10.1016/j.apsusc.2018.05.108.
- [101] S. Khasim, Results in Physics Polyaniline-Graphene nanoplatelet composite films with improved conductivity for high performance X-band microwave shielding applications, *Results in Physics*. 12 (2019) 1073–1081. doi:10.1016/j.rinp.2018.12.087.
- [102] C. Mallada, J.L. Menéndez, O.J. Dura, M.A.L. De, R. Menéndez, R. Santamaría,

- Journal of the European Ceramic Society Spark plasma sintered BaTiO₃ / graphene composites for thermoelectric applications, *Journal of the European Ceramic Society*. 37 (2017) 3741–3746. doi:10.1016/j.jeurceramsoc.2017.02.027.
- [103] A. Deepi, G. Sriresh, A.S. Nesaraj, Nano-Structures & Nano-Objects Electrochemical performance of Bi₂O₃ decorated graphene nano composites for supercapacitor applications, 15 (2018) 10–16. doi:10.1016/j.nanoso.2018.03.003.
- [104] C. Wang, Y. Liu, M. Zhao, F. Ye, L. Cheng, Three-dimensional graphene / SiBCN composites for high-performance electromagnetic interference shielding, *Ceramics International*. 44 (2018) 22830–22839. doi:10.1016/j.ceramint.2018.09.074.
- [105] G. Divyapriya, K. Kumar, I. Nambi, Development of a novel graphene / Co₃O₄ composite for hybrid capacitive deionization system, *Desalination*. 451 (2019) 102–110. doi:10.1016/j.desal.2018.03.023.
- [106] Y. Zhang, H. Li, L. Pan, T. Lu, Z. Sun, Capacitive behavior of graphene – ZnO composite film for supercapacitors, *Journal of Electroanalytical Chemistry*. 634 (2009) 68–71. doi:10.1016/j.jelechem.2009.07.010.
- [107] C. Wang, J. Li, C. Amatore, Y. Chen, H. Jiang, X. Wang, Gold Nanoclusters and Graphene Nanocomposites for Drug Delivery and Imaging of Cancer Cells **, (2011) 11644–11648. doi:10.1002/anie.201105573.
- [108] K. Zhang, Applied Surface Science Fabrication of copper nanoparticles / graphene oxide composites for surface-enhanced Raman scattering, *Applied Surface Science*. 258 (2012) 7327–7329. doi:10.1016/j.apsusc.2012.04.002.
- [109] Q. Zhang, Q. Luo, Z. Qin, L. Liu, Z. Wu, B. Shen, W. Hu, Self-Assembly of Graphene-Encapsulated Cu Composites for Nonenzymatic Glucose Sensing, (2018). doi:10.1021/acsomega.7b01197.
- [110] H. Yang, X. Yao, Z. Zheng, L. Gong, L. Yuan, Y. Yuan, Y. Liu, Highly sensitive and stretchable graphene-silicone rubber composites for strain sensing, *Composites Science and Technology*. 167 (2018) 371–378. doi:10.1016/j.compscitech.2018.08.022.
- [111] L. Wang, Z. Wei, M. Mao, H. Wang, Y. Li, J. Ma, Metal oxide / graphene composite anode materials for sodium-ion batteries, *Energy Storage Materials*. 16 (2019) 434–454. doi:10.1016/j.ensm.2018.06.027.
- [112] R. Cui, Y. Han, Z. Zhu, B. Chen, Y. Ding, Q. Zhang, Q. Wang, G. Ma, F. Pei, Z. Ye, Investigation of the structure and properties of electrodeposited Cu / graphene composite coatings for the electrical contact materials of an ultrahigh voltage circuit breaker, *Journal of Alloys and Compounds*. 777 (2019) 1159–1167. doi:10.1016/j.jallcom.2018.11.096.
- [113] S. Jadhav, R.S. Kalubarme, C. Terashima, B.B. Kale, V. Godbole, A. Fujishima, S.W. Gosavi, Electrochimica Acta Manganese dioxide / reduced graphene oxide composite an electrode material for high-performance solid state supercapacitor, *Electrochimica Acta*. 299 (2019) 34–44. doi:10.1016/j.electacta.2018.12.182.
- [114] X. Jin, F. Chen, D. Jia, Y. Cao, H. Duan, Influences of synthetic conditions on the

- photocatalytic performance of ZnS / graphene composites, *Journal of Alloys and Compounds*. 780 (2019) 299–305. doi:10.1016/j.jallcom.2018.11.271.
- [115] Y. Chai, Z. Li, J. Wang, Z. Mo, S. Yang, Construction of hierarchical holey graphene / MnO₂ composites as potential electrode materials for supercapacitors, *Journal of Alloys and Compounds*. 775 (2019) 1206–1212. doi:10.1016/j.jallcom.2018.10.259.
- [116] B. Sakthivel, G. Nammalvar, Selective ammonia sensor based on copper oxide / reduced graphene oxide nanocomposite, *Journal of Alloys and Compounds*. 788 (2019) 422–428. doi:10.1016/j.jallcom.2019.02.245.
- [117] G. Song, Y. Yang, Q. Fu, C. Pan, Preparation of Cu-Graphene Composite Thin Foils via DC Electro-Deposition and Its Optimal Conditions for Highest Properties, *Journal of The Electrochemical Society*. 164 (2017) D652–D659. doi:10.1149/2.0121712jes.
- [118] K. Jagannadham, Electrical conductivity of copper–graphene composite films synthesized by electrochemical deposition with exfoliated graphene platelets, *Journal of Vacuum Science & Technology B, Nanotechnology and Microelectronics: Materials, Processing, Measurement, and Phenomena*. 30 (2012) 03D109. doi:10.1116/1.3701701.
- [119] K. Jagannadham, Orientation dependence of thermal conductivity in copper-graphene composites, *Journal of Applied Physics*. 110 (2011). doi:10.1063/1.3641640.
- [120] K. Jagannadham, Thermal conductivity of copper-graphene composite films synthesized by electrochemical deposition with exfoliated graphene platelets, *Metallurgical and Materials Transactions B: Process Metallurgy and Materials Processing Science*. 43 (2012) 316–324. doi:10.1007/s11663-011-9597-z.
- [121] K. Jagannadham, Volume fraction of graphene platelets in copper-graphene composites, *Metallurgical and Materials Transactions A: Physical Metallurgy and Materials Science*. 44 (2013) 552–559. doi:10.1007/s11661-012-1387-y.
- [122] Y. Raghupathy, A. Kamboj, M.Y. Rekha, N.P. Narasimha Rao, C. Srivastava, Copper-graphene oxide composite coatings for corrosion protection of mild steel in 3.5% NaCl, *Thin Solid Films*. 636 (2017) 107–115. doi:10.1016/j.tsf.2017.05.042.
- [123] Y.J. Mai, M.P. Zhou, H.J. Ling, F.X. Chen, W.Q. Lian, X.H. Jie, Surfactant-free electrodeposition of reduced graphene oxide/copper composite coatings with enhanced wear resistance, *Applied Surface Science*. 433 (2018) 232–239. doi:10.1016/j.apsusc.2017.10.014.
- [124] C.L.P. Pavithra, B. V. Sarada, K. V. Rajulapati, T.N. Rao, G. Sundararajan, Process Optimization for Pulse Reverse Electrodeposition of Graphene-Reinforced Copper Nanocomposites, *Materials and Manufacturing Processes*. 31 (2016) 1439–1446. doi:10.1080/10426914.2015.1127938.
- [125] G. Huang, H. Wang, P. Cheng, H. Wang, B. Sun, S. Sun, C. Zhang, M. Chen, G. Ding, Preparation and characterization of the graphene-Cu composite film by electrodeposition process, *Microelectronic Engineering*. 157 (2016) 7–12.

doi:10.1016/j.mee.2016.02.006.

- [126] H.S. Maharana, P.K. Rai, A. Basu, Surface-mechanical and electrical properties of pulse electrodeposited Cu/graphene oxide composite coating for electrical contacts, *Journal of Materials Science*. 52 (2017) 1089–1105. doi:10.1007/s10853-016-0405-7.
- [127] H.S. Maharana, S. Jena, A. Basu, K. Mondal, High temperature oxidation resistance of electrodeposited Reduced Graphene Oxide (RGO) reinforced copper coating, *Surface and Coatings Technology*. 345 (2018) 140–151. doi:10.1016/j.surfcoat.2018.04.025.
- [128] Q. Zhang, Z. Qin, Q. Luo, Z. Wu, L. Liu, B. Shen, W. Hu, Microstructure and nanoindentation behavior of Cu composites reinforced with graphene nanoplatelets by electroless co-deposition technique, *Scientific Reports*. 7 (2017) 1–12. doi:10.1038/s41598-017-01439-3.
- [129] S. Li, G. Song, Q. Fu, C. Pan, Preparation of Cu- graphene coating via electroless plating for high mechanical property and corrosive resistance, *Journal of Alloys and Compounds*. 777 (2019) 877–885. doi:10.1016/j.jallcom.2018.11.031.
- [130] Y. Peng, Y. Hu, L. Han, C. Ren, Ultrasound-assisted fabrication of dispersed two-dimensional copper/reduced graphene oxide nanosheets nanocomposites, *Composites Part B: Engineering*. 58 (2014) 473–477. doi:10.1016/j.compositesb.2013.10.036.
- [131] X. Li, Y. Zhao, W. Wu, J. Chen, G. Chu, H. Zou, Synthesis and characterizations of graphene-copper nanocomposites and their antifriction application, *Journal of Industrial and Engineering Chemistry*. 20 (2014) 2043–2049. doi:10.1016/j.jiec.2013.09.029.
- [132] X. Gao, H. Yue, E. Guo, H. Zhang, X. Lin, L. Yao, B. Wang, Mechanical properties and thermal conductivity of graphene reinforced copper matrix composites, *Powder Technology*. 301 (2016) 601–607. doi:10.1016/j.powtec.2016.06.045.
- [133] R. Jiang, X. Zhou, Q. Fang, Z. Liu, Copper-graphene bulk composites with homogeneous graphene dispersion and enhanced mechanical properties, *Materials Science and Engineering A*. 654 (2016) 124–130. doi:10.1016/j.msea.2015.12.039.
- [134] C. Ayyappadas, A. Muthuchamy, A. Raja Annamalai, D.K. Agrawal, An investigation on the effect of sintering mode on various properties of copper-graphene metal matrix composite, *Advanced Powder Technology*. 28 (2017) 1760–1768. doi:10.1016/j.apt.2017.04.013.
- [135] N.V. Ponraj, A. Azhagurajan, S.C. Vettivel, X. Sahaya Shajan, P.Y. Nabhiraj, M. Sivapragash, Graphene nanosheet as reinforcement agent in copper matrix composite by using powder metallurgy method, *Surfaces and Interfaces*. 6 (2017) 190–196. doi:10.1016/j.surfin.2017.01.010.
- [136] Y. Chen, X. Zhang, E. Liu, C. He, C. Shi, J. Li, P. Nash, N. Zhao, Fabrication of in-situ grown graphene reinforced Cu matrix composites, *Scientific Reports*. 6 (2016) 19363. doi:10.1038/srep19363.

- [137] X. Wang, J. Li, Y. Wang, Improved high temperature strength of copper-graphene composite material, *Materials Letters*. 181 (2016) 309–312. doi:10.1016/j.matlet.2016.06.034.
- [138] A. Robin, J.L. Rosa, M.B. Silva, Electrodeposition and characterization of Cu-Nb composite coatings, *Surface and Coatings Technology*. 205 (2010) 2152–2159. doi:10.1016/j.surfcoat.2010.08.124.
- [139] M. Cao, D.B. Xiong, Z. Tan, G. Ji, B. Amin-Ahmadi, Q. Guo, G. Fan, C. Guo, Z. Li, D. Zhang, Aligning graphene in bulk copper: Nacre-inspired nanolaminated architecture coupled with in-situ processing for enhanced mechanical properties and high electrical conductivity, *Carbon*. 117 (2017) 65–74. doi:10.1016/j.carbon.2017.02.089.
- [140] K. Chu, C. Jia, Enhanced strength in bulk graphene-copper composites, *Physica Status Solidi (A) Applications and Materials Science*. 211 (2014) 184–190. doi:10.1002/pssa.201330051.
- [141] H. Yue, L. Yao, X. Gao, S. Zhang, E. Guo, H. Zhang, X. Lin, B. Wang, Effect of ball-milling and graphene contents on the mechanical properties and fracture mechanisms of graphene nanosheets reinforced copper matrix composites, *Journal of Alloys and Compounds*. 691 (2017) 755–762. doi:10.1016/j.jallcom.2016.08.303.
- [142] J. Dutkiewicz, P. Ozga, W. Maziarz, J. Pstruś, B. Kania, P. Bobrowski, J. Stolarska, Microstructure and properties of bulk copper matrix composites strengthened with various kinds of graphene nanoplatelets, *Materials Science and Engineering A*. 628 (2015) 124–134. doi:10.1016/j.msea.2015.01.018.
- [143] X. Liu, D. Wei, L. Zhuang, C. Cai, Y. Zhao, Fabrication of high-strength graphene nanosheets/Cu composites by accumulative roll bonding, *Materials Science and Engineering A*. 642 (2015) 1–6. doi:10.1016/j.msea.2015.06.032.
- [144] G. Xie, M. Forslund, J. Pan, Direct electrochemical synthesis of reduced graphene oxide (rGO)/copper composite films and their electrical/electroactive properties, *ACS Applied Materials and Interfaces*. 6 (2014) 7444–7455. doi:10.1021/am500768g.
- [145] D. Zhang, Z. Zhan, Preparation of graphene nanoplatelets-copper composites by a modified semi-powder method and their mechanical properties, *Journal of Alloys and Compounds*. 658 (2016) 663–671. doi:10.1016/j.jallcom.2015.10.252.
- [146] X. Gao, H. Yue, E. Guo, S. Zhang, L. Yao, X. Lin, B. Wang, E. Guan, Tribological properties of copper matrix composites reinforced with homogeneously dispersed graphene nanosheets, *Journal of Materials Science and Technology*. 34 (2018) 1925–1931. doi:10.1016/j.jmst.2018.02.010.
- [147] X. Zhao, J. Tang, F. Yu, N. Ye, Preparation of graphene nanoplatelets reinforcing copper matrix composites by electrochemical deposition, *Journal of Alloys and Compounds*. 766 (2018) 266–273. doi:10.1016/j.jallcom.2018.06.309.
- [148] H. Jang, S. Yoo, M. Quevedo, H. Choi, Effect of processing route on mechanical and thermal properties of few-layered graphene (FLG)-reinforced copper matrix

- composites, *Journal of Alloys and Compounds*. 754 (2018) 7–13. doi:10.1016/j.jallcom.2018.04.272.
- [149] J. Hwang, T. Yoon, S.H. Jin, J. Lee, T.S. Kim, S.H. Hong, S. Jeon, Enhanced mechanical properties of graphene/copper nanocomposites using a molecular-level mixing process, *Advanced Materials*. 25 (2013) 6724–6729. doi:10.1002/adma.201302495.
- [150] L. Wang, Y. Cui, B. Li, S. Yang, R. Li, Z. Liu, R. Vajtai, W. Fei, High apparent strengthening efficiency for reduced graphene oxide in copper matrix composites produced by molecule-lever mixing and high-shear mixing, *RSC Advances*. 5 (2015) 51193–51200. doi:10.1039/c5ra04782j.
- [151] F. Chen, J. Ying, Y. Wang, S. Du, Z. Liu, Q. Huang, Effects of graphene content on the microstructure and properties of copper matrix composites, *Carbon*. 96 (2016) 836–842. doi:10.1016/j.carbon.2015.10.023.
- [152] L. Wang, Z. Yang, Y. Cui, B. Wei, S. Xu, J. Sheng, M. Wang, Y. Zhu, W. Fei, Graphene-copper composite with micro-layered grains and ultrahigh strength, *Scientific Reports*. 7 (2017) 1–10. doi:10.1038/srep41896.
- [153] D. Zhang, Z. Zhan, Strengthening effect of graphene derivatives in copper matrix composites, *Journal of Alloys and Compounds*. 654 (2016) 226–233. doi:10.1016/j.jallcom.2015.09.013.
- [154] Z. Yang, L. Wang, Z. Shi, M. Wang, Y. Cui, B. Wei, S. Xu, Y. Zhu, W. Fei, Preparation mechanism of hierarchical layered structure of graphene/copper composite with ultrahigh tensile strength, *Carbon*. 127 (2018) 329–339. doi:10.1016/j.carbon.2017.10.095.
- [155] C. Zhao, J. Wang, Fabrication and Tensile properties of graphene/copper composites prepared by electroless plating for structural applications, *Physica Status Solidi (A) Applications and Materials Science*. 211 (2014) 2878–2885. doi:10.1002/pssa.201431478.
- [156] Y. Tang, X. Yang, R. Wang, M. Li, Enhancement of the mechanical properties of graphene-copper composites with graphene-nickel hybrids, *Materials Science and Engineering A*. 599 (2014) 247–254. doi:10.1016/j.msea.2014.01.061.
- [157] X. Zhang, K. Wu, M. He, Z. Ye, S. Tang, Z. Jiang, Facile synthesis and characterization of reduced graphene oxide / copper composites using freeze-drying and spark plasma sintering, *166 (2016) 67–70*. doi:10.1016/j.matlet.2015.12.040.
- [158] X. Zhang, P. Dong, Y. Chen, W. Yang, Y. Zhan, K. Wu, Y. Chao, Fabrication and tribological properties of copper matrix composite with short carbon fiber/reduced graphene oxide filler, *Tribology International*. 103 (2016) 406–411. doi:10.1016/j.triboint.2016.07.027.
- [159] P. Duda, R. Muzyka, Z. Robak, S. Kaptacz, Mechanical properties of graphene oxide-copper composites, *Archives of Metallurgy and Materials*. 61 (2016) 863–867. doi:10.1515/amm-2016-0146.
- [160] M. Yang, L. Weng, H. Zhu, T. Fan, D. Zhang, Simultaneously enhancing the

- strength, ductility and conductivity of copper matrix composites with graphene nanoribbons, *Carbon*. 118 (2017) 250–260. doi:10.1016/j.carbon.2017.03.055.
- [161] K. Chu, X. hu Wang, F. Wang, Y. biao Li, D. jian Huang, H. Liu, W. lin Ma, F. xia Liu, H. Zhang, Largely enhanced thermal conductivity of graphene/copper composites with highly aligned graphene network, *Carbon*. 127 (2018) 102–112. doi:10.1016/j.carbon.2017.10.099.
- [162] W. Li, D. Li, Q. Fu, C. Pan, Conductive enhancement of copper/graphene composites based on high-quality graphene, *RSC Adv.* 5 (2015) 80428–80433. doi:10.1039/C5RA15189A.
- [163] D.B. Xiong, M. Cao, Q. Guo, Z. Tan, G. Fan, Z. Li, D. Zhang, Graphene-and-Copper Artificial Nacre Fabricated by a Preform Impregnation Process: Bioinspired Strategy for Strengthening-Toughening of Metal Matrix Composite, *ACS Nano*. 9 (2015) 6934–6943. doi:10.1021/acs.nano.5b01067.
- [164] G. Xie, M. Forslund, J. Pan, Direct Electrochemical Synthesis of Reduced Graphene Oxide (rGO)/ Copper Composite Films and Their Electrical / Electroactive Properties, *ACS Applied Materials and Interfaces*. 6 (2014) 7444–7455. doi:10.1021/am500768g.
- [165] S.K. Sahoo, A. Mallik, Simple, Fast and Cost-Effective Electrochemical Synthesis of Few Layer Graphene Nanosheets, *Nano*. 10 (2015) 1550019. doi:10.1142/S1793292015500198.
- [166] T.F. Emiru, D.W. Ayele, Controlled synthesis, characterization and reduction of graphene oxide: A convenient method for large scale production, *Egyptian Journal of Basic and Applied Sciences*. 4 (2017) 74–79. doi:10.1016/j.ejbas.2016.11.002.
- [167] S. Yang, S. Brüller, Z.S. Wu, Z. Liu, K. Parvez, R. Dong, F. Richard, P. Samorì, X. Feng, K. Müllen, Organic Radical-Assisted Electrochemical Exfoliation for the Scalable Production of High-Quality Graphene, *Journal of the American Chemical Society*. 137 (2015) 13927–13932. doi:10.1021/jacs.5b09000.
- [168] S. Abdolhosseinzadeh, H. Asgharzadeh, H. Seop Kim, Fast and fully-scalable synthesis of reduced graphene oxide, *Scientific Reports*. 5 (2015) 10160. doi:10.1038/srep10160.
- [169] D.C. Marcano, D. V. Kosynkin, J.M. Berlin, A. Sinitskii, Z. Sun, A. Slesarev, L.B. Alemany, W. Lu, J.M. Tour, Improved synthesis of graphene oxide, *ACS Nano*. 4 (2010) 4806–4814. doi:10.1021/nn1006368.
- [170] S. Park, J. An, J.R. Potts, A. Velamakanni, S. Murali, R.S. Ruoff, Hydrazine-reduction of graphite- and graphene oxide, *Carbon*. 49 (2011) 3019–3023. doi:10.1016/j.carbon.2011.02.071.
- [171] B. ANKAMWAR, F. SURTI, Water Soluble Graphene Synthesis, *Chemical Science Transactions*. 1 (2012) 500–507. doi:10.7598/cst2012.155.
- [172] J. Liu, H. Yang, S.G. Zhen, C.K. Poh, A. Chaurasia, J. Luo, X. Wu, E.K.L. Yeow, N.G. Sahoo, J. Lin, Z. Shen, A green approach to the synthesis of high-quality graphene oxide flakes via electrochemical exfoliation of pencil core, *RSC*

- Advances. 3(29) (2013) 11745–11750. doi:10.1039/c3ra41366g.
- [173] D. Yang, A. Velamakanni, G. Bozoklu, S. Park, M. Stoller, R.D. Piner, S. Stankovich, I. Jung, D.A. Field, C.A. Ventrice, R.S. Ruoff, Chemical analysis of graphene oxide films after heat and chemical treatments by X-ray photoelectron and Micro-Raman spectroscopy, *Carbon*. 47 (2009) 145–152. doi:10.1016/j.carbon.2008.09.045.
- [174] A. Ganguly, S. Sharma, P. Papakonstantinou, J. Hamilton, Probing the Thermal Deoxygenation of Graphene Oxide Using, *The Journal of Physical Chemistry*. 115 (2011) 17009–17019.
- [175] A. Mallik, B.C. Ray, Residual stress and nanomechanical properties of sonoelectrodeposited Cu films, *Surface Engineering*. 27 (2011) 551–556. doi:10.1179/1743294411Y.0000000011.
- [176] K. Jagannadham, electrochemical deposition with exfoliated graphene platelets Electrical conductivity of copper – graphene composite films synthesized by electrochemical deposition with exfoliated graphene platelets, 109 (2016). doi:10.1116/1.3701701.
- [177] S. Park, J. An, J.R. Potts, A. Velamakanni, S. Murali, R.S. Ruoff, Hydrazine-reduction of graphite- and graphene oxide, *Carbon*. 49 (2011) 3019–3023. doi:10.1016/j.carbon.2011.02.071.
- [178] S. Gollapudi, Grain size distribution effects on the corrosion behaviour of materials, *Corrosion Science*. 62 (2012) 90–94. doi:10.1016/j.corsci.2012.04.040.
- [179] T.R. Society, The wear of metals under unlubricated conditions, 236 (2014) 397–410.
- [180] A. Popoola, O.E. Olorunniwo, O.O. Ige, Corrosion Resistance Through the Application of Anti-Corrosion Coatings, *Developments in corrosion protection* 2.12 (2014) 241-270.
- [181] Y. Zhao, Y. Xie, Y.Y. Hui, L. Tang, W. Jie, Y. Jiang, L. Xu, S.P. Lau, Y. Chai, Highly Impermeable and Transparent Graphene as Ultra-Thin Protection Barrier of Ag thin Films, *Journal of Materials Chemistry C*, (2013) 4956–4961. doi:10.1039/c3tc30743c.
- [182] X. Pei, M. Noël, M. Green, A. Fam, G. Shier, Cementitious coatings for improved corrosion resistance of steel reinforcement, *Surface & Coatings Technology*. 315 (2017) 188–195. doi:10.1016/j.surfcoat.2017.02.036.
- [183] A. Mallik, Effects of temperature and ultrasound on nucleation behavior during electrochemical synthesis of copper thin films, Diss.2010.
- [184] D.D. Macdonald, The history of the Point Defect Model for the passive state: A brief review of film growth aspects, *Electrochimica Acta*. 56 (2011) 1761-1772.
- [185] J-E. Bao and D.D. Macdonald, Growth kinetics of the anodic oxide film on platinum under potentiodynamic polarization condition, *Z physic. Chem*. 227 (2013) 541-559.

- [184] D.A. Jones, Principles and prevention of corrosion. 2nd edition. Prentice Hall,1996.pp.34.

Dissemination

Internationally indexed journals

1. **A.K. Behera** and A. Mallik, Ultrasound assisted electroplating of nano-composite thin film of Cu matrix with electrochemically in-house synthesized few layer graphene nano-sheets as reinforcement, **Journal of Alloys and Compounds**,750 (2018) 587. **(I.F-4.65)**.
2. A. Behera, Ramkumar C, Smarajit Sarkar, **Archana Mallik**, An exploration on the use of in-house synthesized reduced few layer graphene nano-sheets as a reinforcement during sono-electroplating of Cu matrix nano-composite, **Journal of Alloys and Compounds**, 817 (2020) 152713. **(I.F-4.65)**
3. Akhya Behera and Archana Mallik, An investigation on anti-corrosion properties of electroplated copper-graphene nano-composite films, **Materials Science Forum** 978 (2020) 499. **Scopus indexed**
4. S. K. Sahoo, A. Behera, Ramkuar C, Archana Mallik, Industrial Scale Synthesis of few-layer graphene nano-sheets – An exploration on electrochemical exfoliation approach **Journal of Applied electrochemistry** 50 (2020) 673. **(I.F-2.384)**
5. **A.K Behera**, A.K. Patel, R. Mehta, S. Sarkar, Sanjeev Das, **Archana Mallik**, Exploration of in-house synthesized and functionalized graphene as reinforcement in Cu-matrix for improved mechanical and anticorrosion properties, **Diamond and Related Materials**, 109 (2020) 108009 **(I.F-2.65)**.
6. **A.K. Behera**, A. Das, S. das, A. Mallik, Electrochemically functionalized graphene as an anti-corrosion reinforcement in Cu matrix composite thin films, **International Journal of Minerals, Metallurgy and Materials** <https://doi.org/10.1007/s12613-020-2124-y> **(IF-1.713)**
7. **A.K. Behera**, R. Chandran, S Das and A. Mallik, Wear performance and nano-mechanical behaviour of sonoelectroplated Cu-graphene nano-composite thin films, **Journal of Materials Engineering and Performance** **(Revision due)**
8. **A.K. Behera** and A. Mallik, A Review on Fabrication Techniques of Copper-graphene Metal Matrix Nanocomposites. **NANO** **(Revision due)**

Conferences

1. **Akhya Kumar Behera**, Archana mallik, National Conference on Contributions of SC/ST Scientists and Technologists towards Advancement of Science and Engineering (NCSCSTASE), 23-25 January 2018, Bengaluru, India.
2. **Akhya Kumar Behera**, Archana mallik, International Conference on Processing and characterization of materials. 6-8 Dec 2018, Rourkela, Odisha, India.
3. **Akhya Kumar Behera**, Archana mallik, International Conference on Processing and characterization of materials. 12-14 Dec 2019, Rourkela, Odisha, India

Article under preparation

1. **Akhya kumar behera**, Archana Mallik, Green reduction of Graphene oxide synthesized from electro exfoliation method using acidic electrolyte. (**Under preparation**)
2. **A. K. Behera, A. Mallik**, Electrochemical corrosion of sono-electroplated Cu-graphene nanocomposite in borate buffer and 3.5% NaCl solution, (**Under preparation**)